UNIVERSITÀ DI PARMA

UNIVERSITA’ DEGLI STUDI DI PARMA

DOTTORATO DI RICERCA IN
“Scienza e Tecnologia dei Materiali”

CICLO XXXIV

Polyaniline-based neuromorphic devices towards interfacing sensing

Coordinatore:
Prof. Enrico Dalcanale

Tutore:
Dr. Salvatore Iannotta

Co-Tutore:
Dr. Pasquale D’Angelo

Dottorando: Roman Sajapin

Anni academici: 2018/19 – 2021/22

Note of thanks

Before all, I would like to thank Dr. Salvatore Iannotta for the assignment of this challenging and interesting topic, the trust he placed in me to accomplish the goals that have been set, and the great opportunity to learn and grow beyond myself in the process. I am very grateful for our fruitful collaboration and admire his readiness for constructive discussions and the ability to find approaches to upcoming challenges. I learned a great deal about scientific work and his guidance throughout this period has been invaluable. I felt and enjoyed a pleasant amount of mutual appreciation for the work we have done which truly motivated me all along.

A huge thank you goes to Dr. Pasquale D'Angelo for his willingness to co-supervise my thesis, the many discussions we had and the many valuable suggestions I received from him. Some of the most interesting ideas were born during our conversations, sharing thoughts and doubts alike. I will always appreciate his upbeat demeanour that was very encouraging and a needed source of optimism for me, especially during the last year of my PhD program.

Dr. Tatiana Berzina deserves my biggest gratitude as she introduced me to our exciting research field and practically showed me everything there was to know about the materials and techniques we worked with. I will remember the times when we worked together as some of the most exciting ones. The work with Tatiana taught me the value of being self-critical and maintaining a healthy amount of doubt about obtained results. At the same time, it taught me to stand by my own convictions, even if they are not initially met with approval. Without a doubt, my thesis would not have been the same without her involvement.

I would like to thank all the other members of our research group at IMEM and the Physics department, Dr. Victor Erokhin, Dr. Svetlana Erokhina, Dr. Silvia Battistoni, Dr. Valentina Ricci, Dr. Regina Burganova, Dr. Adelia Faizullina, Dr. Stefania Boi, Dr. Davide Vurro and Dr. Giuseppe Tarabella. It was an enrichment to work and exchange opinions with them and I have learned lots of valuable lessons over the course of these three years, not only about science, but life in general. A warm thank you to Stefania for our much appreciated, encouraging conversations. As I am sure most who worked with her would agree, the period when she joined our group felt very refreshing.

Special thanks go to the administrative of IMEM and the Physics department and the doctoral office for making my work a lot more trouble-free. I also thank Dr. Davide Vurro once again for his help in operating the AJP and SEM as well as Dr. Matteo Cocuzza and Dr. Simone Marasso for providing the photolithographed electrode samples. I thank Dr. Milad Takhsha for the much-appreciated help with AFM imagery. I am grateful to Salvatore Vantaggio from the group of Prof. Antonella Parisini as well as Dr. Marco Villani, Dr. Riccardo Manfredi and Dr. Andrea Sala from IMEM for being ready to help with one or the other small thing that I needed.

I thank Dr. Mirko Buttrini and Prof. Adriana Calderaro from the Department of Medicine and Surgery for the opportunity to acquire the MALDI-TOF spectra. I also thank Dr. Silvia D'Auria for the recorded IR spectra and other members of the group of Prof. Enrico Dalcanale who treated me very kindly and made me feel welcome in the Chemistry department. Special thanks are due to Prof. Dalcanale himself for generously providing a few valuable reagents and, more importantly, for his teaching and the valuable scientific advice and encouragement I received over these years.

I would like to express my deepest gratitude to Dr. Tobias Gruber for the motivation and support he gave me before and during my doctorate. I am grateful for the education I received during my undergraduate studies at the University of Freiberg. Despite having missed out on one or the other lecture of his (which Tobias likes to remind me of sometimes!), I consider myself lucky to have been his student. He laid the foundation for my views on science and it is safe to say that my interest in research was awoken during my bachelor thesis under his supervision.

A huge thanks is due to all my old friends and the new ones I made along the way. They have been a very welcome distraction that I needed at times and their moral support has kept my spirit up. Especially I would like to mention Igor, who at times seemed to be even more emotionally invested in my doctorate than myself. I hope one day I can make up for the times when I couldn’t be as present as I wish I was.

No words can describe my gratitude for my family. I am glad you don’t expect anything to be said because I don’t quite know how to express it. Thank you for your understanding, patience, and foresight. Thank you for your unconditional support and for always being there when I needed you, even at times when we disagreed on things. Спасибо вам за всё.

Finally, I am grateful to those who motivated me to take this step. It was a rich source of personal growth and probably the best decision I have ever made so far. Without you, none of this would have happened. I’m glad it did.

Abstract

Memristors are electronic elements that belong to a new generation of computational systems with a great potential to contribute to the promising revival of scientific research dedicated to the hardware realization of Artificial Neural Networks (ANNs) towards Artificial Intelligence (AI) and computer-brain interfaces. A distinctive property of these devices is the dependence of their internal resistance on the electrical charge that passed through them. In other words, there is a correlation of the output characteristics of the device and the history of its use, in which it resembles biological synapses and can be considered as their artificial analogue, displaying spike time dependent plasticity (STDP). Furthermore, the ability of controlled switching between different internal resistive states makes memristors some of the most promising candidates for the implementation in memories. Contrary to the conventional Von Neumann architecture, hardware-realized ANNs have the potential of combining the storage and processing of information, carried out by the same kind of elements, mimicking biological neurons in the brain. Parallel information processing would allow to simultaneously work with a whole array of inputs, rather than carrying out one single operation at a time. These properties pave the way towards more energy- and time-efficient computing by avoiding the need to exchange information between the processor and a passive memory. The similarity to biological synapses suggests an excellent biocompatibility and the possibility to emulate some functionalities of biological systems, enabling computer-brain interfaces with a seamless transformation and processing of bioelectronic signals.

The Organic Memristive Device (OMD) is a polymer-based representative of such elements. It is a two-terminal device featuring a conductive channel of polyaniline (PANI) whose resistance is modulated through electrochemically controlled transitions between the polymer's insulating and conductive state. These transitions take place in a heterojunction of PANI and a polyethylene oxide (PEO)-based solid polyelectrolyte (SPE) doped with a source of chloride among other stability enhancing additives, promoting the reaction with a silver counter electrode. Its advantages with respect to other memristors are its low-cost fabrication and the ability of fine-tuning of the channel resistance, granted by accessing intermediary resistive states.

The main goal of the present PhD thesis is to develop OMDs suitable for neuromorphic applications such as the interfacing sensing and signal processing that can be realized by means of multilayer perceptron structures. The combination of a large array of elements in one network as well as working with complex biological systems implies the occurrence of electrical noise, which poses the question how it interferes with the functioning of our device. Preliminary research has shown that the current-state OMD does not possess the necessary level of stability to reliably to carry out such sensitive experiments. Hence, a significant part of our research was devoted to the optimization of the materials employed in OMD fabrication. The goal is to advance towards devices with higher endurance, i. e., reproducible output characteristics over longer periods of time, and to examine how to design the fabrication techniques to improve biocompatibility.

A significant part of our work was focused on the stabilization of the labile, polyethylene oxide-based SPE system by optimizing its composition with particular attention to the dopant salts. This work follows and builds upon an extensive theoretical study of the role of the single dopant ion species on the operation mechanism of the OMD. It was demonstrated that the former concept which attributes a significant role in the switching process to lithium ion doping is inaccurate. Instead, it is shown that the anions are the most critical dopant species in terms of device operation. Furthermore, through a combination of theoretical and extensive practical work, novel recipes of PEO-based SPEs have been developed, providing unprecedented short-term and long-term stability with a remarkable reproducibility of I-V-characteristics, improving the endurance of the OMD by up to two orders of magnitude. A significant part of this success is due to the implementation of aluminium chloride to the SPE system, providing intrinsic acidity and enabling to avoid doping by strong, volatile acids such as HCl. This discovery was followed up by intensive research of routes to stabilize the PEO-based gels and impart them with favourable properties for long-term endurance by preventing aggregation. During this research, the formerly unheeded concept of lyotropicity was introduced to OMDs, recognizing it as a major aspect for the stability of the polyelectrolyte system. Furthermore, silk fibroin solutions have been successfully employed for the first time as an alternative to PEO-based SPEs, further advancing prior research towards the introduction of biocompatible materials into OMD fabrication.

Another important aspect of the implementation of OMDs in complex systems for the interfacing of sensing and signal processing is the integrability with other electronic systems such as OECT-based sensors. This can be most effectively achieved by shifting the paradigm of OMD manufacturing from largely manual towards high-precision, automated fabrication. To this end, we developed materials that can be applied by means of direct-writing techniques such as Aerosol Jet Printing (AJP). Particular attention was paid to the conductive polymeric component of the device. Successful attempts have been made by developing AJP-compatible inks based on pristine PANI in a mixture of organic solvents such as NMP, xylene and isopropanol, that were successfully applied on quartz and Si/SiO$_2$ substrates. Furthermore, a water dispersible composite material of PANI and chitosan was synthesized, further improving the quality of the printed features and the coverage of the substrates. Both printed materials have been implemented to successfully fabricate the first functioning PANI-based OMDs featuring a printed conductive channel, displaying the characteristic properties of a memristor.

The combination of all the experimental results and intensive theoretical work lays the foundation and paves the way towards the implementation of OMDs in advanced, complex, biocompatible, (bio)integrable systems for bio-interfacing purposes.

List of utilized abbreviations

12C4	[12]crown-4 (crown ether compound)
AJP	aerosol jet printing
ANN	artificial neural network
APS	ammonium peroxydisulfate (or ammonium persulfate)
AZ	active zone of the OMD
BHT	3,5-di-tert-butyl-4-hydroxytoluene (an antioxidant)
CGF	carrier gas flow (in AJP)
CPA	chitosan/polyaniline composite
CSA	camphorsulfonic acid
DBSA	*p*-dodecylbenzenesulfonic acid
GndCl	Guanidinium chloride (or guanidine hydrochloride)
I_{EL}	electronic current (in I-V characterization)
I_G	ionic current or gate current (in I-V characterization)
I_{SD} or I_{TOT}	total current or source-drain current (in I-V characterization)
IJP	inkjet printing
IPA	isopropanol (isopropyl alcohol)
LIB	lithium-ion battery
LS	Langmuir-Schaefer technique
NEA	*Norland Electronic Adhesive* (product name)
NMP	*N*-methylpyrrolidone (or *N*-methyl-2-pyrrolidinone)
OMD	organic memristive device
PANI (-LE, EB, ES, PS)	polyaniline (leucoemeraldine, emeraldine base, emeraldine salt, pernigraniline salt)
PEDOT:PSS	poly(3,4-ethylenedioxythiophene) doped with polystyrene sulfonate
PEO	poly(ethylene oxide) (or polyethylene oxide)
TSA or TsOH	tosylic acid (or *p*-toluenesulfonic acid)
SCE	standard calomel electrode
SDS	sodium dodecyl sulfate
SF	silk firoin
ShGF	sheath gas flow (in AJP)
SPE	solid polyelectrolyte (or solid-state polymer electrolyte)
STDP	spike-time-dependent plasticity

Table of contents

1 Introduction and state of the art

1.1 Memristors

Memristors are electronic devices that are among the best candidates for a new generation of information technologies. The reason for the emergence of this promising field is the ever-growing demand for highly efficient computing power which, as it seems, can no longer be satisfied by conventional Complementary Metal Oxide Semiconductor (CMOS) technology alone. Although CMOS technology has experienced a great development over the last decades, constantly increasing the computing performance according to Moore's law, further advances in the realm of sub-10-nanometer nodes seem to become difficult as physical limitations make a sustainable and cost-efficient downscaling increasingly difficult [1]. There is hence a need for a new type of devices whose potential for increased efficiency would lie not primarily in their dimensions but in the fundamental differences of the computing platform that they represent. The idea is to emulate the functioning of natural systems in an approach that is called neuromorphic. In this framework, the great advantage of memristors is that they emulate the functioning of a synapse and combine the properties of a resistor and a memory.

In fact, the memristor's distinctive property is that its resistive state depends on the electrical charge that passed through it, i. e., the history of its use, resembling biological synapses between neurons. In neurosciences, this property is called spike-timing dependent plasticity (STDP), meaning that the connection between two neurons becomes stronger as they are stimulated together. This principle stands behind the so-called unsupervised learning or Hebbian learning in living organisms [2]. This property is the basis for the processing and storage of information in biological neural networks such as the brain. The similarity of memristors to biological synapses allows to implement them in Artificial Neural Networks (ANNs). Their main difference from the Von Neumann architecture is that the same elements carry out the functions of the processor and the memory, while conventional computing relies on a constant exchange of information between a passive memory and the processor, which costs additional time and energy. The realization of ANNs on a hardware level has attracted the attention of researchers since the mid-1950s [3],[4] but temporarily lost in significance due to the quick development of CMOS technology that shifted the focus towards their implementation through software modelling. However, the hardware-realization of ANNs remains relevant as it can potentially significantly increase the computational power while decreasing the energy consumption and improving the economic efficiency.

An early iteration of a synapse-like element called "memistor" has been proposed in 1961 by Widrow *et al.* [5] as an "adaptive vote-taker" that would compare the outputs of paralleled system parts in a binary system, determining the outcome based on past performance. This should allow to prolong the lifetime of an electronic device by eliminating faulty inputs from corrupt elements and thus maintaining the functional integrity of the system. The memistor was a three-electrode device structurally similar to the transistor. The main difference was that the source-drain conductivity of the memistor was modulated by the integral of the current flowing through the gate electrode, as opposed to the applied gate voltage in the case of a transistor.

The term “memristor” has been coined in 1971 by Chua [6] who postulated that in analogy to the four passive circuit elements (resistor, capacitor and inductor coil), there must be a “lost” fourth analogue element. The characteristic physical properties of these three established elements are proportionality coefficients in linear relationships between the four fundamental properties of electric circuits: current, voltage, electric charge and magnetic flux (e. g. $dv = Rdi$ for a resistor). According to Chua’s initial postulate, the memristor should correlate the electric charge and the magnetic flux with the memristance M as the proportionality factor, as shown in Equation 1 and Figure 1-1.

$$d\varphi = Mdq \qquad \text{Equation 1}$$

It was shown that with a constant memristance, the device would behave like a resistor with a linear relationship of voltage and current. However, assuming the memristance as a function of the electric charge, the more generalized relationship in Equation 2 applies.

$$v(t) = M(q)i(t) = M\left(\int_{-\infty}^{t} i(\tau)d\tau\right)i(t) \qquad \text{Equation 2}$$

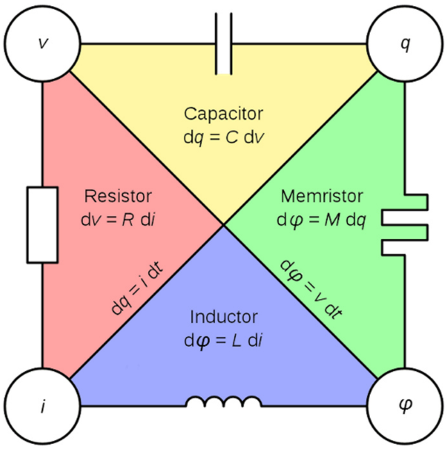

Figure 1-1: Scheme representing the three passive electric circuit elements resistor, capacitor and inductor coil, as well as the postulated memristor and the respective characteristic relationships between the fundamental circuit properties that they represent.

An increased interest in this research field was sparked in 2008 by a publication by Strukov *et al.* (HP Labs) [7] in which the authors claim to have found Chua’s missing memristor. Their device consisted of a 50 nm thin film of titanium oxide between two platinum electrodes, divided in regions with different resistances caused by different levels of doping (by oxygen vacancies), as shown in Figure 1-2. The overall resistance of the device was modulated through the application of a voltage bias across the channel that caused the boundary between these regions to move, caused by a drift of charged dopants. The charge-dependent memristance parameter in this device can be described as:

$$M(q) = R_{off}\left(1 - \frac{\mu_V R_{on}}{D^2} q(t)\right) \qquad \text{Equation 3}$$

where μ_V is the ionic mobility of the oxygen vacancies, D is the thickness of the film, R_{on} and R_{off} are the resistances of the doped and undoped region and q is the charge passing through the channel. The term $1/D^2$ reveals that the memristive effect connected to the difference of memristance in the on and off state only becomes relevant in very short channels, suggesting the need to move towards the nanoscale [7].

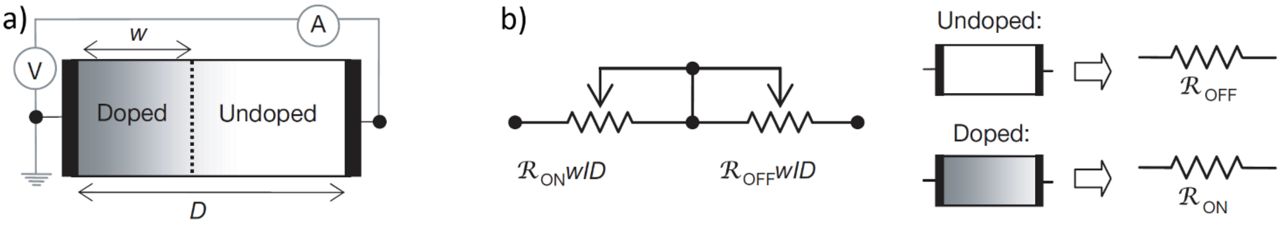

Figure 1-2: Schematic representation of Strukov's TiO_2 film-based memristor (a) with the respective equivalent circuit (b) (adapted from [7]).

Arguably, however, this was not the first developed memristive device as many such devices have been developed earlier [8]–[12], including other metal oxide-based systems or the Organic Memristive Device [13], albeit without naming them "memristors" at their time. This is probably due to the fact that, strictly speaking, none of the existing devices fulfilled Chua's original postulated definition. Even though the original idea of Chua is still under debate, the developments in the field are of ever-growing impact with ever-further reaching achievements in the realization of systems of increased complexity.

Types of memristive devices

Nowadays, the vast majority of memristive devices are based on inorganic materials, most of which have the capacitor-like metal/metal oxide/metal structure described above. Their general functioning mechanism is the generation and disruption of localized conductive paths (filaments) in most of the cases formed by the oxygen vacancies in the oxide region [1]. Besides the TiO_2 used by Strukov, other metal oxides have been employed: SiO_2 [14],[15] and CuO [16], distinguished by their high compatibility with the CMOS process, Al_2O_3 [17], HfO_x [18],[19], ZrO_2 [20], TaO_x [21], Gd_2O_3 [22], CeO_2 [23], ZnO [24]–[26] and NiO [27] and others. Most of the metal oxide based memristive devices display an abrupt switching behaviour, making them suitable for binary data storage and processing, while some display a gradual transition between several transient resistive states, hence being suitable for analog computing. Especially the devices featuring an abrupt resistance change have the advantage of particularly fast switching kinetics, although in some cases, the set and/or reset process (like in the case of NiO) requires comparatively high voltages, which makes them less appropriate for low-power applications.

Another type of memristive devices are the so-called Phase Transition or Phase Change Memristors (PCMs). They are mainly fabricated with chalcogenide materials such as $Ge_2Sb_2Te_5$ [28]. The basic operation principle of PCMs is the change between resistance states caused by a phase transition of the material. It occurs due to Joule heating when current pulses are applied, causing the present phase to melt, whereas rapid cooling (short pulse with a high amplitude that is rapidly decreased) causes a transition to a nonconductive, amorphous phase and slower cooling (longer, smaller pulse) leads to the formation of the conductive, crystalline phase. Such a switching mechanism has the advantage of relatively low volatility of the programmed resistive state. However, it also bears several disadvantages such as slow switching-on because of the slow formation of the crystalline phase; high required current pulses (reset currents above 100 µA); possible thermal crosstalk between adjacent PCM cells in crossbar arrays; possible formation of voids and vacancies between the PCM and the electrode material during repeated cycling [1]. Attempts to solve these issues include careful programming of the amplitude and length of the applied pulses, employing low contact area or porous electrode geometries [29],[30] and pre-treating and doping of the phase change material to improve the thermal properties of the crystalline phase [31],[32].

Memristive devices based on organic materials are generally far less common but are represented by a number of different operation principles depending on the system at hand. Considering their currently overall minor development with respect to inorganic devices, it goes beyond the scope of the present work to make a detailed discussion of all the various switching mechanisms. Instead, we refer the reader to some literature featuring other devices based on organic materials [33],[34] such as Au-nanoparticles functionalized with electropolymerizable thiophene-EDOT units [35], metal-coordinated azo-aromatics [36] or biomaterials such as egg albumen protein [37].

The first reports are based on the polyaniline-based Organic Memristive Device, which is discussed in detail in section 1.2, being an architecture of reference for this thesis, is based on the solid-state electrochemical transition of a conductive polymer in a three-electrode configuration. A similar, electrochemically gated device was developed by Kumar *et al.* [38], featuring essentially the same geometry but a different polymer (poly(3,3-didodecylquaterthiophene)).

Another type of devices features a mechanism based on the formation and disruption of metal filament structures between electrodes, one of which is metallic, as illustrated in Figure 1-3. In the work by Yang *et al.* [39], a layer of fluorenone- and carbazole-based, redox active, small organic molecules (FLOCZ and FLOBCZ) is deposited between an ITO and an Ag electrode. The formation of Ag filaments occurs through the oxidation of silver at the Ag electrode and reduction of the

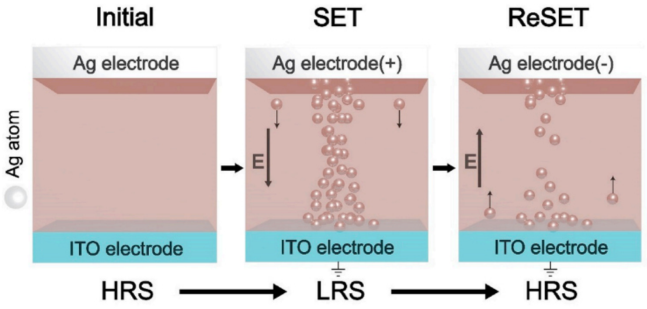

Figure 1-3: The Ag filament-formation mechanism in a fluorenone/carbazole material-based memory device (from [39]).

migrating Ag^+ ions at the ITO electrode, assisted by the redox active material. A similar switching mechanism is reported in other works featuring parylene [40]–[42], or bioinspired materials such as chitosan [43] or silk fibroin [44] as the active material deposited between Ag and Pt electrodes.

1.2 The Organic Memristive Device

An Organic Memristive device (OMD) is essentially a solid polyelectrolyte (SPE) junction of the intrinsically conductive, electrochromic polymer polyaniline (PANI) and a silver electrode that enables the switching between different resistive states [13]. The general structure of the device is shown in Figure 1-4. The OMD is a two-terminal device with two metal electrodes (typically Cr) evaporated on 15 x 7 mm quartz slides as a substrate. The electrodes are connected by a PANI channel which is deposited by the Langmuir−Schaefer technique (LS) [45] with consequent doping in HCl.

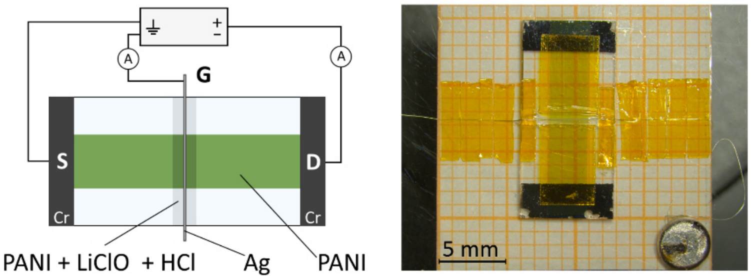

Figure 1-4: Schematic representation of an OMD and a photograph of an assembled device.

This method is a variant of the Langmuir−Blodgett technique in which the target material is deposited on the substrate surface horizontally, as demonstrated in Figure 1-5. LS has been applied for a broad variety of organic and inorganic materials, such as polymers like poly(3-hexylthiophene) (P3HT) [46], MOFs [47], graphene [48] and graphene oxide [49], dimeric phthalocyanines [50] and iron oxide nanoparticles [51]. The technique is based on the formation of self-organized monolayers of the target material on the surface of a liquid subphase through slow compression of the surface area up to a certain surface tension value. This approach bears the great advantage of exceptionally precise control over the thickness of the applied film because it is deposited one monolayer after another. In OMD fabrication, PANI is applied on a water subphase in the form of a diluted solution (0.1−0.2 mg/ml) in *N*-methyl-2-pyrrolidone (NMP) and toluene (9:1 v/v). The toluene is added to prevent that the polymer is dragged into the subface with NMP which is miscible with water and slightly denser. The lighter toluene keeps the PANI afloat as it spreads over the water surface. Because the monolayer is easily distorted when parts of it are removed from the subphase after compression, a separating grid is placed onto the surface to divide it into smaller segments in order to minimize material loss. A typical film consists of 50−60 LS PANI monolayers and is about 100−120 nm thick. An attempt has been made to realize the fabrication of the active channel by the layer-by-layer technique, depositing alternating layers of PANI and polystyrene sulfonate (PSS) [52]. However, the devices produced with this approach showed lower specific conductivity levels and on/off ratios.

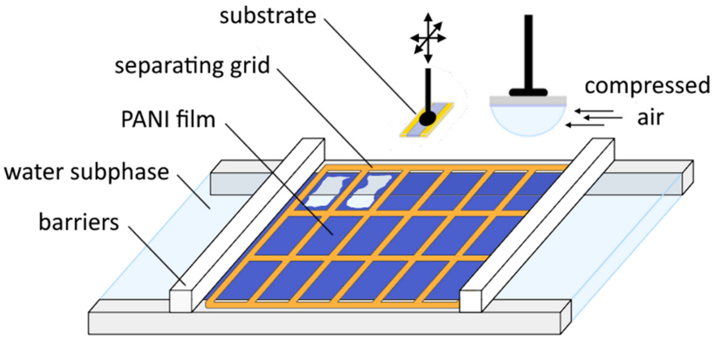

Figure 1-5: Schematic representation of the Langmuir−Schaefer technique.

The resistivity of the deposited PANI can be tuned in a narrow zone in the middle of the channel that is covered by the manually cast stripe of a polyethylene oxide (PEO) gel that solidifies and functions as the SPE. The silver wire is placed at a short distance above the PANI channel, submerged in the PEO gel perpendicular to the channel direction. Because the device somewhat resembles a field effect transistor (FET) schematically, the corresponding denotation has been adapted for the three electrodes. The silver electrode is named the gate (G), and the two electrodes on both ends of the PANI channel are named the source (S) and drain (D). The gate is short-circuited with the grounded source and a voltage is applied to the drain and distributed across the channel, causing electrochemical reactions at certain given potentials. The process of the resistive switching of the device as well as the underlying chemical transformations of the polyaniline are explained below in more detail.

1.2.1 Materials employed in OMD manufacturing

1.2.1.1 Polyaniline as the electrically conductive polymer component

Polyaniline has a basic poly(*p*-phenyleneimineamine) structure, consisting of alternating benzenoid amine and quinoid imine moieties. As shown in Figure 1-6 for a minimum degree of polymerization of 8, in earlier works, five different oxidative states could be isolated and chemically interconverted through oxidation with hydrogen peroxide or reduction with $TiCl_3$ or phenylhydrazine [53]–[55]. The polymerization of the monomer aniline (or its hydrochloride) is most commonly carried out in acidic media with of oxidizing agents such as ammonium peroxydisulfate (APS) or electrochemically, yielding the polymer in its emeraldine salt form (PANI-ES).

The forms of polyaniline can be distinguished with spectroscopic methods. Figure 1-7 shows the characteristic absorption spectra of the three polymer base forms in the UV/Vis range [55],[56]. Leucoemeraldine displays only one significant absorption band at 343 nm which corresponds to the π-π^* transition in the aromatic system. In emeraldine, this band is hypsochromically shifted and a new band at 637 nm appears which is attributed to a molecular exciton associated with the quinone diimine fragment. In pernigraniline, the band at 530 nm is attributed to a Peierls gap transition [57]. FTIR spectra are presented in Figure 1-8 [58],[59]. The most relevant characteristic vibrations for the

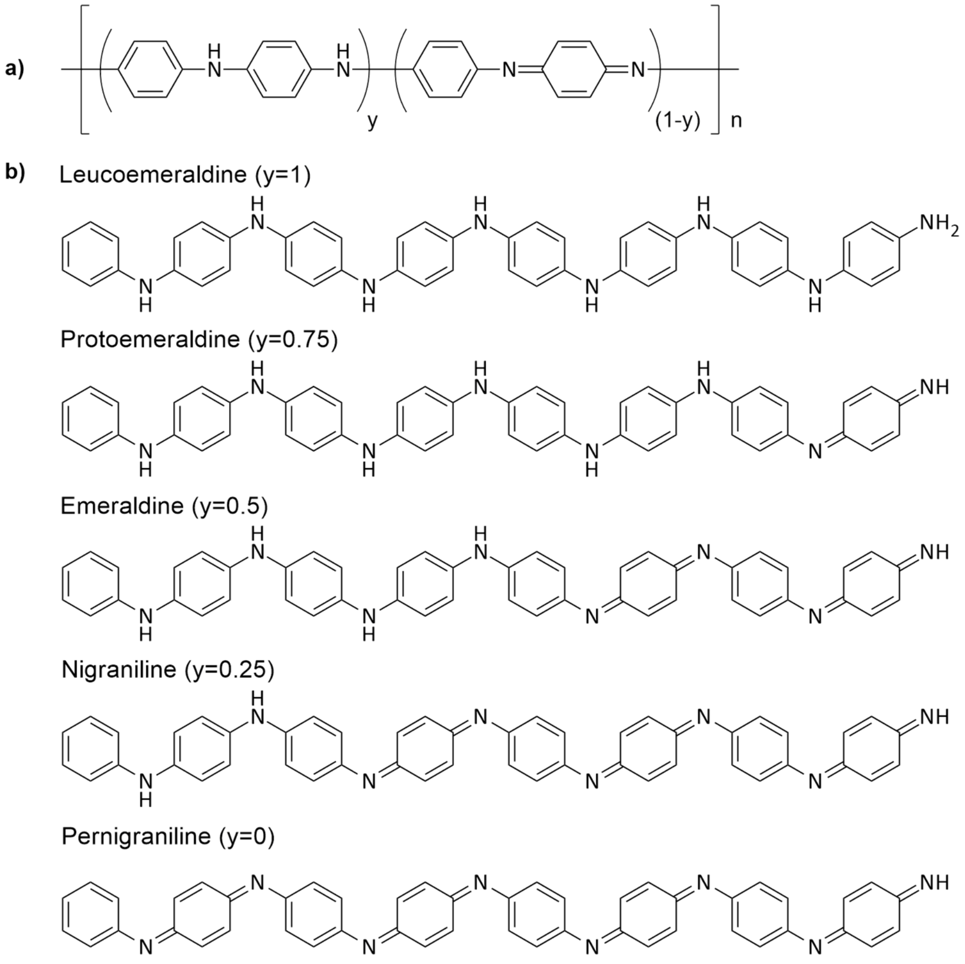

Figure 1-6: a) General chemical structure of PANI and b) its oxidative states for a minimum degree of polymerization of 8 (adapted from [55]).

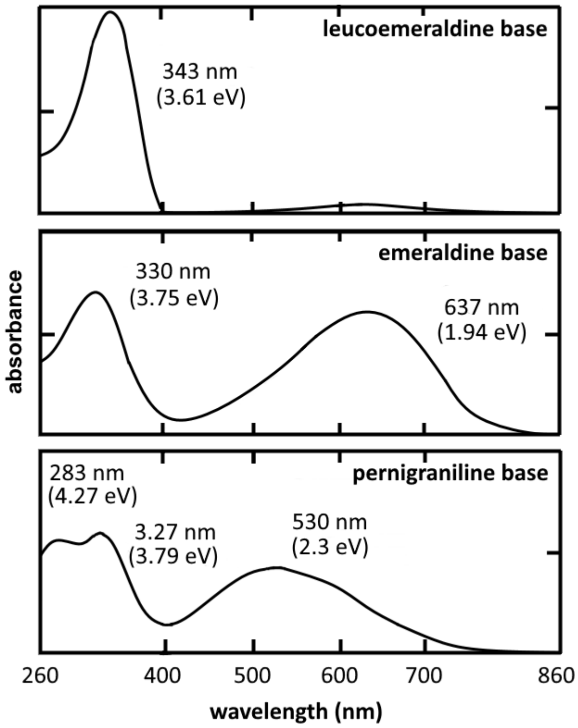

Figure 1-7: Optical absorbance spectra of the base forms of polyaniline, adapted from [56].

base polymer are δ_{op}(C−H) on 1,4-disubstituted rings at 823 cm^{-1} and δ_{ip}(C−H) at 1100−1170 cm^{-1}, ν(C−N) of the secondary amine groups with a band at 1299 cm^{-1}, ν(C−N) of the imine groups at 1378 cm^{-1}, ν(C=C) in benzenoid rings at 1496 cm^{-1}, ν(C=C) in quinoid rings at 1588 cm^{-1} [59]. The latter two bands and their ratio can be used to distinguish between the leucoemeraldine, emeraldine and pernigraniline forms [60]. The conductive emeraldine salt state can be recognized by the appearance of bands at 1238 cm^{-1} and 1140 cm^{-1} that are assigned to the ν(C−N$^{+\bullet}$) and ν(=NH^{+}−) vibrations of the polaron and bipolaron structures, respectively [59], the origin of which is explained below.

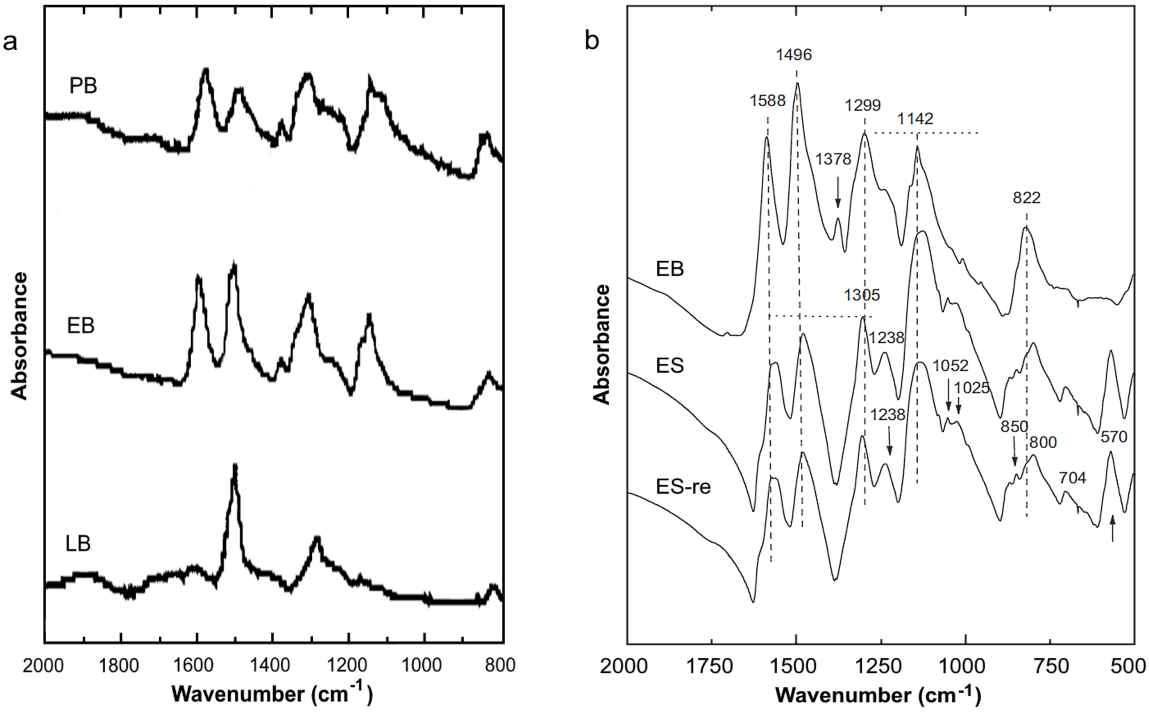

Figure 1-8: a) FT-IR spectra of the base forms of polyaniline: leucoemeraldine (LB), emeraldine (EB), pernigraniline (PB), adapted from [58]; b) FT-IR spectra of emeraldine base (EB), emeraldine salt (ES) and emeraldine salt after exposure to KOH and reprotonation (adapted from [59].

Doping of polyaniline

The emeraldine salt is the transient state with the highest conductivity and hence the most relevant one for OMD operation, reaching conductivity levels in the order of 1−5 S cm^{-1} [61]. All forms of polyaniline can be electrochemically transformed in one another and can exist in their respective base and salt form, depending on the pH of the environment, as demonstrated in Figure 1-9 [62]–[64]. The so-called doping of a base form to its respective salt form occurs due to the acid-base activity of the amine and imine groups of the polymer chains. For instance, the commercially available nonconductive emeraldine base (PANI-EB) can be chemically doped with an acid such as HCl to obtain the conductive emeraldine salt (PANI-ES). The process is fully reversible as treating the doped polymer with an ammonia solution deprotonates it, yielding PANI-EB [61]. This can be seen in Figure 1-8 as the spectra of PANI-ES are largely equal after and prior to

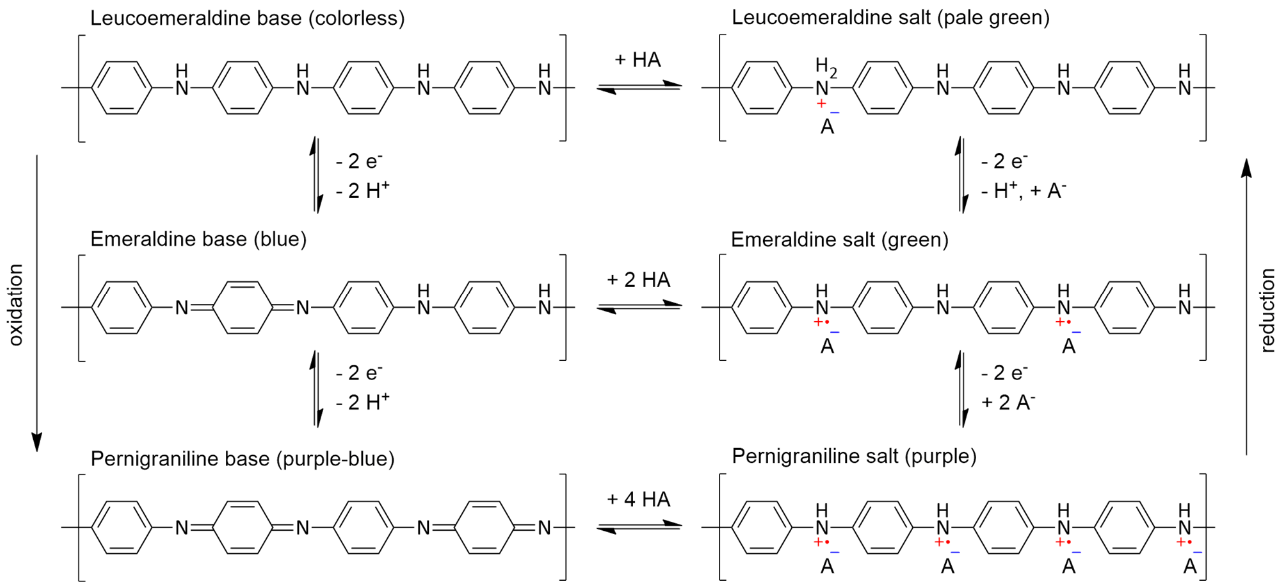

Figure 1-9: Mutual transformations of the forms of PANI by means of redox reactions and chemical doping.

reprotonation. It must be pointed out that in the pernigraniline salt state, the compound becomes unstable due to the imine groups' proneness to hydrolysis in an acidic medium [60]. However, there have been successful attempts to stabilize pernigraniline by means of N-alkylation to increase basicity [65] or by employing hydrophobic ionic liquids [66],[67].

Charge carriers in polyaniline

The doping phenomenon is closely connected to the formation and nature of charge carriers as well as their transfer along the polymer chains. In literature, the process is most commonly described under the assumption that the doping is initiated by the protonation of imine nitrogen atoms [68]–[71]. At first glance, this may seem controversial because the sp^3 hybridization of amine nitrogen atoms suggests a higher basicity with respect to the structurally related, sp^2 hybridized imine counterparts, making the former more prone to protonation than the latter. However, it must be considered that in a dynamic system, the exchange of protons between different basic sites can takes place. The exclusive protonation of amine sites cannot be followed by any redistribution of charge along the polymer chain, whereas the protonation of imine nitrogen atoms leads to electronic rearrangements that result in an energetically more favourable structure. As shown in Figure 1-10, the initial protonation causes the formation of (di)cationic quinone diiminium fragments, named bipolarons. They are then transformed into their resonant radical cationic polaron form which is energetically more favourable due to the extension of the aromatic system [72]. The electrical conductivity of the material is given by the decoupling of the created neighbouring charge carriers and their delocalization along the polymer chain so as to minimize Coulomb repulsion.

The presence of the polaron as a state with unpaired electrons has been proven by means of magnetic susceptibility measurements [73],[74] and electron paramagnetic resonance (EPR) [75]. The coexistence of polarons and bipolarons was further proven by X-ray photoelectron spectroscopy

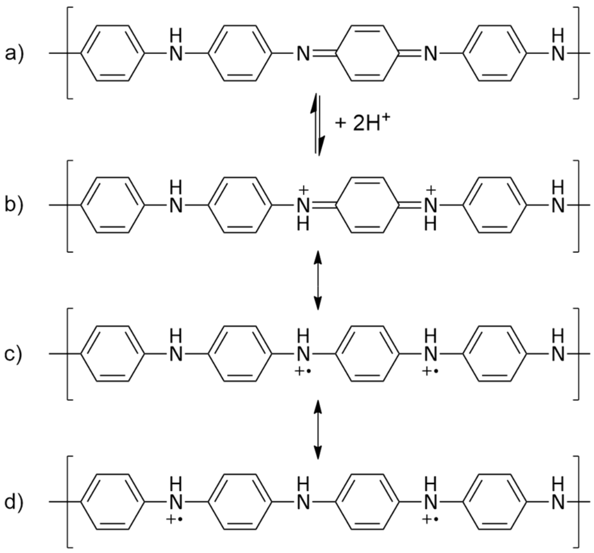

Figure 1-10: Scheme of the process of doping of emeraldine base, anions are omitted (adapted from [72]). a) Emeraldine base polymer, b) formation of the bipolaron lattice upon protonation, c) electronic rearrangement to polaron state, d) resulting polaron lattice as a consequence of charge delocalization.

(XPS) in combination with elemental analysis and optical spectroscopy [76],[77]. Inoue *et al.* [76] estimated a polaron to bipolaron ratio of about 5:1 in a perchlorate doped PANI sample. Furthermore, the XPS technique was employed to gather evidence for the proposed protonation mechanism, taking advantage of the fact that the position and shape of N(1s) line are sensitive to the electronic environment of the nitrogen atoms which changes upon oxidation and doping. The fitted line components in the N(1s) core-level spectrum for the quinoid imine, benzenoid amine and positively charged nitrogen atoms have been identified by Kang *et al.* [78],[79], with band energies at 389.1 eV, 399.3 eV and > 400.5 eV, respectively. To study the doping process, the authors exposed the emeraldine base polymer to non-volatile acids (H_2SO_4 or $HClO_4$) and evaluated the signal intensities from the N(1s) and S(2p) or Cl(2p) core-level spectra, which allowed to estimate the doping level at different acid concentrations [69]. H_2SO_4 and $HClO_4$ were chosen as doping agents because volatile dopants such as HCl are not suited for measurements in ultra-high vacuum and the Cl^-/N ratio seldom exceeds 0.5 even at high acid concentrations [78]. According to their data, upon protonation, the imine signal disappears in favour of the emerging charged nitrogen signals. The intensity of the amine signal remains largely unchanged at doping levels up to 50 % (in 1 N acid) but diminishes in favour of the signals of charged species at higher doping levels (in concentrated acid), as demonstrated in Figure 1-11 a−d). This suggests that amine nitrogen atoms participate in the acid-base reaction only after all the imine nitrogen atoms are protonated. The authors also report that the conductivity of the excessively doped polymer (anion/N ratio > 0.5) diminishes with respect to a doping level of 50 %, which is due to the distortion of the π-conjugation and the polaron lattice by protonated amine units ($-NH_2^+-$). The same is reported by Yue *et al.* [80] for a sulfonated, self-doping polyaniline sample: the conductivity is lower when more than 50 % of quinoid and benzenoid rings are sulfonated. In another work, Snauwaert *et al.* [70] have correlated the percentage of imine nitrogen atoms with the oxidation of PANI starting from its leucoemeraldine base form, recording XPS spectra after the application of different potentials (Figure 1-11 f). Their results coincide with the abovementioned electronic transformation of the polymer, although it must be pointed out that according to the imine percentage (about 75 %), the product of the second oxidation step at +0.8 V appears to be nigraniline rather than pernigraniline. The data also shows that the oxidation occurs at more or less discrete values rather than gradually over the potential range.

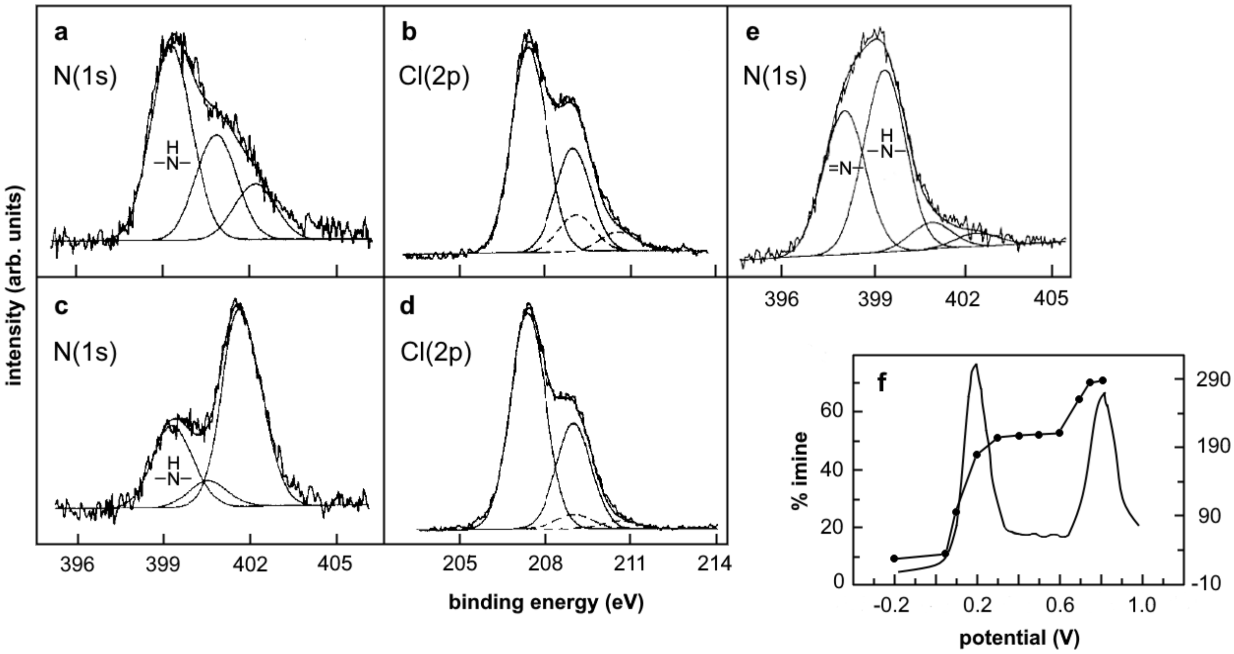

Figure 1-11: N(1s) and Cl(2p) core-level XPS spectra of HClO4 doped emeraldine films with a ClO_4^-/N ratio of a, b) about 0.50 and c, d) about 0.78. e) N(1s) core level spectrum of an emeraldine base film (a–e adapted from [69]). f) XPS-determined imine content in polyaniline as a function of the applied potential at pH = 0 (black dots) in correlation with the CV oxidation scan (solid line), adapted from [70].

In classical semiconductor terms, the radical cationic polarons can be considered as electron holes and thus, PANI is denoted as a p-type organic semiconductor. Contrary to common inorganic semiconductors, PANI, like other electrically conductive polymers, requires high levels of doping, reaching highest conductivity at 50 % protonation which corresponds to a pH of 2 or lower [81]. The reason is the depinning of charge carriers which is best understood considering their environment. Although delocalization is possible throughout the highly conjugated electronic system, at low doping levels the charge defects are widely separated from one another. In order to maintain charge neutrality, each charge carrier migrates as a pair together with its associated counterion, having the relatively slow diffusion of the latter as the limiting factor. At high doping levels, each polaron finds itself in the vicinity of multiple anions, not being pinned to any particular one, and can migrate faster along the polymer chain in the mean field of the surrounding counterions [82]. In the bulk of the polymer, the limiting factor for the conductivity of PANI is the electron transfer from one chain to another, which suggests a dependence of charge mobility from the morphology of the material. In their work, Focke *et al.*, [83] propose a mechanism according to which interchain charge transfer can be facilitated by protonation, as shown in Figure 1-12.

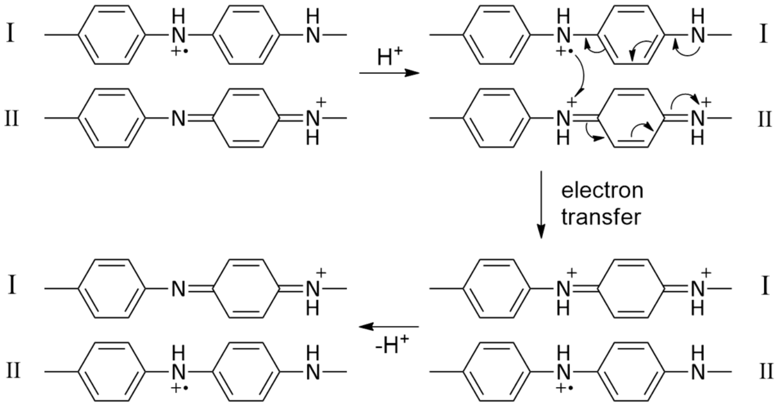

Figure 1-12: Mechanism of interchain charge transfer assisted by protonation (adapted from [83]). Chain II is protonated, enabling a single-electron transfer from chain I to chain II through resonance, after which chain I is deprotonated.

1.2.1.2 Poly(ethylene oxide) as the solid polyelectrolyte

In order to enable electrochemical reactions between the gate electrode and the polyaniline channel that would cause resistive switching, the two must be connected through a material that is a dielectric itself but allows for charge transport from one electrode to another. The realization of memristive devices in microelectronic appliances requires a preferably solid electrolyte for better manageability. To fulfil these requirements, high molecular poly(ethylene oxide) (PEO) (with Mw = 8 MDa) was chosen as it is a solid organic material that swells in water to form a viscous gel which can be easily cast manually. The swelling occurs due to the solvation of the PEO chains with water molecules. Once cast, a pristine PEO gel gradually loses some of its water content due to evaporation. With decreasing water content, the interactions of PEO chains with each other prevail more and more, leading to aggregation and crystallization which can be prevented by adding dopants (i.e., prepare the gel in an aqueous solution of dopant salts).

A lithium salt is used as the main dopant in SPEs for OMDs, which is inspired by the advances in the field of lithium-ion batteries (LIB) [84]–[86] that take advantage of lithium's small ionic radius and its ability to intercalate in carbon or metal oxide matrices. In the operating mechanism that was proposed for the OMD in earlier works, a key role in the switching of the device is attributed to lithium ions as they were thought to be essential for the charge transport between polyaniline and the gate electrode within the active zone of the device. The lithium ions are coordinated by PEOs etheric oxygen atoms through ion-dipole interactions and the charge transport is thought to be due to the hopping of Li^+ between different coordination sites. Analogous to LIB technology, one of the reasons why lithium salts have been the dopant of choice is lithium's small ionic radius which implies a higher ionic mobility. Evidently, to enable a sufficient charge carrier mobility, the PEO gel must be maintained in an amorphous state. Thus, another property of salts such as $LiClO_4$ or $LiBF_4$ is taken advantage of, namely their hygroscopicity that maintains a certain necessary amount of water in the system, preventing the aggregation of PEO chains. Due to the acid-base reactivity of polyaniline it is also necessary to create an acidic environment in the PEO gel that would otherwise deprotonate the polyaniline salt to its nonconductive base form. This requires a second, acidic dopant such as HCl. The aspect of doping in PEO is one of the major topics of the present work, discussed in detail in section 4.1.

1.2.2 OMD switching mechanism

Understanding the processes that take place in the active zone of the device is key to improving it in terms of performance and stability and making it more appropriate for complex applications. For this reason, the OMD's switching mechanism has been studied extensively in the past, providing FTIR spectroscopic [87] or X-ray fluorescence (XRF) [88] data to support the constructed model. Before proceeding to outline the details of the device operation, it must be pointed out that in scope of the present work, the study of the role of SPE dopant ions that is presented in section 4.1 led to a number of findings which reveal several inconsistencies in the formerly assumed model. However, in this section, it appears necessary to present the details of the formerly proposed switching mechanism including the respective supporting data as to allow for a clearer discussion of the new findings reported in section 4.1.

As was stated before, the resistive switching occurs as a consequence of electrochemical reactions of the conductive polymer polyaniline which is transformed from its electrically insulating leucoemeraldine state (PANI-LE) to its conductive emeraldine salt state (PANI-ES) upon oxidation (or vice versa upon reduction). The process can be monitored electrically by plotting the output current against the bias applied to the drain electrode with respect to the grounded source and gate electrodes. For a more precise characterization, two currents are recorded during the I-V measurements – the total current (I_{SD} or I_{TOT}) flowing through the device and separately, the gate electrode current (or ionic current, I_G). The gate current represents the amount of charge that passes through the gate electrode during the electrochemical reaction. Calculating the difference between the two registered currents allows to evaluate the evolution of the so-called electronic current (I_{EL}) that flows between the drain and source electrodes and can be expressed as $I_{EL} = I_{SD} - I_G$. As presented in Figure 1-13, the I-V curve (panel a) shows a hysteresis loop as a characteristic feature of a memristive device, which is due to the difference in applied potentials at which the electrochemical oxidation and reduction take place. Typically, oxidation starts at around +0.3 V during the anodic scan and reduction occurs at around +0.1 V during the cathodic scan. These potentials correspond to the peaks of the ionic current I_G (panel b) which resembles a voltammogram of polyaniline in the given potential range. The peaks mark the growing or decreasing trend of the I_{EL} curve. The position and width of these peaks is determined by the retention time t_R per voltage bias value, i.e., the scan rate. Faster scanning causes a shift to higher potential values for the oxidation peak(s) and lower values for the reduction peak(s), which is due to the fact that the system is not given enough time to equilibrate. On the contrary, the peaks converge at higher retention times, as the respective reactions are finalized sooner at lower applied voltage biases. The shape and width of the hysteresis loop both change accordingly.

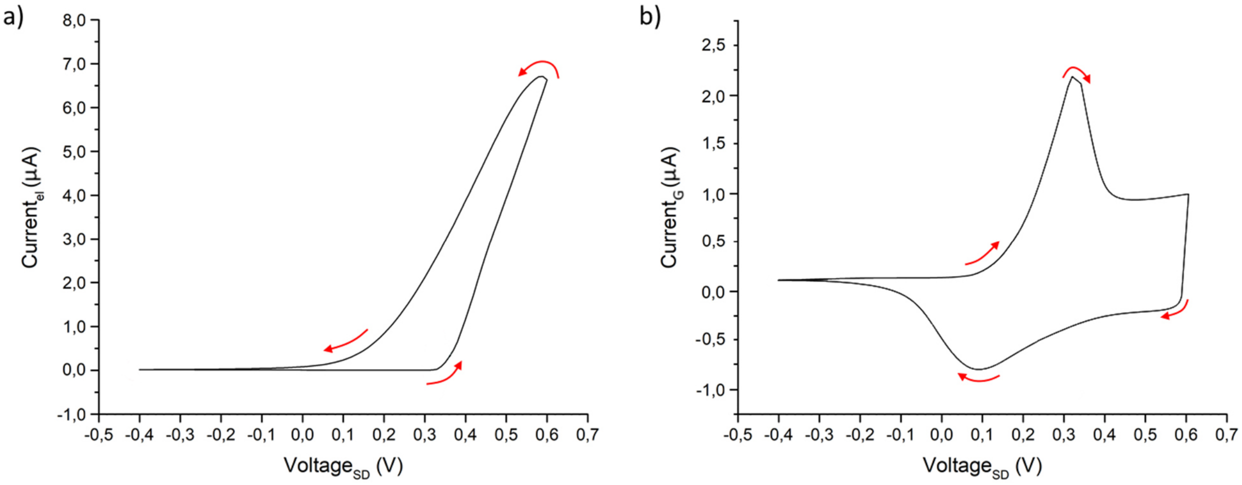

Figure 1-13: Typical I-V characteristic of an Organic Memristive Device, with curves for a) the electronic current I_{EL} featuring a counter-clockwise hysteresis and a rectification at negative voltages and b) the ionic current I_G.

Another characteristic feature of the OMD's I-V curve is the rectification at lower potential values. This is given by the fact that once in its insulating PANI-LE form, the change of the voltage dependent channel current is very low in comparison to the transition to PANI-ES, during which the conductivity increases by up to four orders of magnitude [89]. Ideally, only one couple of redox peaks is expected as the result of the fully reversible transition between these two forms of polyaniline. For comparison, a cyclic voltammogram with the transitions of polyaniline at the respective potentials is shown in Figure 1-14. It can be seen that when the voltage range is extended beyond +0.8 V, a second anodic peak occurs as a result of the oxidation of emeraldine to pernigraniline. As mentioned above, this second oxidation step should be avoided because, with respect to PANI-ES, the fully oxidized pernigraniline form contains twice as many imine groups that are prone to degradation in acidic media [59], with no remaining amine groups to buffer their protonation that, on its turn, facilitates hydrolysis. A smaller oxidation peak may occur at around +0.6 V and is attributed to crosslinking reactions between PANI chains, forming phenazine structures as demonstrated in Figure 1-15. According to Geniès *et al.* [90], a reaction can occur between growing PANI chains and aniline nitrenium ions that are formed as an intermediate during the polymerization [91]. The authors also assume a crosslinking reaction between different PANI chains that carry nitrenium ion moieties. Since the formation of nitrenium ions within polyaniline chains appears to be unlikely, due to the likelihood of electron rearrangement in a conjugated system, the proposed mechanism has been slightly modified and oxidized emeraldine chains are assumed to react with one another. The phenazine structures disrupt the polaron lattice, reducing the material's maximum conductivity over time as the process is not fully reversible, even though the presence of a slight B' peak suggests some degree of reversibility [92]. However, this process takes place more commonly during the electrochemical synthesis of PANI from aniline by means of cyclic voltammetry and is less likely to be observed during OMD characterization.

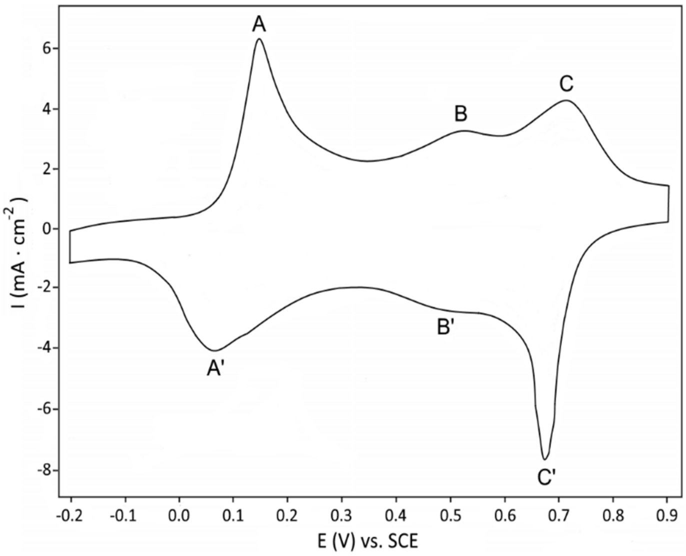

Figure 1-14: Cyclic voltammogram of a $HClO_4$ doped PANI film recorded at a 200 mV s^{-1} sweep rate, in a 1 M aqueous $HClO_4$. A/A': peak corresponding to the transition between PANI-LE and PANI-ES, B/B': peak corresponding to crosslinking reactions between PANI chains and their partial reversion, C/C': peak corresponding to the transition between PANI-ES and PANI-PS (adapted from [92]).

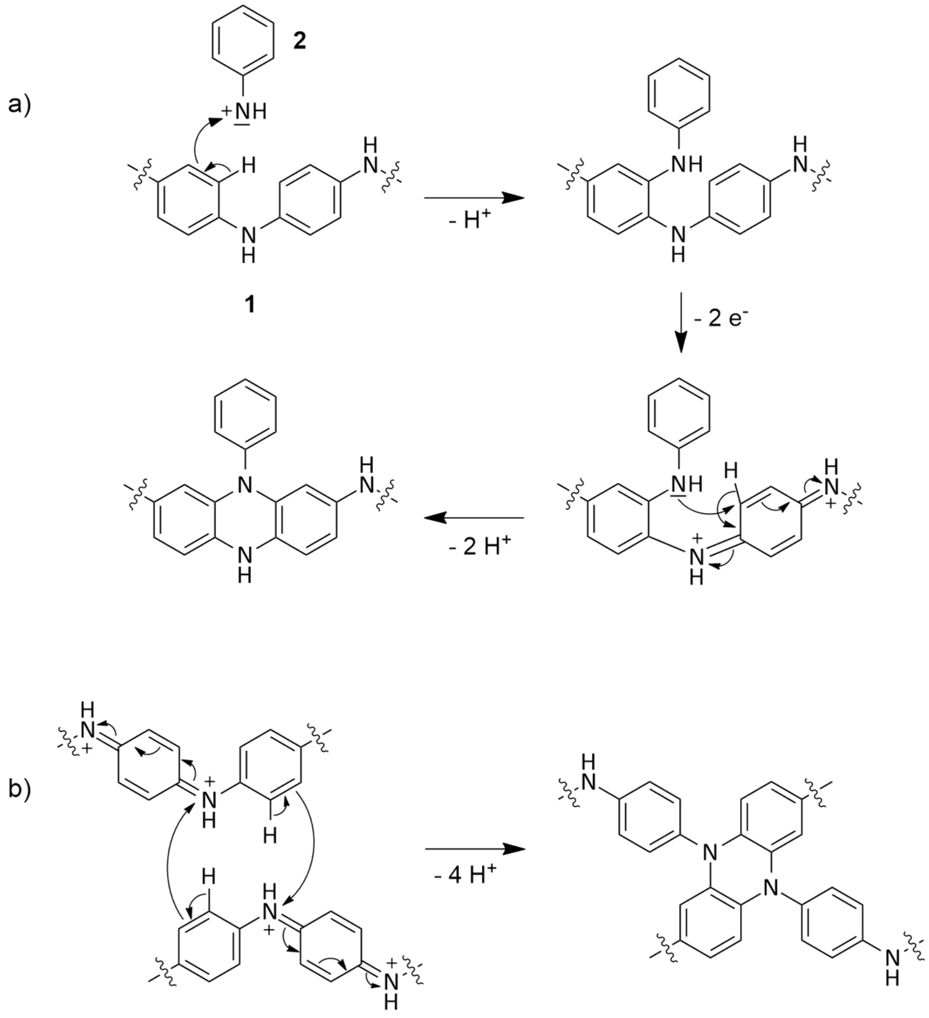

Figure 1-15: Mechanism of crosslinking a) between a growing PANI chain 1 and the nitrenium ion of aniline 2 during the synthesis by means of CV and b) between two PANI chains during oxidation (adapted from [90]).

1.2.3 Electrochemical model of OMD switching

During its operation, the Organic Memristive Device displays some particular behaviour in terms of its kinetics. As it can be seen in Figure 1-13, there is a significant difference in the amplitudes and shapes of the anodic and cathodic peaks of the gate current I_G. Typically, the anodic peak is rather tall and narrow, whereas the cathodic peak is comparatively broad, meaning that the reduction already slowly begins at voltages above the expected reduction potential. The different response to oxidation and reduction also shows itself in on/off switching cycles. When the device is biased at a constant drain voltage, the transition to the conductive PANI-ES state at higher potentials is always slower with respect to the reversion to the insulating PANI-LE state at lower potentials [13],[93],[94]. Both phenomena are related and kinetic in nature, the explanation of which leads to the elaboration of an electrochemical model that has been developed as a result of intensive theoretical research in prior works. Although a more detailed discussion of kinetic phenomena seems more opportune to be developed in chapter 5, one basic principle is elaborated below as to facilitate the understanding of the electrochemical model of the device.

The abovementioned kinetic behaviour has been explained by considering the geometry of the device, which was introduced in the work of Smerieri *et al.* [93] it can be seen in Figure 1-4, the PANI channel spans from the drain to the grounded source electrode. As a consequence, the potential that is applied at the drain gradually decays and is distributed over the length of the channel as shown in Figure 1-16. Since only a fraction of the channel is in junction with the polyelectrolyte and hence electrochemically active, the redistribution of the potential is not homogeneous throughout the whole channel when the conductivity of polyaniline is modified. Looking at the potential distribution profile, when an increasing positive voltage bias is applied, the part of the active zone that is closest to the drain will always be at a higher potential than the rest of it. Thus, the oxidation of polyaniline will be initiated there, gradually progressing towards the source as the applied bias is increased. The contrary applies during the cathodic sweep with a decreasing drain voltage. The distribution profile dictates that even at bias values higher than the reduction potential of PANI (about +0.1 V), the part of the active zone that is closest to the source will be at a lower potential and hence, eventually, the transition of PANI into its insulating state will be triggered, progressing towards the drain. In both cases, as long as (or as soon as) a part of the channel in the active zone is in its insulating state, the major part of the potential decay will occur there as the resistance will be orders of magnitude larger than that of the rest of the channel. On the basis of these observations, Smerieri *et al.* [93] have developed a model that describes the above-mentioned phenomena from an electrical point of view. The authors divided the profile of the active zone in narrow stripes perpendicular to the source-drain axis and considered them as an array of variable resistors connected in series, as shown in Figure 1-17. Eventual gradients and inhomogeneities are neglected, the resistance is assumed as equivalent and the electrochemical processes are assumed to take place simultaneously within the entirety of each individual stripe. Each segment is connected with the gate electrode trough the polyelectrolyte medium, represented by another resistor, respectively. Besides a variable component, these resistors

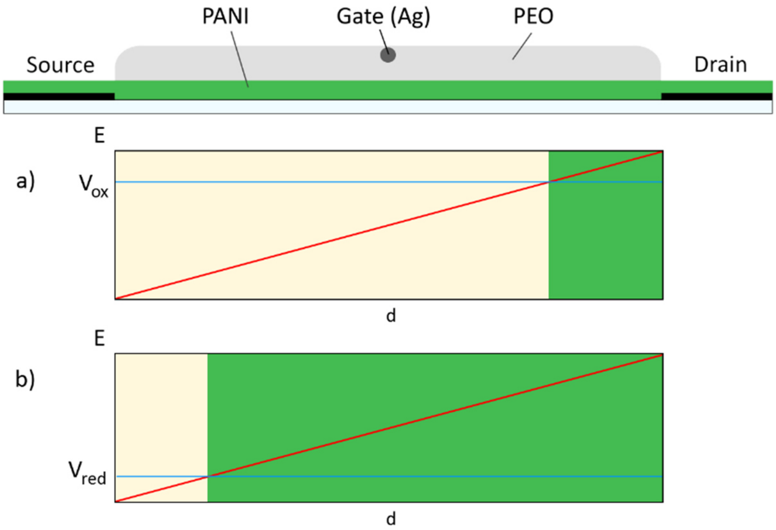

Figure 1-16: Schematic representation of the potential distribution along the PANI channel at an exemplary applied voltage bias for the anodic (left scale) and the cathodic sweep (right scale). For simplicity, the whole length of the channel from the source to the drain electrode is considered as the active zone. The pale yellow (for the insulating PANI-LE) and green colour (for the conductive PANI-ES) represent the respective section of the channel that would undergo a transition at the given voltage. Note that during the anodic sweep (a), a certain bias above V_{ox}, is only sufficient to trigger the transition in the vicinity of the drain. Meanwhile, during the cathodic scan (b), the applied bias is well above V_{red}, yet the reduction can already occur in the part of the channel close to the source.

have a constant contribution which depends solely on the coordinate of each section with respect to the gate electrode (hence, it is the smallest in the middle of the active zone, just below the gate). With the model of Smerieri *et al.*, a successful attempt is made to qualitatively explain the mechanism that defines OMD operation. Additionally, a parameterization of the system helps to quantify the underlying processes, delivering first simulation results with a rather good correspondence to experimentally obtained data.

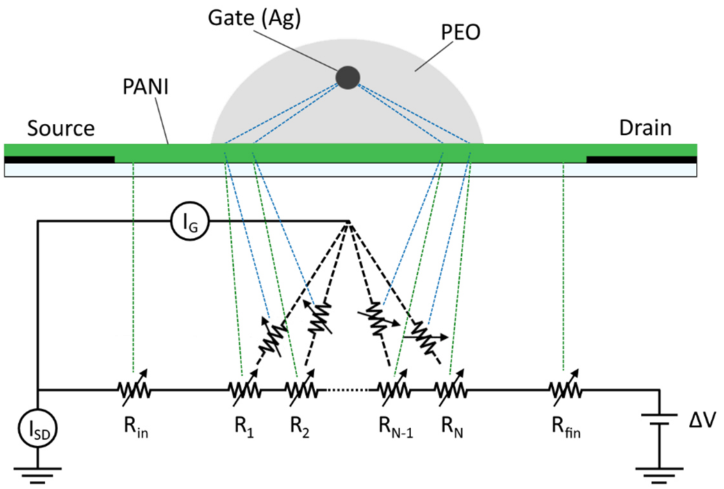

Figure 1-17: Schematic representation of the OMD (not to scale) and corresponding electrical circuit according to the model proposed by Smerieri *et al.* (adapted from [93]). The channel is divided in sections and represented as a series of variable resistors whose resistance depends on the oxidative state of PANI. In the cited reference, the resistors outside of the active zone (R_{in}, R_{fin}) have a fixed value. Here, they are represented as variable elements because their resistance will change according to the redistributing potential decay as explained above and shown in Figure 1-16.

Another step in the direction of theoretically describing and simulating the device's behaviour has been made in the work of Demin *et al.* [94]. Their model is similar to the previous one in that the calculations are based on the establishment of an equivalent electronic circuit with a subdivision of the conducting channel in a series of variable elements. However, the authors take a significantly more in-depth approach, elaborating the molecular processes taking place in the active zone of the device. In particular, an emphasis is put on ionic species that take part in the redox switching, and their accumulation at interface when an electrical field is applied. Smerieri's model is extended by including a capacitive element in the electrolyte section of the equivalent circuit. The details of this model, not discussed here for the sake of brevity, can be found in the cited literature. It must be pointed out that this more sophisticated model delivers much more precise simulation results that are in very good correspondence with experimental data.

One detail that is common for both models and will become relevant in scope of the present work is the fact that the authors emphasize the dopant ions in the polyelectrolyte. The authors argue that lithium ions are essential for the functioning of the device and participate in its switching. The PANI channel and Ag gate electrode are identified as the working and counter/reference electrode, respectively, and it is suggested that the switching takes place according to the following reaction:

$$\mathrm{PANI^{+}\!:Cl^{-} + Li^{+} + e^{-} \rightleftharpoons PANI + LiCl} \qquad \text{Equation 4}$$

A flux of lithium ions is considered in both models, which stems from the perception that lithium ions participate in the redox processes as they supposedly enter and exit the active PANI channel to compensate charge variations upon its transformations. For example, when a positive voltage is applied and oxidation to PANI-ES takes place, lithium ions are repelled from the working (PANI) electrode by the electric field, while chloride ions function as the counterion for the forming positive charges on PANI chains. Inversely, it is assumed that an influx of Li^{+} ions occurs in order to compensate the negative charge of released Cl^{-} ions when a negative voltage is applied and PANI is reduced. This assumption is discussed in section 4.1, where the role of lithium ions in the switching mechanism is questioned, followed by suggested strategies of modified PEO doping.

1.2.4 Experimental evidence for lithium migration

For the sake of completeness, some experimental spectroscopic data will be presented here as evidence for the abovementioned assumptions in order to clarify the reasoning behind them, as well as to facilitate the discussion that will follow in the next section.

The publication of Smerieri's model was preceded by a work from Berzina *et al.* [87] in which spectroscopic data were provided as evidence for the switching mechanism proposed in reference [13]. In this study, FTIR as well as a resonance and vicinity enhanced micro-Raman spectroscopy technique (similar to surface-enhanced Raman scattering (SERS)) were employed to monitor the active zone of the device, including the redox state of polyaniline. The sensitivity to changes in the vibrational spectra of the analysed material and the spatial resolution of this technique allowed to register and map out molecular changes within the device. These transformations were then correlated to the voltamperometric characteristics that have been recorded simultaneously. As a measure for the redox state of polyaniline, the authors used the ratio of quinoid and benzenoid rings in the PANI structure, which can be distinguished in the range around 1500−1600 cm^{-1}, as it has been suggested in other works [58]–[60],[95]. Another particular peak at 930 cm^{-1} that corresponds to the symmetric stretching vibration of the perchlorate ion was chosen to monitor changes in the composition of the PANI/PEO junction. Figure 1-18 shows that this peak only appears when probing in the active zone of the device, suggesting that the eventual diffusion of ions along the plane of the PANI channel outside of the active zone is negligible. The spatial resolution allows to further confirm this, as the appearance of the ClO_4^- peak at the crossover area from PANI to PANI/PEO is sharp.

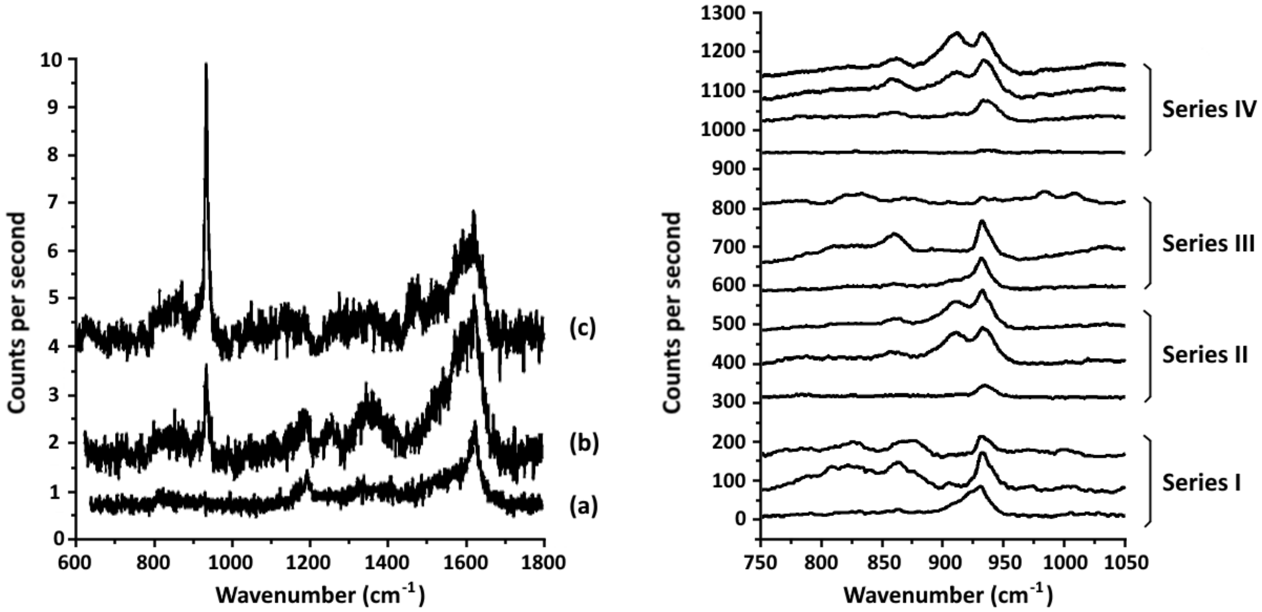

Figure 1-18: Left panel: Raman spectra of the fully doped device taken a) near the drain electrode, b) in the PANI/PEO junction far from the gate electrode, c) in the PANI/PEO junction close to the gate electrode.
Right panel: Raman spectra taken in the PANI/PEO junction (20 µm away from the gate electrode) at different times after the application of a positive or negative voltage bias. From the bottom to the top curve, respectively: Series I) at −0.2 V immediately after voltage application, after 15 and 30 min; Series II) at +0.6 V after 2, 5 and 30 min; Series III) at −0.2 V after 2, 20 and 60 min; Series IV) at +0.6 V after 2, 20, 30 and 60 min (adapted from [87]).

Furthermore, when probing within the active zone, the peak is more intense in closer vicinity to the gate electrode than in the periphery. It is also reported that when focusing the confocal microscope closer to the PANI/glass substate interface, the peak appeared weaker than in the vicinity of the PANI/PEO interface after a (partial) reduction of PANI. These findings suggest an overall inhomogeneous distribution of charges within the active zone as well as that the reduction of PANI appears to happen faster in the layers closer to the gate electrode. Lastly, the authors also showed the evolution of the perchlorate ion peak following the alternating polarization of the device at −0.2 and +0.6 V. As it can be seen in Figure 1-18, when a negative voltage bias is applied and the polyaniline is reduced, the single peak at 930 cm^{-1} slowly disappears. When PANI is oxidized at +0.6 V, the peak reappears and splits into a doublet that, according to the authors, is characteristic for the formation of $LiClO_4$ aggregates. This finding leads the authors to the conclusion that upon oxidation of PANI, lithium ions diffuse out of the channel and into the polyelectrolyte, increasing their concentration until $LiClO_4$ aggregates form, which can be observed in the Reman spectra. Conversely, when a negative voltage is applied, lithium ions flow into the PANI channel to compensate the charge of chloride ions that are released upon the reduction of PANI. Important to point out in this context is the assumption that, due to the difference in ionic mobility, the ionic migration is largely due to the lithium and not to the perchlorate (or chloride) ions.

While this study delivers valuable information on the processes taking place within the device, it could still be argued whether or not the behaviour of the lithium ions can be deduced by association to the data obtained for the perchlorate ions. To further support the proposed model, a more direct and elegant approach is chosen in another work by Berzina *et al.* [88] to monitor the migration of metal ions between the PANI channel and the electrolyte in the active zone of the device. The authors used the X-ray fluorescence technique in the grazing-incidence beam configuration in order to reduce the spectral contribution of the substrate, which has been successfully demonstrated on thin LB films in other works [96]. For the same reason, a strip of polyimide tape (Kapton, 12.5 µm thick) has been used as the substrate instead of quartz. Since lithium ions cannot be detected by XRF under atmospheric conditions, they have been replaced by their heavier homolog rubidium. To compensate for the slower kinetics of the less mobile cation, a dilute gel with a PEO concentration of 5 mg/ml (vs. typically 30 mg/ml) in a 0.1 M aqueous RbCl solution with 0.1 N HCl was prepared as the electrolyte. This gel remained semiliquid throughout the whole measurement, which is why the setup had to be modified as presented in Figure 1-19. A Teflon well with the Ag gate electrode positioned at the bottom was used as a reservoir for the PEO gel and the polyimide tape strip with PANI was placed "face down" on top of the well. The assumed slower kinetics of rubidium ions as well as the larger dimensions of the model device (distance between PANI and the gate electrode increases from a few tens of µm to 1.0 cm) are compensated by the lower viscosity of the diluted electrolyte.

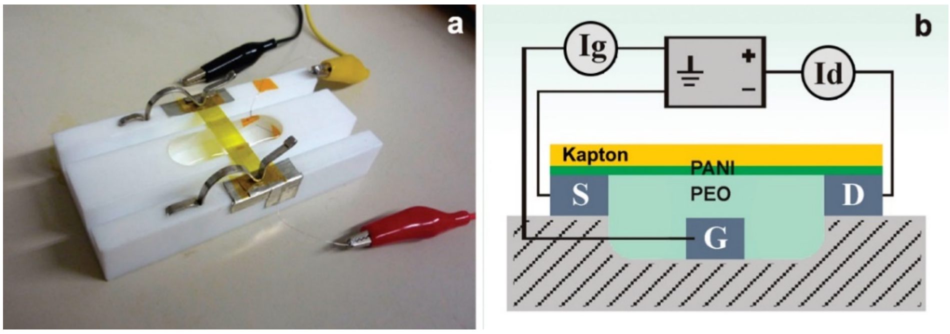

Figure 1-19: a) Experimental setup for the XRF experiments reported in [88], b) schematic representation. The thickness of the polyimide tape substrate was 12.5 µm and the depth of the well determining the distance between the PANI channel and the gate electrode was 1.0 cm.

The X-ray fluorescence of Rb^+ was registered at two characteristic energies (13.39 and 14.96 KeV), as can be seen in Figure 1-20 a). Simultaneously, the voltamperometric characterization of the device was carried out, allowing to correlate the presence of Rb^+ ions with the oxidative state of PANI at any given time. As it can be seen in Figure 1-20 b) and c), the recorded XRF signal coincides very closely with the electrical charge passing through the gate electrode, which is calculated as the integral of the ionic current I_G. The authors conclude that, as assumed in the micro-Raman study, the oxidation of PANI to its conductive state is accompanied by a flux of rubidium ions away from the channel and into the electrolyte, as indicated by the decreasing intensity of the XRF signal. Conversely, as the polyaniline is reduced to its insulating state, the XRF signal intensifies, indicating that Rb^+ ions migrate towards the PANI channel as to neutralize the Cl^- ions that were associated with the positively charged oxidized PANI chains. The direct monitoring of the presence of rubidium in the vicinity of PANI provides more convincing proof for the aforementioned mechanism of PANI switching involving cation migration.

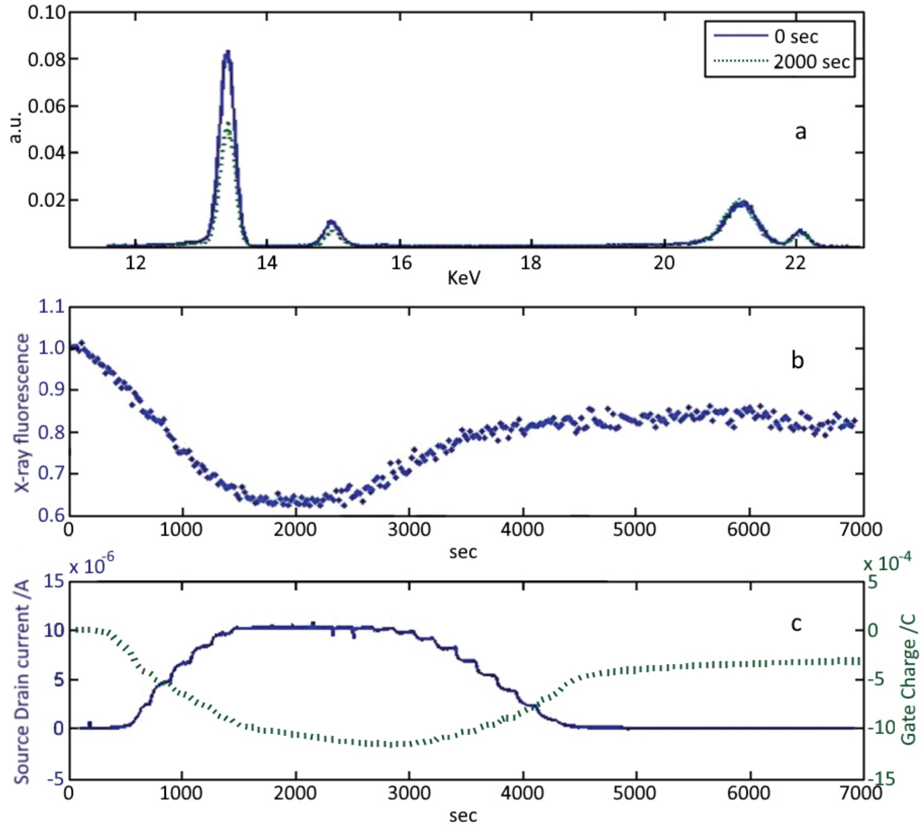

Figure 1-20: a) Grazing-incidence beam XRF spectrum of the sample surface; b) variation of the normalized XRF intensity in time; c) variation of the drain current output in time upon voltamperometric characterization of the device (potential range: from −1.2 V to +1.2 V) and ionic charge (integral of the ionic current), recorded simultaneously (adapted from [88]).

2 Materials and methods

2.1 Chemicals

aluminium chloride $AlCl_3$	Acros Organics
aluminium bromide $AlBr_3$	Alfa Aesar
ammonium persulfate $(NH_4)_2S_2O_8$	Acros Organics
ammonium thiocyanate NH_4SCN	Carlo Erba
calcium chloride $CaCl_2$	Fluka
cerium chloride $CeCl_3$	Carlo Erba
caesium chloride $CsCl$	VWR Chemicals
ferric chloride $FeCl_3$	Acros Organics
ferrous sulfate $FeSO_4$	VWR Chemicals
lithium chloride $LiCl$	Fluka
lithium perchlorate $LiClO_4$	Sigma Aldrich
lithium tetrafluoroborate $LiBF_4$	Merck
lithium hexafluorophosphate $LiPF_6$	Aldrich
lithium thiocyanate $LiSCN$	Carlo Erba
magnesium chloride MgC_{12}	Fluka
magnesium sulfate MgSO4	VWR Chemicals
potassium chloride KCl	Fluka
potassium thiocyanate $KSCN$	Sigma Aldrich
rubidium chloride $RbCl$	Sigma Aldrich
sodium chloride $NaCl$	Sigma Aldrich
sodium bilsulfate $NaHSO_4$	VWR Chemicals
sodium dodecylsulfate $NaSO_4C_{12}H_{25}$	Sigma Aldrich
sodium sulfate Na_2SO_4	Carlo Erba

silver (wire, d = 50 µm and 125 µm)	GoodFellow
silver (foil, d = 125 µm)	Alfa Aesar

acetic acid (100 %) CH_3COOH	VWR Chemicals
hydrobromic acid (48 %) HBr	Carlo Erba
hydrochloric acid (1 N) HCl	Carlo Erba
orthophosphoric acid (85 %) H_3PO_4	VWR Chemicals
perchloric acid (60 %) $HClO_4$	Fisher Scientific
sulfuric acid (98 %) H_2SO_4	Carlo Erba

acetone	Carlo Erba
acetonitrile	VWR Chemicals
aniline	Merck
chitosan (low molecular weight)	Sigma Aldrich
citric acid	VWR Chemicals
1,1,1,3,3,3-hexafluoroisopropanol	Alfa Aesar
isopropanol	Carlo Erba
NEA 121	Norland Products Inc.
N-methyl-2-pyrrolidone	VWR
polyaniline (emeraldine base, Mw = 10^5 Da)	Sigma Aldrich
poly(ethylene oxide) (Mw = $8 \cdot 10^6$ Da, 200−500 ppm BHT)	Sigma Aldrich
poly(ethylene oxide) (Mw = 10^6 Da)	Alfa Aesar
p-toluenesulfonic acid	Alfa Aesar
toluene	Carlo Erba
xylene	Carlo Erba

The solvent purity was analytical grade or ACS reagent grade. All chemicals were used without further purification. LiSCN was dried at 80 °C for 15 h prior to weighing.

2.2 Instruments

Agilent B2902A	electrical characterization (SMU)
Bruker Syrius	MALDI-TOF mass spectrometry
Diener Electronic Femto	low-pressure O_2/Argon plasma surface treatment
Elma Elmasonic P	ultrasound treatment
Hettich Roto Silenta III	centrifugation
Merck Millipore Reference A+	Milli-Q water preparation
Keithley 236	electrical characterization (SMU)
Keithley 6514	electrical characterization (electrometer)
KSV-5000 trough	Langmuir-Schaefer thin film deposition of PANI
Leica DMS300	optical microscopy
National Instruments PXIe-1073	electrical characterization (SMU)
Nikon H550L	optical microscopy
Novascan PSD Pro Series	UV ozone surface treatment
Optomec Aerosol Jet 200	Aerosol Jet Printing
Perkin Elmer Spectrum Two	FTIR spectroscopy
Veeco Dimension 3100 Nanoman	Atomic Force Microscopy
Zeiss Auriga Compact	Scanning Electron Microscopy

2.3 Experimental

2.3.1 LS-deposition of pristine PANI

Solutions of polyaniline (1.0 mg/ml in NMP) were prepared by adding PANI-EB to the solvent portion wise under vigorous stirring. Eventual precipitate was allowed to settle for least 30 min and small portions were taken for dilution to 0.1−0.2 mg/ml in NMP/toluene (9:1 v/v). Standard samples were made from rectangular 15 x 7 mm (unless specified otherwise) quartz substrates covered by chromium (deposited by CVD). Electrodes on each side of the substrate were made by covering 2 mm wide stripes with polyimide tape and etching away the remaining chromium with a proprietary, ceric ammonium nitrate-based etching agent (Sigma Aldrich). The surface was covered by strips of polyimide tape, leaving a 2−3 mm free channel. The substrates were washed and thoroughly rinsed with isopropanol and water prior to use. The deposition of PANI thin films was carried out on a KSV-5000 trough using a modified Langmuir-Schaefer technique. Milli-Q water was used as the subphase, and the PANI solution in NMP/toluene was injected onto its surface and compressed by Teflon barriers at a constant rate of 0.5 cm/min until a target surface pressure of 10 mN/m. The toluene in the solution prevented PANI from being dragged into the subphase by NMP. The formed PANI layer was separated by an acrylic glass grid and 30−60 LS monolayers were deposited on the substrate, alternating the direction of deposition after every 5th layer. The deposited layers were doped for 30−40 s in 1 N HCl twice with an interval of ca. 30 min. Lastly, the polyimide tape strips were removed, leaving a PANI-ES channel stretching between the chromium electrodes.

2.3.2 Synthesis of the chitosan/PANI composite

The chitosan/PANI composite material (CPA) was synthesized by oxidative polymerization of aniline in the presence of chitosan. First, 0.3 g chitosan were dissolved in 50 ml 4 % acetic acid under stirring for 30 min. The viscous solution was poured in a 250 ml round bottom flask. Separately, 0.9313 g (10 mmol) aniline were dissolved in 50 ml 1 N hydrochloric acid, the solution was cooled in an ice bath and added dropwise to the cooled flask under stirring. A few drops of a 1M $FeSO_4$ solution were added to the mixture. Lastly, a solution of 2.7382 g (12 mmol) ammonium persulfate (APS) in 40 ml 1 N hydrochloric acid was cooled and added dropwise to the reaction mixture in the flask over ca. 1 h under stirring, maintaining the temperature below 5 °C. The mixture was stirred for 12 h and its colour changed from pale yellow over blueish green to dark green. The excess APS was quenched by adding 5 ml of 1 M $FeSO_4$ solution. The resulting suspension was centrifuged at 4000 RPM for 5 min. The light green supernatant was discarded, and the dark green solid product was resuspended in 1 N HCl and centrifuged. This was repeated three times. The pellet was then resuspended once more in acetone, centrifuged, and dried at 50 °C for 24 h. Lastly, the dark green, brittle solid product was grinded in an agate mortar. The yield was 1.160 g (94 % relative to the mass sum of aniline and chitosan educts), although it is likely that some traces of solvents remained in the material.

Product analysis

FTIR spectra were kindly taken by Dr. Silvia D'Auria on a Perkin Elmer Spectrum Two spectrometer in the Department of Chemistry, University of Parma, preparing the sample as a KBr pellet. MALDI-TOF measurements were kindly taken by Dr. Mirko Buttrini on a Bruker Syrius mass spectrometer in the Department of Medicine and Surgery, University of Parma. The spectra were acquired in the positive linear mode in the range of 2–20 kDa with a 60 Hz laser frequency and an ion source voltage of 20 kV, using α-Cyano-4-hydroxycinnamic acid (HCCA) as the matrix material.

2.3.3 Preparation of PANI and CPA inks

Inks of pristine PANI were made by pre-dissolving PANI-EB in NMP under stirring. Xylene and/or IPA were slowly added to the stirred solution in different proportions. The resulting solution was treated with ultrasound (P = 120 W, f = 37 kHz, as in all following applications) for 30 min and stored in a refrigerator. In some cases, the solution was filtered through a 0.2 µm PTFE syringe filter. The inks were treated with ultrasound for 20 min prior to use.

CPA-inks were prepared by adding CPA to water/IPA (8:2 v/v) and treating with the sample with ultrasound for 10 s, resulting in a fine suspension (a filtering test with a 0.45 µm PTFE syringe filter yielded a clear, colourless filtrate). The inks were stored in a refrigerator and treated with ultrasound for 30 s prior to use. The concentrations of PANI and CPA as well es solvent ratios are given in section 6.2.

2.3.4 Aerosol Jet Printing experiments

15 x 7 mm quartz slides with chromium electrodes or silicon slides (1 µm thermal SiO_2 layer) featuring T-shaped gold electrodes (by photolithography, d = 200, 10 or 5 µm) were used as substrates. Prior to use, the samples were treated with ultrasound in isopropanol for 1 h, rinsed with acetone and water (Milli-Q). The surface was treated with plasma (O_2/Argon, P = 3 W, t = 9 min) and UV/ozone (t = 3 min, T = 50 °C) immediately before printing. The deposition of PANI and CPA inks was carried out with an Optomec Aerosol Jet 200 system with various printing parameters, such as:

- nozzle diameter: 200 µm
- deposition plate temperature: 90 °C
- speed: 0.5−2 mm/s
- sheath gas: 40 sccm
- carrier gas: 30 sccm
- atomizer current: 0.5 mA

The printed layers were doped with 1 N hydrochloric acid for ca. 30 s.

2.3.5 Preparation of PEO gels

PEO gels were in 3 ml screw-neck glass vials with Teflon gasket spacers. Aqueous solutions of various dopants with concentrations between 0.1 and 1.0 mol/l were added portion wise and filled up to 3 ml with water (Milli-Q, $\rho = 18.2\ \mathrm{M\Omega \cdot cm}$, was used in all further steps). Different amounts of PEO (Mw = $8 \cdot 10^6$ Da, 200−500 ppm BHT as inhibitor, 90−120 mg depending on final concentration) were added portion wise to the vial under gentle agitation, followed by the next portion of dopant solution or water. The suspension was vortexed for 30−60 s and stored for 1−2 days to swell until homogeneity, being vigorously mixed with a stirrer a few times by hand. The resulting gels were stored in a refrigerator unless specified otherwise.

2.3.6 OMD fabrication

All substrates were treated with ultrasound in isopropanol for 15-60 min and rinsed with acetone and water. In the case of quartz samples, the active zone of the OMD (in contact with the (poly)electrolyte was delimited by covering the PANI layer with strips of polyimide tape, leaving a 1 mm wide uncovered stripe in the middle. In the case of T-shaped Si/SiO_2 samples, the channel was active across the whole length. Two steps of 2−3 layers of narrow polyimide tape strips were placed to both sides of the active zone, parallel to the PANI channel. Then, 1−3 layers of PEO gel were cast manually on top of the active zone with a plastic stirrer or micropipette tip. A silver wire (d = 50 µm), with a piece of tin was soldered to one of its ends as a cable connection point, was stretched and fixated over the polyimide tape steps within the active zone, perpendicular to the PANI channel. The wire was covered by another 1−2 layers of cast PEO gel. The device was ready to be used once the polyelectrolyte solidified. In some cases, coating with NEA followed, as described in section 4.3.

2.3.7 Electrical characterization

The acquisition of electrical data was carried out using an SMU to apply voltage biases and register output currents (both the total current I_{SD} and the gate current I_G were registered simultaneously). Cyclic I-V characteristics were recorded by scanning the device in the potential range [−0.4 V; +0.8 V] or [−0.4 V; + 0.6 V], starting with an anodic scan from 0.0 V. The scan rate was determined by the scanning step (0.1 V or 0.02 V) and the respective dwell time, as specified in the experiments. Kinetic measurements were carried out at a constant bias (e. g. +0.5 V for oxidation and −0.2 V for reduction) for 5−10 min. All measurements were preceded by an at least 2 min long conditioning period at −0.2 V to prepare the sample, by complete reduction of PANI to the LE state. Additional steps were added when performing characterizations of OMDs with a series of different liquid electrolytes as described in section 4.1. When changing the electrolyte, the sample and the trough were carefully rinsed with 0.1 N HCl and then rinsed twice more with the next electrolyte. Each experiment was carried out at least in triplicate.

3 Organic memristive devices interfacing biological systems

One of the general long-term goals of our research is the development of systems featuring Organic Memristive Devices for information processing and integration with bioelectronic systems and sensing. Such applications imply the use of large arrays of elements, mimicking biological neural networks and possibly interfacing and/or being usable as parts of a natural nervous system. Since the aim is to mimic some functionalities of biological systems, as a prerequisite for the applicability of OMDs and their compatibility with biological elements, a lot of previous work has been dedicated to the study of relevant analogous properties. In particular, the similarities between an OMDs and biological synapses have been demonstrated.

According to Hebb's principle [2], one of the fundamental properties of synaptic transmission between neuronal cells is the so-called spike-timing-dependent plasticity (STDP), meaning the that the strength of connections between neurons is reinforced by the prior activity of said connections. This is often simplified as "What fires together, wires together", meaning that the connection between two cells becomes stronger the more often these cells are simultaneously activated. This concept has been generally proven to be applicable to memristive devices, since they display a change in conductance as a response to a sequence of received electrical stimuli [97]–[99]. Recently, Battistoni *et al.* demonstrated this property in Organic Memristive Devices [100], showing long-term potentiation and depression caused by series of electrical stimuli with various biologically relevant frequencies. The operability of the device in a pulse mode has been demonstrated earlier by Smerieri *et al.,* including the ability to generate an oscillating response that is assumed to originate from capacitive effects [93],[101]. In the context of biocompatibility, such a behaviour can be seen as analogous to the spike train-like propagation of action potentials in living cells. Lastly, in a work by the groups of Parma and Kazan [102], the OMD has been successfully employed to directly connect two living cortical neurons of a rat. The artificial synapse enabled the communication between the two stimulated cells where the signal propagation fully followed the Hebbian principle, mimicking the natural ones in fine details. This is another great step towards biological and biomedical applications since it displays the ability of OMDs to directly emulate the functionality of biological synapse.

Furthermore, exploratory research has been carried out for the implementation of OMDs in the hardware realization of Artificial Neural Networks (ANNs) in the form of single and double layer perceptrons [103],[104], as schematically shown in Figure 3-1. Such systems allow to solve analogue tasks such as input signal classification, paving the way the perspective to carry out more complex tasks at the hardware level with multilayer structures. Furthermore, it could be demonstrated that OMD-based systems are capable of emulating simple biological behaviour patterns, as it occurs in the feeding of the great pond snail *Lymnaea stagnalis* [105]. Essentially, it resembles the well-known Pavlov's dog experiment which has been later emulated on the basis of inorganic memristive devices by the group of Ziegler *et al.* [106]. The equivalent electronic circuit mimicking the homo- and heterosynaptic learning process were realized with only one and two OMDs, respectively. The results are an adequate representation of the increased response to a conditioned stimulus (in this case, the presence of amyl acetate) after the conditioning procedure, when the conditional stimulus is applied together with the unconditioned one (in this case, the presence of food particles), resulting in an increased output signal (corresponding to the movement of feeding muscles) (see Figure 3-2).

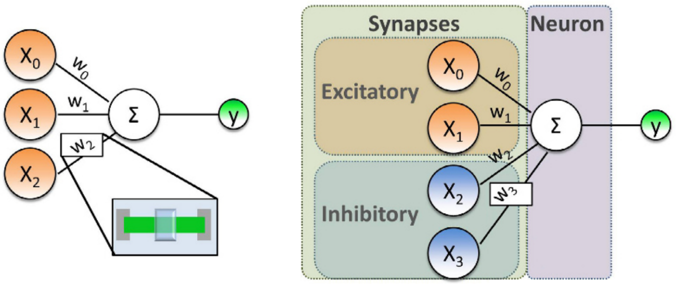

Figure 3-1: Schematic representation of an elementary (left) and a double layer perceptron (right) [104]. The inputs X_i correspond to different stimuli that are weighed by weight functions W_i represented by OMDs, the sum of which results in an output signal Y.

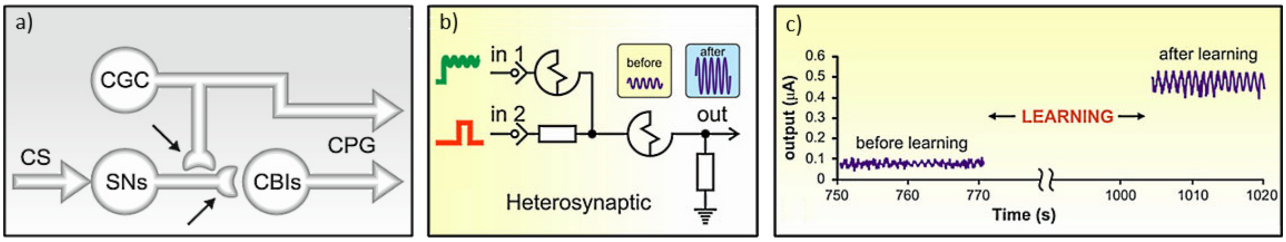

Figure 3-2: Scheme representing a part of the nervous system* of the great pond snail *Lymnea staglalis*, responsible for its feeding behaviour (a) with an equivalent electronic circuit featuring OMDs (b). c) Circuit output signal as a response to the conditioned stimulus (CS) before and after conditioning.

*CGCs: cerebral giant cells; SN: sensory neurons; CBI: cerebrobuccal interneurons; CPG: central pattern generator interneurons. The arrows point at synaptic interconnections, emulated by OMDs in panel (b) (adapted from reference [105]).

3.1 Electrical noise and OMD operation

When going towards large, complex arrays of interconnected devices, it is necessary to consider the occurrence of some degree of crosstalk and interferences including electrical noise. This is especially true when attempting to integrate OMDs with biological systems consisting of a myriad of interconnected elements, where so called noise artifacts are inevitable. The term “electrical noise” means the fluctuation of a signal within a certain distribution, characterized by a spectrum of frequencies and an amplitude, within which range this fluctuation occurs. In the case of a random distribution covering all possible frequencies, the resulting unpredictable fluctuations are called “white noise” in analogy to white light consisting of the whole spectrum of visible wavelengths. Similarly, it is called “coloured noise” when its frequency distribution by a single value over a period of time, or “low pass filtered noise” for a certain interval of frequency values (see Figure 3-3).

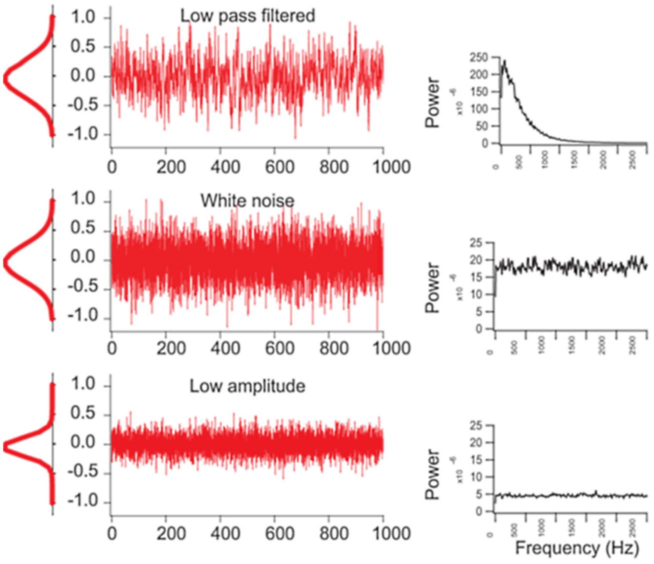

Figure 3-3: Graphical representation of low pass filtered and white noise with amplitude values drawn from a Gaussian distribution (from reference [107]).

Although it is seen mostly as a nuisance and an interference, there are works in the field of neurosciences discovering positive, constructive effects of this phenomenon [107]. In a work by Hunter *et al.* [108] the effect of the parameters of electrical noise on the reliability of the firing pattern of single neurons is studied. The authors distinguish between the contribution of the frequency range and the amplitude of noise (expressed in the form of the so-called coefficient of variability, CV). To this end, the response of slowly adapting motoneurons (*aplysia*) to bursts of large amplitude inputs alternating with low amplitude inputs is analysed. The experiments show a frequency-independent increase in spike time reliability in the presence of fluctuations of the input current with sufficiently high noise amplitude (CV = 1). The dependence on the frequency of the input shows when comparing otherwise equivalent experiments in which a broadband input (Figure 3-4 a) is compared to one lacking the frequencies around the neuron's firing rate f_{DC} (Figure 3-4 b). It can be seen that the firing reliability is maintained when the neuron receives a broadband input, but diminishes soon after the modulation of the noise amplitude to lower values (CV = 0.15) when the frequencies around f_{DC} are not represented. The explanation behind such a response is the stabilization of the firing pattern through interference of the firing rate with harmonics and subharmonics of f_{DC} from the frequency spectrum of the current input, which could be relevant when operating OMDs in the oscillator mode.

Similar results were obtained in a work by Ermentrout *et al.* [107], where populations of interconnected living neuronal cells have been studied by comparing their firing patterns generated by the injection of current pulses with and without superimposed noise signals. The study shows that in analogy to single neurons, despite its chaotic nature, noise can create order in a system, causing a certain degree of synchronization of the response of an array of neurons, as illustrated in Figure 3-4 c). Similar to the previous case, the authors report that the reason behind this phenomenon is a delay or advancement of the next action potential, which is caused by positive or negative interference determined by the phase at which the noise stimulus arrives.

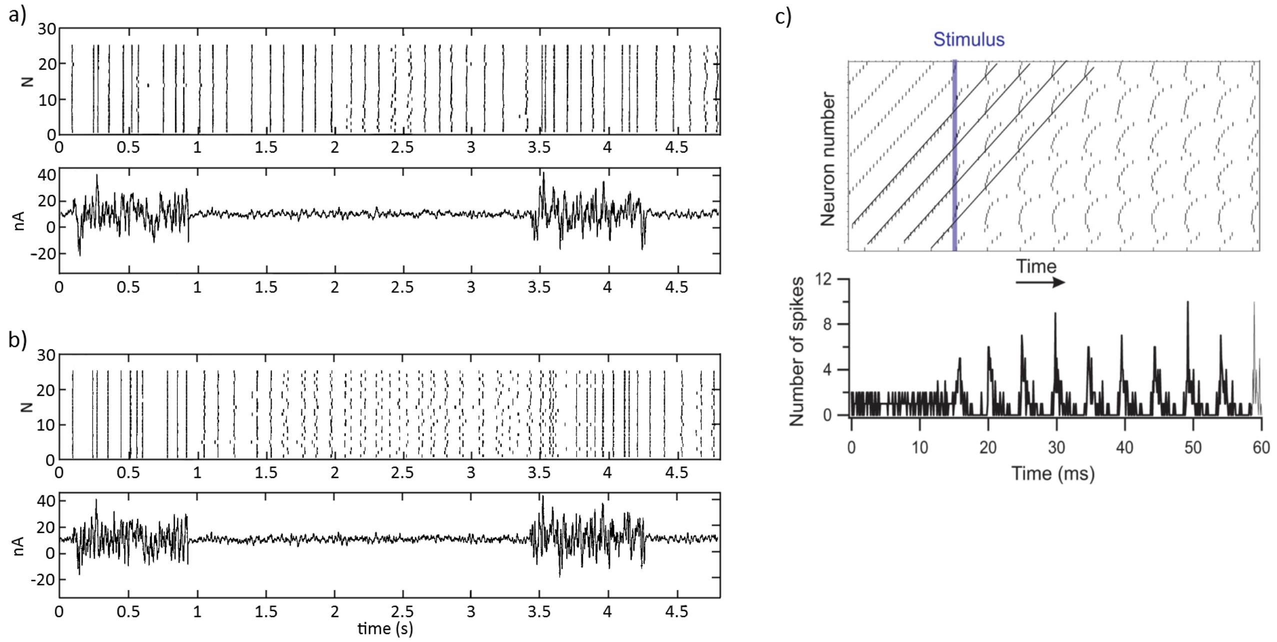

Figure 3-4: Spike time reliability as a function of the magnitude of current fluctuations with a) a broadband current input and b) a current input lacking frequencies around f_{DC} (adapted from [108]). c) Synchronization effect of an electrical noise stimulus on the firing pattern of an array of uncoupled model neurons. The neurons' regular and independent firing in a diagonal pattern is transformed into a clustered pattern with more synchronous firing across the population (adapted from [107]).

In the framework of both mimicking natural functional behaviour and of interfacing ANN with the biological systems it is quite interesting to study the operation of OMD under the exposure to noise. More specifically, we investigated the exposure to noise as a source of potential spikes that could drive OMD switching in analogy to the experiments demonstrating the STDP of the device [100],[105]. To this end, we studied the kinetic response of the device at voltages close to the switching onset potential. As it is known, the electrochemical transition of the PANI channel into its conductive state only occurs above this threshold value (typically at around +0.3 V bias), with faster kinetics at higher applied potentials (within the stability range of PANI-ES). Our expectation was that by applying electrical noise with a sufficient amplitude, a premature switching of the device could be achieved at sub-threshold potentials due to a potentiation by the noise's positive potential spikes, as illustrated in Figure 3-5 a, b).

Figure 3-5 c) shows the kinetic response of an OMD, fabricated using the classical procedure [109], at a constant +0.3 V bias, superimposed by a coloured electrical noise signal of different frequencies, measured in duplicate. A continuous, fast decay of the output current as well as switching kinetics is observed both between and within each set of measurements, indicating some short-term material degradation. Our assumption was that this is due to the solid polyelectrolyte as the most labile component of the OMD, being prone to excessive drying as well as acid dedoping due to HCl volatility. On this basis we carried out an extensive study that is presented and discussed in detail in chapter 4. Within the framework of this experiment, we attempted to circumvent the decay of the device's characteristics by providing a stable humidity environment to the active zone of the device by means of capping, which is described in more detail in section 4.2. As it can be seen in Figure 3-5

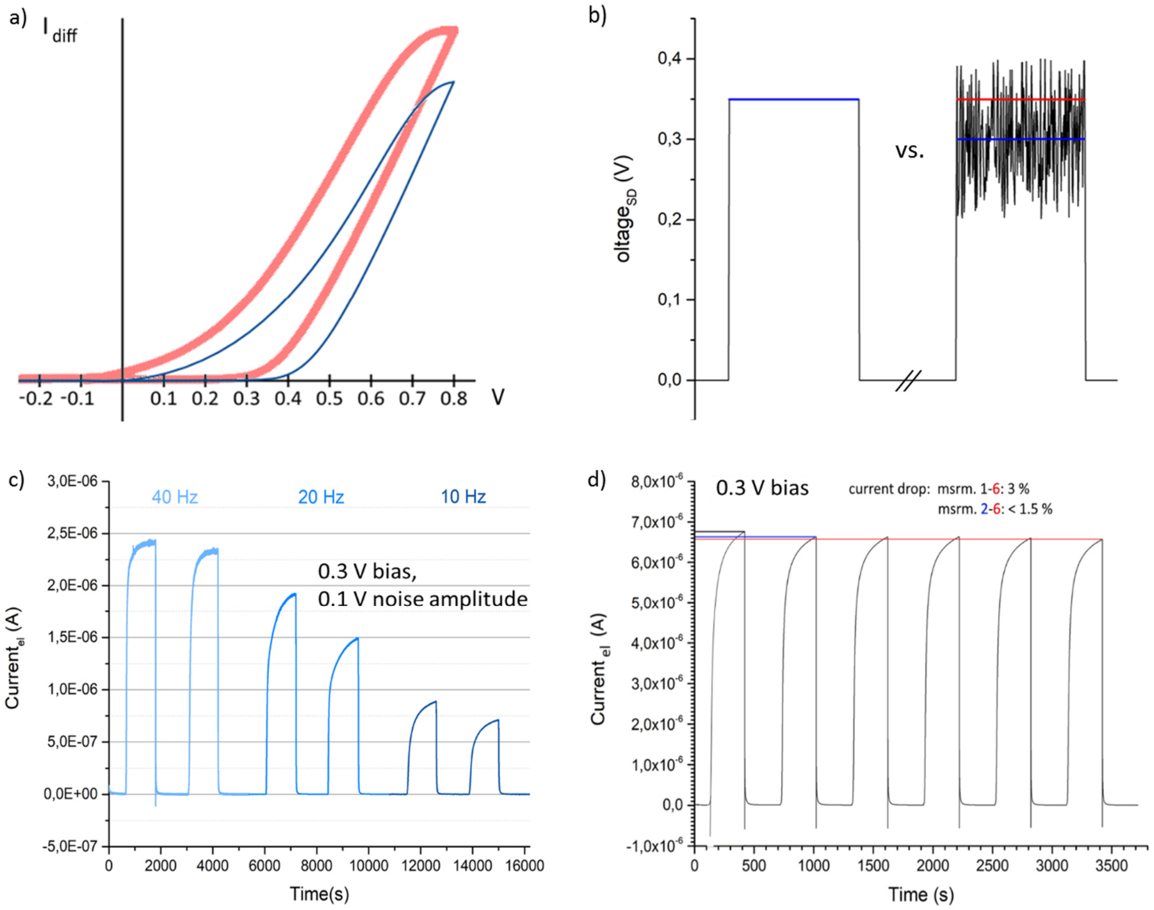

Figure 3-5: a) Graphical representation of a premature initiation of OMD switching at sub-threshold potential values, caused by a potentiation by the positive potential spikes of a superimposed noise signal (b). c) Kinetic response of an OMD at a constant bias of +0.3 V and an applied coloured noise of different frequencies and an amplitude range of 0.1 V, exposed to ambient conditions. d) Kinetic response of the device at a constant +0.3 V bias on a capped device, providing humid conditions around the active zone.

d), this approach indeed gives a relevant stabilization of the system that delivers a much more stable and reproducible output. We hence proceeded by carrying out kinetics measurements at different applied constant voltages close to the onset potential, comparing the response to a bias with and without the application of a 20 Hz noise signal with an amplitude range of 0.1 V, acquired in succession. Two sets of results are presented in Figure 3-6. In the first series of measurements, no difference is visible between the mean output current in the case of the stimulus with superimposed noise and the response at the respective bias without noise application. This suggests that the postulated effect of switching enhancement by noise did not apply, which could be caused by a negation of the potentiation by positive voltage spikes through the inverse effect of negative voltage spikes, before the switching can initiate. On the other hand, a small difference can clearly be seen in the second set of measurements. Considering the constant behaviour in the first series, we assume that the slight decay of characteristics without the application of noise in the second series might, again, be caused by slow material degradation.

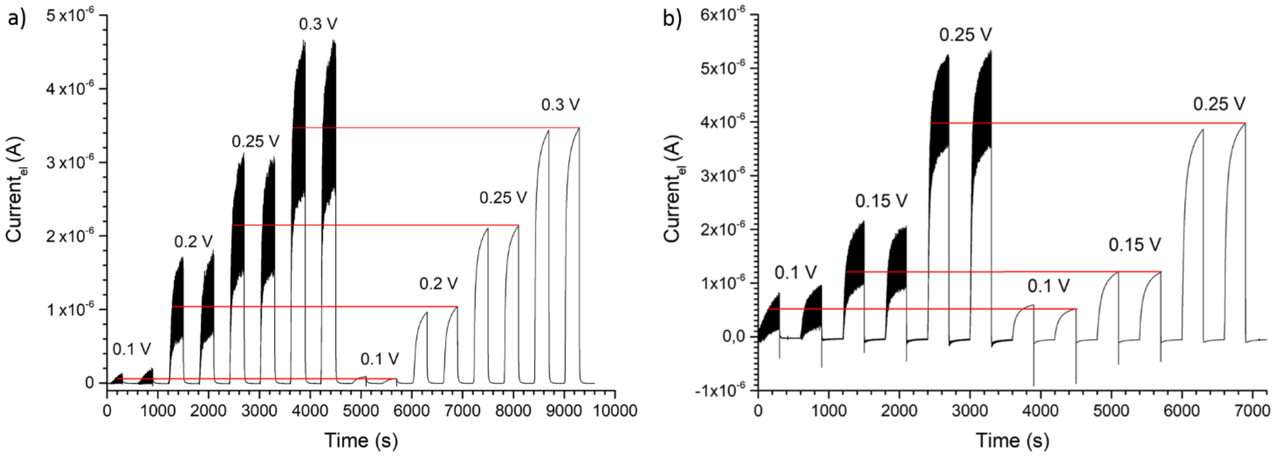

Figure 3-6: Kinetic response of an OMD fabricated with a $LiClO_4$ (0.1 M)- and HCl-doped PEO gel as the SPE, in two different series of measurements. The output current is registered at different constant biases (indicated in the graphs) with (curves on the left) and without the application of a 20 Hz electrical noise signal with an amplitude of 0.1 V (right curves). No difference between the two was observed in the first series (panel a), whereas slightly lower output currents are achieved in the second series, possibly caused by slow material degradation.

As an evolution of this experiment, the dependence of the output characteristics of miniaturized OMDs (200 μm channel length) featuring a liquid electrolyte (1 N HCl) from the applied electrical noise was studied in a work by Battistoni *et al.* [110]. Rather than applying a noise with a constant amplitude range, the gain parameter (in analogy to CV) has been introduced, modifying the noise amplitude (1−100 mV) depending on the current memresistance M of the device: $v_{noise} = M \cdot gain$. Such an approach allows to effectively preserve PANI from undesired overoxidation. Besides, the miniaturization and use of a liquid electrolyte allows to increase the operation speed and sensitivity, and minimize the influence of eventual electrolyte instability, making it a much more suitable model system. The I-V hysteresis behaviour as a function of different noise amplitudes (or gain parameters) is shown in Figure 3-7.

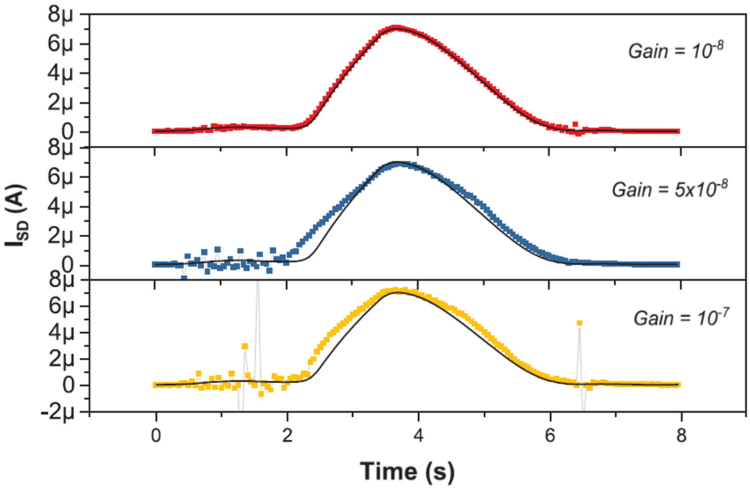

Figure 3-7: I-V characterization of OMDs with different gain parameters [110].

These results suggest that the observations made in Figure 3-6 b) may have been caused by a similar effect. However, the slow response and general instability of SPE-based OMDs makes it difficult to reliably reproduce such behaviour. These studies have directed our research towards the direction of developing devices with a degree of stability and reliability that would make them more suitable for such very refined applications. While this is a quite very relevant goal in general, it is absolutely critical in cases as the ones we are approaching, with systems interfacing and finely emulating natural nervous systems. In fact, experimental data suggests that advancements in the fields of microelectronics, neuroscience and bioelectronic applications require more robust, reliable, fast switching devices that would deliver reproducible results under comparable conditions.

These have therefore become the specific goals of this thesis, to which end the structure, composition and the functioning principle of the PANI based OMD have been investigated, qualified and optimized.

4 PANI-based OMD with improved stability and performance

Section 1.2 is devoted to the structure of an OMD and the basic principles by which the device operates. As already mentioned there, comprehensive studies have been carried out on the working mechanism, among which has been discussed the one reporting an electrochemical model which allows to simulate the device's characteristics with a very good agreement between calculated and experimental data [94]. However, the present thesis extends such studies to some critical aspects concerning the composition of SPEs and the nature of the gate electrode that are analysed in more depth. This chapter illustrates the achieved results, their impact on the optimization of OMD performance and the understanding of the underlying effects.

4.1 The role of SPE dopant additives in device functioning

As previously discussed, a significant role in the device's operation has been attributed to the lithium ions present in the polyelectrolyte (see sections 1.2.1.2 and 1.2.4). As it was discussed in section 1.2.1.1, polyaniline in its oxidized form carries positive charges that cause the material's conductivity and are compensated by chloride counterions. Lithium ions are assumed to be involved in the switching mechanism, compensating the charge of chloride ions in the channel upon reduction of the polyaniline. Hence, it has been argued that the injection of cations into the thin film channel causes the change of conductivity in PANI. Such an argumentation seems quite similar to the mechanism typically proposed for organic electrochemical transistors (OECT) [111]–[113]. Figure 4-1 a, b) illustrates an OECT based on poly(3,4-ethylenedioxythiophene) doped with polystyrene sulfonate (PEDOT:PSS).

Analogous to the notion given for OMDs, the change in conductivity of the device is controlled by the injection of ions into the thin film channel. The difference in the operation of these devices is that in OECTs, a positive voltage is applied to the gate electrode in a way that electrolyte cations are injected into the PEDOT:PSS channel (causing the PEDOT:PSS dedoping: the device works in the depletion mode), whereas in OMDs, the gate is grounded and the electrical field is varied through a voltage applied between the source and the drain. Other than that, if we consider Figure 4-1 c, d) the process occurring in the two systems seems to be very similar on a molecular level. However, it must be noted that in PEDOT:PSS based OECTs, the anions are immobilized, whereas in OMDs, the chloride ions remain mobile.

On this basis, recently, Cifarelli *et al.* [114] suggested that lithium ions (or dopant cations in general) do not play a decisive role in the OMD's electrochemical operation mechanism. Instead, the authors propose a mechanism in which the mobile chloride ions are responsible for the charge transfer between the two electrodes, and thus crucial for OMD functioning. This was shown by successfully operating a device fabricated with a PEO gel that did not contain any additive besides HCl, needed to maintain PANI doped in its emeraldine form. An excellent demonstration of the role of the anion is presented in a study by Orata *et al.* [115], where PANI films are examined with a quartz crystal

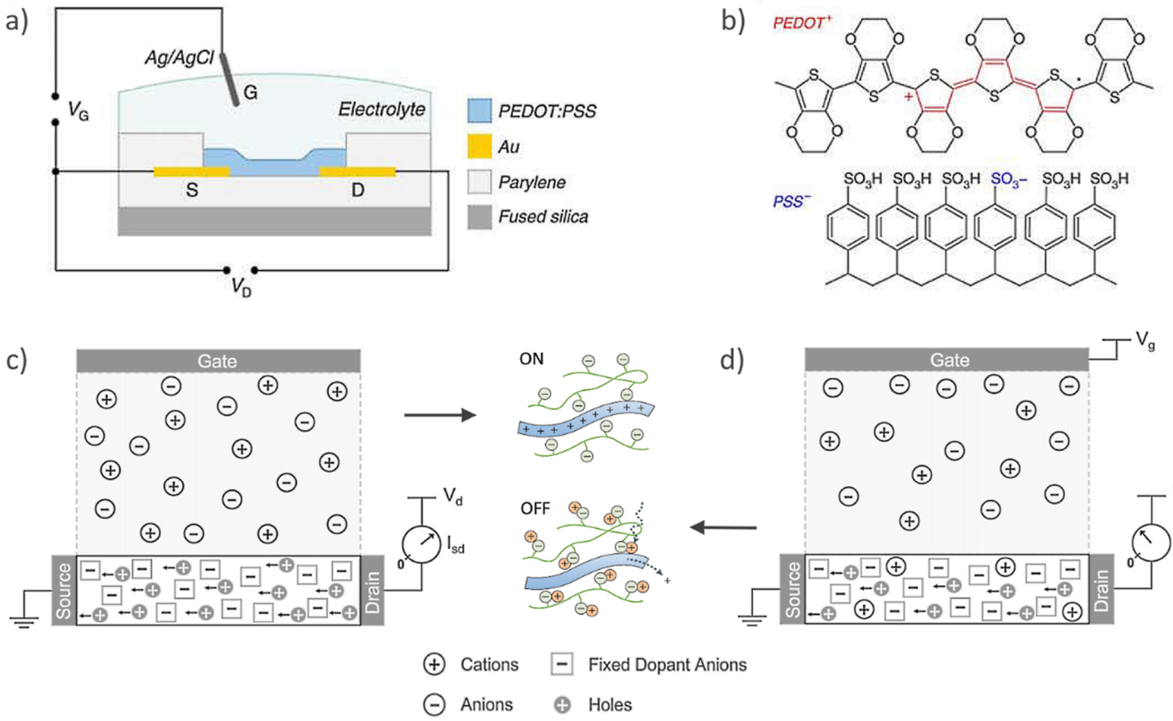

Figure 4-1: a) Schematic representation of a PEDOT:PSS-based OECT device [113]; b) chemical structure of PEDOT:PSS (PEDOT in its oxidized form); c) schematic representation of an OECT in its conductive state with positive charges of PEDOT are compensated by neighbouring PSS-SO_3^- anions and d) in its nonconductive state after a voltage V_G is applied to the gate electrode and cations are injected from the electrolyte into the thin film channel (adapted from [111],[112]).

microbalance (QCM) during voltamperometric measurements (Figure 4-2). This technique allows to register the variation of the weight of the sample in correlation with the occurring redox processes, since the weight change is directly proportional to the change of the resonant frequency of the quartz crystal covered with PANI according to the Sauerbrey equation:

$$\Delta f = f_0^2 \Delta m/(A\sqrt{\rho_q \mu_q}) \qquad \text{Equation 5}$$

where Δf is the resonance frequency change, f_0 is the fundamental resonant frequency of the crystal (5 MHz), Δm is the mass change, A is the piezoelectrically active crystal surface area, ρ_q is the density of quartz (2.648 $g\cdot cm^{-3}$) and μ_q is the shear modulus of quartz (2.947·10^{11} $g\cdot cm^{-1}s^{-2}$ for AT-cut quartz

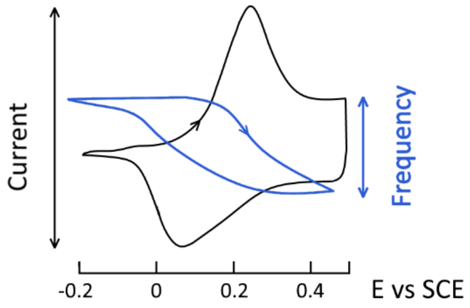

Figure 4-2: Exemplary CV/QCM characterization of a PANI film (adapted from [115]).

Table 1: Exemplary QCM data for PANI in solutions containing various anions [115].

Anion	Δf(Hz)	MW of anion (g/mol)	Δf/MW
Cl^-	46	35.5	1.30
Br^-	72	79.9	0.90
HSO_4^-	89	97.1	0.92
ClO_4^-	88	99.5	0.88
$CF_3CO_2^-$	102	113.0	0.90

crystals). The good agreement of the data summarized in Table 1 strongly indicates that the registered mass change is indeed due to the inserted anions. The comparatively high value for chloride and lower values for other anions are probably due to different diffusion coefficients and ion hydration levels.

On first sight, there appears to be a contradiction with the XRF experiment carried out by Berzina *et al.*, whose data clearly show a flux of Rb^+ towards and away from the PANI channel, which quite probably includes a diffusion inside and out of the film, considering the grazing-incidence beam configuration. While such an observation is coherent with the ionic migration in the electric field that is applied between the polyaniline and the gate electrode, according to Cifarelli *et al.*, there appears to be no causal relation between the migration of cations and the switching of PANI. Following the formerly assumed switching mechanism, it could be argued that in their case, by invoking the Grotthuss mechanism [116] (describing proton or proton defect diffusion through the hydrogen bond network of water molecules, illustrated in Figure 4-3), the mobile cation responsible for the transition (and compensation of released chloride ions) is H^+ or H_3O^+. In that case, however, H^+ should also be considered in the models of Smerieri and Demin, as the ionic mobility of H^+ always exceeds that of other cations when a sizeable percentage of water is present in the system. Yet in references [93] and [94], the argumentation by Smerieri and Demin is clearly focused on lithium ions, including them in the proposed calculations. This apparent misconception possibly arises from the adoption of lithium-doped PEO-based SPE from LIB technology, where lithium ions are indeed directly involved in the charging/discharging process by intercalating into the graphite and metal oxide matrices, as shown in Figure 4-4 [117].

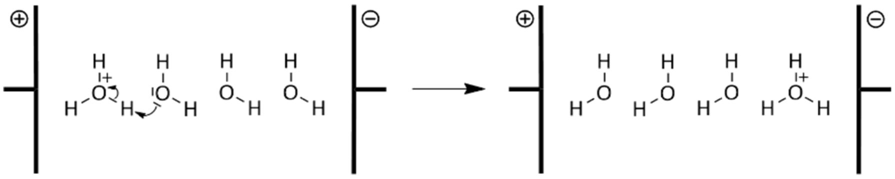

Figure 4-3: Simplified illustration of the "hopping" mechanism of H+ migration through a network of water molecules.

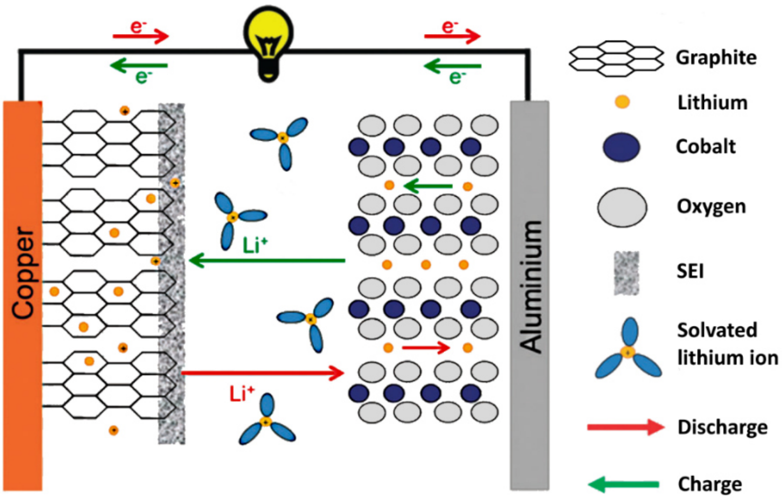

Figure 4-4: Schematic representation of lithium-ion batteries. Due to their small radius, lithium ions can intercalate in graphite and metal oxide matrices during the charging and discharging process, respectively (adapted from [117]).

Another aspect that leads to a rethinking of the switching mechanism is the reaction at the reference/counter electrode, for which the involvement of dopant perchlorate ions, described by the following equation, is suggested in reference [94]:

$$\mathrm{Ag} + \mathrm{ClO_4^-} \rightleftharpoons \mathrm{AgClO_4} + \mathrm{e^-} \qquad \text{Equation 6}$$

In Cifarelli's work, the composition of the silver wire is analysed after a full measurement cycle (oxidation and reduction of PANI and, conversely, reduction and oxidation of silver) by means of SEM-EDX. The SEM images show the corrosion of the wire as its smooth surface becomes porous, as it is well shown in another work [118]. The presence of a chlorine signal and absence of sizeable signals of oxygen in the EDX analysis of the wire suggest the formation of AgCl rather than $AgClO_4$ or Ag_2O. The formation of the latter is additionally ruled out by the fact that the reaction takes place in an acid environment which makes the formation of the oxide thermodynamically unfavourable. Furthermore, other works [117]–[120] show the precipitation of AgCl on the surface of silver occurring at voltages below the thermodynamic reversible potential E^0 (Ag/AgCl) = 0.222 V. The eventual dissociation of silver ions mentioned in the study of Cifarelli *et al.* is considered as negligible. In the cited literature [121],[122], the behaviour of Ag/AgCl electrodes is investigated in liquid electrolytes and the diffusion of Ag^+ ions in a PEO-based SPE is expected to be significantly slower, especially considering the high rate of silver oxidation. In any case, the findings in reference [114] strongly indicate that the reaction that should be taken into consideration for the silver reference/counter electrode is the following:

$$\mathrm{Ag} + \mathrm{Cl^-} \rightleftharpoons \mathrm{AgCl} + \mathrm{e^-} \qquad \text{Equation 7}$$

In this context, it should be pointed out that the designation of the silver electrode as a reference electrode is not appropriate because, by definition, reference electrodes do not participate in the cell's electrochemical reactions. It rather maintains a constant electrochemical potential and serves as a reference point to enable the determination of the potentials of the working or the counter electrode. A grounded gate electrode can only be named as reference in the sense that any potential difference applied at the drain electrode is referred to the half-reaction taking place at the gate, although its electrode potential is not constant throughout the measurement. In this respect, it is advantageous that Ag/AgCl is a reversible system [122],[123] with relatively fast kinetics, improving data reproducibility.

The fact that chloride ions are mobile, together with the experimental evidence that lithium ions do not directly participate in any of the two half-reactions and can be omitted from Equation 4, leads to the following form for the reduction of PANI-ES to PANI-LE:

$$\mathrm{PANI^+\!:Cl^-} + \mathrm{e^-} \rightleftharpoons \mathrm{PANI} + \mathrm{Cl^-} \qquad \text{Equation 8}$$

In this way, with chloride ions being directly involved in both half reactions during the switching process, it makes sense to assume that their concentration gradient, migration and diffusion as well as the related reaction kinetics are the most relevant aspects to be considered in the context of the device functioning. Hence, it becomes clearer which components are essential for a proper OMD operation and which ones, in turn, can be varied in order to improve the system in terms of stability and performance. Although a significant progress was made by the study of Cifarelli *et al.*, there is still the need for a better understanding of the device operation that is crucial for further enhancing the performance of the system. In particular, one challenge is to overcome the present OMD limitations in terms of reproducibility and endurance that are not yet fully adequate for developing a robust technology. Some problems arise from the material degradation of the device's components, concerning PEO, PANI and the silver gate electrode. In all likelihood, it is the deterioration of the former that is mostly responsible for the rather quick decay of the OMD's performance over time. In view of previous findings, in the following section, the revised operation mechanism is further investigated. In particular, the goal is to provide further proof for the assumptions made above for a better understanding of the effects of doping additives in the solid polyelectrolyte, and to suggest viable approaches to improve OMD performance and reliability.

4.1.1 Li^+ free SPE containing other hygroscopic salts

It must be pointed out that, despite not being directly involved in OMD switching, the lithium salt plays a very important role as an SPE additive due to its hygroscopicity, as it provides the necessary water content within the polyelectrolyte gel to lower the fraction of crystallized PEO. This is of paramount importance for the device's performance since, as it is well known, a PEO-based polyelectrolyte demonstrates its best ionic conductivity in a fully amorphous state when sufficiently hydrated [124]. Thus, the concentration of the dopant remains a significant parameter in the fabrication of OMD. From now on, when dopant concentrations are mentioned, they are always related to the preparation of the gel, i.e., the step in which the gel is prepared by adding PEO to an aqueous solution of the respective dopant salt. As the SPE is deposited, it solidifies by losing the majority of its water content upon evaporation, so that the final proportion of the dopant in the SPE increases. A determination of the final water content and PEO or dopant concentration could be made by precise weighing of the gel upon deposition and after its solidification.

To better qualify the role of hygroscopic additives, in the present work we first examined how the device operates when substituting $LiClO_4$ or LiCl in PEO-based polyelectrolyte with other hygroscopic salts. Our experimental finding are the subject of a literature work [125]. To this end, we prepared various PEO gels containing various salts, namely $MgCl_2$, $CaCl_2$, RbCl, CsCl, $CeCl_3$, $Mg(NO_3)_2$, $MgSO_4$ and Na_2SO_4. We also added an acid to the PEO gel to maintain the PANI sufficiently doped upon contact, thus preventing its transition to the nonconductive emeraldine base state. Hydrochloric acid was used mainly to ensure a sufficiently low pH level while in the case of the gel containing $Mg(NO_3)_2$ the HCl also provided the chloride ions which are necessary for both half-reactions to occur. An exception was the gel containing $MgSO_4$ where H_2SO_4 was used instead of HCl. Some of the gels, namely the ones with RbCl, CsCl, $Mg(NO_3)_2$, Na_2SO_4 and $MgSO_4$ salts, proved to be insufficiently hydrated in the solid state, leading to intense PEO and/or salt crystallization. The worst case is the one based on $MgSO_4$. In these SPEs, switching was not achievable because of the limitations on ionic transport. The change from the amorphous state is due to the hygroscopicity of the mentioned salts that is not enough to maintain the needed level of hydration in the gel that, hence, undergoes a drying process when exposed to the surrounding atmosphere in ambient condition. In the context of switching kinetics, this effect was shown by Burganova *et al.* [126] when varying the $LiClO_4$ concentration in a standardly fabricated OMD. In this work, too low dopant concentrations (0.025 M $LiClO_4$) led to stronger PEO crystallization, because the amount of water that could be retained in the gel was not enough to maintain its amorphous state in the whole bulk of the polyelectrolyte. Conversely, the formerly common concentration of 0.1 M $LilO_4$ also appeared to be too high, as in this case, the time required for all of the ionic current to pass through the polyelectrolyte was the highest. In this case, the obstruction of current probably was due to the formation of $LiClO_4$ salt clusters that, in turn, may have served as a source of nucleation for PEO. An intermediate concentration of 0.05 M $LiClO_4$ in the gel preparation showed the fastest kinetics in this work, making the first step towards the optimization of the device.

The behaviour of the gel containing $MgSO_4$ seems odd at first glance, because this salt is known to be very hygroscopic, so it should guarantee a sufficient water content. In this case, the crystallization is due to another type of process, the so-called salt-induced precipitation ("salting out") of PEO in the presence of sulfate. The underlying concept of kosmo-and chaotropicity of dopant ions is presented in section 4.2 of the present thesis work as it will be more relevant for the development of PEO gels with improved durability.

The occurred hindrance with insufficiently hydrated gels was preliminarily resolved by creating an atmosphere with increased humidity around the sample. This was achieved by placing a cap containing a wet ball of cotton on top over the active zone. As shown in Figure 4-5, the gels partially cleared and liquefied within few minutes, allowing to carry out a standard electrical characterization of the memristive device. Examples of current-voltage curves of OMDs prepared with the mentioned SPE are shown in Figure 4-6 a). All devices that were fabricated with polyelectrolytes containing chloride salts displayed typical memristive behaviour. It is noteworthy that the OMD containing $MgCl_2$ shows particularly satisfactory characteristics in terms of the hysteresis shape and, more importantly, reproducibility. This is a good indication of the quality and stability of the PEO gel due to a favourable combination of hygroscopicity and chaotropicity of the salt ions. For the device containing $Mg(NO_3)_2$, no memristive behaviour was observed even by placing the cap with the wet cotton above the active zone, used to maintain the PEO in its amorphous state. This may be well understood by considering the oxidizing character of the nitrate ions, which prevents PANI from being reduced (or maintained) to the leucoemeraldine form when attempting to switch off the device. The same effect, although weaker, likely occurs in the devices with PEO containing $MgSO_4$ and Na_2SO_4. When applying the cap to liquefy the SPE and carrying out standard current-voltage measurements, these devices display characteristics that are somewhat similar to

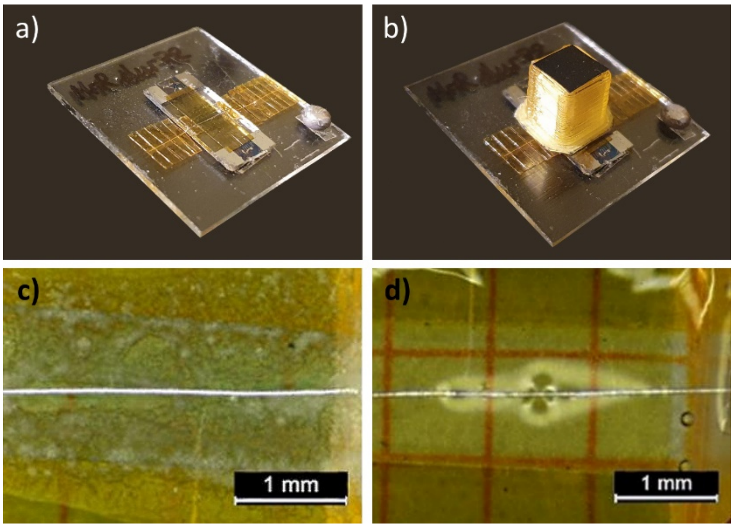

Figure 4-5: a) Photograph of a commonly fabricated OMD, b) covered with a plastic cap with a wet cotton ball under its sealing; Top-view microphotographs of the OMD c) before and d) after the exposure to the humid atmosphere through capping (SPE made with 30 mg/ml PEO concentration and 0.1 mol/l RbCl).

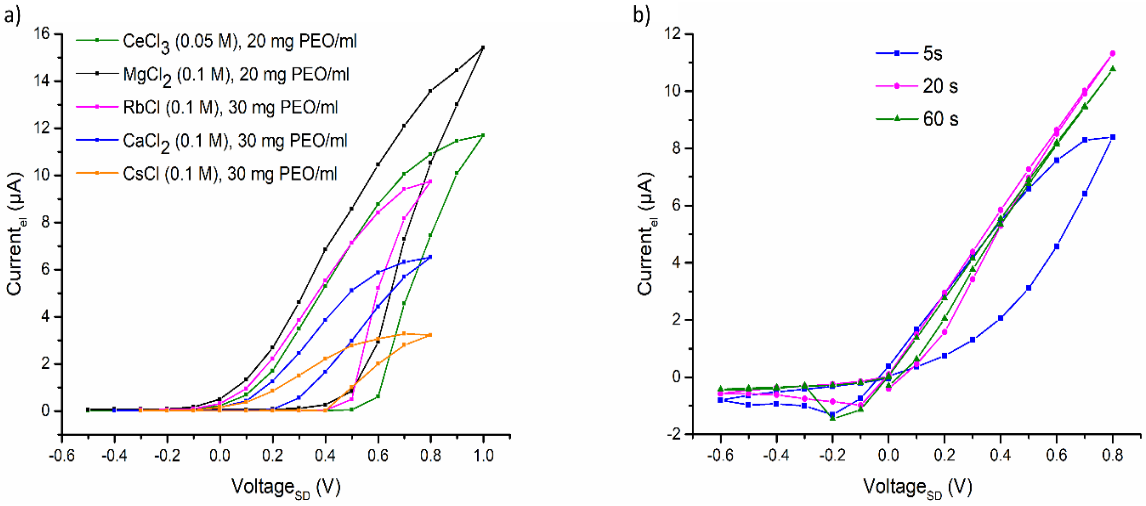

Figure 4-6: a) Hysteresis curves of a series of OMDs with SPE made from PEO solutions (as color-coded and labelled in the figure). The samples with RbCl and CsCl were measured under humid atmosphere by applying a cap with a wet ball of cotton on top of the active zone , dwell time for each acquisition step of 0.1 V = 30 s.

b) I-V characterization of an OMD with SPE made from a PEO solution containing 0.05 M $MgSO_4$, measured under humid atmosphere with different dwell times per voltage step as labelled.

those of a typical OMD. Figure 4-6 b) shows an I-V curve of a device fabricated with PEO containing $MgSO_4$, recorded with a dwell time of 20 s, which exhibits some switching, characterized by the rectification of the curve at negative applied biases and a narrow hysteresis. This indicates that the device shows faster overall kinetics as compared to those in panel a) at similar measuring conditions. When the dwell time is decreased to 5 s per voltage step, a significant broadening of the hysteresis is observed, yet the device is still fast enough to switch. On the contrary, increasing the dwell time to 60 s causes an even stronger narrowing of the hysteresis to a point where it is barely present. This is because during the backward sweep, the kinetics of PANI reduction is faster than the dwell time. It is noteworthy that the electronic current in the “off” state at negative voltage biases remains in the order of µA (compared to nA for a typical OMD) in all three cases. Comparable results were obtained for the devices made with PEO containing Na_2SO_4. They indicate that the switching-off took place only partially and an equilibrium state was established in which some of the material remains in its oxidized, conductive form. In section 4.1.3, the role of the sulfate ion as an oxidizing agent will be discussed in further detail.

4.1.2 The role of dopant cations

Based on the above experimental results, we observed that lithium ions, in specific, are not necessary for OMD operation, since devices fabricated with SPE containing other hygroscopic chloride salts also showed switching. However, this does not exclude the possibility that in these cases, the initially suggested role of Li^+ [93],[94] is performed by another cation (Mg^{2+}, Ca^{2+}, Cs^+ etc.), as it has been implied in the fundamental work dedicated to exploring the device via XRF [88].

As discussed by Cifarelli *et al.* [114], the presence of Li^+ ions in the polyelectrolyte is not necessary for the functioning of the OMD, whereas the role of the silver gate electrode and the presence of chloride ions is crucial. We aim at demonstrating with additional evidence the notion that dopant cations do not play a decisive role in the electrochemical reaction defining the OMD's working principle shown in Equation 7 and Equation 8. Our approach is to show the independence of the OMD's switching kinetics from the type of cation present in the electrolyte. From the XRF experiments of reference [88] it is known that the migration velocity of the bulkier Rb^+ in PEO is lower with respect to Li^+ ions. Hence, if the cations participate in the OMD's switching mechanism, we expect to observe a difference in the characteristics of the corresponding devices. A direct comparison of devices with various compositions of the PEO-based polyelectrolyte (as discussed in section 4.1.1) is difficult because of the different hygroscopicity of the dopant salts defining the SPE's final phase composition. Even with equal ion concentrations and providing a humid atmosphere using the cap, the conditions of the polyelectrolytes could still be significantly different from each other. For this reason, we decided to make the comparison using equally concentrated liquid electrolytes where the salt hygroscopicity has no effect at all, leaving whichever differences may occur to be attributable solely to the dopant ions with different ionic radii and mobilities. This goal required a modified experimental setup similar to the one proposed in reference [88], which is shown Figure 4-7.

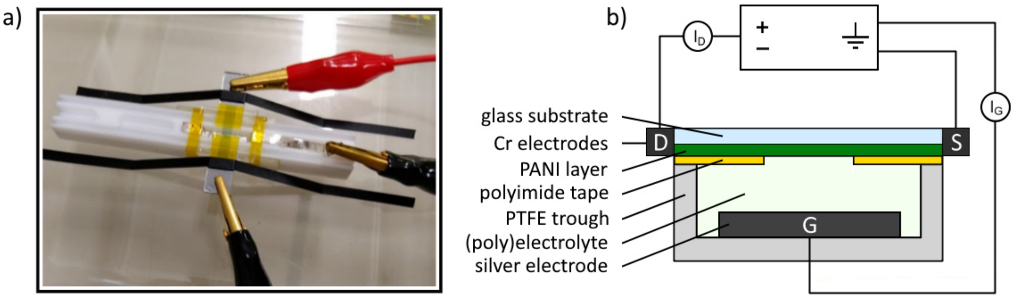

Figure 4-7: a) Photograph and b) schematic representation of the setup for kinetics characterizations of devices with liquid electrolytes. The well depth and width is 3 mm.

A series of solutions of monovalent metal chlorides (LiCl, NaCl, KCl, RbCl, CsCl) in aqueous HCl were chosen to both simplify and unify the system, the latter meaning that the only difference in SPEs would be the added cation. Relatively low concentrations for both HCl and the dopant (0.01 N and 0.001 M, respectively) were chosen because higher concentrations could possibly even out gradients and mask eventual kinetics differences caused by different dopant ions. Because of the need for an acidic environment, we could not reduce further the HCl concentration, since it would lead to the reduction of PANI-ES to PANI-EB and, hence, to a loss of conductivity. To provide even better comparability, all measurements were performed on the same PANI film, thoroughly rinsing it when changing the electrolyte and carrying out each measurement repeatedly in order to monitor the presence of a possible aging of the sample. We carried out three series of experiments using the same PANI film, repeating kinetic measurements when varying polyelectrolyte solutions one by one in each unique series. The obtained kinetics of all the series show the same trend.

The typical kinetic responses of the OMD for different metal chloride electrolytes are shown in Figure 4-8 a). They appear to be quite similar with differences in the normalized curves that are within the margin of error, as confirmed by the fit parameters in Table 2. We could not observe any trend in correlation with the ionic radii and the established ionic mobilities [127]. However, when considering the curves without normalization, one particularity must be pointed out. The saturation current results to be slightly higher for the electrolytes containing caesium and rubidium chloride in most cases. It is especially peculiar that no trend with respect to ionic radii is observed throughout the rest of the series. This observation could not be adequately explained in the framework of the showed study. As a perspective, it would be interesting to assess whether this effect could be associated with the strength of the interactions of these cations with chloride ions. A stronger interaction with chloride ions compensating the positive charges on oxidized PANI chains could cause a stronger depinning of polarons from their counterions, increasing charge mobility and conductivity.

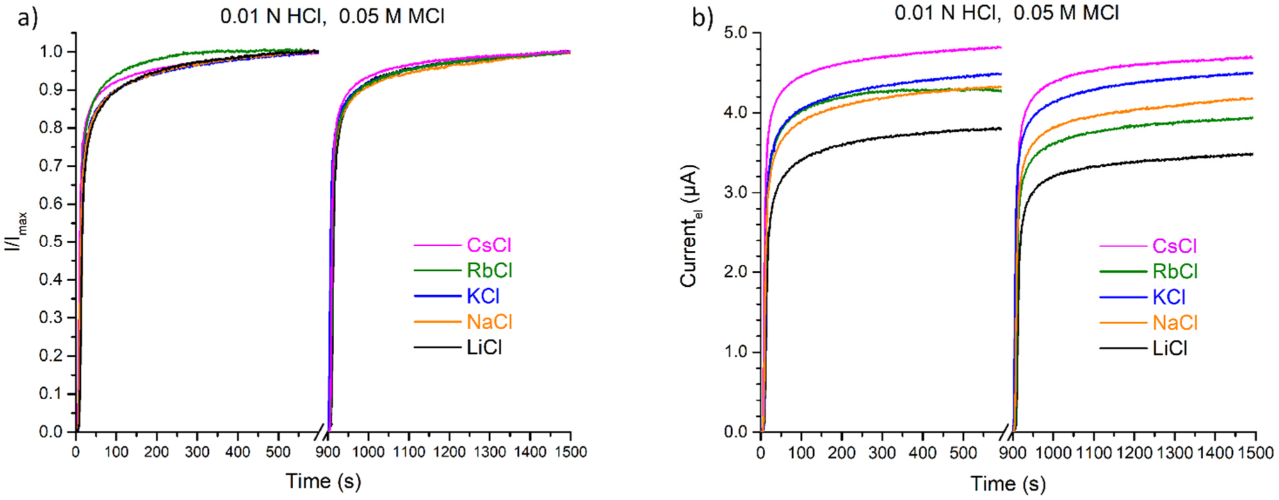

Figure 4-8: a) Normalized and b) not normalized kinetic response of OMD with liquid electrolytes containing different alkali metal chloride salts at an applied voltage bias of +0.5 V. Reduction periods at −0.2 V are omitted.

Table 2: Double exponential fit parameters ((τ represent rate constants) for curves resulting from kinetics measurements as in Figure 4-8 a).

Fit equation: $\frac{I}{I_{max}} = A_1 \cdot exp\left(\frac{t_0-t}{\tau_1}\right) + A_2 \cdot exp\left(\frac{t_0-t}{\tau_2}\right)$

At least nine single measurements have been carried out for each electrolyte with a total number of 52 measurements used for the statistics. In the last row, a mean value of the calculated average τ parameters can be seen with the corresponding standard error.

dopant	avg. τ_1	$\sigma(\overline{\tau_1})$	avg. τ_2	$\sigma(\overline{\tau_2})$
LiCl	7.37	0.78	108.02	7.15
NaCl	7.64	1.03	124.92	6.48
KCl	7.53	0.76	123.18	4.82
RbCl	8.03	1.02	113.65	6.52
CsCl	6.76	0.81	106.03	5.47
mean	7.38	0.19	115.16	3.85

4.1.3 SPE containing Li^+ with an addition of [12]crown-4

The results shown up to now indicate that there is no significant effect of the cation radius on the kinetic response of the device. However, the observed inconsistencies in the saturation currents of devices fabricated with SPE containing different cations could give rise to some doubts. We hence carried out another experiment, similar in design to the previous one, with the idea to observe the kinetic response of a device when adding a substance that interferes significantly with the cationic mobility. In detail, we compared the response of devices with two equal electrolytes containing LiCl as the solute, one of which contained [12]crown-4 (12C4) of equimolar concentration. Crown ethers are representatives of the class of coronands that are known to form stable complexes with alkali metal ions (among others) depending on the size of their cavity. The 12C4 is one such coronand, having a cavity radius of 0.72−0.81 Å [128], matching the ionic radius of Li^+ (0.74−0.86 Å), hence suitable to bind lithium ions, as shown in Figure 4-9.

There are numerous reports in literature showing that such a complexation affects the mobility of ionic species [129]–[132]. Following the former assumption that lithium ions play a role in the operation mechanism of the OMD, a significant difference should be expected in the kinetic response of the devices when comparing the two above mentioned electrolytes. We then carried out the same measurements shown in Figure 4-9 on the same substrate, using the approach discussed in the previous section. We therefore chose the setup with the liquid electrolytes for the same reasons discussed in section 4.1.2 (Figure 4-7). The normalized curves correspond rather well with one another, keeping the same shape and trends, suggesting that the addition of [12]crown-4 to the electrolyte causes no significant change in the kinetic response. The corresponding double exponential fit parameters are reported in Table 3. Some insignificant differences are observed in the I/I_{max} saturation values between the series characterizing the electrolyte with and without the crown ether, where the latter are slightly lower than their counterparts. This is likely due to changes in the material itself because all the measurements were carried out in succession and a consistent, small decay can also be observed within both separate series.

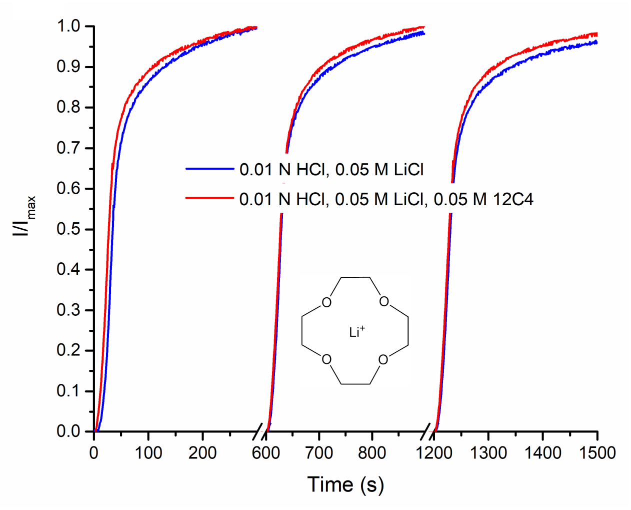

Figure 4-9: Kinetic response of OMD with liquid electrolytes containing LiCl with (red) and without (blue) the equimolar addition of [12]crown-4 at an applied voltage bias of +0.5 V. Reduction periods at −0.2 V are omitted. The molecular structure of the lithium-12C4 complex is shown in the inset. Sandwich complexes of one lithium ion with two 12C4 molecules are also common.

Table 3: Double exponential fit parameters (τ represent rate constants) for curves resulting from kinetics measurements as in Figure 4-9.

Fit equation: $\frac{I}{I_{max}} = A_1 \cdot exp\left(\frac{t_0 - t}{\tau_1}\right) + A_2 \cdot exp\left(\frac{t_0 - t}{\tau_2}\right)$

electrolyte	curve	τ_1	τ_2
LiCl	1	15.64	164.00
	2	12.24	117.51
	3	13.03	107.76
LiCl + 12C4	1	11.45	106.08
	2	12.37	101.91
	3	12.76	98.61

4.1.4 The role of dopant anions

In the above-described experiments, the choice of a liquid electrolyte may lead to think that that eventual differences in the device characteristics could be masked or even neutralized by the fast (cationic) diffusion processes occurring in the liquid state, even at relatively low concentrations of dopants. In order to provide a further insight on the role of ionic species, we also investigated whether changing the anion would affect the memristive characteristics of the OMD. For a better comparison of the results, we decided to confront anions with the same charge but of different size. For our system, the choice of monoprotic acids to be compared with the standardly used HCl is somewhat limited. Common organic acids such as acetic acid are too weak to provide a pH that would dope PANI at appropriate concentrations, while the hydrogen halides HF and HI are toxic, corrosive or could display some redox chemistry of their own, which could interfere with the measurement. Other possible candidates as dopants for PANI are strong organic (sulfonic) acids. Although there are reports [132],[133] of polyanilines doped with CSA, TSA or DBSA, these are typically synthesized compounds, made by polymerization of aniline in the respective acid solution, yielding the self-doped polymer form. Our devices are fabricated with pristine PANI with higher mean molecular weight (Mw = 10^5 Da) in its emeraldine base form, the doping of which was not successful with any of these three sulfonic acids in our experiments. We assume that this is due to the high density of the deposited PANI film and the low mobility of the respective anions. For these reasons, the range of electrolytes that we used was limited to HCl, HBr, $HClO_4$ and H_3PO_4.

In a first series of experiments, a comparison of the device's kinetics in liquid electrolytes featuring different anions (i.e., different diluted acids) was carried out following the measuring routine described in Chapter 2. To provide equal conditions in each experiment, we prepared electrolytes at the same pH and concentration of 0.1 mol/l, assuming the full dissociation for the strong acids HCl, HBr, and $HClO_4$. In the case of the relatively weak H_3PO_4 ($pK_{a1} = 2.124$ [134]), the concentration of choice was 1.43 mol/l in order to provide equal H_3O^+ and anion ($H_2PO_4^-$) concentrations of 0.1 mol/l. While the second and third dissociation steps introduce HPO_4^{2-} and PO_4^{3-} to the system, their concentrations are negligibly low and hence are not considered. As it is shown in Figure 4-10 a), the device switches on and off in each case with a clear difference in the kinetics depending on the electrolyte. This becomes even more evident upon fittings the acquired curves by a double exponential function, giving the rate constants τ_1 and τ_2 listed in Table 4. We observed that in the case of HCl and HBr, the maximum current was decaying during the series. We found that this is probably due to the volatility of these compounds because the same was not observed for the non-volatile $HClO_4$ and H_3PO_4. It appears that the response is quite similar in HCl and HBr, which is in good correlation with the quite similar relative ionic mobilities of chloride and bromide, reported in Table 4 [135]. The small difference observed in the onset time can be considered as negligible. It occurs a few seconds earlier in the case of HBr, likely due to the different reaction kinetics of chloride or bromide on either one of the electrodes (PANI, Ag or both). An instant switching onset is observed for $HClO_4$, which we assume to be due to the oxidizing character of perchloric acid, which promotes the transition of PANI to its conductive state even at low applied voltages. This is further confirmed by the relatively high currents during the reduction period at −0.2 V, suggesting that the transition from the conductive emeraldine salt state to the nonconductive leucoemeraldine state is incomplete and some conductivity is maintained, analogous to solid state devices produced with sulfate salts, mentioned in section 4.1.1. The switching kinetics, however, appears to be slower than in HCl or HBr (see slopes in the inset of Figure 4-10 a), which corresponds to the lower relative ionic mobility of perchlorate with respect to chloride or bromide [135]. A clearer indication of the correlation of kinetics with the ionic mobility is observed in H_3PO_4 which does not feature any additional redox activity of its own. The onset of the switching occurs later than that observed for HCl and HBr, again, possibly because of slower reaction kinetics on Ag and/or PANI. Once the switching is initiated, the current increases significantly slower in comparison to the other acids. This is in good correlation with the significantly lower ionic mobility of dihydrogen phosphate (more than a factor 2).

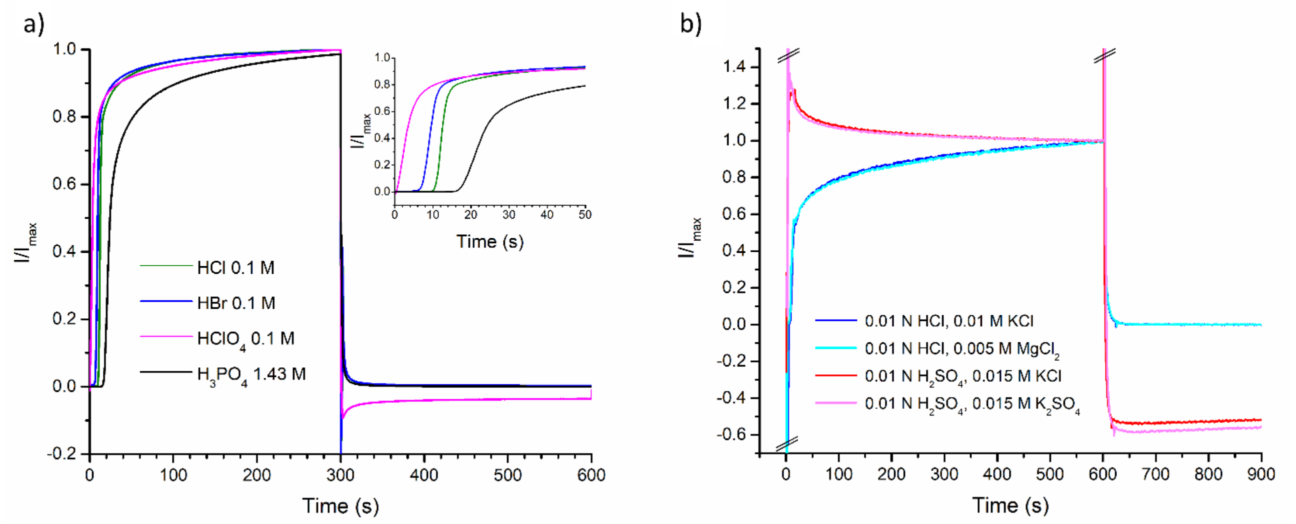

Figure 4-10: a Kinetic response of OMD in HCl, HBr, $HClO_4$ and H_3PO_4 at +0.5 V (oxidation period, 5 min) and −0.2 V (reduction period, 5 min). b) Kinetic response of OMD with HCl (blue, cyan) and H_2SO_4 (red, magenta) based electrolytes at +0.5 V (oxidation period, 10 min) and −0.2 V (reduction period, 5 min). For each electrolyte, from a series of three consecutive measurements, only the first is shown in the figure.

Table 4: Double exponential fit parameters (τ_1 and τ_2 represent the rate constants of the fittings) for curves resulting from kinetics measurements in Figure 4-10 a). The ionic mobility values u_X/u_{K^+} (relative to that of K^+) are taken from reference [135].

electrolyte	τ_1	τ_2	$u_X/u/_{K}+$
0.1 M HCl	1.89	49.86	1.04
0.1 M HBr	1.91	53.24	1.06
0.1 M $HClO_4$	3.35	80.66	0.92
1.43 M H_3PO_4	7.59	79.20	0.45

To further support our findings, in a second series of experiments, we compared the kinetics of the devices in a mono- and a diprotic acid (HCl and H_2SO_4). Although the experiments with $MgSO_4$ discussed in section 4.1.1 show that H_2SO_4, like $HClO_4$, also has an oxidizing character, PANI doped with H_2SO_4 shows very similar conductivity to HCl doping, suggesting that the second oxidation step towards the nonconductive pernigraniline state does not take place without any applied bias voltage. Keeping in mind the divalent character of the sulfate ion, the respective potassium and magnesium salts (KCl and $MgCl_2$ for HCl, K_2SO_4 and $MgSO_4$ for H_2SO_4) were added to the electrolyte for a more meaningful comparison. To keep the pH equal in each experiment, we chose an acid concentration of 0.01 N, assuming complete dissociation of H_2SO_4. Therefore, the amount of salt additive was chosen to obtain that the total concentration of the chloride and sulfate ions, respectively, were also equal in each case (0.02 M). As a consequence, due to the different valencies of the cations, the respective cation concentrations also differed (e.g., when measuring with HCl, 0.005 M $MgCl_2$ or 0.01 M KCl were added to achieve an equal total chloride concentration of 0.02 mol/L). This step allowed us to further assess the role of the concentration, size and electric charge of the cations. As shown in Figure 4-10 b), no significant difference could be observed when comparing electrolytes containing the same acid but different cations, which further proves the conclusions of section 4.1.2. At the same time, the difference between the performance of the OMD with electrolytes containing different anions is very pronounced – a significantly faster response is observed in H_2SO_4. This could be in a first instance attributed to the bivalent nature of the sulfate ion, suggesting that a larger charge per unit of time is carried from one electrode to another compared to the chloride ion. However, this is only one part of the picture since the sulfate ion is also significantly less mobile in aqueous solutions [135]. The final balancing is unclear and hence it is difficult to come to a conclusive understanding. As shown in Figure 4-10 b), there is a clear decay of the current after the maximum achieved after the switching-on. This suggests that a portion of the PANI-ES is further oxidized to the nonconductive pernigraniline state at the applied voltage bias (+0.5 V). Besides, when applying a negative drain voltage, the measured negative current is comparatively high, indicating an effect similar to that observed for the device featuring $HClO_4$ (see Figure 4-10 a). The oxidizing character of diluted sulfuric acid must be considered, since it presumably hinders the reduction of PANI-ES to PANI-LE when switching off the device, giving rise to the large current at negative drain voltage. On this basis, it is debatable whether the remarkable acceleration of the kinetics is due to the nature of the anion alone or assisted by this extraneous electrochemistry. Further experiments with sulfuric acid go beyond the scope of this work since we established that sulfate salts are not suited to be used in SPE formulas based on PEO.

To summarize, we provided a deeper insight and further detailed data that are consolidating and validating the mechanism proposed by Cifarelli *et al.* [114]. The ordinary functioning of the device was successfully shown in a series of experiments with PEO gels containing a series of different dopant salts. Our findings [125] strongly indicate that $LiClO_4$, commonly used in OMD devices, has the sole function of providing favourable conditions for PEO-based polyelectrolyte to maintain its amorphous state, and hence it can be replaced by another sufficiently hygroscopic salt. Therefore, it does not play a specific role in the memristive mechanism. Additional evidence is also gained from kinetics studies proving that the nature of the cation (i.e., its size and valence) have no significant effects on the memristive response of the OMD. A further, possibly more convincing confirmation of this conclusion is given by the fact that no significant difference could be registered when comparing OMD with electrolytes containing Li^+ and its 12C4 complex. Based on our findings, one could conclude that in the OMD switching mechanism, the relevant charge transfer is provided by the chloride ions, confirming what was proposed by Cifarelli *et al.* Additional evidence to support this mechanism is given by the experiments discussed here where the choice of the anion has a pronounced effect on the OMD's kinetics. The effect is evident when chloride ions are replaced by sulfate ions with a different ionic charge and/or mobility in the electrolyte, indicating the relevance of the anion for the OMD's operation. Overall, this work contributes to a more detailed understanding of the chemical processes underlying the switching of the device that is absolutely necessary to both improve the system's performance and overcome its weak points in terms of performance and endurance.

4.2 Improved SPE compositions for increased device performance

This section is devoted to the research of an optimal composition for PEO-based solid polyelectrolytes, aiming to meet the requirements for a lengthier, more consistent operation of OMDs. As the optical condition of the gels (i.e., their homogeneity and transparency) is a good gauge for their quality, the term "drying" will be used repeatedly when speaking about the developed SPEs. In particular, based on the context, it can mean either of two things: 1) The undesirable, *excessive drying* of a deposited PEO sample that leads to aggregation or crystallization of its solid compounds. 2) The ordinary process of *solidification* of the PEO gel after deposition due to water evaporation, but without crystallization, resulting in a functional SPE in its amorphous form. In the latter case, the term "drying" is used out of convenience, although it is technically incorrect because the sample still contains considerable amounts of water within its structure.

4.2.1 Intrinsically acidic $AlCl_3$-doped SPE with increased long-term stability

As it has been established in the study by Cifarelli *et al.* [114], chloride ions are the species that partake in both relevant half-reactions at the polyaniline layer and the silver gate electrode in the active zone of the OMD, as opposed to a switching mechanism reliant on lithium ions. The consequent pursuit of further proof for the suggestion made by Cifarelli has been presented in the previous section as a part of the present work of thesis, where lithium-free chloride salts have been used as dopants in PEO formulas. In principle, any chloride salt would be appropriate to be employed as a PEO additive, although the mid- and long-term stabilities of the resulting gels strongly depend on the hygroscopicity of each salt. Thus, the research of an optimal PEO additive that would enable PANI switching while providing a necessary level of humidity, was initiated. Gels containing magnesium chloride showed themselves as promising candidates as they display a satisfactory level of hygroscopicity, meaning that they were somewhat resistant to crystallization after deposition and exposure to the atmosphere. However, an intriguing development was sent on its way with the employment of aluminium chloride as the main dopant additive. All PEO-based SPEs that have been used up to this point, including the $LiClO_4$-containing standard, required an additional doping step with HCl in order to create an acidic environment in the active zone. Without the addition of the acid, the polyaniline in its emeraldine salt form would be dedoped and turned into the nonconductive emeraldine base. $AlCl_3$-based gels do not require the additional doping with HCl, maintaining the channel in the conductive PANI-ES state. In fact, the great advantage of this dopant over other chloride salts is not only its exceptional hygroscopicity but also its intrinsic Lewis acidity that stems from the chemical properties of the aquo complex of the aluminium ion. According to Equation 9, it can enter an acid-base reaction with surrounding water molecules (forming the pentaaqua-hydroxoaluminium complex and a hydronium ion), therefore lowering the pH of the gel.

$$[\mathrm{Al(H_2O)_6}]^{3+} + \mathrm{H_2O} \rightarrow [\mathrm{Al(H_2O)_5OH}]^{2+} + \mathrm{H_3O^+} \qquad \text{Equation 9}$$

This means that as long as there is water in the system, the acidic environment will conserve itself. In turn, the necessary water content is maintained by the salt's hygroscopicity. Hence, $AlCl_3$-containing SPEs remain a lot more stable over long periods of time. In comparison, in devices featuring gels where HCl is added upon deposition, we observed a steady decay of current output over the course of a few hours because of the volatility of this component. The evaporation of chloride in $AlCl_3$-doped SPEs due to chemical equilibria leading to the formation of HCl is theoretically possible. However, being a very strong acid, the chemical equilibrium of HCl is far on the side of the dissociated form. Accordingly, in the course of this work, the dedoping of PANI has never been observed as the cause of failure of aluminium containing SPEs. Thus, the implementation of aluminium chloride allows to eliminate one source of device instability and significantly decreases the overall volatility of the output characteristics.

In general, OMDs fabricated with $AlCl_3$-containing polyelectrolytes display the same electrical behaviour as those made with other chloride salts. Figure 4-11 shows the I-V characteristics of a device made with an SPE with 20 mg/ml PEO in a 0.1 M aqueous $AlCl_3$ solution, equivalent to a $AlCl_3$:PEO ratio of $5 \cdot 10^{-3}$ mmol/mg. Subsequently, preliminary endurance tests have been carried out to further demonstrate the gel's stability over time, as it is shown in Figure 4-12. The best results were achieved when measuring a device covered with a plastic cap containing a wet ball of cotton (see Figure 4-5), allowing the acquisition with a dwell time of 2 s per 0.1 V. Interestingly, similarly good results were obtained solely by capping the device to conserve the condition of the gel but without adding extra moisture. A slow decay of the peak current can be observed over time due to the tendency of PEO to aggregate and crystallize as the humidity decreases. However, this degradation process has proven to be reversible at least to some extent, as a liquefaction of dried out samples is possible in more favourable atmospheric conditions. To demonstrate this, in an environment with sufficient relative humidity, a device was placed on a heating plate and forced to dry out and crystallize at 40 °C. Then, it was taken down from the heating plate and placed under an optical microscope to record the transformation of the active zone over a period of six minutes. The micrographs reported in Figure 4-13 show how the initially dried out sample begins to regenerate, becoming amorphous. Another interesting observation was the improved kinetics of the device when favourable conditions were provided. Formerly, standard OMDs were typically measured with a dwell time of 60 s per acquisition step of 0.1 V, while the devices with improved gels prove to remain functional at dwell times as low as 2 s, as it is shown in Figure 4-11.

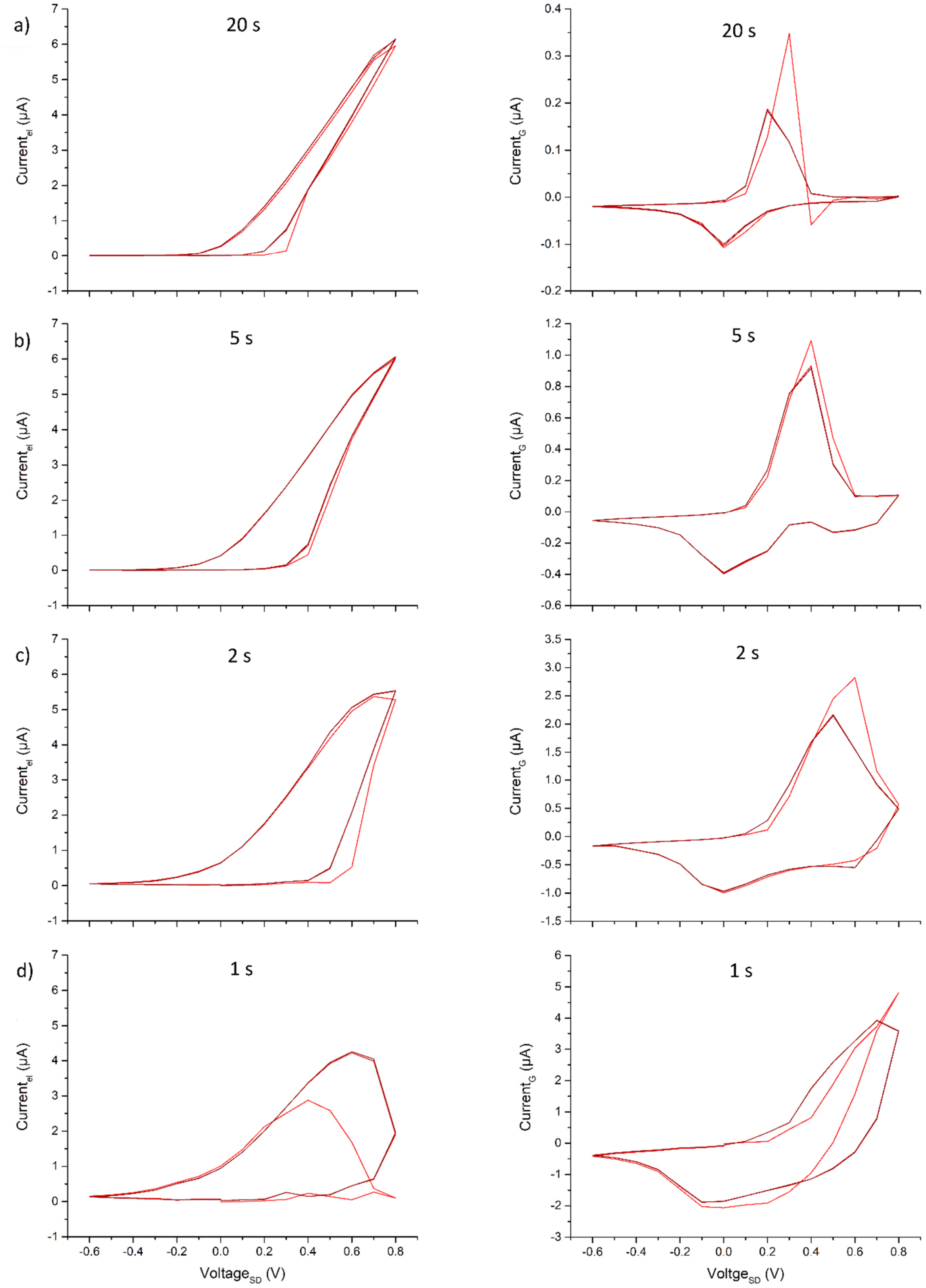

Figure 4-11: I-V characteristics of an OMD fabricated with a 30 LS PANI layer and an SPE with an $AlCl_3$:PEO ratio of $5\cdot10^{-3}$ mmol/mg at different scan rates. The left panels display with output current I_{el} and the right panels show the gate current I_G. The dwell time per acquisition step of 0.1 V is indicated in each individual graph. In each case, 20 consecutive measuring cycles are acquired, represented by the 1st, 10th and 20th cycle, respectively (from the lightest to the darkest color code). With increasing scan rate, the anodic IG peak is shifted towards more positive V biases. A dwell time of 1 s per 0.1 V is not sufficient for the system to switch.

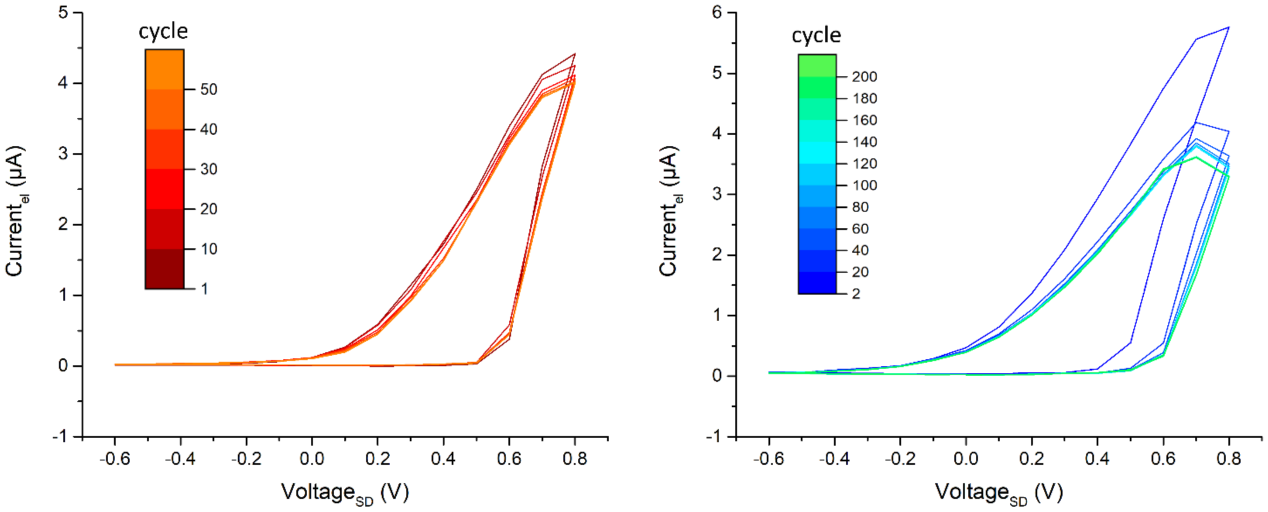

Figure 4-12: Endurance measurements of a device fabricated with a 20 mg/ml PEO gel made with a 0.1 M $AlCl_3$ solution. Left panel: measurements of the as-fabricated device (no capping) with a dwell time of 6 s per 0.1 V. Right panel: measurements of the same device at a dwell time of 2 s per 0.1 V after the initial 50 cycles, after applying a cap with wet cotton to extend the lifetime by preventing PEO aggregation. The first few cycles vary due to adjustments of the system to the new environment.

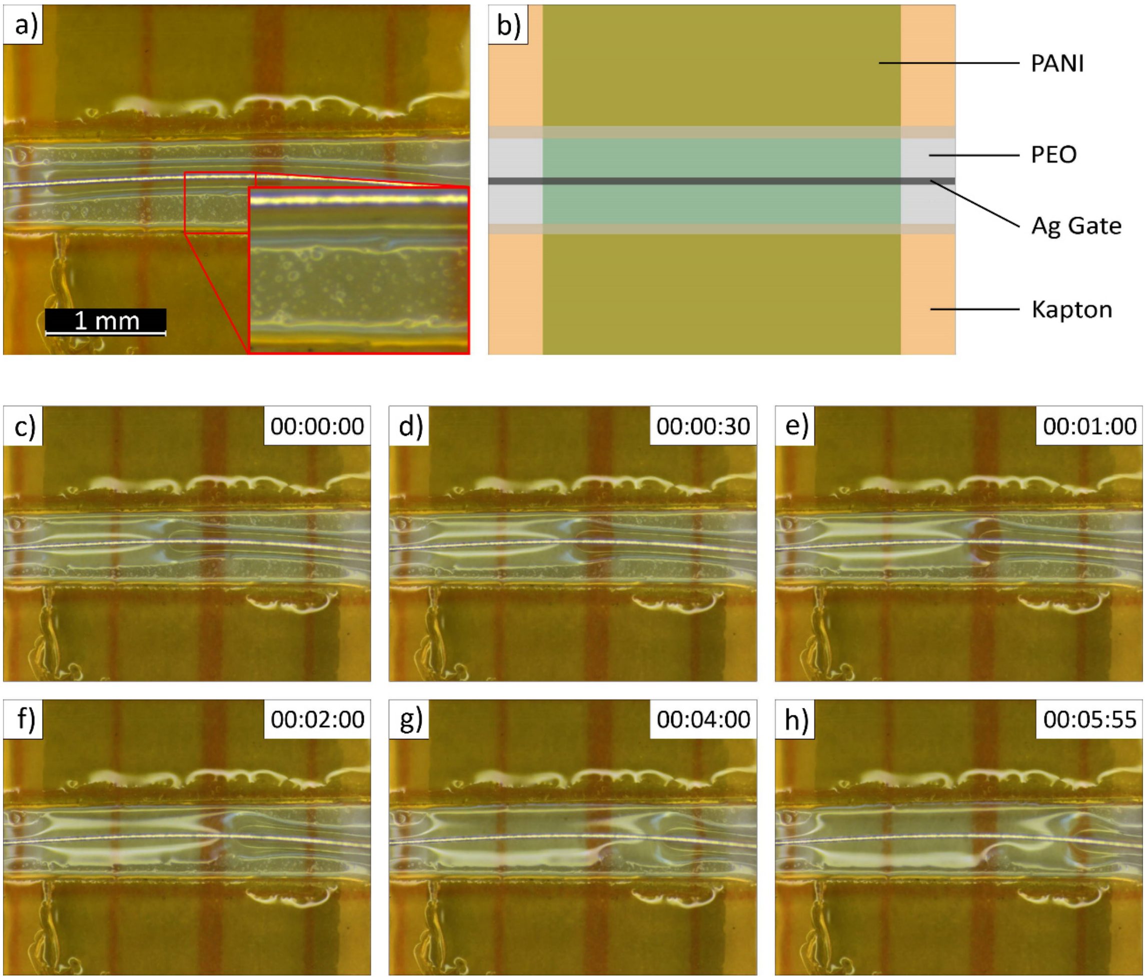

Figure 4-13: a) Microphotograph of the device right after the drying process at 40 °C; PEO aggregates can be seen on the boarders of the active zone, as opposed to the otherwise amorphous structure in the middle, around the gate electrode. b) Schematic representation of the observed area. c)−h) Process of liquefaction of the PEO gel over a period of 6 min.

As expected, the increased scan rate leads to a shift of the anodic I_G peak towards higher biases, and a widening of the hysteresis in the recorded I_{el}-V curve, as the time for the completion of the electrochemical reaction becomes more and more limited. A well-defined hysteresis can still be observed at a dwell time of 2 s/0.1 V, whereas at 1 s dwell time, the kinetics of the device is not fast enough to complete the switching process during the anodic scan. Although results with such fast kinetics could not always be achieved afterwards, scanning could be reliably carried out with a dwell time of 10 s, meaning an at least sixfold increase in operation speed with respect to formerly fabricated devices. It must be pointed out that two factors have contributed to the possibility of operating the OMD at such scan rates other than the improved morphology of the SPE that increases the ionic mobility. On the one hand, the thickness of the PANI channel was lowered from the former 60 to 30 Langmuir-Schaefer layers. In this way, a portion of achievable peak current and on/off ratio are sacrificed for the sake of faster kinetics that is favoured by the smaller bulk of PANI available for the reaction. Furthermore, it can be seen in Figure 4-11 that the applied voltage ranged from −0.6 V to +0.8 V with the purpose of giving the system sufficient time for the PANI transition during the anodic scan. However, as it was mentioned earlier, the redox chemistry of polyaniline earmarks a second transition of the polymer from the emeraldine salt state to the fully oxidized pernigraniline state, which may happen as indicated by the second reduction peak in the I_G-V in Figure 4-11 b). For this reason, the upper voltage range has been decreased to +0.6 V in later experiments to avoid undesired side reactions.

Alternatives for aluminium chloride

One point of concern arises when the pH of a freshly prepared gel from a 0.1 M $AlCl_3$ solution is measured, being relatively high with a value ranging around 4. It is known that polyaniline's conductivity depends on the acidity of the environment which influences the degree of protonation of quinoid diimine units of the emeraldine structure, making PANI a suitable material for pH sensors [136]–[138]. It has been mentioned above that the conductivity of polyaniline is highest at 50 % protonation of all nitrogen atoms, corresponding to a pH of 2 [81]. Focke *et al.* [83] have shown that maximum conductivity values slowly decrease in the pH window of 1−4 and then decrease more sharply at pH ≥ 5. Even though it is possible that the pH decreases to some extent upon solidification, as the concentration of H^+ increases with decreasing water content, it could happen that $AlCl_3$ might not provide optimal conditions for OMD operation. In an attempt to further decrease the pH of the active zone and possibly improve both the peak performance and the device's on/off ratio, we considered other intrinsically acidic salts that could replace or complement aluminium chloride. Sodium bisulfate, ferric chloride and citric acid were considered as possible candidates.

$NaHSO_4$, although more acidic (pK_a = 1.99 [139]), has proven to be unsuitable to be employed in PEO-based SPEs, as the gels containing these salts crystallized at any reasonable concentration. Such gels could only be measured in the semiliquid state through capping under a humid atmosphere, whereas $AlCl_3$ was added to introduce chloride ions. The reason for such behaviour is the same as in the earlier discussed case of the gels containing sulfate salts. The underlying concept of kosmo- and chaotropicity will be presented in the next section. The similarities of ferric chloride and aluminium chloride in their chemical structures and properties let hope that $FeCl_3$ might be an appropriate dopant in place of $AlCl_3$. For instance, both are used as catalysts in chemical reactions such as Friedel-Crafts alkylation and acylation, although $FeCl_3$ is known to be significantly more acidic. However, $FeCl_3$-based PEO gels couldn't be utilized in OMDs for various reasons. First of all, such gels turned out to have very low viscosities and, hence, it is difficult to apply them as done in the case of other SPEs. This is likely due to the fact that the increased acidity and catalytic activity of the salt promotes the degradation of PEO chains. Furthermore, even when carrying out measurements using an aqueous $FeCl_3$ solution as the electrolyte, no switching was observed, and the device had the linear I-V profile, similar to that of a resistor. One explanation for this could be the redox activity of the Fe^{3+} ion which can be reduced to Fe^{2+}, preventing the reduction of PANI to its nonconductive state. Citric acid is a triprotic acid with a relatively low $pK_{a1} = 2.79$ [140]. It also has the great advantage of being highly biocompatible as it is an important metabolite in the citric acid cycle of aerobic organisms. $AlCl_3$ was added to gels containing citric acid in order to increase the overall hygroscopicity, hence allowing to maintain a sufficiently humid environment for PEO over longer periods of time. As it can be concluded from the I-V characteristics of a device fabricated with citric acid (reported in Figure 4-14 a), the added value by the effect of the slightly increased overall gel acidity is questionable, as the response does not significantly differ from that of devices with PEO containing only $AlCl_3$. Citrate-containing gels were prone to drying out. The appearance of the dry gels with the formed aggregates can be seen in Figure 4-14 b). The aggregates have a rather crystalline morphology, indicating the precipitation of the dopant (probably citric acid itself and aluminium citrate) rather than PEO. Such precipitation is likely caused by the poor solubility of citric acid in water which amounts to ca. 60 % w/w at ambient temperature [141]. Thus, even with the addition of the hygroscopic $AlCl_3$, the water content maintained in the gel after drying is not sufficient to keep it dissolved.

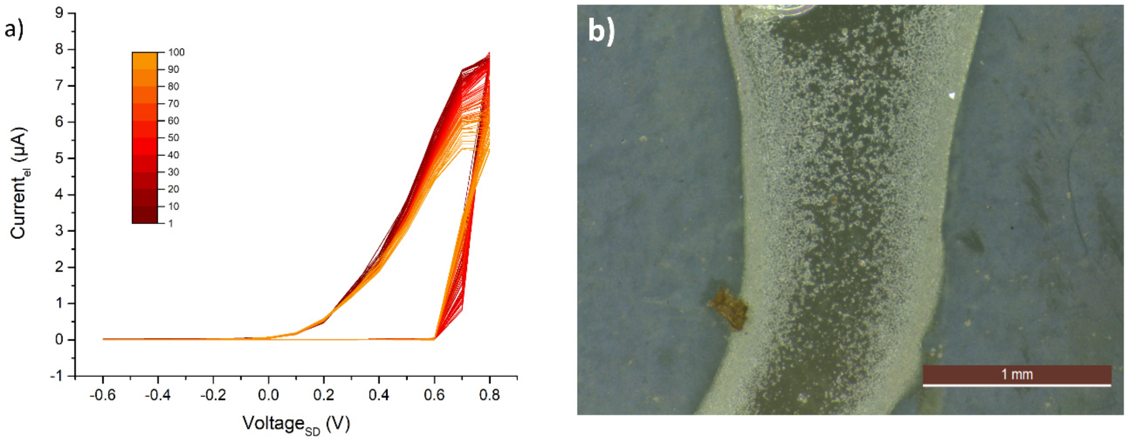

Figure 4-14: a) 100 consecutive I-V cycles of a device fabricated with a PEO gel made with a 0.05 M $AlCl_3$ and 0.1 M CitH solution. b) Microphotograph of the gel 60 min after deposition on quartz.

Overall, the attempts to replace aluminium chloride as the acidic component of the SPE were unsuccessful as this dopant appears to have a superior combination of properties such as acidity and hygroscopicity. One last acidity-enhancing additive, namely p-toluenesulfonic acid (TSA), has also been employed, and the related device performance will be discussed below, in section 4.2.3.3.

4.2.2 The concept of kosmotropicity, chaotropicity and the Hofmeister series

As it has been established above, the hygroscopicity of the dopant is a crucial parameter to provide a necessary content of water to the SPE system. However, experiments carried out with gels containing very hygroscopic sulfate salts, such as Na_2SO_4 and $MgSO_4$, resulted in SPEs that were nevertheless very prone to crystallization upon drying. This important piece of information shows that there must be another parameter to be considered when developing a new polyelectrolyte mixture. Conceptually, the issue with sulfate ions lies in the same area as hygroscopicity, being the interactions of sulfate ions with water molecules. As it has been mentioned above, the kosmo- or chaotropicity of the dopant ions has been established as the second crucial concept for the selection of appropriate additives in a PEO gel composition.

The concepts of kosmotropicity (from "*kosmos*" – order) and chaotropicity (from "*chaos*" – disorder) was conceived in the field of protein purification [142]–[144]. According to these concepts, the addition of certain salts to an aqueous solution of macromolecules, such as proteins, can influence the stability of their native state. A distinction is made between the so-called "salting out" caused by kosmotropic agents, meaning that the added solute causes the precipitation of the protein, and "salting in" caused by chaotropic agents and implying a stabilization in the dissolved state. Depending on their kosmotropic or chaotropic activity, ionic solutes as well as organic amphiphilic compounds, hydrotropes, surfactants and even organic solvents can be categorized and ordered in a so-called lyotropic series. The lyotropic series for cations and anions is commonly referred to as the Hofmeister series, according to which different ions are ordered according to their capacity to precipitate proteins. Overall, anions appear to have a stronger effect than cations. In earlier studies, the kosmotropic and chaotropic effects were said to stem from the ordering or disordering of the structure of water and increasing or decreasing its surface tension, respectively [145]. More recent studies indicate that ions do not affect the bulk water properties [146]–[149], indicating that direct interactions between the ions and macromolecules must be considered to understand lyotropic phenomena [150]. The individual effects of the ions depend on the macromolecule. For instance, in proteins, many different amino acid moieties are attached to the peptide backbone and may be hydrophobic, polar, or charged. The sum of the interactions of said side chains dictates the native folding and the tertiary/quaternary structure of the macromolecule. Chaotropic ions interact with the backbone or side chains of the protein in such a way that the natural framework of water-mediated interactions is disrupted. The hydrophobic effect is weakened and the tertiary structure unfolds, promoting the solubilization and causing a denaturation of the protein. Conversely, kosmotropes, such as the commonly used ammonium sulfate, strengthen the hydrophobic effect, causing the precipitation of the protein, ideally preserving its native structure.

In the case of the SPE containing $MgSO_4$, correspondingly, the precipitation of PEO is caused by sulfate ions as an early member of the Hofmeister series. These ions interact more readily and frequently with water molecules than the PEO chains. As water becomes less prone to interact with the polar −O− units of PEO molecules, the hydrophobic effect is strengthened, decreasing the chain mobility and hydration, and hence causing stronger PEO aggregation [151],[152]. Conversely, the former standard gels containing $LiClO_4$ displayed a very favourable morphology as the chaotropic ClO_4^- ion decreases the hydrophobic effect and prevents PEO chains from aggregating. The effect of kosmotropic and chaotropic ions on the morphology of PEO is shown in Figure 4-15. The chloride ion is usually listed as a neutral anion in terms of lyotropicity, meaning that the tendency of uncapped $AlCl_3$-based gels to crystallize, as described in section 4.2.1, is likely due to the Al^{3+} ion, despite the high hygroscopicity of the salt. In reference [153], Al^{3+} is featured as a kosmotrope, given its small size, high ionic charge and low polarizability that suggest strong interactions with water. However, this study focuses on the interaction of ions with water and the presented lyotropic series for cations severely contradicts the trend given in other works [154]. For comparison, two different sets of anionic and cationic Hofmeister series are shown in Figure 4-16. The different results obtained in various works indicate that the prevalent effects of ions cannot always be generalized and depend on the system at hand. However, there appears to be a more solid consensus concerning the effect of anions.

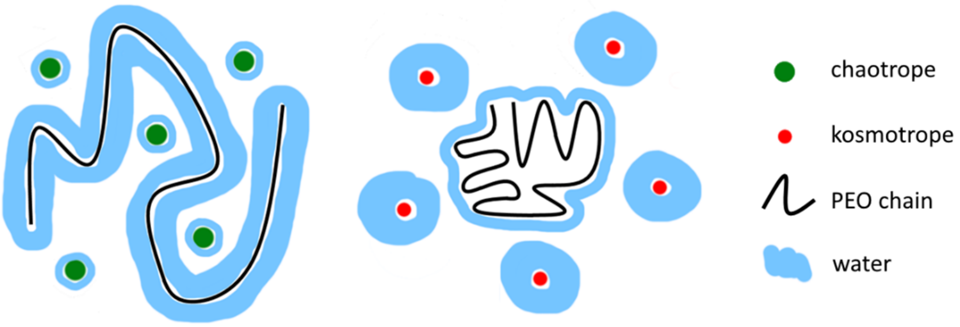

Figure 4-15: Simplified schematic representation of the interactions of chaotropic and kosmotropic ions with water and PEO chains. Chaotropes tend to interact more with PEO chains and less with water molecules, PEO chains are maintained hydrated and amorphous. Kosmotropes tend to interact more frequently with water, making it less available for interactions with PEO, leading to a strengthening of the hydrophobic effect and aggregation of PEO chains.

Sharma *et al.* [155] presented a study of the effects of inorganic ions and other compounds (such as surfactants) on the cloud point of a solution containing a PEO-PPO-PEO-block-copolymer. Their results are consistent with the anionic Hofmeister series. This confirms that the concept of kosmo- and chaotropicity can be applied to the interactions of additives in PEO-based SPEs. However, caution must be taken when evaluating the applicability of some of the results presented in that reference. For instance, the authors report an increase of the cloud point when sodium dodecyl sulfate (SDS) is added, whereas in our case, the addition of SDS to the PEO gel caused rapid

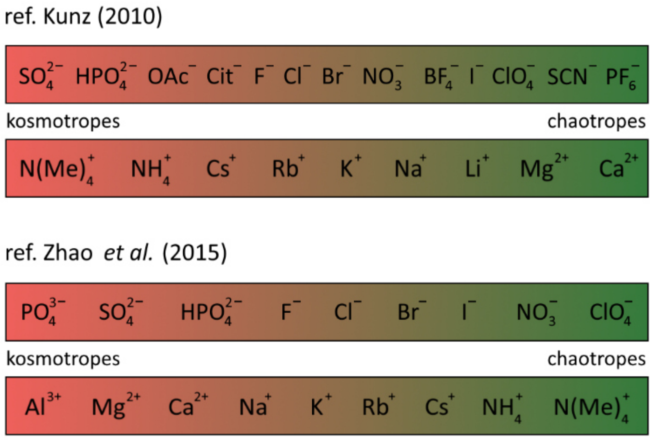

Figure 4-16: Two sets of anionic and chaotropic series from references [154] (some anions from the original publication are omitted) and [153]. Note that the cationic series strongly differs between the two references.

precipitation after its deposition. The two systems must be differentiated on the basis of the different molecular weight of the (co)polymers and its water content. Because water is significantly less abundant in our system, the hygroscopicity of the solutes starts to play an important role, as it was established above. The lack of hygroscopicity may cause that the solute claims a significant portion of water for its own hydration without contributing to its overall content, thus cancelling possible positive lyotropic effects. It is also worth noting that specific preferential interactions such as the formation of ion-specific coordination complexes may cause deviations from the classical Hofmeister series [142],[152]. This circumstance makes comparisons of the kosmo- and chaotropic character of ions difficult, especially in the case of cations. For instance, the Mg^{2+} ion is presented as a kosmotrope in some studies [151], while conversely, it is said to have rather chaotropic properties in other works [144].

The following section shows the usefulness of the Hofmeister series as a concept that complements the abovementioned importance of the hygroscopicity of the dopant salt. It paves the way to the perspective of further exploring favourable SPE compositions containing solutes that will eliminate the negative effects of salt or polymer aggregation and precipitation caused by drying or salting out processes. These developments are fundamental for fabricating devices suitable for advanced applications in neuromorphic technologies, as reproducibility and endurance remain some of the most relevant challenges in current state OMDs.

4.2.3 Optimization of intrinsically acidic SPE

The implementation of aluminium chloride as an additive in the first generation of novel PEO gels is an important step in the development of high performance SPEs. While fulfilling the hygroscopicity requirement, the dopant also endows the gels with intrinsic acidity, allowing to avoid the addition of a volatile acid to the preparation. SPEs containing $AlCl_3$ enable faster switching kinetics and show increased durability, leading to a more stable operation, as the polyaniline remains doped at all times. However, problems emerge as the hygroscopicity of the salt competes with the kosmotropic character of the aluminium ion, which can cause the PEO to aggregate when the surrounding atmosphere is insufficiently humid. The development of stable and performing SPEs requires the fulfilment of some fundamental criteria for the selection of dopant candidates:

- *Solubility*: the additive must be water-soluble to be employed in water-based PEO gels, especially considering the comparatively low level of hydration after deposition;
- *appropriate anion*: the anion must participate in both half-reactions in the active zone (i.e. it both serves as a counterion for PANI-ES and reacts with the Ag gate electrode);
- *intrinsic acidity*: avoiding the addition of volatile acid compounds ensures a stable pH;
- *hygroscopicity*: upon solidification of a deposited gel, the dopant must maintain enough water in the system to keep PEO in its amorphous state under ambient conditions;
- *lyotropicity:* the ions constituting the dopant must have a net chaotropic character, in order to decrease the hydrophobic effect of PEO chains and to prevent aggregation.

4.2.3.1 $AlCl_3$-based SPE with secondary doping

Among all possible dopant candidates, aluminium chloride has been selected as the main dopant because it meets all the above requirements besides the lyotropicity, which may be compensated by the introduction of a secondary additive. For this, we used the Hofmeister series as an aid to choose suitable salts showing lyotropicity. While it is not necessary that the secondary solute participates in PANI switching or provides acidity, it must be taken into account that it also must remain hydrated after the drying process. As it claims a part of the water content for itself, a combination of sufficient hygroscopicity and chaotropicity is desirable also for the secondary salt. For example, in PEO gels with a mixture of $AlCl_3$ and $MgCl_2$, an intense aggregation still occurred, as it can be seen in Figure 4-17. In this particular series of gels, it appears that a higher fraction of $MgCl_2$ improves the quality of the gel. However, even though the magnesium salt is both hygroscopic and has a chaotropic effect [144],[152],[154], either one or both properties appear to be insufficiently pronounced to fully compensate the drawback of aluminium. It has been reported that the affinity of Mg^{2+} to proteins may be influenced by the pH because the ion affinity depends on the charge of the

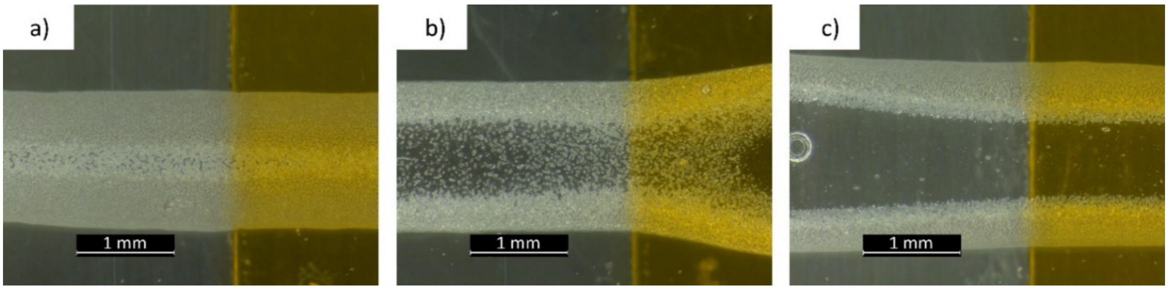

Figure 4-17: Micrographs of solidified PEO gels (20 mg/ml) made from aqueous solutions of a) 0.09 M $AlCl_3$, 0.01 M $MgCl_2$, b) 0.75 M $AlCl_3$, 0.25 M $MgCl_2$, c) 0.05 M $AlCl_3$, 0.05 M $MgCl_2$. The quality of the gel increases with a decreasing Al:Mg ratio. The $AlCl_3$ concentration was not lowered further to maintain an acceptable pH.

protein [156]. A lowered pH created by aluminium chloride might cause a similar effect, altering the interactions between Mg^{2+} and PEO.

In the following experiments, the gels' morphology was studied under the microscope and used as a measure for the assessment of their quality. The general correlation between morphology and performance is quite reliable, since excessively drying gels with aggregates always perform worse in terms of switching kinetics and achievable peak currents. Considering the good experience made with the lithium perchlorate-based gels, widely used so far, we decided to use mixtures of $AlCl_3$ and $LiClO_4$ in the second generation of high performance SPEs. In fact, lithium perchlorate is an excellent dopant by itself if we disregard the necessity to add the volatile HCl to provide both acidity and chloride ions in earlier preparations. The salt has a favourable combination of both hygroscopicity and lyotropicity since the perchlorate ion is a late member of the Hofmeister series (see Figure 4-16). We have observed that the gels prepared with mixtures of salts were notably more fluid than their single-doped counterparts, which is probably due to the extra added water content. Increased fluidity poses the risk of poorly enveloping the gate electrode, thus inhibiting the proper switching of the device. For this reason, the PEO concentration was increased from 20 to 30 mg/ml with the aim of increasing the gels' viscosities and facilitating their deposition.

Three gels have been prepared; The first gel was made with a PEO concentration of 30 mg/ml in a 0.05 M $AlCl_3$ and 0.05 M $LiClO_4$ solution; we named it as P30-Alli-0111, (P30 stands for the concentration of PEO; Alli stands for Aluminium and Lithium; the first two digits, 01, denote the overall salt concentration (0.1M) and the last two digits (11) indicate their ratio. The second and third gels are made of 0.075 M $AlCl_3$ and 0.025 M $LiClO_4$ (P30-Alli-0131) and 0.025 M $AlCl_3$ and 0.075 $LiClO_4$ (P30-Alli-0113).

Figure 4-18 demonstrates a comparison of the morphology of these three gels. It is worth noting that the quality of the gel increased with increasing $LiClO_4$ content which is in accordance with its chaotropicity. P30-Alli-0113 and P30-Alli-0111 remained amorphous and transparent after

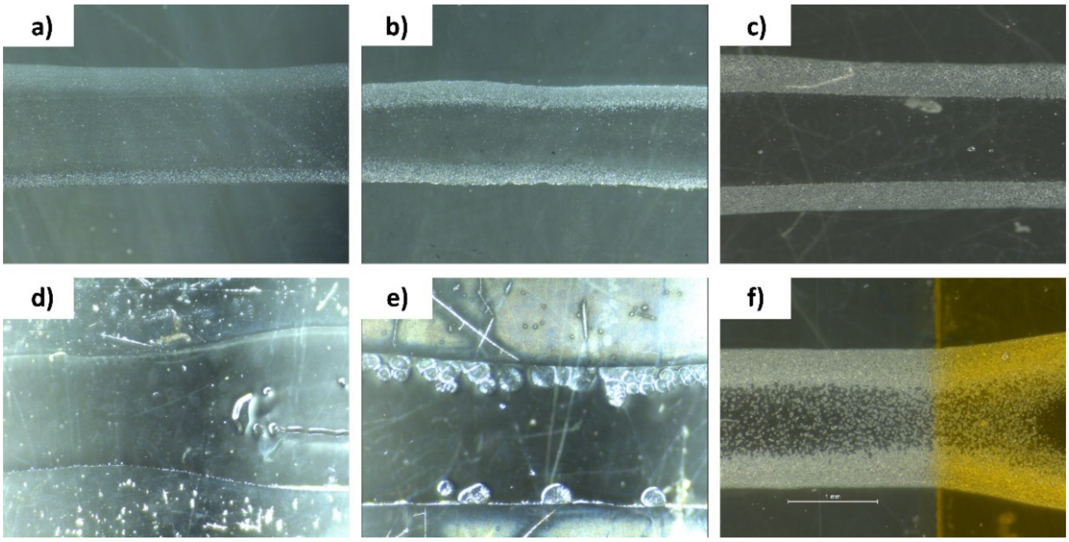

Figure 4-18: a) Gel P30-Alli-0111 30 min after deposition; b),c) progressing drying of P30-Alli-0111. d) P30-Alli-0113 30 min after deposition. e) P30-Alli-0131 30 min after deposition; f) progressing drying of P30-Alli-0131.

deposition while P30-Alli-0131 crystallized after a short period of time. Devices made with the first two gels both showed promising results in terms of endurance with respect to $AlCl_3$-only SPEs. Figure 4-19 and Figure 4-20 show the I-V characteristics of two series of three different devices made with gels P30-Alli-0113 and P30-Alli-0111, respectively, demonstrating a good level of cycle-to-cycle reproducibility over 300−500 cycles. One device was cycled over a total of 1500 times (two series of 500 and 1000 consecutive cycles), which corresponds to over 80 hours of continuous operation. It is noteworthy that despite an eventual decline of peak current, any 20 consecutive cycles were almost identical to one another. In general, the shape of the I-V curve remained unchanged over the whole series of measurements. A shorter series of 20 measuring cycles was carried out on some devices 2−3 days after the endurance series to show that their functionality is maintained even when the device is left in ambient conditions in an idle state. The eventual fluctuations of output characteristics are caused by slight changes of the measuring conditions throughout the series (temperature, humidity) since the experiments were intentionally carried out in a non-controlled environment. Such an endurance level is precluded to standard devices with SPEs containing $LiClO_4$ and HCl. In our experience, such devices usually lasted for only about 50 equivalent cycles before no switching could

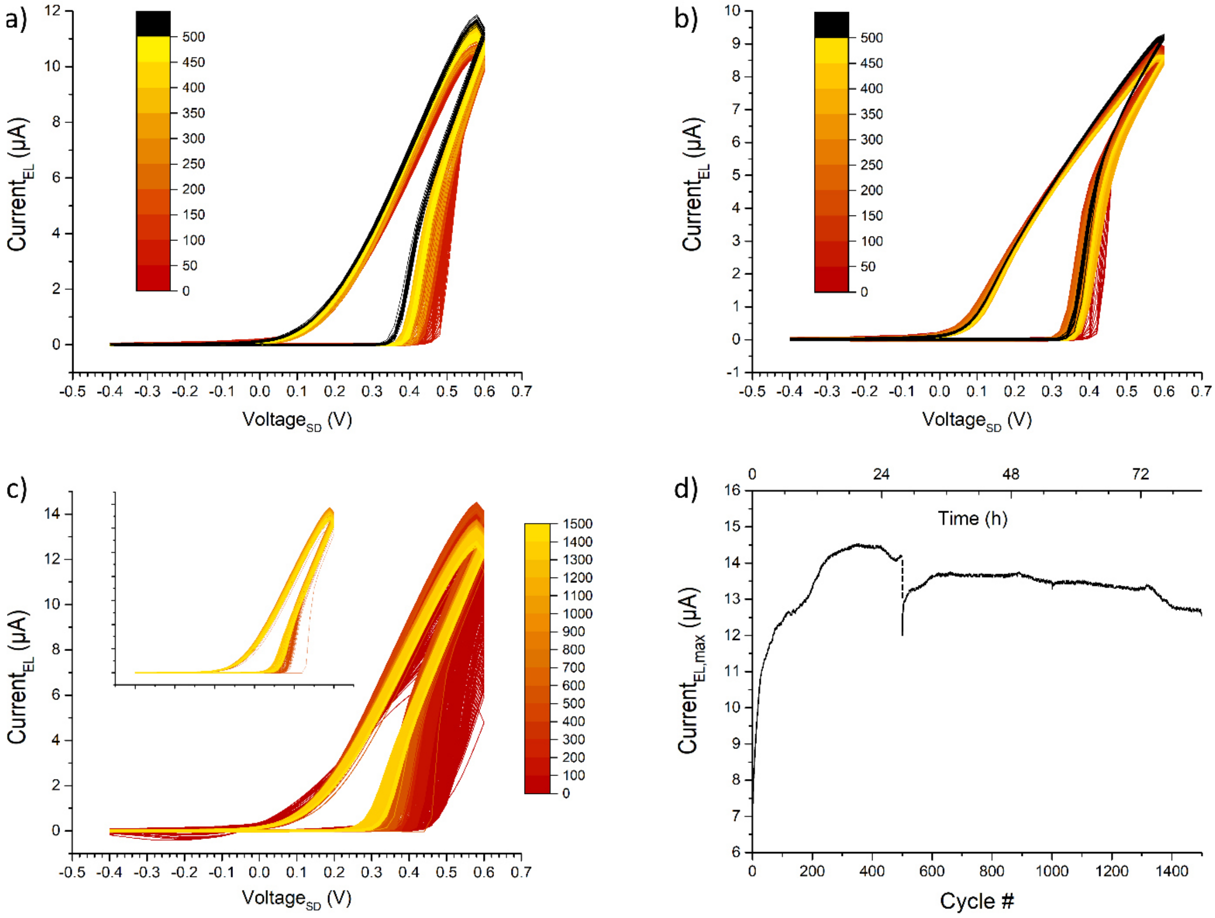

Figure 4-19: Endurance series of I-V characterizations of different OMDs fabricated with gel P30-Alli-0111 as the SPE, measured with a dwell time of 2 s/0.02 V. a,b) 500 consecutive cycles, followed by a short series of 20 cycles acquired after 2 and 3 days, respectively. c) Series of 500 consecutive cycles followed by another 1000 cycles acquired 2 days after the first series. The inset demonstrates cycles 501-1500. d) Development of the peak output current I_{el} of the series in panel c). The discontinuity at 500 cycles is caused by the break between the two series of measurements, during which partial drying of the sample has occurred.

be observed, due to the PANI dedoping caused by HCl evaporation. The endurance of our modified SPE is unprecedented for solid state OMDs, surpassing the record set by Lapkin *et al.* [157] who have measured a PANI- and PEO-based microdevice over 11000 short on/off cycles (10.5 s each, amounting to ca. 32 h in total). Arguably, the comparison is not entirely correct as we confront kinetic on/off cycling with hysteresis measurements. However, the reproducibility of the shape of the hysteresis and the related stability of the output current over time leads to think that our device may work properly on very long timescales. The increase of the output current in the beginning of the series (best seen in Figure 4-20 c) and Figure 4-19 c)) is due to a conditioning process during which the SPE morphology adjusts to the environmental conditions and the device parameters stabilize.

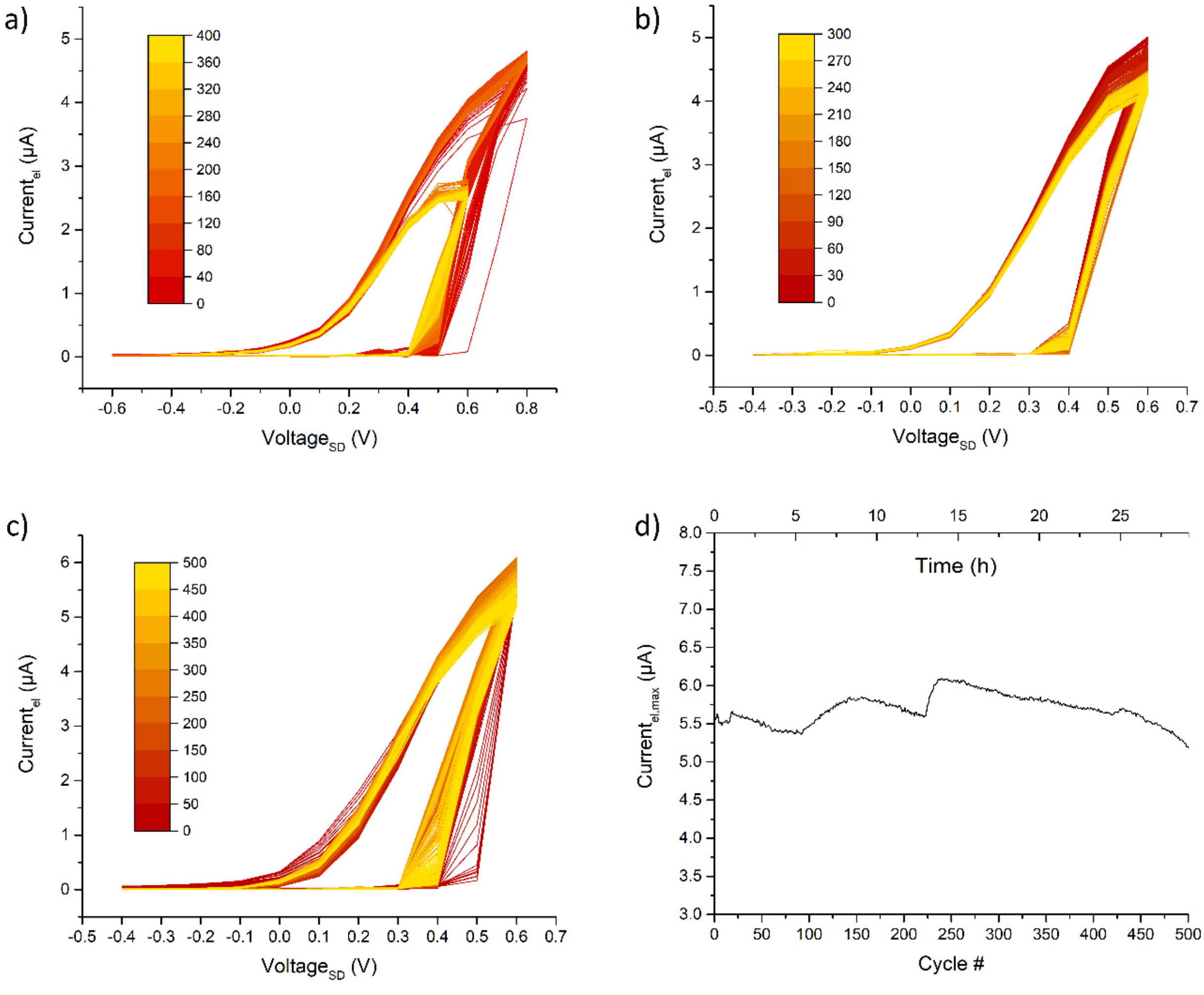

Figure 4-20: Endurance series of I-V characterizations of different OMDs fabricated with gel P30-Alli-0113 as the SPE, measured with a dwell time of 10 s/0.1 V. a) 200 cycles in the bias interval [−0.6 V; +0.8 V] followed by 200 cycles in the bias interval [−0.4 V; +0.6 V]. The strong decrease of peak current after the first 200 cycles is due to the lower applied voltage at the end of the anodic scan. The switching onset remains unaffected by the changed voltage range. b,c) 300 and 500 consecutive cycles, respectively. d) Development of the peak output current I_{el} of the series in panel c).

Eventually, each series showed a decreasing trend of the output current which is caused by the slow drying of the $AlCl_3/LiClO_4$ gel. We attribute this to the lowered ratio of dopants and PEO, since the concentration of PEO was increased from 20 to 30 mg/ml. It appears that the resulting decreased overall salt:PEO ratio of about $3.3 \cdot 10^{-3}$ mmol/mg is insufficient for the hydration of the

SPE under changing surrounding conditions. For this reason, the concentrations of the added salts have been adjusted accordingly to a summed dopant concentration of 0.15 mol/l, corresponding to the initial salt:PEO ratio of $5\cdot10^{-3}$ mmol/mg. Figure 4-21 shows two of such gels with different salt ratios. The gel P30-Alli-01521 remains transparent with minimal crystallization on the stripe profile, while P30-Alli-01512 tends to crystallize in the whole bulk of the layer. This suggests that the benefit of added moisture in the gel with a 2:1 $AlCl_3$:$LiClO_4$ ratio is higher than that of the excess of chaotropic agent in the gel with a reversed ratio of 1:2. With a further increased $LiClO_4$ concentration, the gel solidifies very slowly and forms inhomogeneous aggregates.

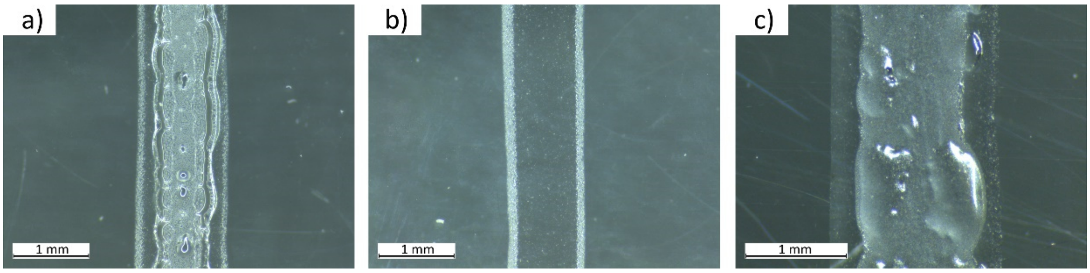

Figure 4-21: Gels a) P30-Alli-01512 , b) P30-Alli-01521 and c) P30-Alli-0211 six hours after deposition.

Given the improved stability over time, we fabricated a device with the P30-Alli-01521 gel as the solid polyelectrolyte and an endurance measurement series was carried out to determine the long-term stability/reproducibility of the device response. We established that the humidity of the surrounding atmosphere has a strong influence on the quality of the SPE, which is why it is desirable to keep the measuring conditions stable. In addition, the conductivity of PANI is also dependent on humidity, meaning that a gel with a higher water content should enhance the performance. This property has been used to fabricated PANI-based humidity sensors as water is said to facilitate the protonation of PANI's imine nitrogen atoms through hydrogen bonding [158],[159]. To show the potential of our modified PEO gels under stable conditions, we carried out another endurance experiment in which a device fabricated with the gel P30-Alli-01521 was subjected to an even longer series of measurements. In order to provide stable and favourable humidity levels throughout the series, the device was placed in a home-made closable chamber together with a petri dish filled with water. The experimental setup is shown in Figure 4-22. After installing the device and closing the chamber, the system was let to equilibrate for an hour. This was done in order to avoid large fluctuations of the electrical response, as it was the case during the endurance series in Figure 4-19 c) and Figure 4-20 c). The results of the continuous, 3000 cycles long endurance series corresponding to almost 7 full days (about 167 h) of continuous operation are presented in Figure 4-23. As it can be seen in panel a), some equilibration still took place over the first 500 cycles, during which the onset voltage shifted towards lower values.

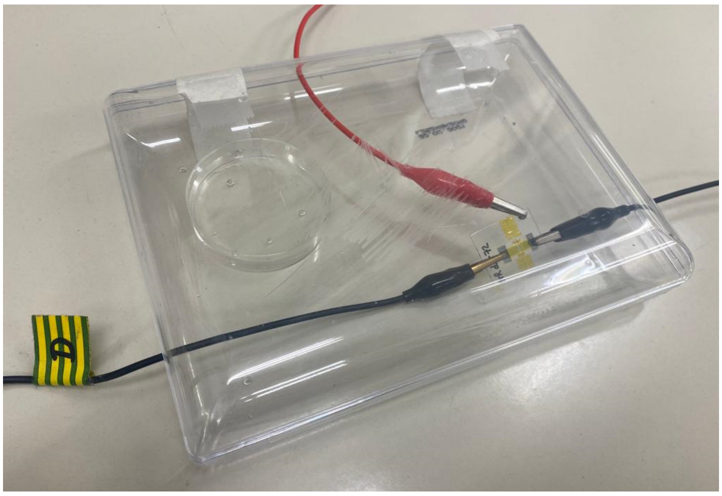

Figure 4-22: Experimental setup for the 3000 cycles endurance series. Holes were drilled in the perimeter of the chamber to insert cables. A water-filled petri dish was used as a source of humidity to provide more stable measuring conditions.

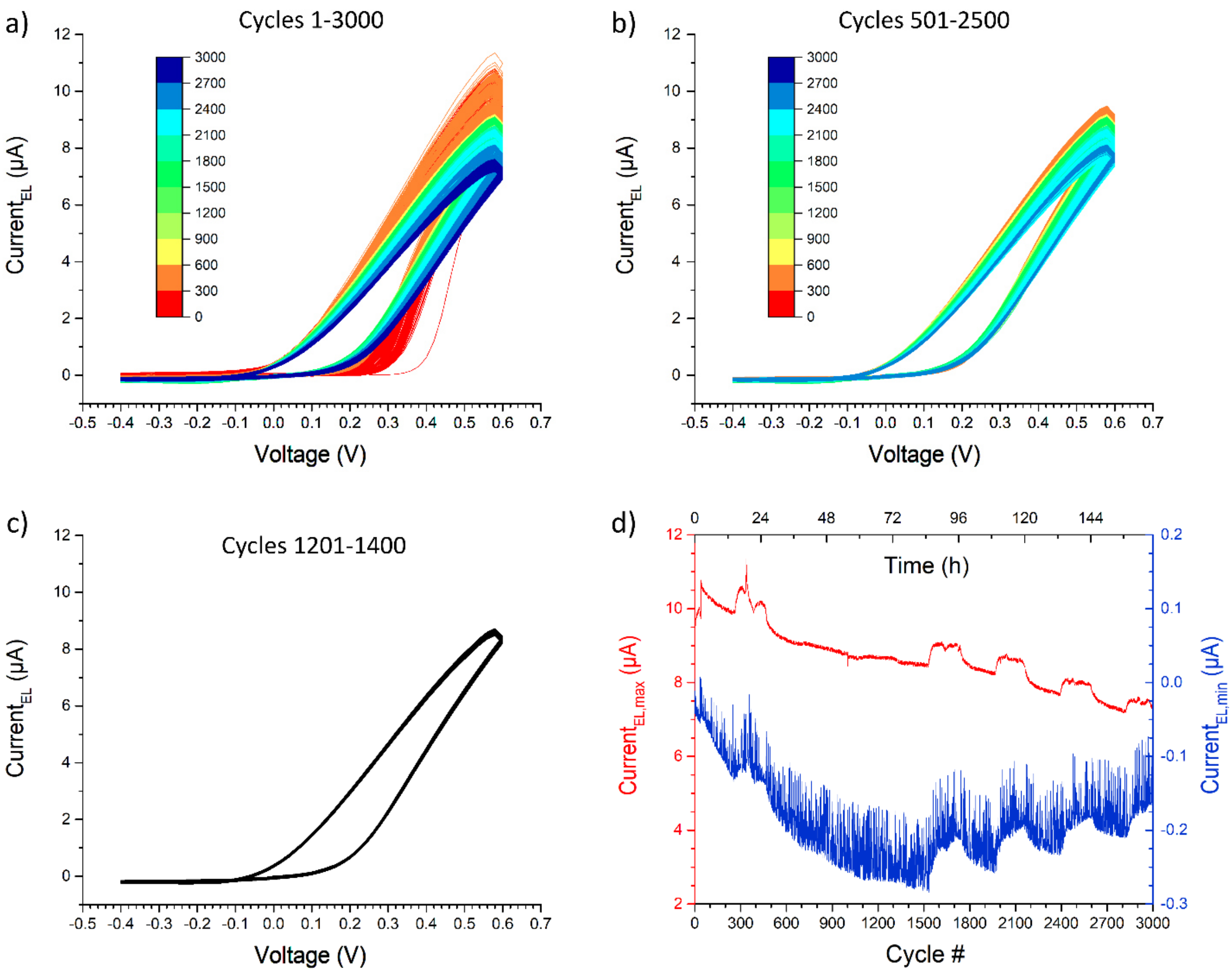

Figure 4-23: The results of the endurance test of a device fabricated with the gel P30-Alli-01521 as the SPE which was cycled 3000 times with a dwell time of 2 s per step of 0.02 V in the voltage range [−0.4 V; +0.6 V]. The measurements took place in a partially air-conditioned laboratory (turned on during weekdays and off during the night). Shown are the I-V characteristics of the device during cycles a) 1-3000, b) 501-2500 and c) 1201-1400. d) I-t profiles for the maximum and minimum currents $I_{EL,max}$ and $I_{EL,min}$ throughout the series.

The middle 2000 cycles (501-2500) display a relatively stable response in terms of the shape of the hysteresis and onset voltage. Although a slow decay of peak output current over time is evident, the differences between any 200 successive cycles within this span are negligible, displaying a remarkable reproducibility of I-V characteristics. The development of the maximum and minimum registered output currents during the anodic and cathodic scans in panel d) reveals an interesting detail about the performance of the device. Five plateau-like spikes (one in the first and four in the second half of the series) can be seen in the profile of the maximum output current $I_{EL,max}$. These spikes are caused by temperature differences between day and night since the air conditioning in the laboratory was not continuous throughout the day. It is known that the conductivity of polyaniline as an organic semiconductor is temperature-dependent, increasing at higher temperatures (valid for values around room temperature) [160]. The collected data reflect this property, as the conductivity rises every other day except for days 2 and 3 when the air conditioning remained off and the temperature remained low. On the other hand, $I_{EL,min}$ also displays spikes towards less negative values (lower absolute values) at the same times as $I_{EL,max}$ spikes. Higher (absolute) currents during the cathodic scan are an indication for an incomplete reduction of the polymer, causing some residual conductivity. Since the reaction kinetics depend on the diffusion of ions through the SPE and PANI layer, it can be argued that the viscosity of PEO, which also depends on temperature, is another factor for such behaviour. This seems particularly plausible because the device is measured close to the scan rate limit with a dwell time of 2 s/0.02 V. A high scan rate means that the reduction and oxidation of the PANI layer will start lagging behind the scan at suboptimal conditions. This is further confirmed by the fact that $I_{EL,min}$ is gradually restored to lower absolute values once the temperature is increased. Conversely, disregarding the temperature spikes, $I_{EL,max}$ displays a steady decay throughout the whole series, indicating a slow degradation process, the cause of which is not fully understood. On the one hand, a gradual drying of the SPE could be a reason of a progressing worsening of the device's performance. However, it is unlikely in this case, as this endurance test was carried out in a closed chamber of relatively low volume, with a controlled humidity. This indicates that some form of material degradation is the more likely cause.

The decomposition of PANI appears to be more probable due to the hydrolysis and cleavage of the polymer chains in its emeraldine salt state, as it has been discussed above. With a lower average chain length, the charge transfer between different chains becomes more predominant as the limiting factor for conductivity. The decomposition of PANI seems especially plausible when considering the increased water content of the PEO gel given by the humid environment. Other undesired reactions cannot be excluded, such as crosslinking [90],[91], and covalent binding of chlorine to benzenoid or quinoid rings in PANI [161], both of which disturb the regular electronic structure of the polymer. According to reference [161], the latter reaction can take place at sufficiently high acid concentrations, even though the chloride ion is a poor nucleophile.

Another source of degradation could be the silver wire as it is also subjected to continuous redox cycles during which the porosity of the AgCl layer may gradually change. Though, given the fact that the kinetics of the Ag/AgCl electrode are generally faster than those of PANI, the morphology of the gate electrode should not be the limiting factor for the switching kinetics in general.

The decomposition of PEO cannot be ruled out completely because ethers are known to be prone to (auto)oxidation [162],[163] which seems likely in the presence of a strong oxidant such as perchlorate. The hydrolysis of the polyether seems less probable because of the poor nucleophilicity of water molecules, chloride and perchlorate ions. However, an acid-catalysed reaction following the mechanism in Figure 4-24 is imaginable, considering that upon cleavage, the formed shorter PEO chains become more flexible and increase the entropy of the system. Besides, the formed −OH capping groups can be better solvated than the former −O− unit.

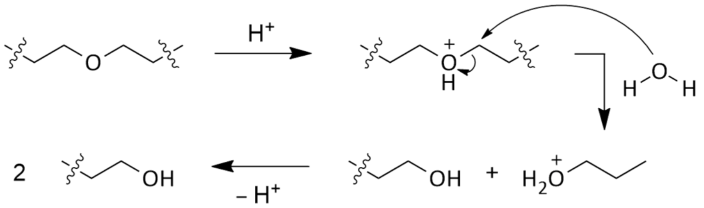

Figure 4-24: Suggested mechanism of the acid-catalysed hydrolysis of the −O− unit of a PEO chain, resulting in two shorter, −OH capped chains.

At first glance, the cleavage of PEO chains seems to be irrelevant for the decay of the output current observed in the endurance series because the viscosity of PEO would decrease with lower average chain length, hence facilitating ion diffusion instead of inhibiting it. However, we noticed a curious detail when handling old gel samples. All the samples containing both $AlCl_3$ and $LiClO_4$ lost their initial viscosities after 2-3 weeks, despite being in sealed vials. The process was especially fast in samples that were stored at room temperature. Furthermore, milky precipitate deposited itself on the bottom of the vials, forming string-like, floating structures when agitating the gel, as it is shown in Figure 4-25.

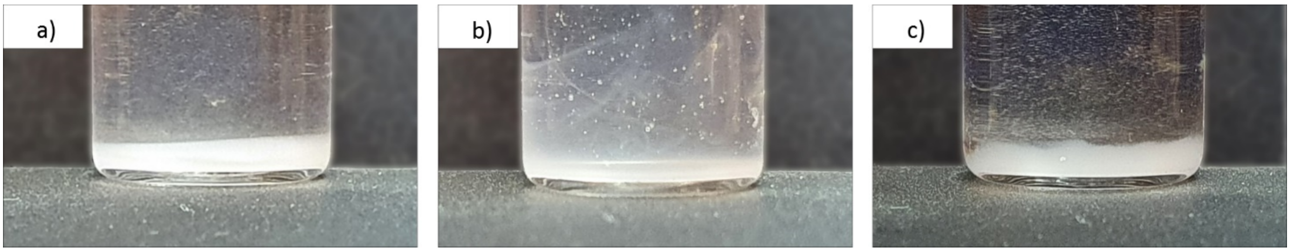

Figure 4-25: Precipitate on the bottom of a vial containing a one-month-old, 30 mg/ml PEO gel sample made with 0.1 M $AlCl_3$ and 0.05 M $LiClO_4$ a) prior to agitation, b) immediately after, c) 30 min after agitation. The dots that can be seen in the bulk of the gel after agitation are air bubbles.

Interestingly, the same did not happen in samples that contained only $LiClO_4$ without any acid, or $AlCl_3$ in combinations with a few other secondary dopants, which will be presented below. This indicates that there must be another deterioration process caused by a combination of these two salts, but not by any one of them separately. According to a study by McGary Jr. [163], poly(ethylene oxide) is susceptible to oxidizing agents in the presence of certain metal ions. The oxidative decomposition of PEO by such oxidants as H_2O_2 is shown to be faster in the presence of iron, copper or silver ions. Other oxidants used in this study were peracetic acid, $KMnO_4$ and bromine. Although the deteriorating effect of strong acids on PEO in aqueous solutions is mentioned, the author argues that it is doubtful that the acidity of the added salts alone is responsible for the decomposition of PEO. For instance, salts such as ferric chloride or zinc chloride were shown to be relatively ineffective in promoting the degradation of PEO without the addition of an oxidant. We assume that a similar reaction could take place in gels containing perchlorate as the oxidant and $AlCl_3$ as the acidic agent assisting and promoting the oxidation, probably through the formation of intermediates. The formation of a precipitate within a gel subjected to such a process (as shown in Figure 4-25) seems counterintuitive because of the lowering of the average chain length that are, on the contrary, more soluble. The preferential solvation of the shorter, more flexible PEO chains could be a possible explanation for this phenomenon. In particular, because the interaction with long PEO units becomes less favourable, their hydrophobic effect increases, leading to the formation of coils and other entangled structures that eventually precipitate in the gel solution [164].

4.2.3.2 $LiClO_4$-free SPE with increased resistance to decomposition

As it was discussed in the previous section, the introduction of $AlCl_3$ allowed a breakthrough in terms of performance and stability of the OMD's output characteristics thanks to its intrinsic acidity. Nonetheless, these gels have shown poor long-term stability due to drying. In the second generation of novel PEO-based gels, we have shown that the addition of a secondary dopant such as $LiClO_4$ to $AlCl_3$ drastically increases the long-term stability of the OMD. However, some issues with the stability of the polyelectrolyte material arose as we observed a relatively fast deterioration of poly(ethylene oxide), resulting in the loss of viscosity and precipitation of PEO residues. We assume that this degradation is caused by the presence of perchlorate that acts as an oxidant, leading to the decomposition of PEO and hence decided to replace $LiClO_4$ by another dopant. The Hofmeister series (see Figure 4-16 and Figure 4-26) has proven to be a helpful tool when choosing dopant candidates. We decided to replace perchlorate by another late member of the lyotropic series for anions with even higher chaotropicity. Thus, in the third generation of our modified PEO-based SPEs, we chose thiocyanate (SCN^-) as the secondary dopant anion as it is not an oxidant and many of its salts are hygroscopic. At first, ammonium (NH_4SCN) and potassium thiocyanate (KSCN) were chosen to fabricate gels (AlAS and AlKS, respectively) with different dopant concentrations. Assuming that the high chaotropicity of thiocyanate would make a small addition of these salts sufficient, we first prepared the gels P30-AlAS-00651 and P30-AlKS-00651 with PEO concentration of 30 mg/ml in a 0.05 M $AlCl_3$ and 0.01 M SCN^- salt solution to avoid possible oversaturation. These gels were very viscous after swelling and dried out excessively upon deposition, which was thought to be due to insufficient overall hygroscopicity. We hence proceeded with higher SCN^- concentrations in gels P30-AlAS-0111, P30-AlKS-0111 and P30-AlKS-0211 in analogy to some of the earlier $AlCl_3$/$LiClO_4$-based SPE. Despite the higher content of the chaotropic secondary dopant, these gels

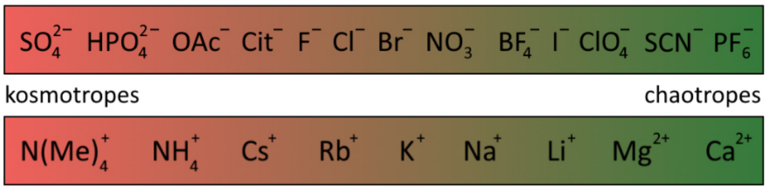

Figure 4-26: Reminder: Hofmeister series adapted from the study by Kunz *et al.* [154]

also crystallized excessively. The reason for such a behaviour lies in the nature of the two cations. Our results show that in the case of PEO, the cationic lyotropic series must be handled with care. While NH_4^+ is indeed identified as a kosmotrope, the poor quality of the $AlCl_3$/KSCN-based gels is not in line with the rather neutral position of the K^+ ion in the Hofmeister series, especially considering that the cations generally have a weaker influence than anions. To explain the increased crystallization of the gels, other interactions with PEO macromolecules must be considered as well. More specifically, we assume that the interactions of the cations with PEO's ether units through hydrogen bonds in the case of NH_4^+ and cation-dipole interactions in the case of K^+ may serve as a starting point for noncovalent crosslinking and the formation of growing PEO clusters. It appears that this effect far outweighs the chaotropic nature of the thiocyanate ion. The morphology of some of the solid $AlCl_3/NH_4SCN$- and $AlCl_3$/KSCN-based SPEs is demonstrated in Figure 4-27.

Knowing from the example of $LiClO_4$ that lithium ions in combination with a chaotropic anion do not cause precipitation, we hence added LiSCN as the secondary dopant in order to assess the effect of thiocyanate (or rhodanide). Another great advantage of LiSCN is its high hygroscopicity and solubility in water, making it deliquescent. Unlike the dopants we used before, this salt (or, in fact, the salt/solution mixture) needed to be dried for 15 h at 80 °C before it was quickly weighed, as it would instantly attract water from the atmosphere. For this reason, ideally, LiSCN should be handled under a protective atmosphere prior to dissolving it. Like in the previous case, given the salt's excessive hygroscopicity and high chaotropicity of the thiocyanate ion, lower concentrations were chosen at first, fabricating a P30-AlliS-00651 gel in 0.05 M $AlCl_3$ and 0.01 M LiSCN. However, analogous to the gels featuring the ammonium and potassium salt, this gel crystallized in a similar manner, as it is demonstrated in Figure 4-29 a). However, at higher LiSCN concentrations, the SPEs performed better, such as gel P30-AlliS-01521. In analogy to P30-Alli-01521 from the previous section, the LiSCN based homologue showed a reasonable morphology and was relatively stable,

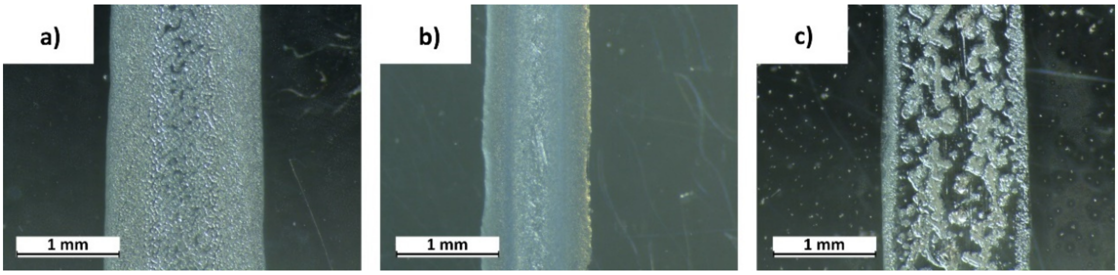

Figure 4-27: Microphotographs of 30 mg/ml PEO gels a) P30-AlAS-0111 (0.05 M $AlCl_3$, 0.05 M NH_4SCN), b) P30-AlKS-0113 (0.025 M $AlCl_3$, 0.075 M KSCN) and c) P30-AlKS-0211 (0.1 M $AlCl_3$, 0.1 M KSCN) in the solid state.

although the long-term stability was lower since drying on the layer edges initiated earlier. Such a result seems odd, because given the deliquescent property of pure LiSCN and its higher chaotropicity with respect to $LiClO_4$, we would expect P30-AlliS-01521 to outperform P30-Alli-01521. Hence, the conclusion must be drawn that the level of hygroscopicity and lyotropicity of a salt depends on the whole ensemble of substances within the SPE and is difficult to estimate based on the properties of pure dopants.

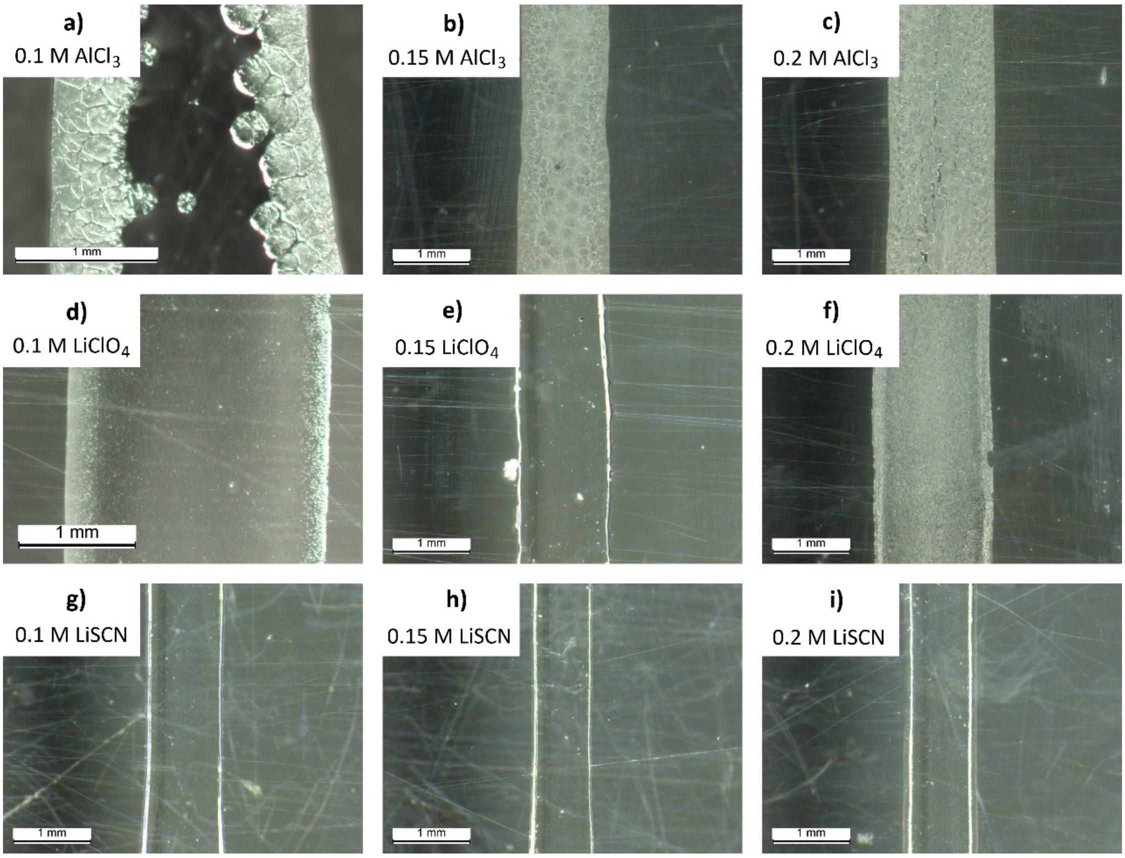

Figure 4-28: Influence of the salt concentration in 30 mg/ml PEO gels containing a)-c) $AlCl_3$, d)-f) $LiClO_4$ or g)-i) LiSCN as the single dopant (concentrations indicated in the respective microphotographs).

For this reason, we decided to study some model gels for their structure in the solid state in an attempt to identify some general correlations between the dopants' concentrations and the quality of the SPEs. We started by preparing single-doped 30 mg/ml PEO gels containing $AlCl_3$ (Al), $LiClO_4$ (Li) or LiSCN (LiS) of different concentrations (0.1 M, 0.15 M and 0.2 M solutions, respectively). The results presented in Figure 4-28 were in accord with the dopant lyotropicities. The LiSCN based gels remained transparent and homogeneous at all three concentrations, while the SPE with the slightly less chaotropic $LiClO_4$ showed higher transparency when increasing the concentration from 0.1 to 0.15 mol/l, but crystallized at 0.2 mol/l. It is likely that at high concentrations, the hygroscopicity of $LiClO_4$ does not suffice to maintain all the components of the SPE hydrated. A similar trend was observed with $AlCl_3$-based electrolytes which showed a decreasing SPE quality with increasing dopant concentration. In this case, the aggregation already started at 0.1 mol/l caused by the more kosmotropic character of the salt, which outweighs its hygroscopicity. These findings indicate that both the summed dopant concentration and the ratio of primary and secondary dopant must be adjusted to find the balance between the hygroscopic contribution of each salt as well as their chaotropic and kosmotropic characters. It appears that a more chaotropic secondary dopant allows to use overall higher (summed) concentrations. Higher $AlCl_3$ concentrations cause more hygroscopicity, but they may also cause crystallization due to the kosmotropic character of the salt.

Based on these results, we fabricated a series of $AlCl_3$/LiSCN-based SPEs with 30 mg/ml PEO, the most relevant of which were: P30-AlliS-01521 (0.1 M $AlCl_3$, 0.05 M LiSCN), P30-AlliS-017552 (0.125 M $AlCl_3$, 0.5 M LiSCN) and P30-AlliS-0211 (0.1 M $AlCl_3$, 0.1 M LiSCN). The structures of these gels in the solid state are demonstrated in Figure 4-29. As was mentioned above, despite the higher degree of chaotropicity of thiocyanate with respect to perchlorate, gel P30-AlliS-01521 is not as stable as P30-Alli-01521 over longer periods of time. The structure of the SPE was improved by increasing the fraction of the secondary dopant LiSCN and the overall salt:PEO ratio to $6.67\cdot10^{-3}$ mmol/mg (in P30-AlliS-0211). SPE cast from this gel have proven to have comparable stability under ambient conditions while the gel did also not tend to visibly lose viscosity and precipitate in vials over long periods of time (months).

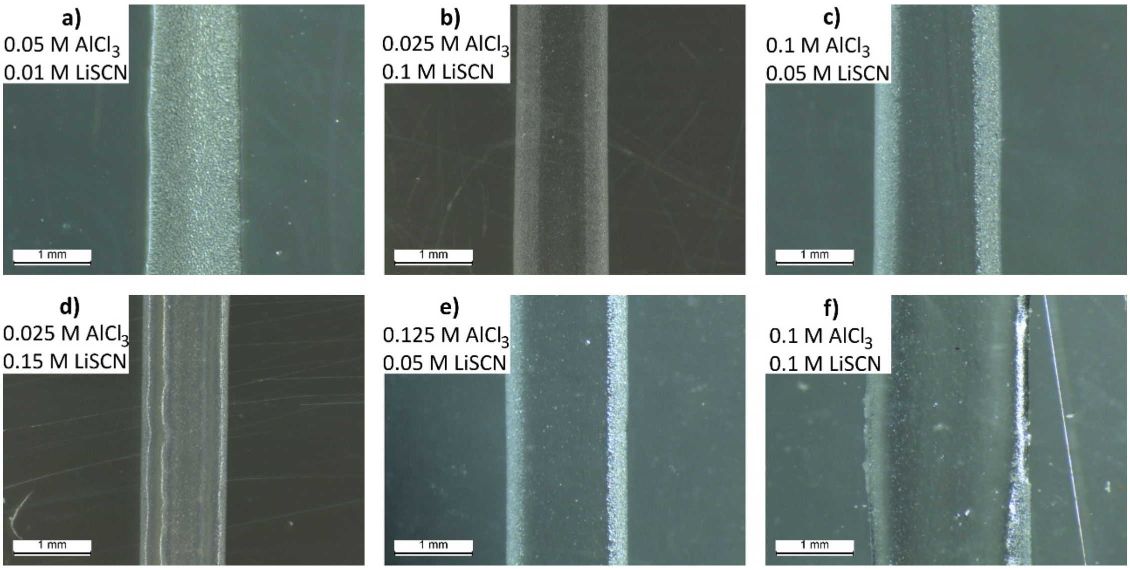

Figure 4-29: Microphotographs of the SPEs a) P30-AlliS-00651, b) P30-AlliS-012514, c) P30-AlliS-01521, d) P30-AlliS-017516, e) P30-AlliS-017552 and f) P30-AlliS-0211 in the solid state, 6 h after deposition in ambient conditions.

We have tried to implement gel P30-AlliS-0211 as the solid polyelectrolyte of an OMD but all attempts failed as the device switched off but seemed to be unable to switch back on when applying the characteristic positive voltage bias. Furthermore, the solid SPE happened to dry faster after attempting to measure a device in which LiSCN based gels were employed, as opposed to samples simply deposited on quartz. Interestingly, some on/off switching was observed when using a liquid aqueous electrolyte containing 0.5 N HCl and 0.5 M LiSCN, although the process was somewhat slower in comparison to measurements in a pure 0.5 N HCl electrolyte. The reason for such behaviour was found in the literature, suggesting that the thiocyanate ion is susceptible to (electro)chemical oxidation within the voltage range in which the OMD is operated. The polyaniline switches off during the cathodic scan but competes with the oxidation of SCN^-. Partial oxidation of PANI in a liquid electrolyte is possible thanks to an increased ionic mobility. A study by Itabashi [165], shows that the products of an electrochemical oxidation of thiocyanate in acidic medium are thiocyanogen $(SCN)_2$ and trithiocyanate $(SCN)_3^-$ according to the following reaction equations:

$$\mathrm{SCN^- \rightarrow SCN^\bullet + e^-} \qquad \text{Equation 10}$$

$$\mathrm{SCN^- + SCN^\bullet \rightleftarrows (SCN)_2^{\bullet -}} \qquad \text{Equation 11}$$

$$\mathrm{2\ (SCN)_2^{\bullet -} \rightarrow \mathbf{(SCN)_3^-} + SCN^-} \qquad \text{Equation 12}$$

$$\mathrm{2\ (SCN)_2^{\bullet -} \rightarrow \mathbf{(SCN)_2} + 2\ SCN^-} \qquad \text{Equation 13}$$

These products can be further hydrolysed in an acidic aqueous medium to sulfuric acid and the toxic cyanide [165]–[168]. The formation of the highly kosmotropic sulfate would explain the worsening structure of the otherwise stable $AlCl_3$/LiSCN-based SPEs when attempting to carry out the I-V characterizations. Since the functioning of the device relies on an acidic medium useful to maintain PANI doped, and since the SPEs necessarily contain water, these side reactions of SCN^- cannot be avoided. Hence, despite being a great secondary dopant candidate in terms of the exceptional stability of the gels, lithium thiocyanate does not meet the requirement of inertness and is unsuitable as a PEO additive.

Our last attempt to replace perchlorate with another chaotropic dopant anion was made again following the Hofmeister series. We chose the perfluorinated tetrafluoroborate BF_4^- and hexafluorophosphate PF_6^- that are relatively large and polarizable ions, finding themselves among the chaotropic members of the series, where PF_6^- ranks even above SCN^-. Their lithium salts are known to be employed in polyelectrolytes for lithium-ion batteries, whereas $LiPF_6$ is preferred because of its higher chemical stability. We prepared several gels with 30 mg/ml PEO with $LiBF_4$ and $LiPF_6$ as the secondary dopant, all of which performed in a similar manner. Examples for such gels are P30-AlLiBF-0211 (0.1 M $AlCl_3$, 0.1 M $LiBF_4$) and P30-AlLiPF-01521 (0.1 M $AlCl_3$, 0.05 M $LiPF_6$). Especially in the case of $LiPF_6$, the highly chaotropic PF_6^- ion initially leads to the formation of a transparent solid polyelectrolyte layer. However, the crystallization of these seemingly stable SPEs began only few tens of minutes after solidification and resulted in highly aggregated structures, as it can be seen in the microphotographs reported in Figure 4-30. The larger the portion of the secondary dopant in the gel, the more pronounced was this effect. This behaviour is due to the hydrolysis of tetrafluoroborate and hexafluorophosphate, which results in the formation of F^- ions. Fluoride is a very small, nonpolarizable ion and an early member of the anionic Hofmeister series, thus salting out PEO and causing its precipitation. Larger amounts of BF_4^- or PF_6^- ultimately lead to more fluoride in the system. It must be pointed out that such effects appear only in already deposited samples, but not within the gel preparations (in vials), because there is always enough water to solvate all components, even in the presence of kosmotropic agents. In any case, tetrafluoroborate and hexafluorophosphate have proven themselves as yet another class of dopants unsuitable for OMDs. The application of $LiBF_4$ and $LiPF_6$ in LIB technology is possible because, in this case, nonaqueous solvents that do not react with the solutes at such meaningful rates, such as ethers or organic carbonates, are employed [169].

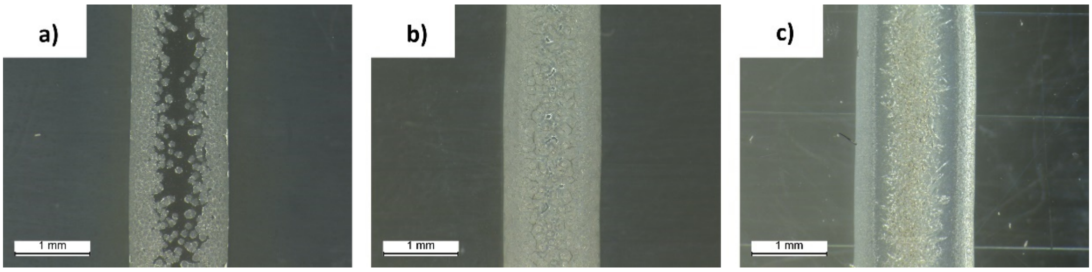

Figure 4-30: Microphotographs of gel P30-AlliBF-0211 a) 15 min after solidification, b) 30 min after solidification; c) gel P30-AlliPF-01521 30 min after solidification.

4.2.3.3 SPE with bromide as the primary or secondary dopant anion

For the fourth generation of our SPEs with increased stability, we decided to switch our attention back towards alternatives for aluminium chloride as the primary dopant. With the experience gained from our previous research, adhering to the criteria that qualify an additive as an appropriate dopant, our idea was to replace $AlCl_3$ by a salt with similar properties. We were searching for a Lewis-acidic, hygroscopic salt with higher chaotropicity, whose anion would participate in the redox reactions involving both the PANI channel and the silver electrode. To minimize the number of systematic changes brought by the replacement of the dopant, we used a homologue of aluminium chloride. At the same time, the salt should have no redox chemistry of its own in the potential range between −0.4 V and +0.6 V, i.e., where the OMD is operated. For this reason, we refrained from using aluminium iodide because of the low standard electrode potential of the couple $3\ I^-/\ I_3^-$ ($E° = +0.53$ V [170]). On the other hand, a similar side reaction is not expected for bromide because it remains stable under our experimental conditions. According to the electrochemical series of standard electrode potentials, the oxidation of Br^- to Br_2 occurs at potentials above +1.0 V (+1.087 V in aqueous solutions [171]. Aluminium bromide is comparably hygroscopic, with the $[Al(H_2O)_6]^{3+}$ ion providing acidity while having a larger, more polarizable and hence more chaotropic anion than chloride. OMD operation mediated by bromide ions has already been shown in section 4.1.4 of this work, where measurements in aqueous HBr have been carried out successfully. The experiments have also shown an overall similar behaviour in comparison with an equimolar HCl electrolyte, given that chloride and bromide have comparable ionic mobilities [135]. Nevertheless, those results (obtained using liquid electrolytes) must be handled with caution, since the obstruction of the bulkier bromide (ionic radii: $r(_{Br^-}) = 1.95$ Å, $r(_{Cl^-}) = 1.81$ Å [172]) could be stronger in a solid polyelectrolyte. Another source of concern is the bromide's higher chemical activity, since it is a much better nucleophile than chloride, possibly causing substitution reactions or the cleavage of PEO chains, which will be assessed below.

We started by preparing a 30 mg/ml PEO gel containing 0.1 M $AlBr_3$ as the sole dopant (P30-AB-01). Surprisingly, although chloride and bromide are neighbouring each other in the lyotropic series, the deposited gel was considerably more stable than its equimolar $AlCl_3$ analogue from section 4.2.1, remaining transparent after solidification. The gels displayed satisfactory long-term stability, showing some moderate drying on the edges of the deposited layer after 11 days of storage in ambient conditions. Moreover, a noteworthy property of the $AlBr_3$-based gel was a superior resistance to heat, as it remained stable upon heating the sample to 60 °C on a hot plate, as it is shown in Figure 4-31 c). However, OMDs assembled with P30-AB-01 as the SPE displayed no switching. We assume that the acidity of the gel was insufficient to maintain polyaniline in its conductive PANI-ES form, because $AlBr_3$ solutions had higher pH levels than the equimolar solutions of $AlCl_3$. In an attempt to lower the gel's pH, we increased the dopant concentration, preparing gels with 0.2 M (P30-AB-02), 0.5 M (P30-AB-05) and 1.0 M $AlBr_3$ (P30-AB-10). Figure 4-31 d-f) show that the resulting SPE became more homogeneous and transparent, while also becoming more and more soft, to the point where P30-AB-05 and P30-AB-10 remained in the form of a viscous liquid. This also meant that it became more difficult to ensure that the gate electrode was in good contact with the SPE when assembling devices, as it would flow down from it rather than enveloping it, as shown in Figure 4-32. Thus, such gels were not used further.

The issue with the assumed insufficient acidity of the gel could not be solved by using mixtures of $AlBr_3$ and $AlCl_3$. Low concentrations of $AlCl_3$ had no considerable effect on the acidity of the gel while higher concentrations caused excessive hygroscopicity, so that the gels would not solidify sufficiently. On the contrary, low concentrations of $AlBr_3$ did not provide enough chaotropicity, leading to poor stability and crystallization over time. For this reason, it was decided to use another additive as a source of acidity. As we have established above, the additive must be

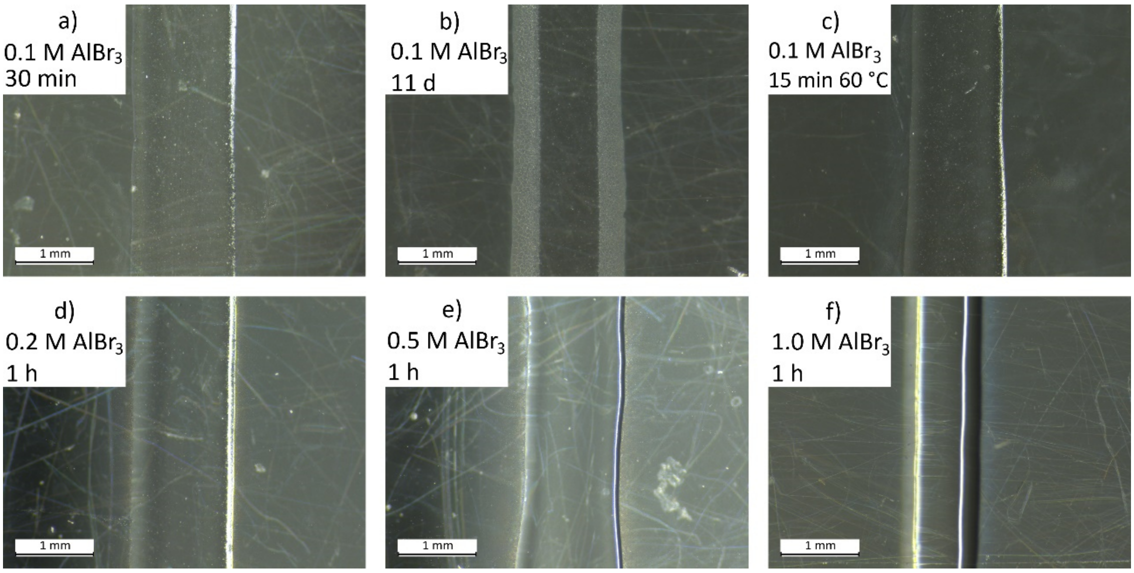

Figure 4-31: Microphotographs of $AlBr_3$-doped SPE with 30 mg/ml PEO.
Gel P30-AB-01 (0.1 M $AlBr_3$) a) 30 min after deposition, b) 11 days after deposition, c) after 15 min at 60 °C.
d) P30-AB-02 (0.2 M $AlBr_3$), e) P30-AB-05 (0.5 M $AlBr_3$), f) P30-AB-10 (1.0 M $AlBr_3$) 1 h after deposition.

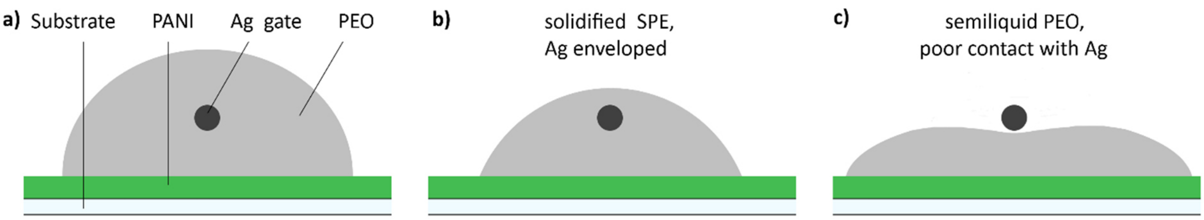

Figure 4-32: Schematic representation of the deposition of a PEO gel in the active zone of an OMD a), followed by an ordinary drying process with the gate electrode staying emerged in the SPE (b). c) Supposed drying process of gels with excessive dopant hygroscopicity and/or chaotropicity (such as P30-AB-05, P30-AB-10), leading to insufficiently contact of the gate electrode with the electrolyte.

non-volatile and have no salting-out effect on PEO. When discussing the concept of lyotropicity in section 4.2.2, hydrotropes have been mentioned among other substances (besides chaotropic salts) that are capable of salting-in of macromolecules. One such hydrotrope is the organic, non-volatile *p*-toluenesulfonic acid (TSA or *p*-TsOH, see Figure 4-33), whose ability to salt-in stems from its amphiphilic structure, allowing it to interact with both water and unipolar moieties. TSA is known to be somewhat soluble in water and forms sols in alcohols and ethers as well as saline solutions. Its pK_a is estimated by different techniques to be between −1.4 and −6.2 [173], which is in any case sufficiently low to maintain PANI in its doped state in the active zone.

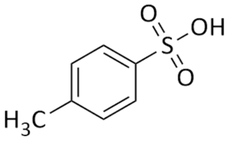

Figure 4-33: Chemical structure of *p*-toluenesulfonic acid (TSA).

The $AlBr_3$- and TSA-based PEO gels required some optimization in terms of the content of both salts. The micrographs of some examples are shown in Figure 4-34 a-d). However, the best SPEs were obtained using concentration ratios similar to the ones familiar from our previous research, i.e., the gels P30-ABT-01521 (0.1 M $AlBr_3$, 0.05 M TSA) and P30-ABT-0211 (0.1 M $AlBr_3$ and 0.1 M TSA). While we can empirically determine the dopant:PEO ratio to be optimal around $5\text{-}7 \cdot 10^{-3}$ mmol/mg, a thorough examination of optimal levels of hygroscopicity and lyotropicity require the study of various parameters of a wide array of salts, which goes beyond the scope of this work of thesis. The two mentioned gels have shown outstanding long-term and thermal stability and withstood the continuous exposure to temperatures as high as 110 °C for over 16 hours, as it is shown in Figure 4-34 e, f). Such a property is of particular interest for the standpoint of automated manufacturing, since one of the steps (the printing of polyaniline) requires the substrate to be heated during the film deposition, as will be shown in Chapter 4.

The operation of OMDs assembled with $AlBr_3$- and TSA-based SPEs was unsuccessful. We assumed that the reason was one of the concerns expressed when we first employed aluminium bromide, namely that it is bulkier than chloride which might hinder it from migrating through PEO to enable the switching reaction. For this reason, given the exceptional thermal stability of polyelectrolytes containing TSA, we decided to return to $AlCl_3$ as the primary dopant with an addition

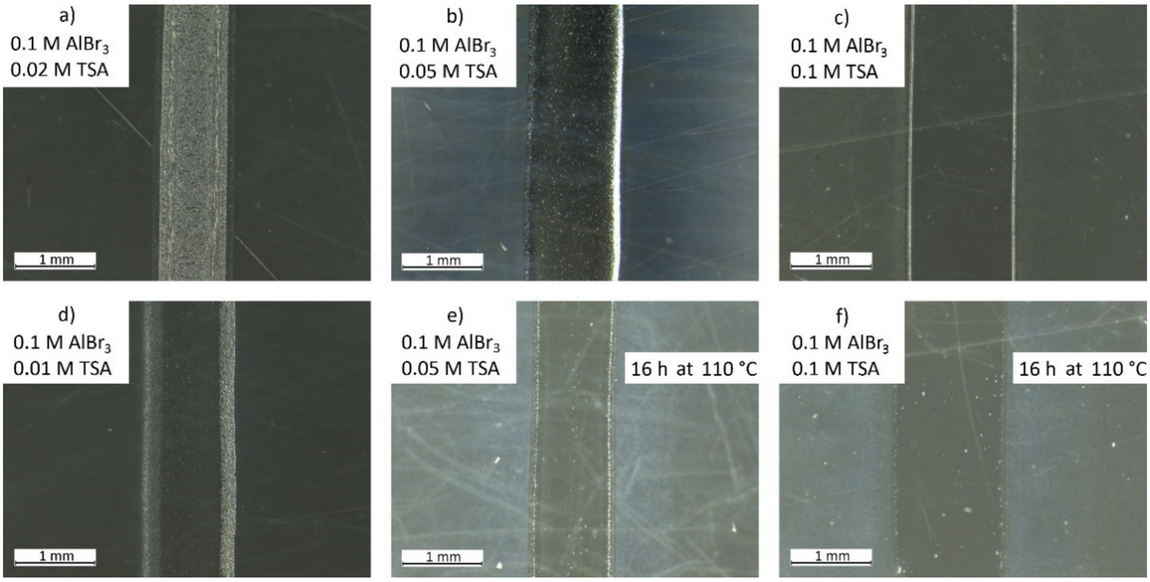

Figure 4-34: Microphotographs of AlBr$_3$- and TSA-doped SPE with 30 mg/ml PEO. a) Gels P30-ABT-01251 30 min after deposition; b) P30-ABT-01521 30 min after deposition; c) P30-ABT-0211 30 min after deposition; d) P30-ABT-011101 30 min after deposition; e) P30-ABT-01521 after 16 h at 110 °C; f) P30-ABT-0211 after 16 h at 110 °C.

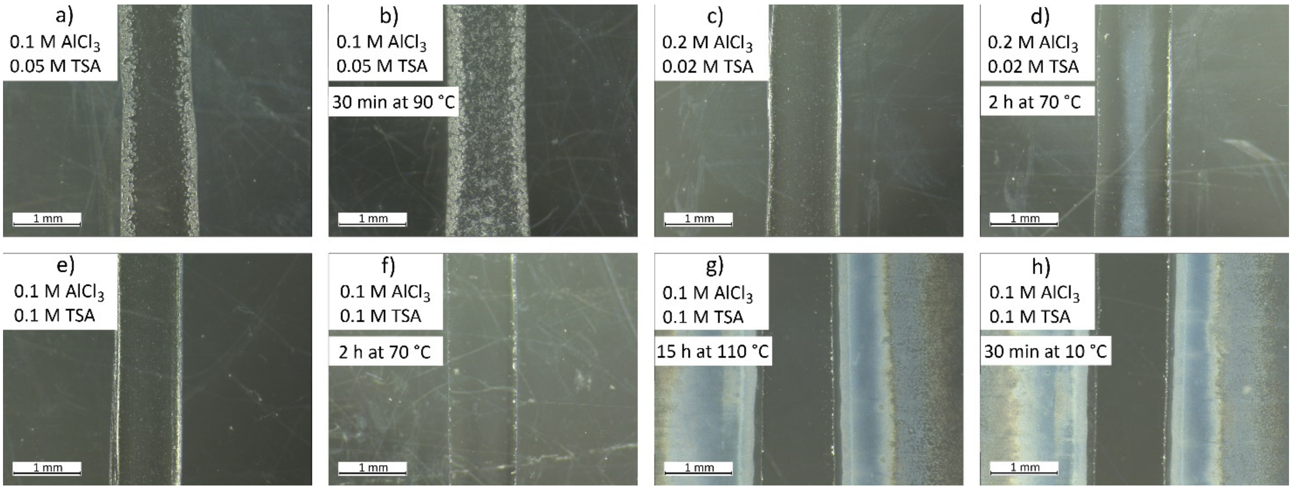

Figure 4-35: Microphotographs of various AlCl$_3$- and TSA-based PEO gels. a) P30-ACT-01521 30 min after deposition; b) after 30 min at 90 °C. c) P30-ACT-022101 30 min after deposition; d) after 2 h at 70 °C. e) P30-ACT-0211 30 min after deposition; f) after 2 h at 70 °C; g) after 15 h at 110 °C; h) after 30 min at 10 °C.

of the sulfonic acid. As expected, due to the lower overall chaotropicity of the dopants, such gels were generally less stable than their bromide-based analogues, which can be seen in the structure of the solidified P30-ACT-01521 gel (0.1 M AlCl$_3$, 0.05 M TSA) in Figure 4-35. Since the P30-ACT-0211 gel remained stable, we can assume that the TSA itself exerts a salting-in effect, even without the presence of another chaotropic salt. Moreover, the transparent appearance of the gel P30-ACT-022101 reveals that this effect must be very pronounced, since a relatively low concentration of TSA (0.02 mol/l) is enough to counteract the effect of the 0.2 M AlCl$_3$. As it was shown earlier in Figure 4-28, such high concentrations of AlCl$_3$ in gels without a secondary dopant caused the crystallization of the SPE after deposition. However, its thermal stability was not as high as that of AlBr$_3$-/ TSA-based ones. Gel P30-ACT-0211 on the other hand showed remarkable stability even after 15 h at

110 °C on a hot plate. The sample also remained stable after 30 min at 10 °C. It is noteworthy that during the long heating at 110 °C, the substrate became covered by a pale deposit to each side of the cast SPE layer. The same could be seen in Figure 4-34 e, f), although less pronounced. This is likely due to the sublimation of aluminium chloride in the form of Al_2Cl_6 (although, according to literature, this normally occurs in harsher conditions [174].

Despite the excellent stability of the SPE, devices assembled with P30-ACT-0211 were not functional, as it was the case with analogous bromide-based SPEs. Given the fact that bromide-based liquid electrolytes allowed switching in section 4.1.4, it is hence more probable that the switching is prevented by TSA in bromide- and chloride-based gels. In a study by Stöffler and Luft [175], various routes of chemical oxidation of TSA with hydrogen peroxide are shown. Considering the electron-withdrawing character of the $-SO_3^-$ group, a similar electrochemical process (possibly assisted by $AlCl_3$ or $AlBr_3$) seems to be plausible in our case, preventing the oxidation of PANI-LE to PANI-ES. Although the PEO gels discussed in this section could not be used to fabricate OMDs, the impressive stability of gels containing bromide and/or TSA is encouraging for further research in this direction. For instance, TSA could be replaced by other, more stable sulfonic acids such as camphorsulfonic acid, which would provide the necessary level of humidity, chaotropicity and, possibly, thermal stability.

4.2.3.4 $AlCl_3$-based SPE with a cationic chaotrope as a secondary dopant

Our previous attempts to replace $LiClO_4$ as the secondary dopant led to the development of new SPEs based on different chaotropic anions. Despite the remarkable stability of some of these SPE, they could not be employed in OMDs because the switching did not occur for various reasons. Thiocyanate and TSA have been shown to display some redox chemistry of their own which could have prevented polyaniline from switching; bromide, although shown to be functional in liquid electrolytes, probably did not provide the necessary level of acidity in form of $AlBr_3$ to maintain PANI protonated; tetrafluoroborate and hexafluorophosphate most likely decomposed due to hydrolysis, releasing kosmotropic fluoride ions that led to precipitation. Perchlorate itself has shown the disadvantage of being a strong oxidant, which likely leads to the degradation of PEO over time.

As shown by a few examples of gels such as P30-ACT-022101, a relatively low concentration of the (anionic) chaotropic agent can be enough to stabilize a gel with a high concentration of $AlCl_3$. This leads us to the conclusion that although cations are generally known to have a weaker salting in-/out effect on macromolecules than anions, a strong cationic chaotrope might be able to provide the necessary conditions as well. Hence, in the fifth generation of our modified PEO-based SPEs, we decided to focus on introducing the chloride salt of a chaotropic cation to the system in order to stabilize PEO's structure. According to literature (mostly dedicated to protein research), guanidinium chloride (GndCl) is a strong chaotrope [176]–[179], capable of salting-in of proteins, decreasing the hydrophobic effect and causing the unfolding of their tertiary structure, hence denaturalizing them. While this effect is undesired in protein purification and isolation, it is the goal in our case as it keeps PEO from precipitating and crystallizing. The cause of guanidinium's chaotropicity is its interactions with the macromolecules and water. The cation is highly polarizable, since its charge is evenly distributed over the whole molecule, as shown in Figure 4-36.

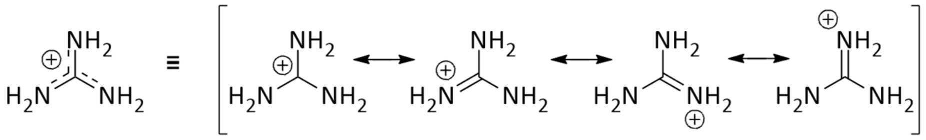

Figure 4-36: Chemical structure of the guanidinium cation.

Unlike some of the dopants we used before (TSA, $AlBr_3$), guanidinium chloride has a high pK_a of 13.71 [180], which is why the acidity in the SPE had to be provided entirely by the primary dopant $AlCl_3$. Furthermore, based on previous results, adjustments of the dopant concentrations had to be made to make up for guanidine hydrochloride's lack of hygroscopicity. We found out empirically that concentrations of $AlCl_3$ above 0.2 mol/l or GndCl above 0.1 mol/l caused crystallization due to an oversaturation of the mixture. We prepared a series of 30 mg/ml PEO gels that are presented in Table 5. Once cast, most of these gels dried out and crystallized after a few hours. Some of the more stable SPEs are shown in Figure 4-37. The gel P30-ACG-0231 emerged as the one with the most favourable composition as it remained transparent 2 days after deposition, while all the other ones (including those in Figure 4-37 a-d) eventually began to dry out during the same period.

Table 5: Compositions of 30 mg/ml PEO gels based on $AlCl_3$ and GndCl, and their visual appearances 2 hours and 2 days after casting on quartz substrates in ambient conditions.

gel symbol	[$AlCl_3$] (mol/l)	[GndCl] (mol/l)	appearance after 2 h	 after 2 d
P30-ACG-0131	0.025	0.075	dry edges	–
P30-ACG-0111	0.05	0.05	dry edges	–
P30-ACG-01512	0.05	0.1	very dry edges	–
P30-ACG-01521	0.1	0.05	dry ends; slightly dry edges	–
P30-ACG-0213	0.05	0.15	overall turbid; dry edges	–
P30-ACG-0211	0.1	0.1	transparent; slightly dry ends	dry, crystallized
P30-ACG-0231	0.15	0.05	transparent	transp.; one end slightly dry
P30-ACG-02532	0.15	0.1	transparent *	dry, crystallized
P30-ACG-02541	0.2	0.05	transparent	dry patches
P30-ACG-0321	0.2	0.1	transparent	small, dry patches

*casting of this gel was particularly difficult due to low viscosity/density

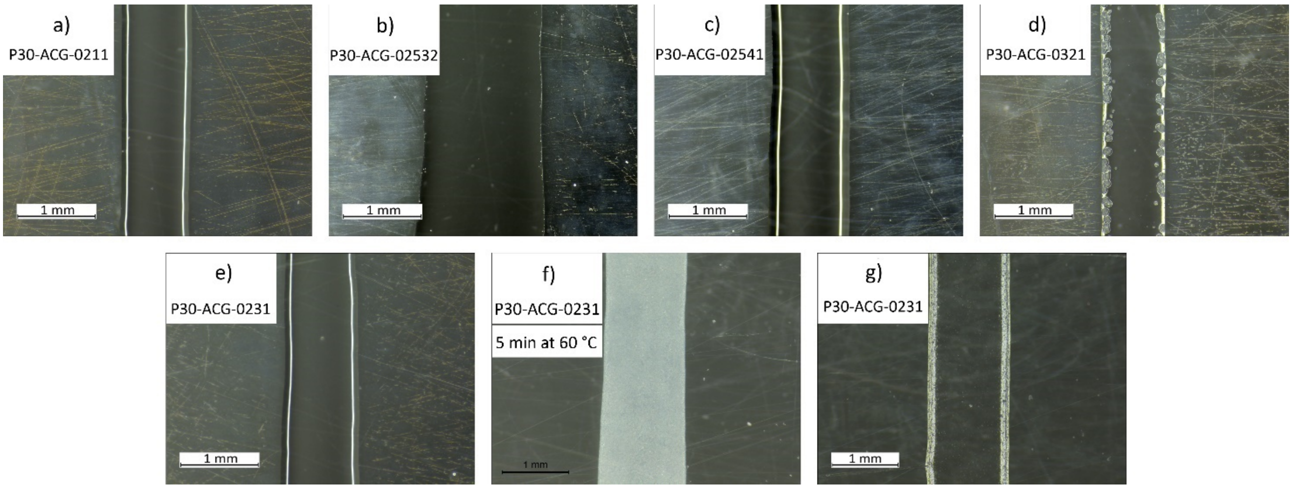

Figure 4-37: Microphotographs of various $AlCl_3$- and GndCl-based PEO gels 2 h after deposition: a) P30-ACG-0211; b) P30-ACG-02532; c) P30-ACG-02541; d) P30-ACG-0321; e) P30-ACG-0231. f) P30-ACG-0231 5 min after 60 °C on the heating plate; g) P30-ACG-0231 regenerated for 15 min in humid conditions.

The thermal stability of the gel P30-ACG-0231 (0.15 M $AlCl_3$, 0.05 M GndCl) was tested by placing the cast sample on a heating plate at 60 °C for 5 min. Much unlike the gels containing aluminium bromide and/or TSA, this gel crystallized within tens of seconds, as shown in Figure 4-37 f). However, the sample regenerated almost completely after 10-15 min in a humid chamber (with a water-filled petri dish, as used in the endurance series in section 4.2.3.1). Looking ahead, such a behaviour is satisfactory when planning the implementation of such gels in automated OMD manufacturing. The gel P30-ACG-0231 was then chosen to assess the operability of OMDs featuring $AlCl_3$- and GndCl-doped PEO. It was done using the gel as the electrolyte in its semiliquid form in the setup shown in Figure 4-7. The devices operated ordinarily in the bias range of [−0.4 V; +0.6 V] with a regular hysteresis shape and kinetics similar to earlier examples. This means that the pH of the SPE was sufficient and no undesired side reactions inhibiting the switching took place. A PEO-concentration of 30 mg/ml has proven to be too low in the case of $AlCl_3$- and GndCl-based gels because their viscosity and density was generally rather low, making the deposition by manual casting more difficult. Thus, we increased the concentration of PEO to 35 or 40 mg/ml while maintaining the overall salt:PEO ratio ($6.67\cdot10^{-3}$ mmol/mg) and proportion of dopants. The advantage of denser gels besides the better applicability is that they solidify faster than the more liquid 30 mg/ml analogues. The gel P35-023331 (0.175 M $AlCl_3$, 0.058 M GndCl) was used to assemble an OMD that was subjected to an endurance test over 1000 cycles. The device was placed in a protective chamber, but without humidifying the atmosphere inside with a water-filled petri dish like it was the case with the device featuring gel P30-Alli-01521 in section 4.2.3.1.

The series started off with relatively slow kinetics and a low output current which normalized within the first 10 cycles through conditioning of the system (for instance, refreshing Ag/AgCl surface). A slow but steady decay of peak current throughout the series of 1000 continuous I-V-cycles can be observed, becoming almost linear after ca. 27 h. It is noteworthy that no plateau-like peaks were observed like in the 3000-cycle series in Figure 4-23. The current fluctuations in that I-t profile were clearly dependent on the time of day and the air conditioning in the laboratory. We argued that the cause for such behaviour was either the temperature or humidity and emphasized the former, reasoning that the water remaining in the petri dish within the chamber should have provided an equal level of humidity throughout the series. However, the more recent results for the device shown in Figure 4-38 indicate that the humidity has a much larger effect on the performance of the OMD than the temperature. This entire endurance 1000-cycles series was recorded without any air conditioning, however, some temperature fluctuations between day and night still occurred. The lack of an additional source of humidity in the chamber combined with the linear decay of the current suggests that the temperature fluctuations alone had no visible effect. On the contrary, in the presence of a source of humidity, an increase of temperature has a visible effect in that the relative humidity increases as well, causing a stronger hydration of PEO and facilitating diffusion processes. Regardless of this detail, the OMD featuring the SPE P35-ACG-023331 displays quite good endurance, considering that the measurements took place in non-optimized, ambient conditions. The gradual decay of output characteristics is most likely caused by partial drying and nucleation of aggregates from which the crystallization could propagate, as demonstrated in Figure 4-38 d). The shape of the

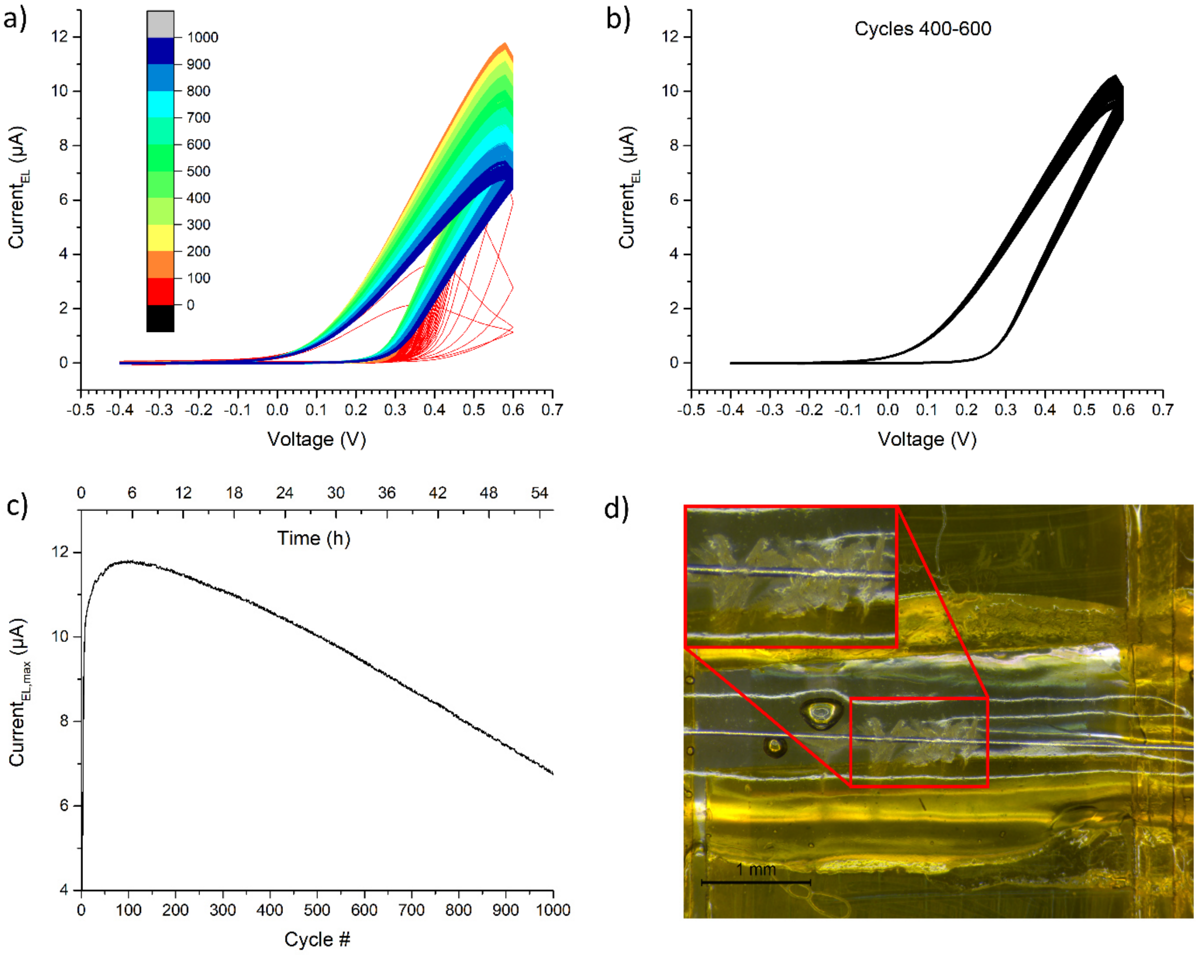

Figure 4-38: Endurance series of I-V characterizations of an OMDs fabricated with gel P35-ACG-0231 as the SPE, measured with a dwell time of 2 s/0.02 V. a) 1000 consecutive cycles with the bias interval [−0.4 V; +0.6 V] followed b) Cycles 400−600. c) Development of the peak output current $I_{EL,max}$ throughout the series. d) Microphotograph of the active zone of the device with partial nucleation/ crystallization by the end of the endurance series.

hysteresis showed good reproducibility throughout the whole series, recognizable by the switching onset at the exact same bias in any 200 consecutive cycles (except the first few).

Summarizing the results of section 4.2 it can be stated that the introduction of intrinsically acidic PEO dopants was very successful at eliminating one of the major sources of instability. The best achieved results are compiled in Table 6. The following attempts to improve the SPE composition for better performance and endurance led to a deeper understanding of the effects that affect the stability of the gel, as well as factors that can cause material degradation. The most notable results were obtained with gels containing aluminium bromide and/or *p*-toluenesulfonic acid, displaying outstanding thermal stabilities. Although these SPEs did not allow OMD switching in one way or another, their interesting properties motivate to work with other, similar substances to create optimized, functioning gels with superior endurance. Finally, the introduction of guanidinium chloride to $AlCl_3$-doped SPEs allowed to fabricate devices with satisfactory stability in ambient conditions, enabling more sophisticated experiments in the future.

Table 6: Summary of the most representative results of our research of novel, multiply doped, PEO-based SPE.

	gel composition (30 mg PEO/ml)		stability		applicability in OMD
gel symbol	prim. dopant	sec. dopant	short-term (2 h)	long-term (2 d+)	
Alli-0113	0.025 M AlCl3	0.075 M LiClO4	good	poor	yes
Alli-01521	0.1 M AlCl3	0.05 M LiClO4	very good	good	yes
AlAS-0111	0.05 M AlCl3	0.05 M NH4SCN	bad	bad	n. a.
AlKS-0113	0.025 M AlCl3	0.075 M KSCN	poor	bad	n. a.
AlliS-0211	0.1 M AlCl3	0.1 M LiSCN	very good	very good	no
AlliBF-0211	0.1 M AlCl3	0.1 M LiBF4	very bad	bad	n. a.
AlliPF-01521	0.1 M AlCl3	0.05 M LiPF6	bad	bad	n. a.
ABT-0211	0.1 M AlBr3	0.1 M p-TsOH	excellent	excellent**	no
ACT-0211	0.1 M AlCl3	0.1 M p-TsOH	excellent	very good**	no
ACG-0231	0.15 M AlCl3	0.05 M GndCl*	very good	good	yes

* guanidinium chloride, ** very good thermal stability at 90 °C

4.3 Increased device stability through coating with NEA

So far, we have shown that some of the gels such as $AlCl_3$-/ $LiClO_4$-based ones display a remarkable reproducibility of device characteristics over long periods of time when provided with a favourable level of humidity surrounding the sample. In this respect, the degree of swelling is a property of PEO-based SPEs that poses a certain cause of instability, as it makes the system dependent on the available content of water. As it was shown in some of our experiments, the relative humidity of the atmosphere surrounding the sample can significantly affect the SPE's structure and the performance of the related OMD, specifically the output current and the switching kinetics. This source of fluctuations in the device response is intrinsic to PEO-based SPEs and is inevitable, independent from the dopants. Recently, microdevices featuring liquid electrolytes (aqueous HCl solutions) have been presented by Battistoni *et al.* [181]. While such an approach bears advantages like increased switching kinetics and overall reproducibility, it is rather more suited for model devices for theoretical, proof-of-concept experiments because of the impracticality of liquid electrolytes in electronic devices and systems. Besides, the issues of dopant evaporation (in this case HCl), which was solved in the present work, would persist in such devices, albeit probably less pronounced than in HCl-doped, PEO-based SPE.

One way of circumventing the issue of the environmental influence could be the sealing of the devices after the assembly, maintaining the SPE in an optimal state and leaving it unaffected by ambient humidity. Sealing would also hinder the diffusion of air oxygen into the system, preventing oxidative degradation.

To apply the concept of device sealing to our OMDs, we have chosen the commercially available NEA 121 (Norland Electronic Adhesive). According to the manufacturer (Norland Products Inc.), the product is a urethane-related resin-based formulation and consists of a mixture of benzophenone and a number of mercapto esters (the exact composition is not disclosed). At room temperature, it appears as a viscous, colourless liquid with a distinct smell. It contains a catalyst that allows it to be cured by irradiation with UV light or at elevated temperatures (e.g., 10 min at 125 °C in a convection oven or 3 h at 80 °C). Curing through heating has the advantage of a more homogeneous process, i.e., the polymerization progresses evenly throughout the whole thickness of the deposited layer. Curing by UV light depends on the thickness of the layer and acts stronger on the layers that are closer to the light source. Nevertheless, due to the sensitivity of most of our SPEs to high temperatures, we resorted to UV-irradiation. The polymerization of monomers occurs in the wavelength range from 320 to 380 nm with peak sensitivity around 365 nm, resulting in a transparent, solid polymer coating. The curing is said to be a very exothermic process. The manufacturer claims that NEA 121 displays very good adhesion on glass, metals, printed circuit boards and many plastics, making it an appropriate candidate for the type of manufacturing techniques envisioned for our devices. Some of the properties of the coating material are presented in Table 7.

Table 7: Properties of NEA 121 (source: Norland Products Inc. data sheet).

property	
viscosity at 25 °C	300 cps
elongation at failure	30 %
modulus of elasticity	160000 psi
tensile strength	3500 psi
dielectric constant (1 MHz)	4.04

Prior to coating experiments with assembled OMDs, we tested whether the conductivity of PANI changes when it is irradiated with UV light or when in contact with NEA. The change of conductivity after irradiation with a 10 W 365 nm torchlight from 10 cm distance for 30 s was negligible. Practically no decay of conductivity was observed when covering the PANI layer with NEA, both prior to and after the polymerization, indicating that deprotonation or chemical reactions did not occur to any considerable extent. Our first successful attempt to coat a functional OMD with NEA featured a modified version of the device that is shown in Figure 4-39. The conductive PANI layer was deposited on a flexible, 3 mm wide strip of polyimide tape by means of the Langmuir-Schaefer technique, which was then applied on a flat glass substrate. The source and drain electrodes were made from strips of copper tape that were applied on each end of the PANI-covered polyimide tape. The electrical connection between the copper tape and PANI was realized by another overlapping strip of conductive carbon tape. A drop of NEA was applied manually with a plastic stirrer over the solidified SPE and polymerized with a 10 W 365 nm UV torchlight from 10 cm distance over 10 s. More NEA was added dropwise on top of the PANI layer left and right from the active zone and distributed over the surface with a razor blade, followed by polymerization.

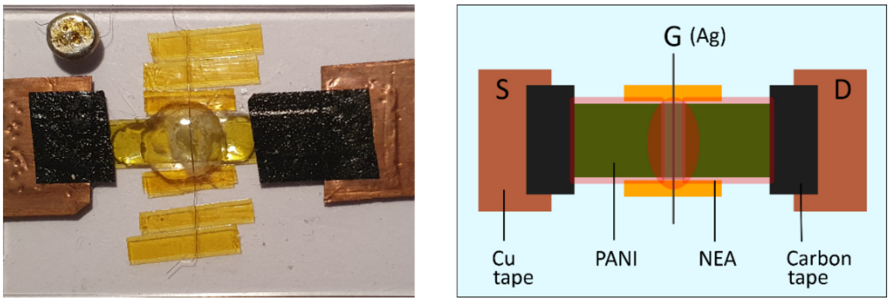

Figure 4-39: Modified OMD used in the first successful NEA coating experiment, including a schematic representation. The red colour for the otherwise colourless, transparent NEA layer was chosen arbitrarily for better visibility.

A series of 1000 I-V-characterization cycles in the voltage range [−0.4 V; +0.8 V] with a dwell time of 10 s per step of 0.1 V has been carried out on this coated device. The number of cycles corresponds to over 69 h of continuous operation. The results of this endurance test are shown in Figure 4-40. We observed a remarkable stability and reproducibility of the output characteristics with some variation of the registered peak output current. The lowest registered value was ca. 75 % of the highest one. There is a noteworthy difference compared to the 3000-cycles-series with the humidified atmosphere setup in section 4.2.3.1. While a steady decay of output current occurred there, during the endurance test with the NEA-coated device, there was no clear decreasing trend. The observed fluctuations showed no clear dependence from the time of day, and the influence of humidity on the morphology of the SPE can be excluded due to the airtight sealing by NEA. This was proven in a separate test where a semiliquid layer of PEO was completely covered with NEA which was then polymerized. After one week, the NEA cover was carefully removed with a razor blade. The solid NEA piece had a smooth dent formed by the underlying PEO layer prior to polymerization, and the gel itself remained fully intact in its semiliquid form.

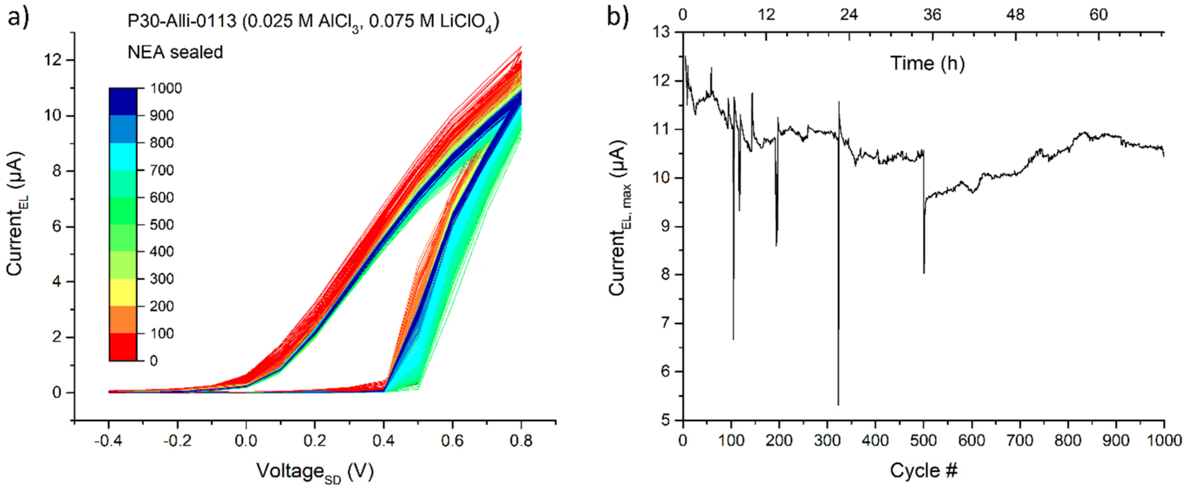

Figure 4-40: a) The results of the endurance test of a NEA-coated device fabricated with the gel P30-Alli-0113 as the SPE, cycled 1000 times with a dwell time of 10 s per step of 0.1 V in the voltage range [−0.4 V; +0.8 V]. b) The I-t profile of the peak output current throughout the series. The series was recorded in successive groups of 50 cycles. The outliers present in the I_{max}-t profile have been removed from the graph in panel a) for clarity.

These results have proven to be difficult to reproduce, since in most next attempts, the output characteristics indicated no switching. There could be different reasons causing the device operation failure, such as degradation processes occurring in the PEO and/or the silver electrode during UV-irradiation, the short-circuiting of the gate electrode with the PANI channel (occurred during the first reproducibility test) or the prevention of the redox half-reaction of PANI or silver. Short-circuiting seems to be unlikely to have caused device failure as increasing the distance between the silver electrode and the PANI channel (to prevent eventual sagging of the wire) did not improve the outcome of the measurements. Mixing of NEA with water and/or PEO, that would lead to an alteration of the SPE's properties, also seems unlikely due to its hydrophobic nature. Another possible explanation could be a wetting of the silver electrode by NEA before polymerization, which would inhibit chemical reactions at the gate electrode, thus preventing switching. In general, the inhibition of the switching at the gate electrode seems to be the most probable cause of device failure, as indicated by the results presented below.

OMDs with PEO-reservoirs for an optimized way of device sealing

Because of the large number of failed attempts to reproduce the endurance series in Figure 4-40 with NEA-coated OMDs, a new way of fabricating OMDs was developed with the goal to reduce the probability of eventual inhibition of switching. This was sought to achieve by making sure that the silver wire would remain in contact with PEO at all times. To this end, the assembly of the active zone has been changed. A layer of PEO is first cast onto a narrow, bare stripe of the PANI channel, then the silver wire is placed at some distance above the channel and is covered with another cast layer of PEO. This is because the thickness of the PEO layer might not have been sufficient to cover the gate electrode, allowing for the penetration of NEA. Hence, we decided to increase the thickness of the SPE layer by casting it into a well-like reservoir with a height of 1−2 mm.

In our first attempts, alternating and overlapping strips (2 mm wide, 6 or 4 mm long) of polyimide tape were stacked on top of one another to create the well structure. NEA was applied on the outer side of the well walls one by one and immediately polymerized with UV light. The PEO gel was then cast into the well, let to solidify and refilled until the well was filled with the SPE. Then, a 5x5 mm square piece of glass was tightly pressed on the rim of the well and NEA was applied on its edges and immediately cured. Lastly, the well structure was covered by another layer of NEA, followed by curing. Upon this modification, most devices still showed little to no switching. The reason could be the penetration of NEA or PEO in or out of the well through eventual gaps between the individual polyimide tape strips. Another possible reason could be the insufficient wetting of the gate electrode by the SPE, as indicated in Figure 4-41 a).

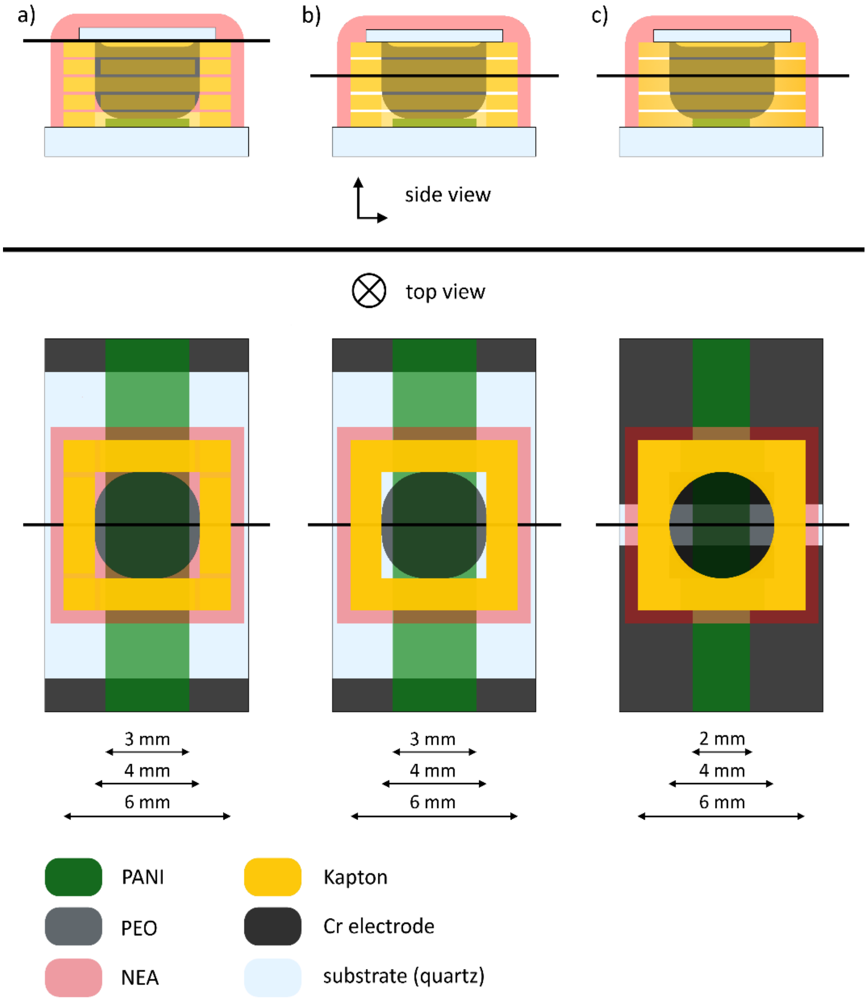

Figure 4-41: Schematic representation of the cross section and the top view of OMDs with SPE wells for improved NEA coating. The red colour for otherwise colourless, transparent NEA is chosen arbitrarily for the sake of better visibility.
a) A square-shaped well, made from 2 mm wide, overlapping polyimide tape strips, capped by a 5x5 mm square piece of glass with the gate electrode fixated on its bottom side. NEA was applied on the outer walls after filling the well with PEO. (b) A square-shaped well, made by stacking pre-cut squares of polyimide tape on top of each other. The gate electrode is placed between these segments at around half the well height. NEA was applied on the outer walls prior to filling the well with PEO. (c) A round-shaped well, made from 10 stacked 6x6 mm squares with a circular hole in the middle, made with a punch. A narrower, 2 mm PANI channel was deposited on a substrate with S and D chromium electrodes stretching all the way to the center of the device, delimiting the active zone. The gate electrode was fixated like in panel b). NEA was applied on the outer walls prior to filling the well with PEO.
All the wells are capped with a 5x5 mm square piece of glass and coated with NEA.

In order to ensure full coverage of the gate electrode and prevent eventual leakage of PEO or NEA, we hence modified the well structure by using pre-cut 6x6 mm square pieces of polyimide tape with a 4x4 mm hole in the middle and stacking 6-10 such squares on top of one another, stretching and fixating the gate electrode at around half the height of the well, as demonstrated in Figure 4-41 b). Still, an ordinary operation of the OMD could not be achieved with this modified geometry. Again, the reason can be better understood with the help of the graphical representation. We propose that the viscosity and surface tension of the cast PEO gel could lead to an incomplete filling of the well, especially in the bottom corners, as it is indicated in the upper panels of Figure 4-41. Looking at the lower panels a) and b), we can see that the 4 mm wide polyimide tape well was placed relatively tightly around the 3 mm wide polyaniline channel. Assuming that the PEO does not properly penetrate into the lower corners, it could be that the edges of the conductive layer remain untouched by the polyelectrolyte and the PANI does not switch off when applying an appropriate voltage bias. This way, a fraction of the channel always remains conductive, and the switching-off is never complete.

To prevent this from happening, in the second modification of our OMDs featuring wells, a narrower, 2 mm wide PANI channel was deposited prior to assembling the device. A circular shape was used for the well geometry, which was achieved by cutting a hole in a stack of ten 6x6 mm, square shaped polyimide tape pieces with a punch. We expected this to facilitate the wetting of the inner walls of the well with PEO, leading to a better contact of the SPE with the PANI channel, as demonstrated in Figure 4-41 c).

We hence carried out a 1000 I-V-cycles endurance series as a proof of concept, using the relatively stable gel P35-ACG-023331 (35 mg/ml PEO, 0.175 M $AlCl_3$, 0.058 M GndCl) from the previous chapter as the SPE. The results of the endurance test are shown in Figure 4-42. The first 100 cycles in panel a) show a good reproducibility of the hysteresis shape and peak output current, similar to the series in Figure 4-40. This confirms that the coating with NEA is an effective way of preserving

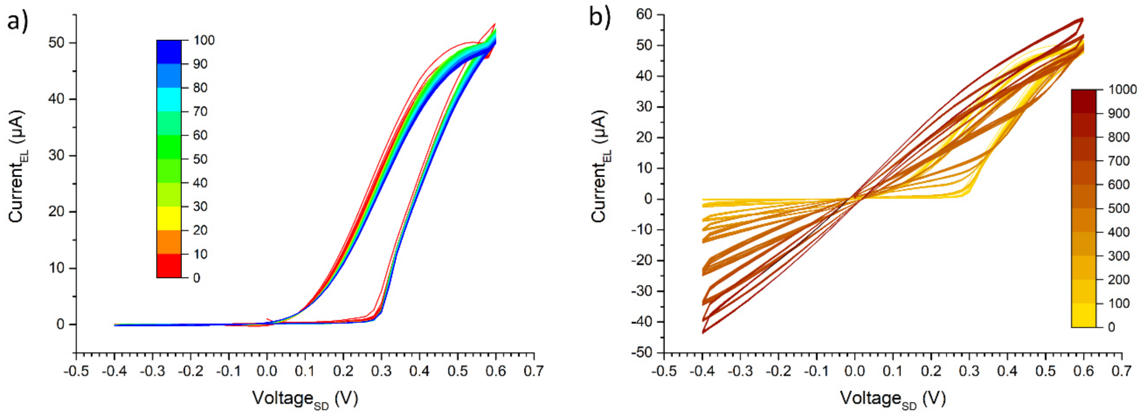

Figure 4-42: The results of the endurance test of a NEA-coated device featuring a well structure, fabricated with the gel P35-ACG-023331 as the SPE, cycled 1000 times with a dwell time of 2 s per step of 0.02 V in the voltage range [−0.4 V; +0.6 V].
a) Cycles 1-100, corresponding to over 5.5 h of continuous operation.
b) Cycles 1-1000 (only the first 20 cycles of each following 100 cycles are shown for better visibility).

the OMD and its performance. However, the situation changes rapidly after the first 100 cycles as the current at negative biases starts to increase (in absolute terms), indicating an incomplete reduction of polyaniline to its nonconductive state. The drying of PEO could be ruled out as a cause for such a behaviour since no crystallization or turbidity occurred. The real cause for the gradual failure of the device revealed itself when observing it under the microscope. Bubbles are observed to form and accumulate at or around the gate electrode, preventing the oxidation of silver. Air leaks are very unlikely to be responsible for their formation because the coating with NEA was carried out very thoroughly and in multiple layers. Based on the data sheet provided by Norland Products Inc., considering that the curing is a very exothermic process, we assume that the bubbles could form as a consequence of volume contraction of the PEO gel, as it cools down after being warmed up during the curing process. Since we expect the coating to be airtight, we propose that the bubbles are, in fact, void and contain no air. Once the bubble grows large enough to limit the contact of one of the electrodes with the polyelectrolyte, the switching is compromised. A few examples of NEA-coated devices with such bubbles are shown in Figure 4-43. Considering the thermal expansion and contraction of PEO, curing of NEA through heating can be definitively excluded because it would likely reinforce this undesired effect even further. A possible solution for this problem could be device cooling prior to the application and curing of NEA (especially when sealing off the capping glass piece) in order to dissipate the generated heat as fast as possible. Another solution could be to reduce the thickness of the coating layer, thus reducing the amount of heat generated during PANI polymerization. In this context, another advantageous characteristic of NEA is its processability via Aerosol Jet Printing (AJP). This technique allows to print thin layers of NEA with a high resolution, which could potentially result in the automation of the coating process while reducing material costs.

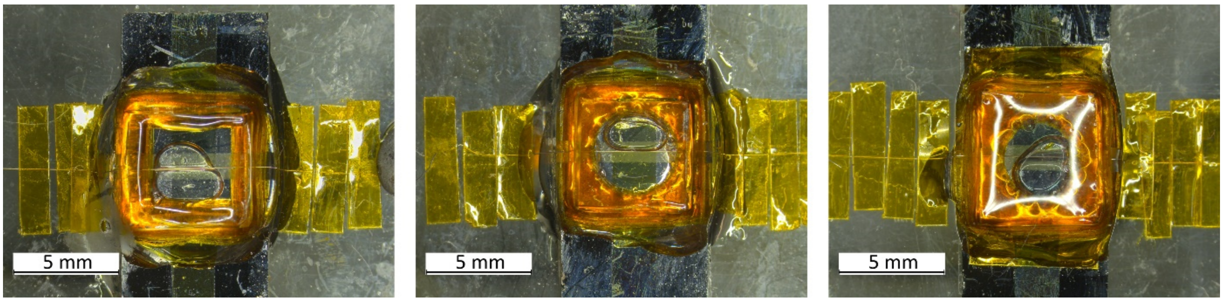

Figure 4-43: Microphotographs of NEA-coated OMDs featuring a well (1x square, 2x round) filled with gel P30-ACG-023331 with bubbles forming at or around the gate electrode.

4.4 Addendum

During the publication of the final version of this thesis work, some new results on the behaviour of OMDs with multiply doped PEO gels were acquired. As was described in section 4.2.3, some of the gels prepared with secondary doping by LiSCN (e. g. P30-AlliS-0211) or TSA (e. g. P30-ACT-0211) appeared exceptionally stable but ultimately failed as SPEs because no switching occured in the OMDs featuring these polyelectrolytes. However, most recent measurements of devices featuring equally composed gels in the semiliquid state were successful and resistive switching was observed. A more careful contemplation of measurements in respective solid-state devices revealed formerly unconsidered details. While the electronic current ($I_{EL} = I_{TOT} – I_G$) remains largely unchanged (on the scale of a few nA) throughout the measurement, an anodic and a cathodic peak appear in the gate current I_G at around the typical bias values (ca. +0.4 and 0.0 V). This is an indication that a redox reaction takes place, but without a change in conductivity, as the channel's resistance remains high. It appears that while the SPEs allow the oxidation of PANI from the leucoemeraldine to the emeraldine state, the doping of the latter is inhibited. Thus, PANI remains in a nonconductive state (PANI-EB) and switching does not occur. We assume that this is due to the morphology of the SPE. While it appears clear and amorphous over long periods of time after casting and solidifying, it seems that the interactions between the PEO-chains, dopant ions and water molecules create a tightly bound framework in which an effective transport of chloride ions is prevented. At any rate, this observation shows that an amorphous state of the gel (as gauged optically) is not a sufficient suitability condition for an SPE candidate. Besides, it indicates that the explanations given for the malfunctioning of TSA- or thiocyanate-containing SPEs might not have been entirely correct because side reactions should occur even more willingly in the (semi)liquid state. These new insights will be treated more in-depth in future works dedicated to optimized SPE formulations. For instance, an on-line optical observation of the active zone of the channel during a scan cycle could be carried out in the solid state, similarly to the experiment described in section 5.3. This might give some proof for the assumption of the appearance of PANI-EB instead of PANI-ES, since the forms of this electrochromic polymer can be distinguished by their colour.

5 Kinetic and dynamic aspects in OMD operation

5.1 The role of the device's geometry

The kinetic behaviour of OMDs has been a subject of theoretical research in the past. The electrochemical model proposed by Smerieri *et al.* [93] and further developed by Demin *et al.* [94] (see section 0) adequately describes the OMD's switching process. Although their arguments related to the role of lithium ions is flawed (as demonstrated in section 4.1), the main concepts of their model remain the basis for the theoretical background on the OMD's switching mechanism. The present chapter deals with relevant kinetic and dynamic aspects of OMD operation. While some related aspects have been discussed in previous works, the available literature does not address some relevant features. Hence, it appears beneficial to provide a summary and explain said effects and their cause.

One of the fundamental aspects of OMD's operation, already discussed in this chapter is the discrepancy between the rates of oxidation and reduction. The reason for such behaviour is essentially the geometry of the OMD. We have shown that in our three-terminal device, the on/off state is determined by the conductivity of the PANI channel. The conductivity of PANI can be controlled through redox reactions that are triggered by the applied electrical potential. This takes place in the active zone (AZ) of the device, which is *de facto* an electrolytic cell. A central concept that needs to be understood is the distribution of the voltage along the PANI channel, as it is shown in Figure 1-16. At any given source-drain voltage bias, the potential profile in PANI decays towards the grounded source electrode. As a consequence, during the anodic scan the oxidation is triggered in the section that is closest to the drain once the threshold value V_{ox} is reached there, progressing towards the source as the bias increases. On the contrary, during the cathodic scan, the reduction in the part of the AZ closest to the source will be triggered at a drain voltage bias that is higher than the threshold value ($V_{bias} > V_{red}$).

Furthermore, during the anodic scan, the PANI-channel as a whole becomes conductive only once the majority of PANI-LE in the active zone transitions into PANI-ES. Conversely, during the cathodic scan, the conductivity of the channel starts decreasing as soon as a fraction of the active zone transitions into the insulating PANI-LE. In other words, when comparing the applied bias with the theoretical redox potentials, during a standard I-V characterization we observe a somewhat delayed switching-on and a premature switching-off of the device. This effect may be better understood from the so-called kinetic characterizations, when the switching occurs at a constant bias. Typical applied voltage values are +0.5 V or +0.6 V for switching-on and −0.2 V for switching-off. As it was mentioned above, the transition of the OMD from the insulating to the conductive state occurs gradually as the oxidation progresses from the drain towards the source electrode. The transition back to the insulating state occurs faster because the conductivity of the whole channel decreases immediately after the reduction of PANI initiates. Furthermore, unlike with positive bias values, when applying a negative voltage, the whole channel is at a potential below V_{red}, so that PANI is reduced simultaneously in the entire active zone. This is also the reason for the seemingly paradoxical appearance of the I_{EL}-t curve, displaying positive current values at a negative applied voltage, as shown in Figure 5-1 b). Such behaviour could be observed in the kinetic measurements from section 4.1.4. As the switching-off initiates, the S-D-current drops rapidly by a few orders of magnitude, while the gate current remains high (in absolute values) as the reaction progresses. Because the electronic current is calculated as the difference between the two, the resulting value is positive, as it was the case in Figure 4-10. Interestingly, the shape of the curve for $HClO_4$ resembled the one in Figure 5-1 a), which is due to the higher off-state currents caused by an inhibited reduction process.

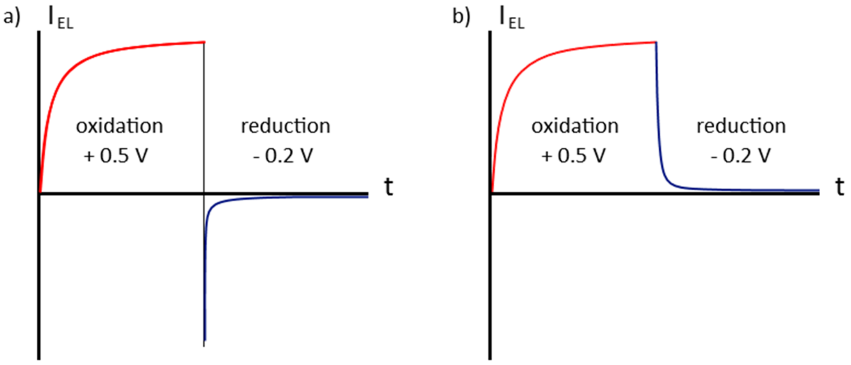

Figure 5-1: Schematic representation of an OMD’s kinetic response at + 0.5 V (oxidation, switching-on) and −0.2 V (reduction, switching-off). a) Expected curve shape with a negative electronic current at a negative bias. b) Typically observed curve shape with a positive electronic current at a negative bias.

The role of the position and width of the active zone

Another factor that emphasizes the importance of the geometry of the device is the influence of the position and width of the active zone, which again is connected to the distribution of the voltage across the PANI channel. This mostly affects the switching-off process, when the entire active zone is in the conductive state. According to Figure 5-2 a), the potential difference within the AZ decreases with its width, resulting in a more uniform response. Similarly, positioning the active zone closer to the drain causes PANI's potential within it to match more closely the applied bias (Figure 5-2 b). This leads to a more predictable and responsive switching behaviour, since the applied voltage required for switching better matches the theoretical redox potentials. The switching-on is less affected by such geometrical changes because, in any case, all the voltage drop mostly occurs in the active zone. Overall, it becomes clear that, in principle, the position and width of the AZ can be used as a tool to control the I-V characteristics of the OMD.

However, in practice, a precise control of the position of the active zone becomes difficult in application-oriented, miniaturized devices as it is more convenient to resort to a geometry where the whole PANI channel is covered with the (poly)electrolyte and is hence active. In this case, another effect becomes relevant when considering the switching behaviour at constant biases. As it was mentioned in section 0, the switching rate also depends on the distance between the gate electrode and the conductive channel. This effect becomes more significant with an increasing ratio of the

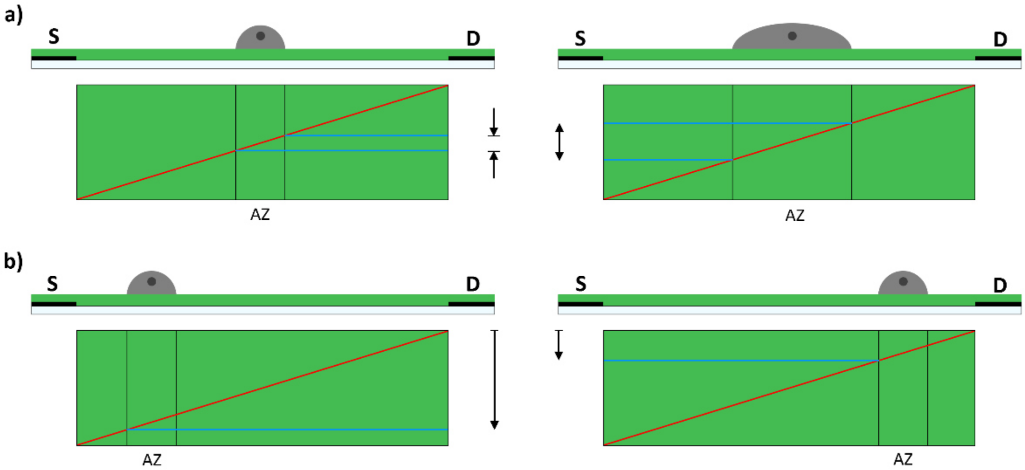

Figure 5-2: a) The effect of the width of the active zone, affecting the potential range between the parts close to the drain and source. b) The effect of the position of the active zone with respect to the source and drain electrodes, affecting the deviation of the actual potential values within the AZ from the voltage bias applied at the drain (schematic).

channel thickness and its length. In a bottom-contact/top-gate configuration, the upper layers of PANI react sooner than the lower ones, as shown in Figure 5-3. This may be an additional source of delay for both the switching-on and -off because the conductive state of the lowest PANI layers are the most relevant, since they are in direct contact with the source and drain electrodes. In this respect, a bottom-contact/bottom-gate configuration could be beneficial in terms of switching rates (see Figure 5-3 b). Such a configuration can only be realized with a solid polyelectrolyte that could better support a layer of PANI deposited on top it. Together with the fact that this effect only applies for short channels, this makes the idea of a bottom-gate OMD configuration better suited to be implemented by high-resolution printing techniques, which will be discussed in chapter 4.

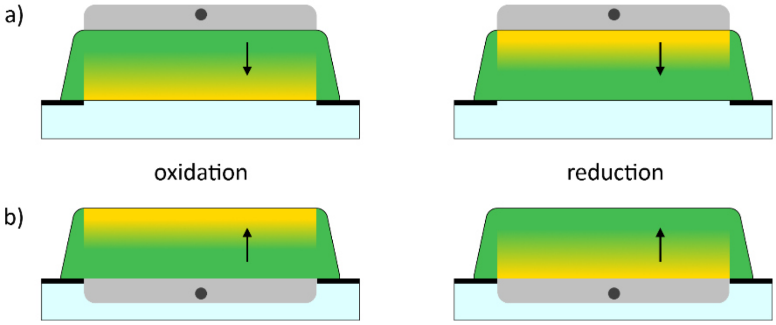

Figure 5-3: Schematic representation of the oxidation and reduction process for an organic memristive microdevice a) in the standard configuration and b) in the bottom-gate configuration. The arrows represent the propagation of the transition of PANI.

5.2 The relationship between electrode potentials and the applied bias

It has been established that the actual electrode potential of PANI does not correspond to the applied drain voltage bias. However, assuming a central position of a narrow active zone in the on-state and an applied bias of +0.4 V, the true electrode potential of PANI in that region would not be

+0.2 V, as suggested solely by the potential distribution profile. As we mentioned above, from an electrochemical point of view, the PANI and the silver electrode that are in contact with the SPE in the active zone form an electrolytic cell. Hence, the applied bias can be seen as the potential difference between the anode and cathode that is imposed upon the system:

$$\Delta V = V_{an} - V_{cath}$$ Equation 14

In our case, when a positive bias is applied to the drain, the PANI electrode represents the anode, and its potential can be calculated as the sum of the applied bias (corrected by the voltage distribution profile) and the electrode potential of the Ag/AgCl cathode. At this point, the fact that the OMD's gate electrode is not a true reference electrode becomes relevant, as its electrode potential is not constant throughout the measurement. It rather depends on the activity of chloride ions whose concentration is also variable due to the formation of ion gradients caused by the applied voltage. The electrode potential can be calculated following the Nernst equation (Equation 15). However, it would be necessary to determine the concentration and activity coefficients of the chloride ions at different bias values.

$$E = E^{\circ} - \frac{RT}{zF} \cdot ln\frac{a_{red}}{a_{ox}}$$ Equation 15

for Ag/AgCl: $$E = E^{\circ} - \frac{RT}{F} \cdot ln\, a_{Cl^-}$$ Equation 16

R … universal gas constant ($R = 8.314$ J mol^{-1} K^{-1})
F … Faraday constant ($F = 9.6485 \cdot 10^4$ As/mol)
$E°$… standard electrode potential ($E° = 0.222$ V for Ag/AgCl [182])
a_i … ion activity ($a_i = f_i \cdot c_i$)
f_i … activity coefficient

According to this relationship, the OMD switching onset at around +0.3 V (theoretical V_{ox} of PANI) in some cases is rather coincidental, and means that under the given conditions, this bias equals the difference between the electrode potentials of PANI and Ag/AgCl. This also explains how the switching may sometimes initiate at low voltage biases such as ca. + 0.14 V in one of our endurance series Figure 4-23.

Since the chloride ion partakes in both half-reactions, both electrode potentials depend on chloride concentration. This means that the dopant concentration in PEO gels is not only important from the point of view of SPE stability but may also be used as a tool to control the switching onset potential. It is possible that the improved kinetics observed with $AlCl_3$-doped SPEs were caused by the increased chloride concentration. It should be noted that since chloride ions partake in both half-reactions, the electrode potential of both Ag/AgCl and PANI depends on their concentration. However, due to the applied electrical field, the chloride concentration is higher at the positive pole and lower at the negative one. According to the Nernst-equation, during the switching-on with a positive applied bias, the concentration gradient causes a correction of the electrode potential of Ag/AgCl to slightly higher values, and that of PANI to slightly lower ones. Consequently, a lower applied bias should suffice to trigger the reaction according to Equation 14. For the switching-off reaction, the situation is reversed because of the inversed polarization of the electrodes and orientation of the concentration gradient.

5.3 On-line observation of OMD switching

Although the importance of the effects connected to the potential distribution across the conductive channel has been established in early works on PANI-based OMD, there is still little evidence for the proposed switching mechanism. In section 1.2.4, we presented some early spectroscopic data aimed to reaffirm the alleged participation of lithium ions in the switching process, corrected by our own data in section 4.1. However, those results are merely indirect indications of the involvement of one or the other ionic species. A more direct approach has been taken by Battistoni *et al.* [183], featuring a spectrophotometric observation of the transition of PANI from the insulating to the conductive state, correlated with simultaneously recorded electrical characteristics. As a development of this approach, we have carried out a study to optically visualize in real time the switching between the transient states of PANI in the active zone. The results of this study were presented at the MEMRISYS 2019 conference in Dresden (2019) [184].

The experimental equipment resembled the one used in section 4.1.2 for measurements in liquid electrolytes (see Figure 4-7), featuring a Teflon trough on top of which the OMD was mounted "face-down". The transparent quartz substrate allows to observe under a microscope the 52 LS layers thick PANI channel from below, without the interference of the gate electrode. A silver wire or a foil (125 µm in diameter or thickness) were used as the gate electrode, attached to the bottom of the Teflon well, filled with a semiliquid PEO gel with 0.05 M $LiClO_4$ and 0.1 N HCl or aqueous 0.1 N HCl as the electrolyte. The transient state of PANI was determined by the colour of the channel in the active zone on which the microscope's digital camera was focused. The electrical characteristics were acquired simultaneously in the kinetic mode at constant applied biases. The predictable colour transitions of PANI between yellow and green, corresponding to PANI-LE and PANI-ES, are shown in Figure 5-4 b) and e), with the propagation of the PANI-ES front from the drain to the source electrode presented in panel f). Meanwhile, panels a), c) and d) display an unexpected second transition from green to blue and back.

Initially, this second transition was attributed to the temporary oxidation of PANI-ES to PANI-PS, with an explanation based on the voltage distribution across the channel, as schematically shown in Figure 5-5. The initial potential profiles (lighter lines) indicate that at high enough voltage biases, there are regions of the AZ close to the drain that are at a potential exceeding V_{ox}(ES-PS), triggering the second oxidation step towards the purple-blue pernigraniline form. As the voltage is redistributed (darker lines), eventually, the potential in these regions drops below V_{ox}(ES-PS) again, so that the green PANI-ES is reformed. An indication for such behaviour was interpreted in the

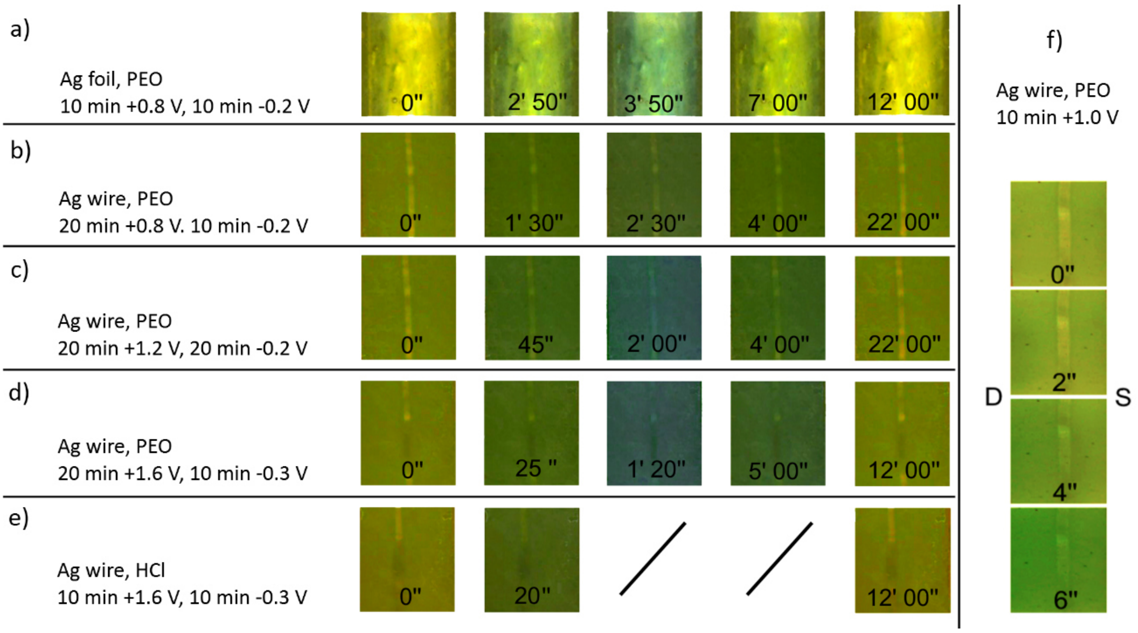

Figure 5-4: a-e) Series of snapshots from digital on-line records of the transition of PANI in the active zone of an OMD during kinetic measurements at different measuring conditions. No change was observed after 20 s in panel e). f) Representation of the propagation of the PANI-ES front from the drain to the source electrode. The colour saturation in series a) and f) was digitally edited for clarity.

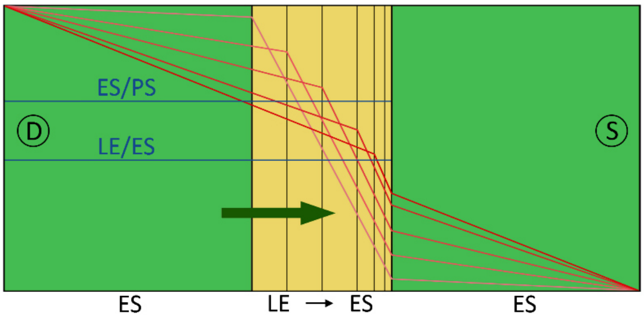

Figure 5-5: Schematic illustration of the proposed potential distribution across the PANI channel during kinetic measurements at high voltage biases (the position of the two oxidation steps is chosen arbitrarily). The arrow represents the propagation of the oxidation of PANI-LE. The red lines are a simplified representation of the potential profile at different times, with the respective would-be oxidized region of the active zone indicated by the vertical lines.

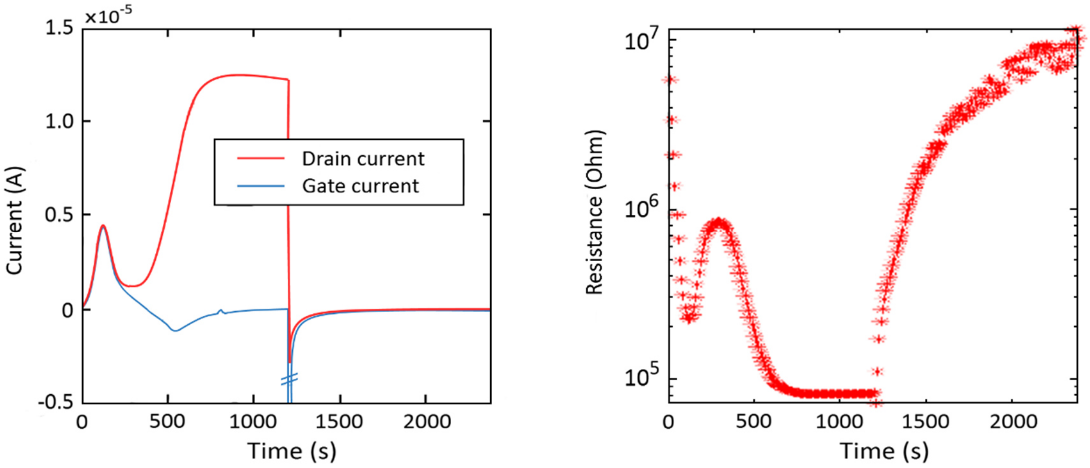

Figure 5-6: Recorded electric characterization of the OMD corresponding to the measurement in Figure 5-4 c).

recorded I-t characteristics (Figure 5-6), displaying a negative peak in the ionic current at a positive applied bias that was attributed to a reduction of PANI-PS to PANI-ES. This is accompanied by a temporary increase of resistivity, corresponding to the insulating state of PANI-PS. The fact that no such transition is observed in Figure 5-4 b) is explained by the lower applied bias. In panel e), the measurement takes place in a liquid electrolyte in which the second transition remains undetected due to faster kinetics, favoured by faster diffusion processes.

The reasoning behind these observations was later reconsidered as some of the above arguments are flawed. The first and foremost source of doubt is the colour of the polymer after the alleged second oxidation step. Although colours might appear altered due to the superimposition of different transient states of PANI in the same film, the blue colour of the polymer corresponds much rather to emeraldine base than pernigraniline which should show a shade of purple. Secondly, although the voltage (re)distribution profile is illustrated schematically, the insulating character of PANI-PS is not represented. This fact cannot be ignored because it would significantly change the picture, since the potential drop mostly occurs within the insulating regions. Lastly, it becomes clear that this explanation does not take into account the geometry of the device with a central position of the active zone. This would mean that PANI's geometry-corrected potential values within the AZ would be significantly lower than the theoretical oxidation potential for the transition from PANI-ES to PANI-PS, with the possible exception of Figure 5-4 d) and e) where the applied bias is +1.6 V.

We hence assume that the occurrence of the blue colour at high biases and the increase of resistance in Figure 5-6 correspond to the appearance of emeraldine base as a consequence of PANI dedoping. The negative peak of the ionic current is attributed to the polarization of the electrode rather than to a chemical reaction. It is reasonable to assume that such dedoping was caused by the strong channel electric field expelling the protons from the positively charged PANI electrode. This also explains the absence of a green-blue transition in the cases with lower applied voltages, where the electric field is weaker. The returning green colour, meaning the re-doping of PANI, is due to the gradient of chloride ions that is inverse to the one of protons. The accumulating negative charge is gradually reduced through the reprotonation of progressively formed imine nitrogen sites, providing the possibility for the formation for ionic couples with chloride. This assumption is consistent with the fact that a slight blue colour appears in panel a) of Figure 5-4 while none is observed in panel b), although the applied bias is equal in both cases. The reason is that in the first case, the strength of the electric field is amplified by the surface area and parallel orientation of the silver foil as opposed to the wire. Lastly, no transition to PANI-EB is observed in panel e) because of the increased ionic mobility of protons (following the Grotthuss mechanism) and chloride ions in an aqueous electrolyte. This effect is also likely the reason for the shape of the hysteresis curve in Figure 4-19 b). The slope of the curve slightly decreases after +0.4 V, indicating a lower conductivity of the channel that may have been caused by deprotonation driven by the electric field. The influence of the counterion, pH and the ingress/egress of H^+ or anions in and out of the polymer on the switching process and on the conductivity of PANI have been discussed in the works by Focke *et al.* [83] and Kalaji *et al.* [185].

The reasoning behind the behaviour of the OMD's active zone is confirmed by similar results by Xia *et al.* [186] who have studied a NiO/PANI composite material that responded in a similar manner to the application of different voltage biases. In a combination of our work and that of Battistoni *et al.* [183] Lapkin *et al.* [187] presented a study where the absorbance of the PANI layer in the active zone of the OMD has been registered by the CCD matrix of an optical microscope. These results are in accordance with the ones presented in our work, although no intermediate transition was observed there, since the measurements were carried out at lower biases.

In conclusion, the concepts introduced in Chapter 4 add to the understanding of the factors affecting the stability and endurance of OMDs. Specifically, the demonstrated dependence of the performance of the devices on the pH and the concentrations of chloride ions gives rise to speculation as to whether more extensive modification of the materials could further increase the stability. Modified polyanilines such as poly(N-ethyl aniline) [158],[159] could partially solve the pH dependency because the trisubstituted nitrogen atoms do not require protonation for the formation of polarons upon oxidation. Besides, the susceptibility to chain cleavage through hydrolysis would be lowered because the nitrogen atoms would be stabilized by the +I-effect of another substituent. Consequently, the development of more stable SPEs would also be facilitated, since the focus could be completely shifted towards the stability of the PEO gel, with no regard to the addition of acidic dopants. On the other hand, sulfonated [80] or otherwise self-doping polyanilines with a carefully controlled ratio of dopant groups and nitrogen atoms would eliminate the channel's dependency from anion gradients within the electrolyte. Thus, a sulfonated, N-alkylated polyaniline (see Figure 5-7) seems to be an interesting candidate for further research.

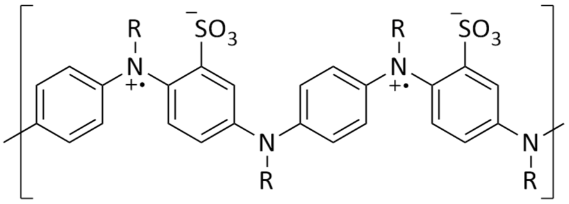

Figure 5-7: Chemical structure of a sulfonated, N-alkylated polyaniline as a potential candidate as a conductive polymer for future OMDs with increased endurance.

6 Towards automated OMD manufacturing – printed neuromorphic devices

In the previous chapter, we explored ways to prolong the lifetime of the OMD by improving the solid polyelectrolyte as one of its most labile components and by sealing the devices with NEA to protect them from environmental effects. These approaches allowed us to significantly increase the endurance and cycle-to-cycle reproducibility of individual OMDs with respect to earlier standards. So far, the device assembly has mostly been done manually, inherently bringing a certain degree of variability with each manufacturing step. For instance, although the Langmuir−Schaefer technique enables a precise control over the thickness of the deposited polyaniline layer, the quality of each layer may vary and depends on the experience and proficiency of the operator. Another source of variability during manual fabrication is the positioning and width of the active zone, as well as the thickness of the SPE layer that affect the kinetics, as we have shown earlier. These and other factors lead to a relatively poor device-to-device reproducibility of electrical characteristics, even after improving each individual device's endurance. The statistics in our case gives the peak output current ranging between 5 and 30 μA, with most recurring values of 10−20 μA. While it is mostly required a stable kinetics, among other features the reproducibility of the on/off ratio value also plays an important role insofar as its control represents a key for implementing more complicated, sophisticated systems such as ANNs and sensing interfaces.

Hence, from a technological standpoint, there has long been a need for steps towards the automation of the manufacturing process. In fact, besides minimizing variability among different devices, other advantages of automated manufacturing are the timesaving (i.e. the so-called rapid prototyping) and ease of downscaling routes, the latter being a prerequisite for higher performance, faster kinetics and mass production. While OMD downscaling has been attempted earlier by Lapkin *et al.* [157] and Battistoni *et al.* [181] (both worked with channel lengths of 200 μm instead of a few millimetres), those works still featured a manual deposition of PANI with the LS technique. The present chapter is hence devoted to developing methods for automated deposition of the OMD's individual components by means of manufacturing protocols based on 3D printing techniques.

6.1 Printing techniques (state of the art)

A rough overview of the various printing techniques is shown in Figure 6-1. Because of their versatility and efficiency, we focused on non-contact, direct writing (DW) technologies, such as Inkjet (IJP) and Aerosol Jet Printing (AJP), that are considered as promising methods in organic microelectronics manufacturing. Direct writing techniques stand out as purely additive methods alternative to standard techniques such as photolithography widely employed for the manufacturing of standard (e.g. metal/metal oxide junctions) and organic-based electronic devices. In particular, they compare favourably to other printing techniques, e.g. screen printing, nanoimprinting or gravure printing, due to their gentleness and versatility in terms of compatible substrates, including flat, flexible and even fragile ones, such as optical fibre glass [188]. Despite the relative simplicity combined with the industrially scalable character, these techniques are highly efficient in that the material waste is minimized and the fabrication cost is reduced, while still allowing to generate complex patterns. Major drawbacks come from the difficulty to achieve fast mass-production of devices and systems. The basic principles of the Inkjet and Aerosol Jet Printing methods, as well as their advantages and limitations, are presented in the following sections.

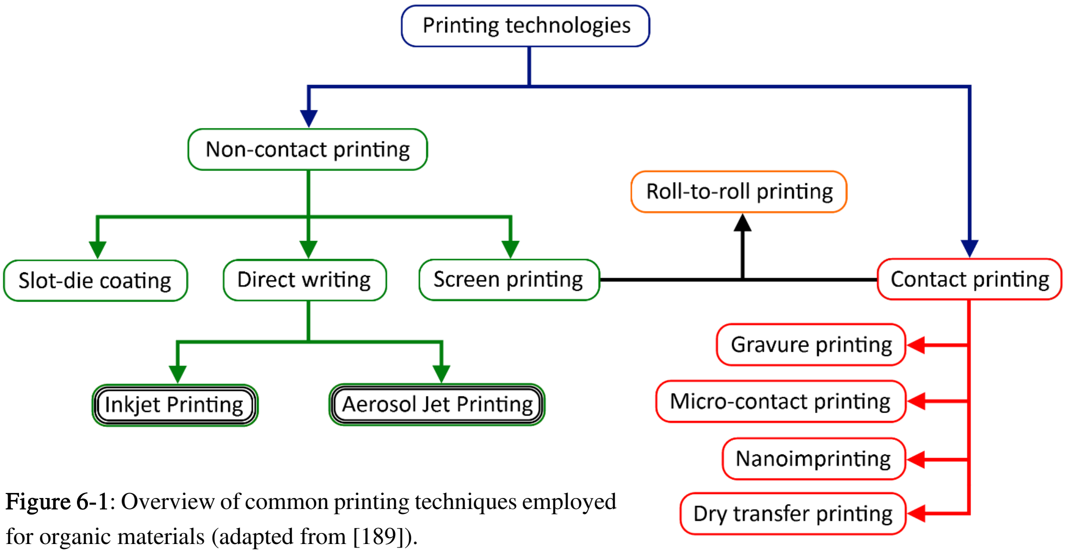

Figure 6-1: Overview of common printing techniques employed for organic materials (adapted from [189]).

6.1.1 Inkjet Printing

Inkjet Printing (IJP) is a contactless, direct-writing method based on the ejection of microdroplets containing the functional material to be deposited. The ink (a mixture of solvents and the functional material) is fed into the deposition head as a solution or colloidal suspension and it is directly patterned onto the substrate, heated to assist solvent evaporation. The ink is released through a nozzle in the form of microdroplets, controlled by a piezoelectric, thermal or electrohydrodynamic actuator [189], as shown in Figure 6-2. The droplet jet is produced due to pressure pulses, generated through deformation of the fluid cavity, through thermal expansion of the ink and the sudden formation followed by a collapse of vapour bubbles, or by generating an electric field between the nozzle and the substrate, respectively. The ejection of droplets can occur in either of the two following modes. The continuous ink jet (CIJ) mode involves the application of a DC field between the nozzle and the substrate plate, resulting in an uninterrupted release of charged droplets in a stream that breaks down into a column of individual droplets, due to Rayleigh instability [190],[191]. The ink is recycled by directing the jet towards a gutter or deflected towards the substrate by applying an electric field between two metallic plates. The droplet-on-demand (DOD) mode is characterized by a pulse-like release of droplets when requested by the pattern to be printed, thus saving ink material when the nozzle is not actuated. Ejection frequencies of 1−20 kHz can be achieved with piezoelectric transducers [190]. Electrohydrodynamic actuators enable the nozzle operation in both the CIJ and DOD mode, depending on the type of applied current (DC or AC, respectively) [189],[192].

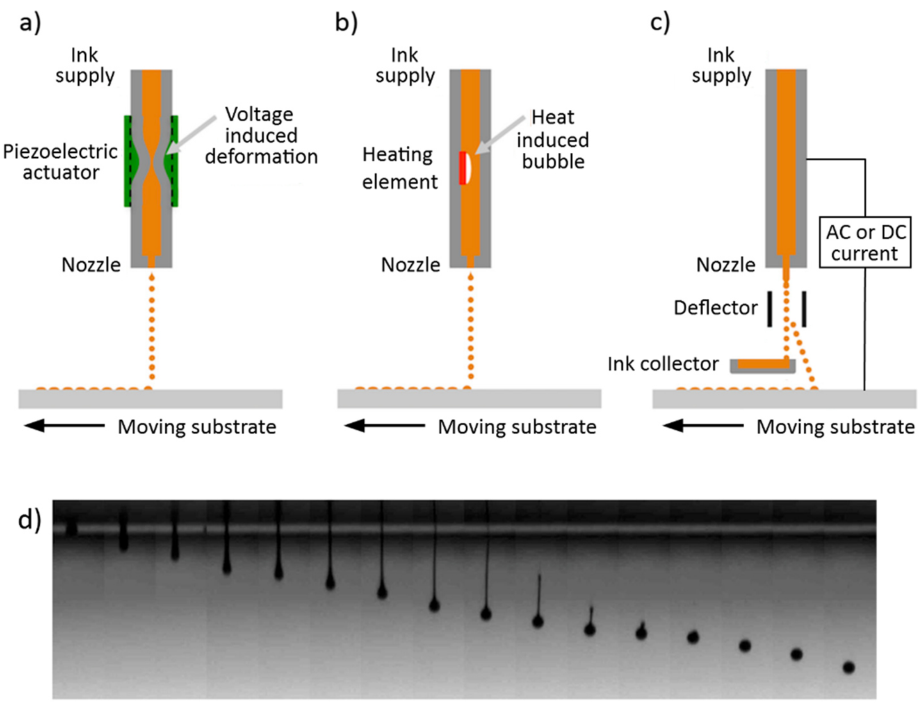

Figure 6-2: Schematic representation of the injection methods for Inkjet Printing. Droplet-on-demand (DOD) operation with a nozzle featuring a) a piezoelectric and b) a thermal actuator. c) Continuous ink jet (CIJ) operation featuring an electrohydrodynamic actuator. Similar setups are possible with piezoelectric transducers, where a charging electrode would precede the deflector. d) Sequence of photographs demonstrating the drop formation process using a piezoelectric transducer with a 5 µs time interval between two adjacent frames (adapted from [190]).

The size of the droplets generated by IJP ranges between 10 and 150 µm, depending on the ink and ejection mode. Inks with viscosities of 2−10 cP can be handled in the CIJ mode with common droplet diameters around 120 µm, while typically smaller droplets around 50 µm are generated from inks with viscosities of 10−100 cP in the DOD mode [191]. Besides the viscosity of the ink, other hydrodynamic properties that influence the deposition are the surface tension and density of the ink, as well as the volatility of the solvents. A requirement for a well-controlled ink ejection is the formation of a thin jet that breaks up into droplets as it leaves the nozzle, as shown in Figure 6-2 d). The process is driven by an interplay of inertial, viscous, and surface tension forces and can be parametrized by putting them in relationship with one another. An important parameter for inks, defining the regime for the breaking of the ink jet, is the Ohnesorge number *Oh* [190] (Equation 17):

$$Oh = \frac{\sqrt{We}}{Re} = \frac{\eta}{\sqrt{\rho \gamma d_N}} \qquad \text{Equation 17}$$

$$Re = \frac{\rho V d_N}{\eta} \qquad \text{Equation 18}$$

$$We = \frac{\rho V^2 d_N}{\gamma} \qquad \text{Equation 19}$$

where η is the viscosity, ρ is the density, γ is the surface tension of the ink, V is the speed of the ejected droplet and d_N is the diameter of the nozzle orifice.

The Reynolds number *Re* is defined as the ratio of inertial to viscous shear forces and gives a quantitative measure of the features of a fluid, while the Weber number *We* is the ratio between the kinetic energy and the surface tension forces, realizing the cohesion of the generated droplets. At low Oh values, the droplet stability is favoured, as viscous surface tension effects are prevalent during the droplet formation process, whereas at high Oh values, it is dominated by a viscous dissipation [190],[191],[193]. Typically, a stable drop ejection occurs at Oh values between 0.1 and 1, whereas in some cases it is preferred to refer to as $Z = 1/Oh$ (varying between 1 and 10) [194]. At $Z < 1$, the low ink density causes the formation of polydisperse droplets in terms of size, whereas at $Z > 10$ droplets do not form because of too high ink density.

The choice of the solvents affects the quality of deposited patterns in that a non-uniform evaporation of solvents may lead to an uneven profile of the printed features. As the evaporation is faster at the edges, the increased loss of liquid is compensated by a flow outward from the center of the printed drop or line. Such a pattern instability is called the "Coffee Stain Effect" or "Coffee Ring Effect" (CRE), with printed lines being accordingly characterized by a thin core and thicker edges [190],[191],[195],[196]. Strategies to reduce this effect include the addition of surfactants [197], or the use of organic solvents such as ethylene glycol [198] or *n*-butanol [199], providing higher homogeneity in colloidal inks. Furthermore, adding highly volatile solvents such as isopropanol to the mixture reduces the outward migration of nanoparticles by inducing a compensating Marangoni flow and an overall faster drying of the ink at the substrate interface [199],[200].

IJP applications and impact

IJP experienced an intensive development over the last decades and has been successfully applied in many fields such as photonics and photovoltaics, sensing and organic electronics. Being compatible with different kinds of materials, ranging from inks containing metal nanoparticles to organic materials, IJP has been used for a wide set of elements. It is suitable for printing basic metallic interconnections, for the realization of passive elements for electronic circuits [201], up to for developing electronic devices, with an exploding literature basis. For instance, photovoltaic modules [202],[203], pressure and temperature sensors [204],[205], all-inkjet-printed organic thin film transistors (OTFTs) [206],[207] or transducing systems using both for biosensing and neuromorphic applications, known as organic electrochemical transistors (OECTs) [208], have been developed. It is noteworthy that many of these examples were realized on flexible, stretchable and wearable substrates, which underlines the versatility of direct writing techniques. IJP has also successfully been applied to polyaniline-based materials, such as PANI-nanofibers [209] or sulfonated polyanilines [158],[210]. However, printing of pristine, high molecular weight polyaniline is difficult because of the polymer's poor solubility in most common solvents compatible with IJP systems, except for NMP that is unsuited for IJP due to its excessively high boiling point.

6.1.2 Aerosol Jet Printing

Aerosol Jet Printing (AJP) is an emerging technique that has been gaining more and more attention over the last two decades, with some of the first research works published by Marquez, Renn and Miller in as early as 2001 [211]. Being another non-contact, direct writing technique based on the generation and controlled deposition of ink droplets, it can be considered as an evolution of the conceptually similar IJP. However, both techniques differ significantly in how exactly the ink droplet stream is formed and conveyed onto the substrate. AJP features much smaller droplets from 1 to 5 µm [212], that can be composed of nano systems with particle sizes ranging from 10 to 700 nm. It is characterized by a significantly higher achievable definition, with line resolutions down to about 8 µm [213].

In Aerosol Jet Printing, the generation of ink droplets is disconnected from the deposition head (DH) and occurs priorly in an atomizer. Typically, two different types of atomizers can be employed depending on the viscosity of the ink, both of which are schematically shown in Figure 6-3, including the general functioning principle of an AJP [214]. Ultrasonic atomizers (UA) are compatible with low-density inks, with a viscosity between 1 and 10 cP. They are made of a chamber containing a glass ink reservoir (ca. 2 ml operation volume) surrounded by water. An ultrasonic transducer is used to generate and transfer a surface acoustic wave from the chamber to the ink in the reservoir, creating an aerosol mist that is transported toward the deposition head by a nitrogen carrier gas flow. The droplet generation follows a certain mass and size distribution, whereby heavier droplets tend to collapse and recombine, and only sufficiently small, lightweight droplets are captured by the carrier gas flow. Pneumatic atomizers (PA) consist of a plastic jar containing a pressurized mist tube that reaches into the ink (ca. 20 ml operation volume). The aerosol is formed by applying a high-pressure gas flow on the ink and directed toward a mist tube. The appropriately sized droplets are selected in a filter known as the 'virtual impactor' and then directed toward the deposition head. PA are used to atomize dense inks with a viscosity between 10 and 1000 cP (comparable to that of glycerine). This allows an ink loading with a compositional percentage of functional (nano) material up to 70 %.

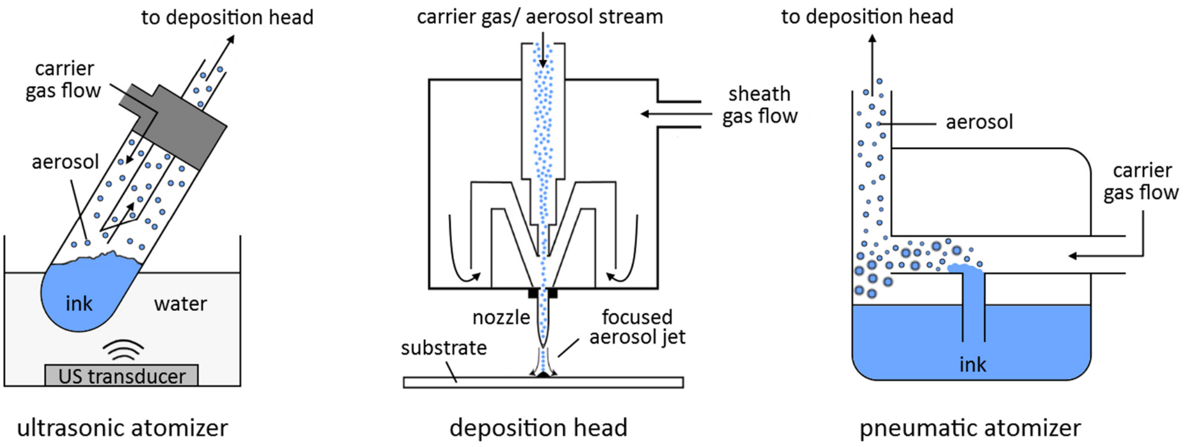

Figure 6-3: Schematic representation of the Aerosol Jet Printing system featuring am ultrasonic (left) and pneumatic (right) atomizer (adapted from [214]).

The principle of deposition of the aerosol also differs significantly from IJP. Instead of an actuator, the deposition head consists of a focusing chamber in which a stream of ink aerosol is coaxially focused and directed toward a 100-300 μm ceramic nozzle. The focusing of the stream is ruled by an interplay of the carrier gas flow (CGF) containing the aerosol, and a nitrogen sheath gas flow (ShGF). The sheath gas flow enhances the stream velocity within the pipeline and forces the aerosol droplets along the ideal central axis of the stream, limiting the spreading of droplets that would tend to deviate from the streamline. Another function of the ShGF is to limit the clogging of the nozzle due to collisions between some droplets and the inner walls of the deposition head.

The substrate is placed on a heated, motorized deposition plate at a typical working distance of 3−5 mm from the nozzle. The plate is controlled by a 2D (or 3D in some printer models) motion control system that enables an accuracy of up to 6 μm [215]. The plate speed affects the thickness of a printed line, obtaining thinner lines with higher speeds for a given set of CGF and ShGF parameters. The plate temperature is crucial in determining the final quality features of the printing process by controlling the solvent evaporation rate and the related drying process of the ink upon deposition. In commercial AJ printers, it can range from room temperature to 120 °C, depending on the ink composition.

The AJP technology is less mature than its inkjet counterpart, which is why the aerodynamic processes determining the formation and stabilization of the ink stream are not yet completely understood. Nevertheless, some works have been dedicated to providing an overview of the relevant aspects governing the AJP process [215],[216]. AJP systems ideally operate under a subsonic, laminar flow regime, with a corresponding Reynolds number < 2500 [217]. The aerosol stream collimation may be used to quantitatively define the line width (LW) in the case of laminar flow conditions for a nozzle with a given diameter d_N [215], expressed as:

$$LW = d_N \sqrt{1 - \sqrt{\frac{FR}{1+FR}}} \qquad \text{Equation 20}$$

where, FR is the focus ratio between ShGF and CGF, defining the features of a line regardless of the ink properties. According to Equation 20, the line width decreases with increasing FR, consistent with a stronger confinement of the stream by the sheath gas.

In the context of the line width, a typical printing instability should be mentioned, namely the so-called overspray (OS) effect. It describes an ill-defined profile for printed lines caused by a deposition of individual or coalesced droplets out of the main line profile [214],[215],[218]. The effect occurs because the operating flow conditions of an AJP are not ideally laminar and the deposited stream is characterized by a somewhat non-uniform size distribution, Hence, minimal turbulences cause a deviation of the smallest droplets from the coaxial aerosol stream. This is accompanied by the drying of external droplets at the nozzle exit, induced by a strong sheath gas flow, reducing their volume/mass and a consequently reducing their inertia. Strategies to overcome

OS include the use of nozzles with larger diameters which lowers the turbulences at the nozzle outlet. The annular drying effect may sometimes be overcome by adding small amounts of low volatile co-solvents, such as ethylene glycol [218].

AJP applications and impact.

Aerosol Jet Printing is characterized its high efficiency due to low material waste, and exceptional versatility thanks to a wide range of processable inorganic and organic materials. Even more than IJP, it is suitable for printing on non-conventional, flexible and rough materials, making AJP a promising technique for applications in the field of 2D and 3D microelectronics. For instance, it has been implemented to print conformal structures following a curved substrate profile or even 3D structures such as micro-pillars and antennas [219]. Similar to IJP, conductive inks have been utilized to realize interconnections for integrated electronics [220],[221] including vertical ones, manufactured by appropriately tilting the deposition head along the z-axis, which is possible with some AJ printer models [222].

The realization of passive electronic elements such as resistors and capacitors has also been reported, using a silver-based ink for electrical pads and PEDOT:PSS or SU-8 photoresist as conducting and dielectric materials, respectively [223]. Within a fast growing literature, 3D printed electronics manufactured by means of AJP systems include several examples of all-printed devices such as ITO-based thin film transistors [224], poly (3- hexylthiophene) (P3HT)-based electrolyte gated transistors [225], organic solar cells [226], photodiodes [227], and flexible OTFTs made with carbon nanomaterials such as single-walled carbon nanotubes (SWCNT) [228] and reduced graphene oxide (rGO) [229].

Interestingly, in some of the pioneering works on AJP, the technique was exploited to print biomaterials such as enzymes, proteins and even cells on 2D substrates [211] validating the viability of the deposited materials, which indicates once more the AJP's very mild deposition conditions. Intact DNA strands were successfully deposited by Grunwald et al. using pneumatic atomization, verifying the integrity prior, during and after the deposition [230]. These works pave the way towards the use of aerosol-based printing techniques for biotechnological applications, for instance in the deposition of cell cultures on scaffolds for tissues regeneration, as well as the implementation of all-printed biosensors based on biocompatible organic materials, possibly even featuring specific biofunctionalization. As a recent development, aerosol jet printed OECT platforms have been developed for the selective detection of bioanalytes [231] such as glucose [232], δ-9-tetrahydrocannabinol [233] or cytokines like the interferon gamma and interleukin-10 [234].

Despite the versatility of the AJP technique, and although it has been realized by IJP in the past (as mentioned in the previous section), there are only a few recent works where polyaniline was successfully printed using the aerosol jet method for microelectronic applications. For instance, Fisher et al. [235] published a work describing an all-aerosol-printed ammonia-sensor featuring the DBSA-doped PANI nanoparticle ink that has been priorly used for inkjet printing [210]. Difficulties with PANI are likely due to the poor processability of the polymer itself rather than the deposition method. It is worth to mention that, so far, no works have been published on neuromorphic systems produced with AJP.

6.2 Aerosol jet printed polyaniline for OMDs

6.2.1 Aerosol jet printing of pristine PANI-EB

While some works have been dedicated to inkjet-printed polyaniline-based inks, the polymers at hand either had a nanofibrous structure or were doped with organic sulfonic acids. However, printing of pristine, higher molecular weight PANI (Mw = 10^5 Da) in its emeraldine base form has not yet been achieved by DW techniques. The main reason is the poor processability of PANI-EB in that it is insoluble in most common organic solvents, except NMP. The high boiling point and low volatility of this solvent makes it unsuitable for inks based solely on NMP because appropriate evaporation rates are not achieved even with 1−5 µm small droplets generated by AJP, leading to spotting and an overall very inhomogeneous material distribution.

We approached this problem by adding isopropanol as a volatile co-solvent to the PANI-solution in NMP to increase the overall ink volatility. The PANI concentration was kept low, at 0.1 mg/ml, in order to maintain a low viscosity compatible with the use of the ultrasonic atomizer. The solution remained stable with a proportion of isopropanol from 10 up to 50 % (v/v), while at higher ratios, precipitation of PANI occurred.

First printing attempts were made with a 0.1 mg/ml PANI solution in NMP/IPA (1:1 v/v) as the ink. Quartz sheets or flexible fibroin films (gained from a solution with 20 % $CaCl_2$) were used as the substrate, whereby quartz samples were treated with ultrasound in isopropanol and treated with UV/ozone at 50 °C prior to deposition, while fibroin samples were used without ozone treatment and avoiding the deposition plate heating, since fibroin is sensitive even to moderately high temperatures. A 200 µm nozzle was used to avoid clogging. ShGF and CGF were set to 25 and 20 sccm, respectively, depositing at a plate speed of 1 mm/s. The results of these first printing attempts are presented in Figure 6-4 a, b).

It can be seen that the features printed on quartz were characterized by a strong dewetting of the substrate, to a point where the PANI solidified in the form of islands along the direction of the print. The preliminary tests with fibroin showed a much more homogeneous coverage due to better interactions of the solvents with the substrate, with line widths around 200 µm. The results with fibroin are promising as they show the applicability of printed PANI on flexible, uneven substrates, which is one of the great advantages of AJP.

A combination of different strategies was adopted to circumvent the strong dewetting effect on quartz substrates. A new ink formulation was proposed, increasing the concentration of PANI to 1.0 mg/ml and introducing xylene to the mixture as another co-solvent. In this way, the content of the nonvolatile NMP could be reduced, while the addition of xylene prevented excessive premature

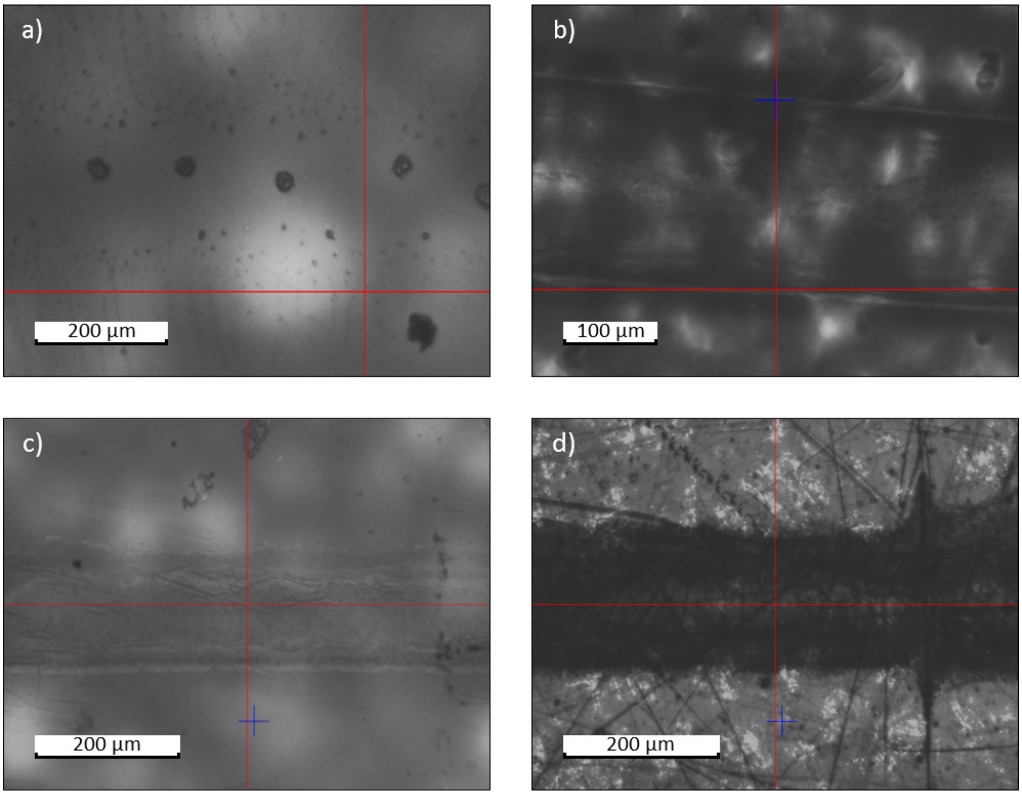

Figure 6-4: Upper panels: micrographs of aerosol jet prints of a pristine 0.1 mg/ml PANI ink in NMP/IPA (1:1 v/v) on a) quartz and b) fibroin, with line widths of ca. 200 µm. Printing on quartz resulted in inhomogeneous drying and the formation of PANI islands while the features were better defined on fibroin. Lower panels: micrographs of aerosol jet prints with a 1.0 mg/ml PANI ink in NMP/xylene/IPA (1:1:2 v/v) on c) quartz and d) polyimide tape, with line widths of ca. 160 µm. The sharp lines coming off the printed line in panel d) are scratches on the tape surface.

drying of the droplets caused by the sheath gas flow. The optimal NMP/xylene/IPA ratio was found to be 1:1:2 v/v, since lower percentages of NMP led to PANI precipitation. This new ink was printed on quartz and polyimide tape substrates with the same CGF and ShGF settings, whereas the higher PANI concentration allowed a faster deposition at a plate speed of 2 mm/s. The new ink formulation in combination with the UV/ozone treatment of the substrate (which is not suited for fibroin substrates) allowed to obtain well-defined, 160 µm wide lines without any notable overspray or spotting, as shown in Figure 6-4 c, d).

Other preparations, such as ink filtering with a 0.2 µm PTFE syringe filter, were excluded because it was detrimental for the printing process, causing spotting. The reason is that due to the low portion of NMP, some of the PANI precipitated, forming a colloidal suspension that was removed by filtration, lowering too much the material load of the ink. Hence, filtering was omitted in the following tests and ultrasound treatment was found to be the only process allowing a better PANI dispersion in the chosen solvent mixture. With this approach, six stacking layers of PANI were printed onto a 15x7 mm quartz substrate equipped with Cr electrodes defining the OMD channel. Large-area films on quartz have proven problematic as we observed a poor layer adhesion as well as gaps between the printed lines, as shown in Figure 6-5 a). Hence, high resistance values, in the order of MΩ, were found after the film doping with HCl. For comparison, LS-deposited channels (30 layers) of equivalent dimensions displayed resistance values between 5 and 50 kΩ. The same ink was printed onto Si/SiO$_2$ substrates (1−2 µm thermal oxide layer) with gold electrodes prefabricated by photolithography (d_{SD} = 200, 10 or 5 µm; w = 6 mm). The line definition was largely improved because of the better wettability of the substrate, as shown in Figure 6-5 b). After doping in HCl, the measured channel resistances were in the ranges of 10−50 kΩ for 200 µm channels, 450−1500 Ω for 10 µm channels and 230−1000 Ω for 5 µm channels. Hence, resistance values scaling was consistent with the scaling of channel length, indicating the films' quasi-ohmic behaviour. These values are comparable to standard OMDs, albeit lower values are to be expected considering the geometry of the channel. Despite the improved coverage, narrow gaps between the printed lines were still recognizable upon optical microscopy. Furthermore, the SEM images and micrograph in Figure 6-7 a, b, e) revealed that the deposited layer was again quite inhomogeneous, with cracks and pores up to 1 µm (with the deposition of a few larger ones up to 10 µm) in diameter.

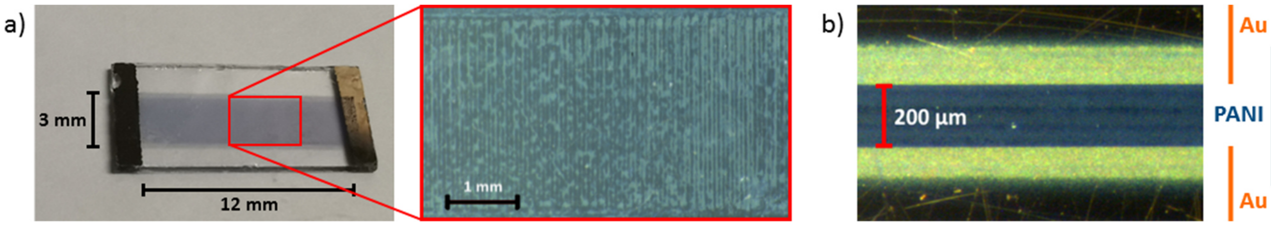

Figure 6-5: Micrographs of PANI printed with the 1.0 mg/ml ink in NMP/xylene/IPA (1:1:2 v/v) onto a) a standard quartz substrate (6 printed layers) and b) a silicon substrate (1−2 µm oxide layer) with prefabricated gold electrodes (d_{SD} = 200 µm, 10 printed layers).

Using the above PANI films, the first ever made OMD with a printed PANI layer was fabricated on test patterns with d_{SD} = 200 µm and using P30-Alli-0113 as the SPE. The scheme and I-V characteristics of the device are shown in Figure 6-6, displaying an ordinary memristive characteristics, featuring a hysteresis and rectification of the I-V curve and proving the concept of printed organic memristive devices.

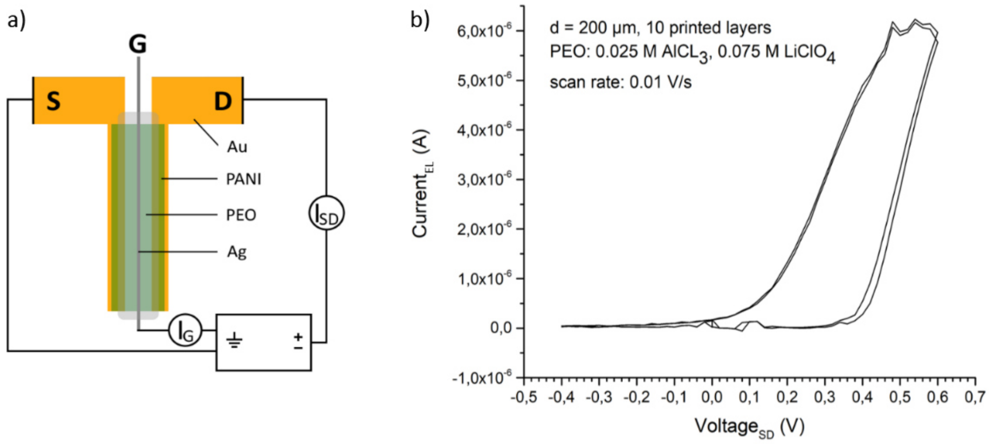

Figure 6-6: a) Schematic representation and b) I-V characteristics of an OMD fabricated with P30-Alli-0113 as the SPE, featuring an AJ printed PANI layer on Si/SiO$_2$ with Au electrodes (d_{SD} = 200 µm). Scanning was done with a dwell time of 2 s per step of 0.02 V.

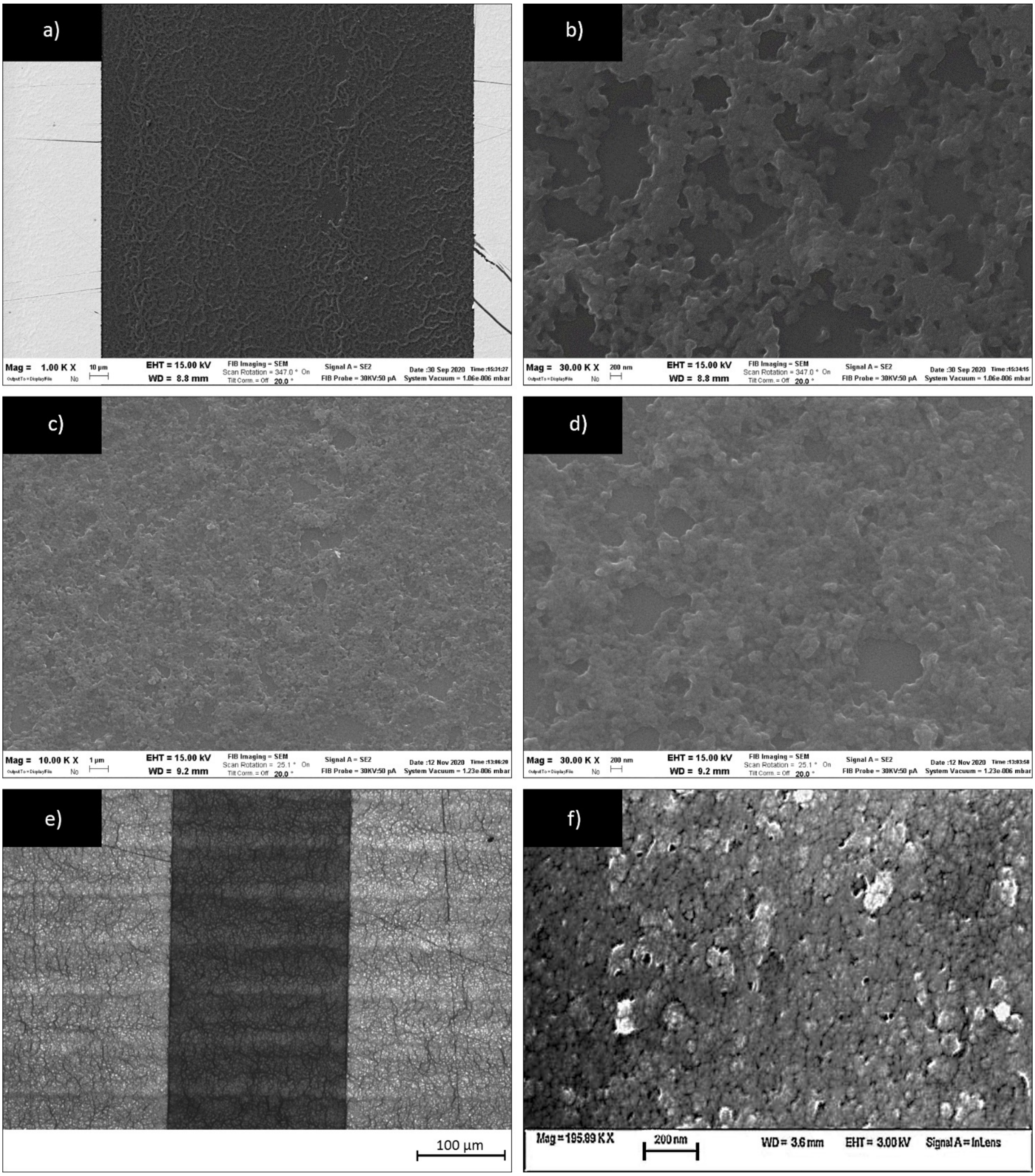

Figure 6-7: SEM images of aerosol jet printed pristine PANI on Si substrates with the 1.0 mg/ml ink in NMP/xylene/IPA (1:1:2 v/v): a, b) 10 printed layers without plasma pre-treatment of the substrate at 1K and 30K magnification, respectively; c, d) 4 printed layers with plasma pre-treatment of the substrate at 10K and 30 K magnification, respectively. Noteworthy is the improved coverage and reduced pore amount and average diameter in c, d). Panel e) shows a micrograph of the sample from panels a, b). Note the profile difference between the bulk and edges of the lines as well as the cracks within the printed layer. For comparison, panel f) shows a SEM image of an LS-deposited PANI channel (24 LS-layers) from reference [109]. The LS layer has a granular morphology while the printed structures are rather fibrous.

Nevertheless, such defective films imply the need of a new printing pattern, consisting of an enhanced overlapping between adjacent printed lines, as demonstrated in Figure 6-8. This pattern has been adopted in all the following deposition runs, aiming to reduce the gaps between adjacent lines and the porosity of the layer. Additionally, to further improve the wettability of the substrate, it was subjected to a O_2-plasma pre-treatment, aimed at both removing eventual residual organic contaminants and making it more hydrophobic by eliminating surface-bound water molecules. Using this approach, the resistance of the printed layers was further lowered to about 340−6500 Ω and 30−500 Ω for substrates with d_{SD} = 200 and 10 μm, respectively. As shown by the SEM images in Figure 6-7 c, d), the morphology of the deposited layer is significantly improved, giving a much better conducting channels made of fewer printed layers.

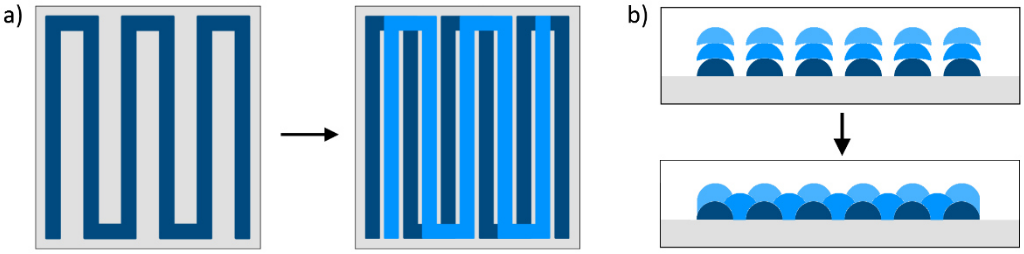

Figure 6-8: Schematic representation of the new adopted printing pattern, a) top view, b) side view. In one case each next layer is printed on top of the previous one and in the other, there is an offset of half a step with each next layer.

6.2.2 Aerosol jet printing of a chitosan:PANI composite material

Although our approach produces PANI films with reduced defects and lower resistance values, it seemed to be too much dependent on the processing route. So, it appeared to be more convenient to change the strategy and develop a new PANI-based ink that would allow a better coverage of the substrate. The dewetting issues connected to the ink composition are difficult to overcome even by means of surface treatment, with the main problem being the presence of NMP. As a nonvolatile solvent, NMP is generally not well-suited for printing applications. Besides, it poses severe health risks being classified as toxic and teratogenic. For this reason, we proceeded by searching to modify the printed material itself since pristine PANI is insoluble in other solvents.

We took inspiration from the work by Ratuchne *et al.* [236], describing a chitosan:PANI composite material that is reported to be more conductive than polyaniline (due to a higher surface area). According to that work, this material is also more thermally and electrochemically stable, making it a promising material for electrochromic devices and capacitors. Most importantly for the present thesis work, the material is reported to be water-soluble, making it an interesting candidate as a PANI surrogate for printing applications. The water-solubility is imparted to the blend by chitosan – a biocompatible polymer that has already been used in OMDs as an SPE [237].

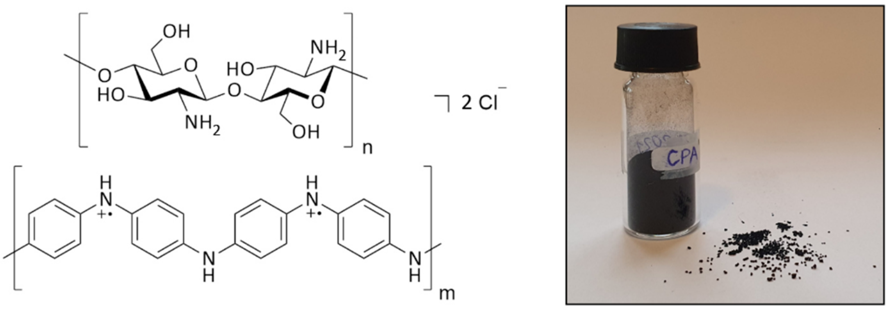

Figure 6-9: Chemical structure of the chitosan:PANI composite (on the left) and a photograph of the obtained product (on the right).

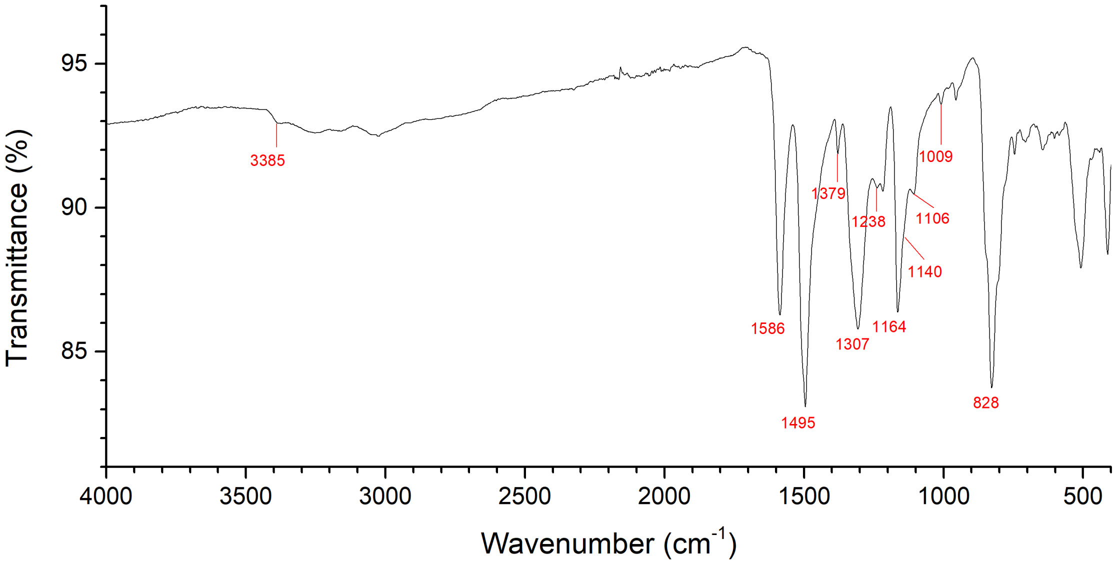

Figure 6-10: FTIR spectrum of the synthesized CPA composite (KBr pellet).

According to the procedure from literature [236], the chitosan:PANI blend (CPA, see Figure 6-9) was synthesized from aniline in hydrochloric medium in the presence of pre-dissolved, low molecular chitosan, following an oxidative polymerization mechanism. The full synthesis instruction is given in section 2.3. A dark green product was obtained, indicating the emeraldine salt form of PANI. The IR spectrum in Figure 6-10 features the characteristic absorption bands: δ_{op}(C−H) and δ_{ip}(C−H) in 1,4-disubstituted rings at 828 cm^{-1} and 1106−1164 cm^{-1}, respectively; bipolaron ν(=NH^{+}−) at 1140 cm^{-1} (as a shoulder band); polaron ν(C−N$^{\bullet+}$) at 1238 cm^{-1}; ν(C−N) of secondary aromatic amines at 1307 cm^{-1}; ν(C=N) in the vicinity of quinoid rings at 1379 cm^{-1}; benzenoid ν(C=C) at 1495 cm^{-1}; quinoid ν(C=C) at 1586 cm^{-1} [17]. The absence of a sharp band around 3610−3645 cm^{-1} indicates that no free −OH groups are present, suggesting that they participate in intermolecular hydrogen bonds, characterized by a broad band around 3200−3400 cm^{-1}. The same applies to a broad band around 3000−3200 cm^{-1} which can be attributed to H-bound NH groups. The band at 3385 cm^{-1} corresponds to free NH groups of PANI that do not participate in H-bonding. The small band at 1009 cm^{-1} corresponds to ν(C-O) of the secondary cyclic alcohol moieties in chitosan. Overall, the chitosan-related signals are weak with respect to those of PANI, indicating that the blend most likely consists mainly of polyaniline.

Additional structural information could be gained from MALDI-TOF measurements, although no precise information could be given about the molecular weight distribution of the formed PANI chains. The analysis has proven difficult because the composite is insoluble in the most common solvents like water, NMP, isopropanol, ethanol, DMSO, acetonitrile (ACN), chloroform or THF. Dispersions on the other hand adhered too weakly on the substrate/matrix, often making an effective ionization difficult. As exemplified in Figure 6-11 a), there was a group of three signals around 3400 u that reoccurred in the majority of all the acquired spectra. It appears as though this particular formation is especially abundant in our material and/or more stable under the ionization conditions. Although information could be gained about the structure of this species, it is reasonable to assume that the signals arise from chain-like or cyclic polyaniline structures. An indication of this are the differences in the m/z of the individual peaks, being ca. 71.3 u between the second and the first, and ca. 115.8 between the third and the first one. These atomic weights correspond to a doping of imine nitrogen atoms by two HCl units (ca. 72.9 u) or two CH_3COOH units (ca. 120.1 u, remaining solvent traces from the synthesis). The periodically occurring, weaker signals in Figure 6-11 a) also have a difference of ca. 72 between them, further indicating the presence of PANI chains with various levels of HCl doping. Similar results can be seen in Figure 6-11 b), exhibiting the same periodicity of signals in the inset and indicating chain lengths of up to 8 kDa. However, considering the solubility issues, it is likely that the majority of the product has a significantly higher molecular weight, since only a fraction of it could be dissolved in HFIP. In the future, a more detailed analysis of the product (e. g. deposited as a solution or directly printed by AJP) could deliver more insight about its structure.

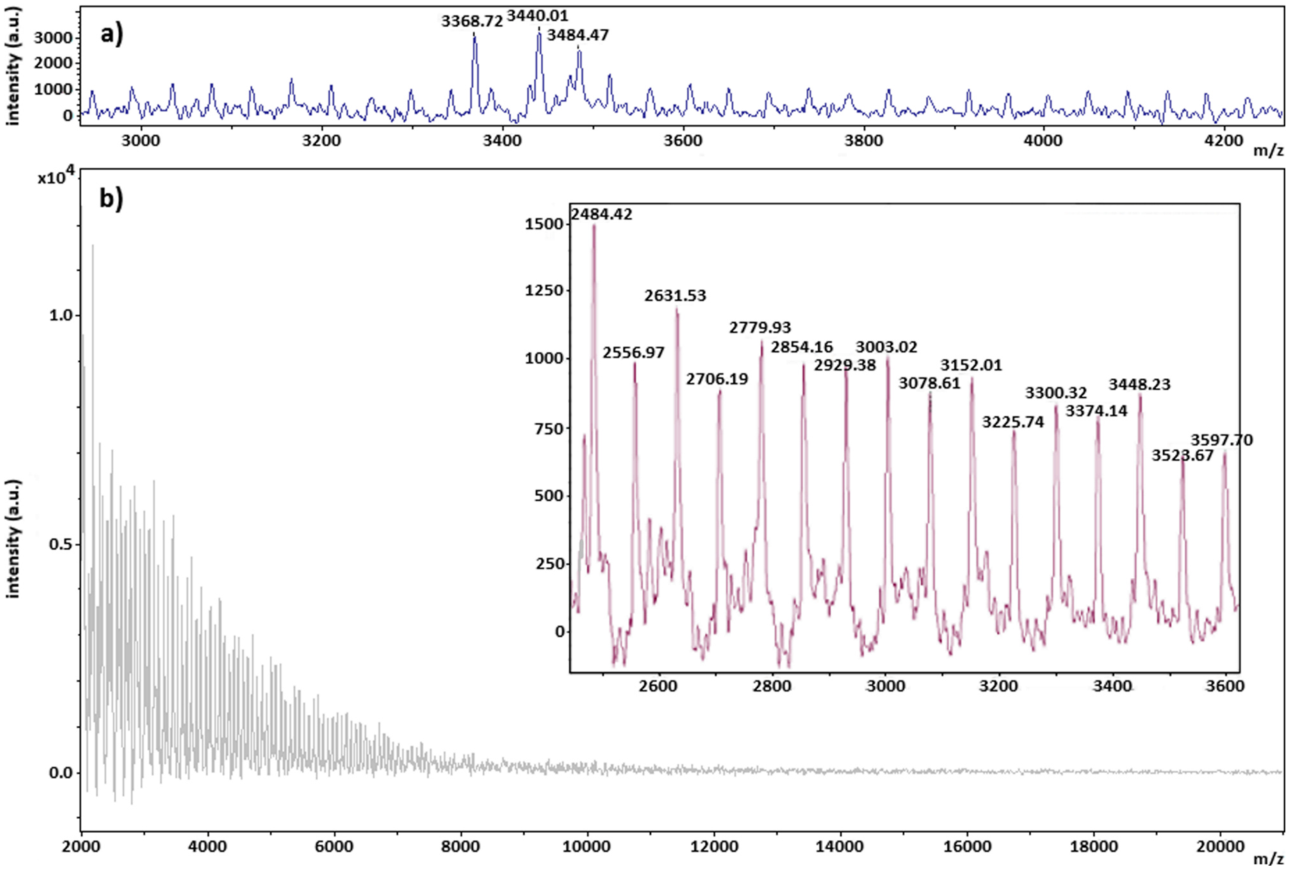

Figure 6-11: MALDI-TOF mass spectra of the synthesized CPA composite deposited on the substrate a) as a dispersion in H_2O/ACN (1:1 v/v), b) as a solution in H_2O/HFIP (1:1 v/v). The baselines are subtracted, the margin of error is 1000 ppm.

Despite the solubility issues of CPA, it could easily be dispersed within 10 s by means of ultrasound treatment in water/IPA (8:2 v/v), forming a dark green suspension that remains stable over long periods of time, with minimal reprecipitation after weeks. The fact that the material is fully dispersed and not dissolved is proven by filtration with a 0.45 µm PTFE syringe filter, resulting in a clear, colourless filtrate. We attribute such behaviour to the relatively small fraction of chitosan in the blend, as suggested by IR, as well as its presumably high molecular weight. In the original paper [236], the molecular weight of the utilized chitosan was not specified, but the reported particle size and plate-like morphology of the material obtained by Ratuchne *et al.* (see SEM image in Figure 6-12 d) suggest that it might have been larger than in our case (low molecular weight, 20−50 kDa). For comparison, Figure 6-12 a, b) shows SEM images of CPA printed with the water/IPA-based, 2.0 mg/ml ink (8:2 v/v) on Si/SiO_2 substrates. The morphology results to be fibrous and rather similar to the deposited pristine PANI samples from the previous section. The coverage of the substrate is largely improved, even though the surface has not been pre-treated with plasma, suggesting a much better wetting of the substrate and evaporation rate of the ink. The resulting printed lines were very well defined, with widths down to 120 µm. The SEM images show that the printed layer is quite porous and rough, with randomly occurring sites where some aggregation of the material occurs. The thickness of the layer was estimated from ATM measurements of single-layer films on the edge of

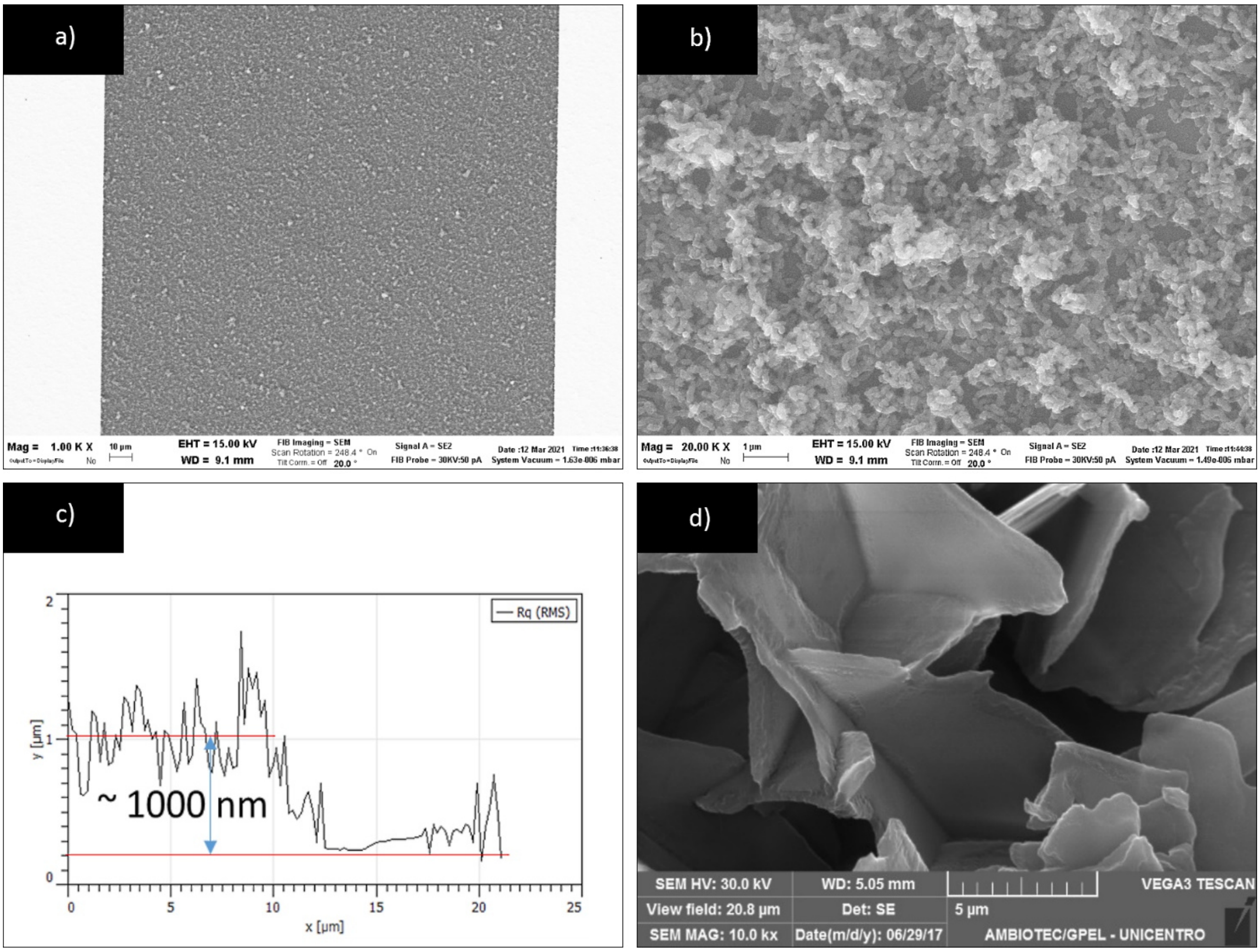

Figure 6-12: a, b) SEM images of single layer printed CPA on a Si/SiO_2 substrate at 1K and 20K magnification, respectively. c) Profile of the printed layer measured by means of AFM. d) SEM image of the blend from reference [236], for comparison.

the printed layer (see Figure 6-12 c). Typically, values around 1 µm per layer were obtained. Despite the excellent definition of features, the adhesion of the layer was quite poor as it could be mechanically removed with ease. Plasma treatment of the substrate could possibly solve this issue in future experiments. Resistance as low as 14 Ω could be achieved after doping in HCl. Considering a channel width of 4 mm, length d_{SD} of 10 µm and estimated thickness of 2 µm (1 µm per layer), this corresponds to a conductivity of ca. 1.8 S/cm. For comparison, pristine PANI films deposited with the LS technique (30 layers) on standard 15x7 mm quartz substrates show conductivity levels around 50 S/cm. In its doped, emeraldine salt state, the layer displays nearly ideal ohmic behaviour, as shown in the inset of Figure 6-13 a).

A memristive device has been fabricated by printing two CPA layers as the conductive channel on a Si/SiO_2 substrate equipped with gold electrodes (d_{SD} = 10 µm), using the gel P30-Alli-01521 as the SPE and a silver wire as the counter electrode. The I-V characterization are shown in Figure 6-13 a). The device displays a very high performance with a well-defined, reproducible hysteresis of the I-V curve. Further tests have shown that the OMD remains fully functional at scan rates as high as 100 mV/s, with minor widening of the hysteresis, although the oxidation reaction starts to notably lag behind the applied bias at scan rates above 40 mV/s (Figure 6-13 b).

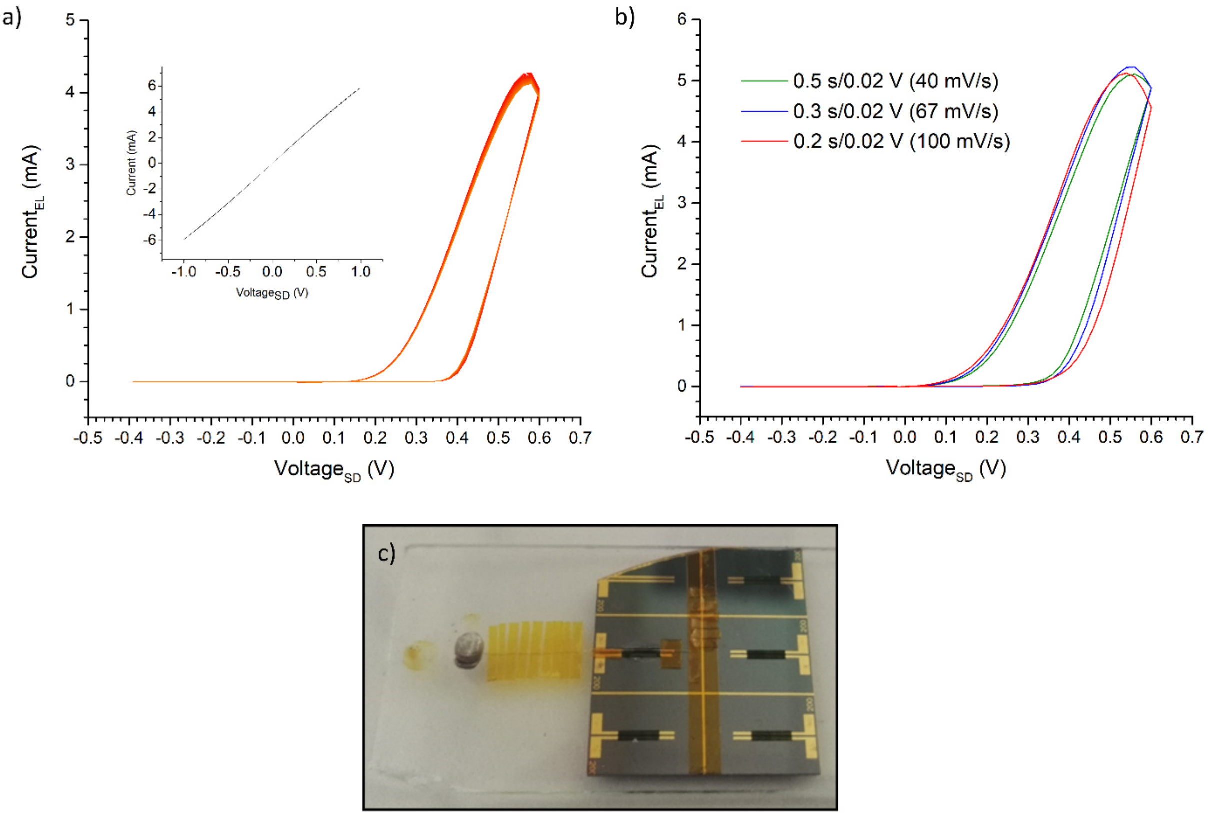

Figure 6-13: a) 40 consecutive I-V cycles measured with a dwell time of 2s per step of 0.02 V (10 mV/s scan rate) on an OMD fabricated with 2 printed CPA layers as the conductive channel and P30-Alli-01521 as the SPE (on Si substrate with Au electrodes and d_{SD} = 10 µm). In the inset, the almost ideal ohmic behaviour of the layer is demonstrated. b) I-V characterization of the device at different scan rates. c) Photograph of the device (only the middle left layer is involved).

6.3 Towards AJP-compatible polyelectrolyte materials

Although the quite good and novel results obtained from devices fabricated with the CPA-based ink from the previous section, there is a switching kinetics that is not matching the expectation based on the reduced channel dimensions. Such a behaviour can be explained considering the thickness of the printed CPA layer. With a thickness of 1 µm, on a scale of a channel length of only 10 µm, the layer attains bulk properties in that its conductivity strongly depends on the charge transfer between the single deposited layers, or in the case of printed CPA, rather between the single fibre microstructures. This is especially relevant for the bottom-contact/top-gate geometry used so far, where the switching of the channel initiates closer to the gate electrode, but only comes into effect once the conductive connection is established with the source and drain terminals. As was discussed in section 5.1, this issue could be circumvented by adopting a different kind of device architecture with a bottom-contact/bottom-gate arrangement, where the bulk properties of the channel play a minor role.

The versatility of AJP provides the necessary tools to approach the sought-after goal of fabricating fully printed devices, including all the components of an OMD. With the ability to print conductive metal nanoparticle inks, AJP allows us to fabricate a silver gate [218] and gold source and drain electrodes [238], with the final step of interconnecting them with the conductive CPA ink developed above. The missing link is the deposition of the polyelectrolyte material to create the junction between the gate and the conductive channel. By consequence, it would be required to print CPA onto the latter, however it is not expected to be an issue since AJP is suitable for the deposition on a variety of substrates, including flexible, uneven, and soft ones. The following section is dedicated to making steps towards developing printable polyelectrolyte materials.

6.3.1 Low-viscosity PEO-based hydrogels

Our development of printed polyelectrolytes relies on the knowledge acquired when improving the PEO-based SPE composition in chapter 4. Since the properties of the gel remain unchanged when maintaining the same dopant:PEO ratios, it seems possible to prepare a less concentrated gel with a low enough viscosity for being printed. However, gels fabricated with high-molecular PEO (Mw = 8 MDa) have proven too viscous to be processed at reasonable concentrations, even down to 5 mg/ml. We hence proceeded to prepare PEO gels with lower average chain length (Mw = 1 MDa), yielding more fluid solutions of sufficiently low viscosity at 30 mg/ml. The durability of the gels has been assessed optically as in the previous cases. Out of all the prepared gels, the three most promising candidates were P_{1M}30-Alli-01521 (0.1 M $AlCl_3$, 0.05 M $LiClO_4$), P_{1M}30-Alli-01532 (0.09 M $AlCl_3$, 0.06 M $LiClO_4$) and P_{1M}30-ACG-0231 (0.15 M $AlCl_3$, 0.05 M GndCl). The P_{1M}30-ACG-0231 gel has proven the most durable in comparison to the $LiClO_4$ doped counterparts, as shown in Figure 6-14 a, b), whereas both types of doping were on par in analogous gels with 8 MDa PEO. We assume that in the case of lower molecular, 1 MDa PEO, the overall hygroscopicity of the dopant ensemble becomes less critical because the chains become easier to hydrate, while the benefit of the strong chaotropic character of the guanidinium cation becomes more significant and comes into effect more.

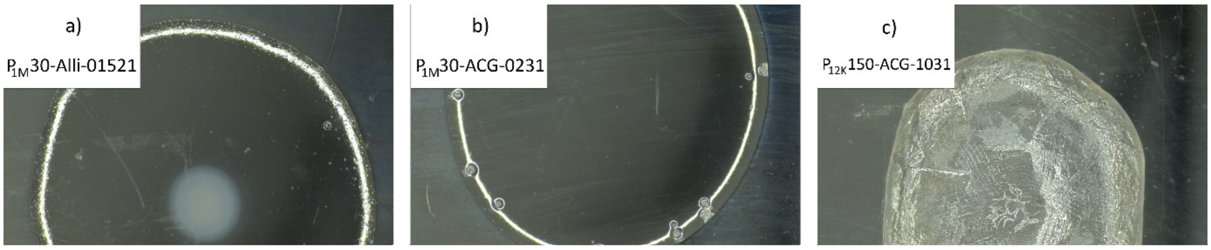

Figure 6-14: Photographs of lower molecular PEO gels with Mw = 1 MDa, 6 h after deposition. a) Gel P1M30-Alli-01521 (30 mg/ml PEO, 0.1 M AlCl3, 0.05 M LiClO4) with incipient drying in the centre of the cast drop. b) Gel P1M30-ACG-0231 (30 mg/ml PEO, 0.15 M AlCl3, 0.05 M GndCl). The aggregates on the perimeter did not grow considerably over time. c) An even lower molecular PEO gel with Mw = 12.5 kDa after drying at 40 °C. The crystallized PEO could not be regenerated in a humid atmosphere or by directly adding water to the system.

Despite the low viscosity of the gel, the atomization of the SPE ink could not be achieved and hence it could not be used in the AJP. This is likely due to the still very high mean molecular weight of PEO chains, which prevents them from effectively entering the aerosol created by the ultrasonic atomizer. On the other hand, further lowering of the molecular weight of PEO also was unsuccessful as the prepared gels of comparable concentrations (30−150 mg/ml) did not solidify even overnight, potentially making it unsuitable for the deposition at room temperature. Assisting the water evaporation through mild heating at 40 °C resulted in rapid and irreversible drying out of the samples, as shown in Figure 6-14 c). It appears that the system becomes less effective at containing humidity with decreasing PEO Mw, while the interactions between the shorter PEO chains are too strong to invert the formation of aggregates by increasing the humidity.

While the application of P_{1M} gels was unsuccessful by means of AJP, it is possible that printing could succeed with the otherwise less advanced IJP technique, thanks to its more straightforward mechanism of the formation of the ink jet that requires no provisional atomization of the material. Issues might arise from the need to heat the deposition plate for a better deposition and definition of printed features, regarding the temperature and humidity sensitivity of the SPE system. This does not concern the deposition process of the PEO gel itself, since in this case, the heating of the plate in particular and the precision of printing in general is not required, since it is applied as a bulk and only serves to provide the medium for the electrochemical reactions between the channel and the gate. Much rather, it is the last manufacturing step, being the deposition of CPA in a bottom-contact/bottom-gate geometry, which is most likely to cause drying out and crystallization of PEO. However, it has been shown in section 4.2.3.4 that gels based on guanidine chloride can be quickly regenerated in a humid atmosphere after drying, making P_{1M}30-ACG-0231 it a promising candidate for future attempts of printing with IJP.

6.3.2 Silk fibroin-based hydrogels for AJP

The difficulties with the implementation of PEO gels with AJP prompt the search for new polyelectrolyte materials for OMDs. Given that the SPE is the most labile part of the device and most prone to degradation, stable, biocompatible materials become even more desirable to be implemented alongside PEO. The first steps in this direction were made by Cifarelli *et al.* who implemented hydrogels of polysaccharide biopolymers [239] such as chitosan [237] and pectin doped with $CaCl_2$ [240] to replace polyethylene oxide. Devices with both polymers displayed memristive behaviour analogous to that of standard, PEO-based ones, albeit with slower kinetics and worse long- and short-term stability. Having proven the concept of applying biopolymers to OMD technology, these pioneering works pave the way towards more biocompatible systems. Considering the reported density and viscosity of the utilized gels, it seems unlikely that they could be compatible with DW printing technologies. With this in mind, we proceeded by developing Cifarelli's approach towards potentially printable systems, shifting our focus towards the biopolymer fibroin

6.3.2.1 Structure and applications of silk fibroin

Fibroin is one of the two silk proteins along with sericin, produced, among others, by the larvae of the domestic silk moth *Bombyx mori*. The general structure of a silk fibre is reported in Figure 6-15 a, b). It consists of two strands of fibroin surrounded by a glue-like coating of sericin, and this fibre structure is further covered by a shell consisting of other proteins. The fibroin itself is composed of three different types of protein structures: the hydrophobic, heavy H-chains (ca. 350 kDa), providing crystalline moieties that are responsible for the high tensile strength of the material; the hydrophilic, light L-chains (ca. 25 kDa), giving the material its elasticity; and a glycoprotein P25 (ca. 30 kDa), mostly responsible for the integrity of the complex structure. The molar ratio of these structures is ca. 6:6:1 [176]. H-and L-chain structures are interconnected via disulfide bonds while the P25 structure partakes in hydrophobic non-covalent interactions. The origin of the crystalline

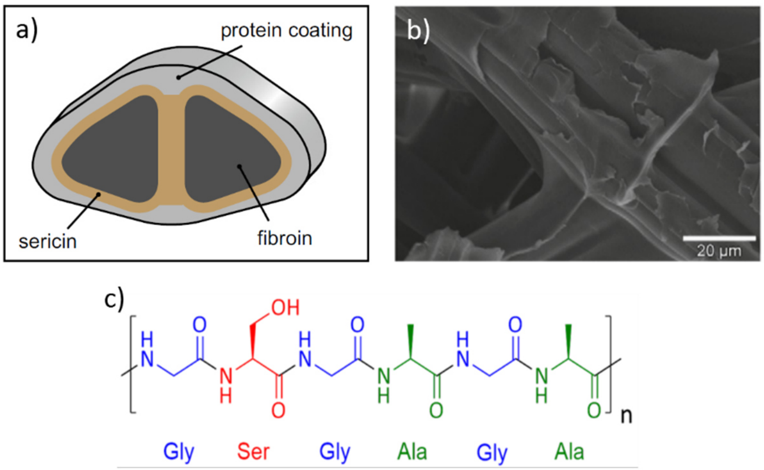

Figure 6-15: a) Schematic representation and b) SEM image of a silk fibre produced by the larvae of *Bombyx mori* [176]. c) The repetitive amino acid sequence of the hydrophobic subdomains of the H-chain structure of silk fibroin.

structures in native fibroin lies within the composition of the H-chains. A H-chain consists of 12 regular, hydrophobic subdomains with a repetitive amino acid sequence (Figure 6-15 c), alternated by 11 hydrophilic subdomains with an unregular amino acid sequence [241]. Such an arrangement allows for the formation of β-sheet structures through an interplay of intramolecular interactions.

Processing of fibroin in form of solutions is made possible by extraction and was first demonstrated by Rockwood *et al.* [242]. The procedure is schematically represented in **Figure 6-16.** It begins with boiling of cut-up cocoons in soda which leads to the so-called degumming by denaturing and removing the fibre shell as well as the sericin surrounding the two fibroin strands. In the next step, the silk fibroin (SF) is solubilized by incubating in concentrated LiBr, followed by dialysis against ultrapure water to remove the salt from the solution. After undergoing a transformation during this extraction process, the fibroin in the resulting solution is present in the Silk I form. It is characterized by a lower degree of crystallinity with a reduced number of β-sheet domains in favour of α-helix and random coil structures. The fibroin solution obtained by extraction is stored at 4 °C to prevent premature gelation and can be used to produce films [243],[244], microspheres [245],[246], nanomats [244], sponges [247],[248] or hydrogels [249]. The latter are especially relevant for our research field since hydrogels can likely be adopted as SPE.

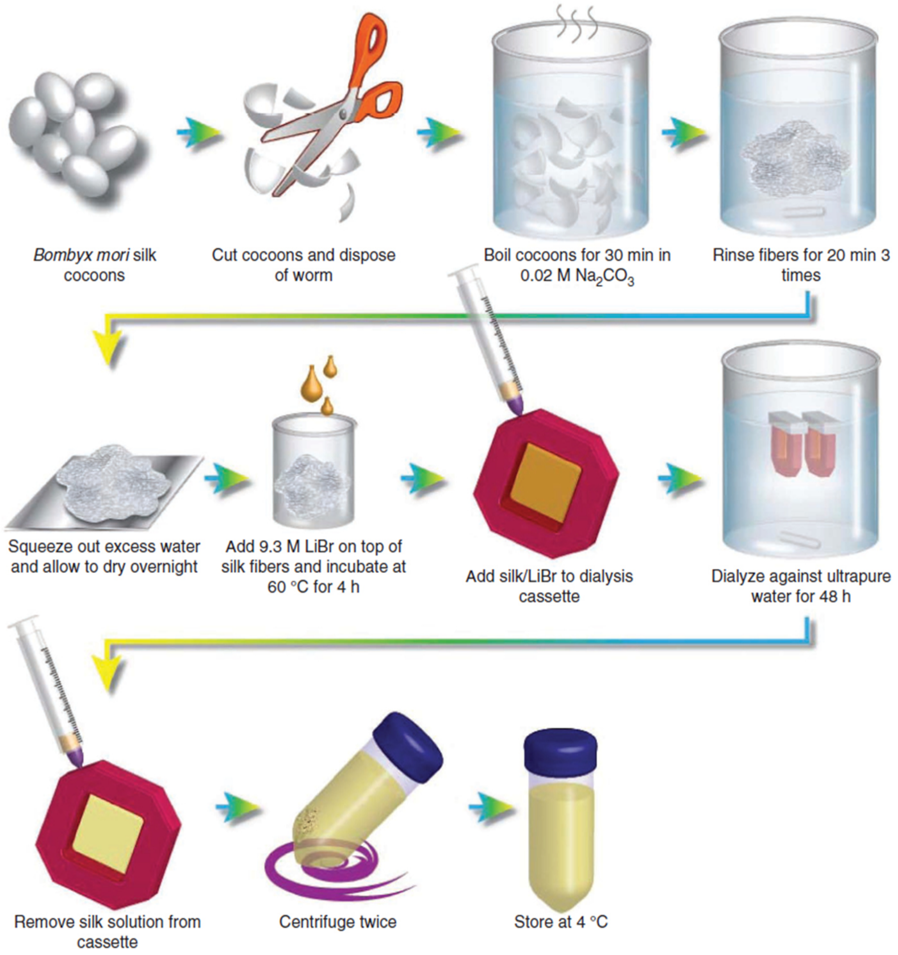

Figure 6-16: Schematic representation of the extraction process of fibroin from Bombyx mori cocoons, including degumming, solubilization and dialysis steps [242].

In many applications, the regeneration of a β-sheet-rich structure (Silk II) is desirable to regain the mechanical properties of fibroin, which can be achieved by thermal or chemical treatment of the polymer, e. g. with methanol. In our case, for the implementation in polyelectrolytes, the prevalence of the less ordered α-helix and random coil structures is actually beneficial because an amorphous structure of the SPE facilitates the diffusion and migration of ions. Electronic devices featuring SF as a dielectric have been fabricated in the past [250]. Most importantly, AJP has successfully been applied to print SF [251], whereby the influence of the degree of degumming is discussed in relationship to such undesired effects as pooling or gelation. However, these effects seem not to be as critical when implementing AJP-compatible SPEs since an especially precise definition of the printed features is not required.

6.3.2.2 Silk fibroin as a polyelectrolyte

Silk fibroin solutions have been prepared following the procedure by Seo *et al.* [252], where the dissolution of degummed SF is carried out in HCOOH with $CaCl_2$, with varying contents of $CaCl_2$. This modification of the original procedure by Rockwood aims at affecting the structure of the protein such that the interactions with Ca^{2+} ions increase the flowability, cohesion and energy dissipation of the solution, which are all beneficial properties for a polyelectrolyte material to be employed in DW techniques. Two samples, one with 10 % and one with 20 % (w/w) $CaCl_2$ were first analysed under the microscope. The micrographs in Figure 6-17 show the differences in the morphologies of the two solutions, whereby the one containing 20 % $CaCl_2$ appears homogeneous while the one with 10 % $CaCl_2$ contains fibrous filaments.

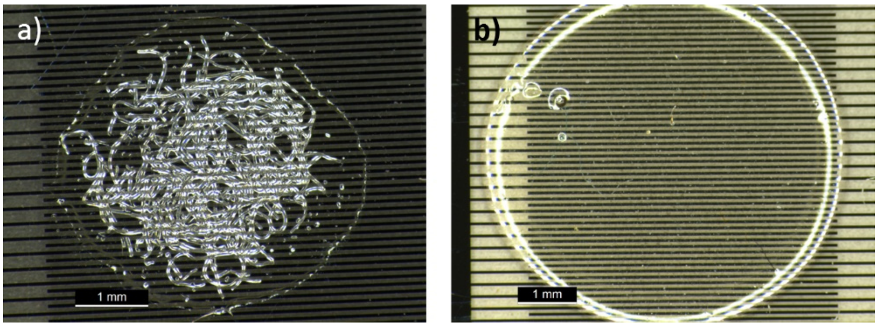

Figure 6-17: Photographs of a cast drop of a fibroin extract containing a) 10 % and b) 20 % (w/w) $CaCl_2$.

Nevertheless, devices fabricated with both solutions displayed memristive characteristics after their solidification, as it can be seen in Figure 6-18. The gels perform quite well in comparison to the former standard OMDs based on PEO doped with $LiClO_4$ and HCl, both in terms of output characteristics and kinetics. The on/off-ratio was ≥ 3 orders of magnitude. The 20 % $CaCl_2$ solution allows I-V characterizations with dwell times of 15 s per 0.1 V, which is approaching the speeds achieved with the modified PEO gels from section 4.2 (routinely measured at 0.1 V/10 s, with the fastest samples functioning at 0.1 V/2 s). Besides, the 20 % $CaCl_2$ SF SPE displayed a remarkable long-term stability while exposed to dry, warm ambient conditions (up to 35 °C) over three months. The device remained functional, even though the decreased current output and the slower kinetics bring to the conclusion that the quality of the gel deteriorated over time, given that the system is dependent on humidity like its PEO-based counterpart.

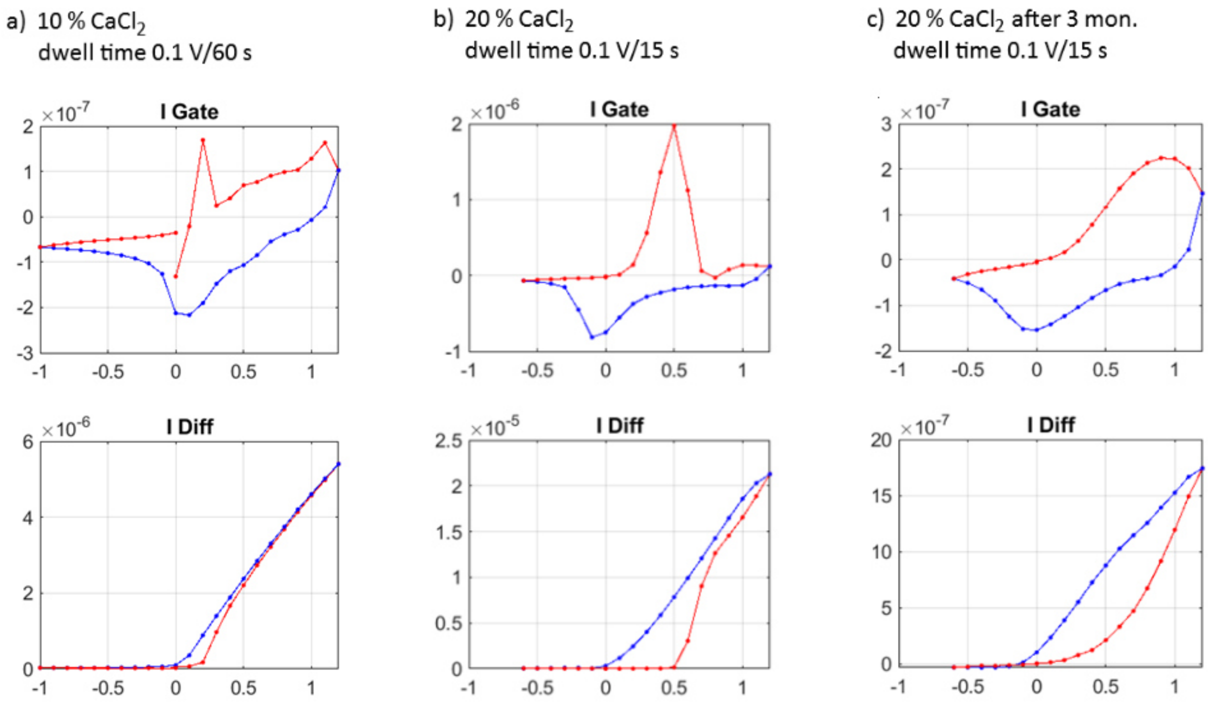

Figure 6-18: I-V characteristics of OMDs fabricated with silk fibroin solutions with a) 10 % (w/w) CaCl2, measured with 60 s dwell time per 0.1 V step; b) 20 % CaCl2, measured with 15 s dwell time per 0.1 V step; c) the same device from (b) measured after three months in warm ambient conditions.

These results prove the concept of SF solutions or hydrogels as viable materials for biocompatible SPEs. The quality of the fabricated gels, their short- and long-term stability and their consistencies allow to assume their applicability in AJP, making SF the prime candidate to be implemented in automated manufacturing of fully printed Organic memristive Devices.

Conclusions and outlook

With a focus on implementing Organic Memristive Devices in sensing and computing systems, the present research work initiates by continuing the ongoing research of the effects of noise on OMD switching. The results reveal some difficulties in the interpretation of data obtained on standard, SPE-based devices due to the reliability of the devices themselves. In fact, a comparison with literature data devoted to analogous biological systems suggests that such effects are quite sensitive to the reproducibility of the output data and their study requires more robust and reliable systems.

Thus, we proceeded by consequently optimizing the OMD in order to achieve a level of stability that would allow to carry out such refined and sensitive experiments. Having identified the solid polyelectrolyte as the system's most labile component, we focused on improving its performance and long-term stability by changing its dopant composition. In the process, we have shown that the former understanding of the contribution and role of the individual cationic and anionic dopant additives was not adequate and possibly erroneous. We hence initiated and carefully carried out an extensive study of the role of lithium ions in OMD operation. In fact, while the formerly proposed mechanism postulates an involvement of lithium ions in the transition of PANI between its isolating and conductive states, our results demonstrate that they do not actively participate in the switching process.

This acquired knowledge prompted the extensive exploration of a series of new dopant salts to replace or complement the formerly used lithium perchlorate. One such additive, aluminium chloride, has opened new horizons in terms of device stability as its intrinsic acidic character allowed to omit the step of HCl doping of PEO during OMD fabrication. Thus, solving one of the major doping issues, we could significantly improve the short-term and long-term output reproducibility of the device. In further steps towards SPE optimization, the concept of lyotropicity was introduced to OMD fabrication technology, providing a more profound understanding of the dopant properties affecting the morphology of the polyelectrolyte. We then implemented multiply doped PEO hydrogels containing salts such as aluminium chloride and lithium perchlorate or guanidinium chloride. This approach resulted in an unprecedented OMD endurance that allowed to extend the series of reproducible characterization to over 3000 consecutive cycles, corresponding to a full week of continuous measurements.

Our work further confirmed an undesired dependence of the SPE's structure on environmental conditions that affect the quality of measurements and hampering eventual OMD applications. To mitigate this issue, we proceeded by making the first attempts to seal the OMD by coating it with a protective layer of NEA 121. This likewise resulted in an increase of overall device stability by excluding the detrimental effects of oxygen or dry atmosphere. A combination of both approaches as well as further research of advanced dopant candidates has great potential to further increase the device stability. In particular, our preliminary tests with TSA have shown that hydrotropes such as organic sulfonic acids are able to imbue the SPE with a remarkable, unprecedented thermal stability.

Further developments in the direction of device optimization were based on a study of kinetic effects in OMD operation. To provide a summary as a reference point for further research, we compiled known effects such as the voltage distribution across the conductive channel, as well as other aspects that we found to be somewhat underemphasized in earlier works. Specifically, we turned our attention to some effects of the device geometry and the resulting relationship between the electrode potential and the applied bias. Furthermore, an experimental study was carried out, dedicated to the optical on-line observation of the switching process of PANI in the active zone, revealing that dedoping of the PANI-ES channel may occur due to the applied electric field at high enough biases.

Proceeding with the improvement of the OMD towards its implementation in systems interfacing sensing, computing, and biological systems, we focused on miniaturization as a prerequisite for high-performance, fast switching devices. To this end, the Langmuir-Schaefer technique was rather impractical because of its intrinsic limitations. Furthermore, we sought to introduce a rapid prototyping approach that would make the research development faster and more effective. We chose the direct-writing (DW) Aerosol Jet Printing (AJP) technique to experiment with the printing of the conductive layer of the OMD. To this end, we designed inks based on pristine PANI-EB in the solvent system NMP/xylene/IPA, achieving well-defined printed features with line widths resolved down to 160 μm. With a fully functional, printed PANI layer, the first-ever PANI-based OMD with a printed conductive layer was fabricated and successfully characterized. The consistency of printing and the coverage of the substrate was substantially increased with a new ink based on a water-dispersible chitosan:PANI (CPA) composite material. An OMD with a printed CPA layer displayed excellent, reproducible memristive characteristics. We envisage that the kinetics of the device can be largely improved by optimizing the ink composition and printing parameters towards a flatter layer profile, reducing the bulk properties of the conductive channel. Moreover, the prognose that the implementation of DW techniques will enable the realization of a bottom-contact/bottom-gate (as opposed to the current bottom-contact/top-gate) geometry of the device. We expect such a modification to further improve the switching kinetics down to the sub-second scale.

With the implementation of the AJP technology, we propose to focus future research on the DW deposition of the solid polyelectrolyte as the last component that is yet to be applied in an automated manner. First steps in this direction have been taken in this work by successfully applying silk fibroin solutions, replacing PEO hydrogels as a biocompatible alternative for an SPE. Consequently, an interim goal should be the realization of a 100 % printed OMD, including the electrodes, the conductive channel and the SPE. The implementation of such a technology would open new horizons for the integration of OMDs in electronic circuitry, interconnecting them with sensors, OECTs or biological cells. Such sophisticated systems could potentially allow not only the study of abovementioned noise-related and other effects, but also make advances in the biotechnological, biomedical, computer science, neuroscience and robotics fields.

In conclusion, with our research work we believe we achieved important, fundamental steps in this direction by developing materials and method of fabrications that allow to produce much better performing, more stable, reliable and reproducible OMDs with materials that make the interfacing with the bio-world viable.

Bibliography

[1] Y. Li, Z. Wang, R. Midya, Q. Xia, J. J. Yang. “Review of memristor devices in neuromorphic computing: materials science and device challenges.” *J. Phys. D: Appl. Phys. 51*, 503002 (2019).

[2] D. O. Hebb. *“The Organization of Behavior: A Neuropsychological Theory.”* (Wiley, 1949).

[3] N. Rochester, J. H. Holland, L. H. Haibt, W. L. Duda. “Tests on a cell assembly theory of the action of the brain, using a large digital computer.” *IRE Trans. Inform. Theor. 2*, 80–93 (1956).

[4] F. Rosenblatt. “The perceptron: A probabilistic model for information storage and organization in the brain.” *Physiolog. Rev. 65*, 386–408 (1958).

[5] B. Widrow, W. H. Pierce, J. B. Angell. “Birth, life, and death in microelectronic systems.” *IRE Trans. Mil. Electron. MIL–5*, 191–201 (1961).

[6] L. O. Chua. “Memristor − The missing circuit element.” *IEEE Trans. Circuit Theor. 18*, 507–519 (1971).

[7] D. B. Strukov, G. S. Snider, D. R. Stewart, R. S. Williams. “The missing memristor found.” *Nature Lett. 453*, 80–84 (2008).

[8] A. Asamitsu, Y. Tomioka, H. Kuwahara, Y. Tokura. “Current switching of resistive states in magnetoresistive manganites.” *Nature 388*, 50–52 (1997).

[9] H. Pagnia, N. Sotnik. “Bistable switching in electroformed metal–insulator–metal devices.” *Phys. Status Solidi A 108*, 11–65 (1988).

[10] Y. B. Nian, J. Strozier, N. J. Wu, X. Chen, A. Ignatiev. “Evidence for an oxygen diffusion model for the electric pulse induced resistance change effect in transition-metal oxides.” *Phys. Rev. Lett. 98*, 146403 (2007) (2007).

[11] S. Q. Liu, N. J. Wu, A. Ignatiev. “Electric-pulse-induced reversible resistance change effect in magnetoresistive films.” *Appl. Phys. Lett. 76*, 2749–2751 (2000).

[12] A. Beck, J. G. Bednorz, C. Gerber, C. Rossel, D. Widmer. “Reproducible switching effect in thin oxide films for memory applications.” *Appl. Phys. Lett. 77*, 139–141 (2000).

[13] V. Erokhin, T. Berzina, M. P. Fontana. “Hybrid electronic device based on polyaniline-polyethyleneoxide junction.” *J. Appl. Phys. 97*, 064501 (2005).

[14] J. Yao, Z. Sun, L. Zhong, D. Natelson, J. M. Tour. “Resistive switches and memories from silicon oxide.” *Nano Lett. 10*, 4105–4110 (2010).

[15] A. Mehonic, S. Cueff, M. Wojdak, S. Hudziak, O. Jambois, C. Labbé, B. Garrido, R. Rizk, A. J. Kenyon. “Resistive switching in silicon suboxide films.” *J. Appl. Phys. 111*, 074507 (2012).

[16] J. W. Han, M. Meyyappan. “Copper oxide resistive switching memory for e-textile.” *AIP Adv. 1*, 032162 (2011).

[17] L. Alekseeva, T. Nabatame, T. Chikyow, A. Petrov. “Resistive switching characteristics in memristors with Al2O3/TiO2 and TiO2/Al2O3 bilayers.” *Jap. J. Appl. Phys. 55*, 08PB02 (2016).

[18] Y. E. Syu, T. C. Chang, J. H. Lou, T. M. Tsai, K. C. Chang, M. J. Tsai, Y. L. Wang, M. Liu, S. M. Sze. “Atomic-level quantized reaction of HfOx memristor.” *Appl. Phys. Lett. 102*, 172903 (2013).

[19] J. Sun, E. Lind, I. Maximov, H. Q. Xu. “Memristive and memcapacitive characteristics of a Au/Ti-HfO 2-InP/InGaAs diode.” *IEEE Electron. Device Lett. 32*, 131–133 (2011).

[20] W. Gee Kim *et al.* “Dependence of the switching characteristics of Resistance Random Access Memory on the type of transition metal oxide; TiO2, ZrO2, and HfO2.” *J. Electrochem. Soc. 158*, H417–H422 (2011).

[21] A. Prakash, D. Jana, S. Maikap. “TaOx-based resistive switching memories: Prospective and challenges.” *Nanoscale Res. Lett. 8*, 418 (2013).

[22] X. Cao, X. Li, X. Gao, W. Yu, X. Liu, Y. Zhang, L. Chen, X. Cheng. “Forming-free colossal resistive switching effect in rare-earth-oxide Gd2 O3 films for memristor applications.” *Journal of Applied Physics 106*, (2009).

[23] A. Younis, D. Chu, S. Li. “Oxygen level: The dominant of resistive switching characteristics in cerium oxide thin films.” *J. Phys. D Appl. Phys. 45*, 355101 (2012).

[24] A. Kumar, Y. Rawal, M. S. Baghini. “Fabrication and characterization of the ZnO-based memristor.” *International Conference on Emerging Electronics 2012, Proceedings* 4–6 (2012) doi:10.1109/ICEmElec.2012.6636244.

[25] F. M. Simanjuntak, D. Panda, K. H. Wei, T. Y. Tseng. “Status and prospects of ZnO-based resistive switching memory devices.” *Nanoscale Res. Lett. 11*, 368 (2016).

[26] G. Milano, L. Boarino, C. Ricciardi. “Junction properties of single ZnO nanowires with asymmetrical Pt and Cu contacts.” *Nanotechnology 30*, 244001 (2019).

[27] V. Jousseaume *et al.* “Back-end-of-line integration approaches for resistive memories.” *IEEE International Interconnect Technology Conference Proceedings* 41–43 (2009) doi:10.1109/IITC.2009.5090335.

[28] Q. Wang *et al.* “Reliable Ge2Sb2Te5 based phase-change electronic synapses using carbon doping and programmed pulses.” *J. Materiomics in press*, (2021).

[29] S. I. Oh, I. H. Im, C. Yoo, S. Y. Ryu, Y. Kim, S. Choi, T. Eom, C. S. Hwang, B. J. Choi. “Effect of electrode material on the crystallization of GeTe grown by atomic layer deposition for phase change random access memory.” *Micromachines (Basel) 10*, 281 (2019).

[30] D. Ielmini, A. L. Lacaita. “Phase change materials in non-volatile storage.” *Mater. Today 14*, 600–607 (2011).

[31] G. Betti Beneventi *et al.* “Carbon-doped GeTe: A promising material for Phase-Change Memories.” *Solid-State Electron. 65–66*, 197–204 (2011).

[32] B. S. Lee, R. M. Shelby, S. Raoux, C. T. Retter, G. W. Burr, S. N. Bogle, K. Darmawikarta, S. G. Bishop, J. R. Abelson. "Nanoscale nuclei in phase change materials: Origin of different crystallization mechanisms of Ge2Sb2Te5 and AgInSbTe." *J. Appl. Phys. 115*, 063506 (2014).

[33] G. Liu, Y. Chen, C. Wang, W. Zhang, R.-W. Li, L. Wang. "Polymer memristor for information storage and neuromorphic applications." *Mater. Horiz. 1*, 489–506 (2014).

[34] L. Yuan, S. Liu, W. Chen, F. Fan, G. Liu. "Organic memory and memristors: from mechanisms, materials to devices." *Adv. Electron. Mater. 7*, 2100432 (2021).

[35] T. Zhang *et al.* "Negative differential resistance, memory, and reconfigurable logic functions based on monolayer devices derived from Gold nanoparticles functionalized with electropolymerizable TEDOT units." *J. Phys. Chem. C 121*, 10131–10139 (2017).

[36] S. Goswami *et al.* "Robust resistive memory devices using solution-processable metal-coordinated azo aromatics." *Nature Mater. 16*, 1216–1224 (2017).

[37] G. Zhou, Z. Ren, L. Wang, B. Sun, S. Duan, Q. Song. "Artificial and wearable albumen protein memristor arrays with integrated memory logic gate functionality." *Mater. Horiz. 6*, 1877–1882 (2019).

[38] R. Kumar, R. G. Pillai, N. Pekas, Y. Wu, R. L. McCreery. "Spatially resolved Raman spectroelectrochemistry of solid-state polythiophene/viologen memory devices." *J. Am. Chem. Soc. 134*, 14869–14876 (2012).

[39] J. Q. Yang *et al.* "Fluorenone/carbazole based bipolar small molecules for non-volatile memory devices." *Org. Electron. 78*, 105584 (2020).

[40] A. A. Minnekhanov, A. v. Emelyanov, D. A. Lapkin, K. E. Nikiruy, B. S. Shvetsov, A. A. Nesmelov, V. v. Rylkov, V. A. Demin, V. v. Erokhin. "Parylene based memristive devices with multilevel resistive switching for neuromorphic applications." *Sci. Rep. 9*, 10800 (2019).

[41] A. N. Matsukatova *et al.* "Resistive switching kinetics and second-order effects in parylene-based memristors." *Appl. Phys. Lett. 117*, (2020).

[42] A. N. Matsukatova, A. A. Minnekhanov, V. v. Rylkov, V. A. Demin, A. v. Emelyanov. "Resistive switching kinetics of parylene-based memristive devices with Cu active electrodes." *J. Phys. Conf. Series 1758*, 012025 (2021).

[43] N. Raeis Hosseini, J. S. Lee. "Resistive switching memory based on bioinspired natural solid polymer electrolytes." *ACS Nano 9*, 419–426 (2015).

[44] M. K. Hota, M. K. Bera, B. Kundu, S. C. Kundu, C. K. Maiti. "A natural silk fibroin protein-based transparent bio-memristor." *Adv. Funct. Mater. 22*, 4493–4499 (2012).

[45] M. K. Ram, M. Adami, M. Sartore, M. Salerno, S. Paddeu, C. Nicolini. "Comparative studies on Langmuir-Schaefer films of polyanilines." *Synth. Met. 100*, 249–259 (1999).

[46] R. C. Sanfelice, D. T. Balogh, F. Lederle, J. Adams, S. Beuermann. “Studies of Langmuir and Langmuir-Schaefer Films of Poly(3-Hexylthiophene) and Poly(Vinylidene Fluoride).” *J. Phys. Chem. B 124*, 7037–7045 (2020).

[47] M. Navarro, J. Benito, L. Paseta, I. Gascón, J. Coronas, C. Téllez. “Thin-Film Nanocomposite Membrane with the Minimum Amount of MOF by the Langmuir-Schaefer Technique for Nanofiltration.” *ACS Appl. Mater. Interfaces 10*, 1278–1287 (2018).

[48] R. Y. N. Gengler, A. Veligura, A. Enotiadis, E. K. Diamanti, D. Gournis, C. Józsa, B. J. van Wees, P. Rudolf. “Large-yield preparation of high-electronic-quality graphene by a Langmuir-Schaefer approach.” *Small 6*, 35–39 (2010).

[49] Z. U. Khan, A. Kausar, H. Ullah, A. Badshah, W. U. Khan. “A review of graphene oxide, graphene buckypaper, and polymer/graphene composites: properties and fabrication techniques.” *J. Plast. Film Sheet. 32*, 336–379 (2016).

[50] A. v. Kazak, M. A. Marchenkova, K. S. Khorkov, D. A. Kochuev, A. v. Rogachev, I. v. Kholodkov, N. v. Usol’tseva, M. S. Savelyev, A. Y. Tolbin. “Ultrathin Langmuir–Schaefer films of slipped-cofacial J-type phthalocyanine dimer: Supramolecular organization, UV/Vis/NIR study and nonlinear absorbance of femtosecond laser radiation.” *Appl. Surf. Sci. 545*, 148993 (2021).

[51] J. Stanley, Y. Dai, L. Boucheron, B. Lin, M. Meron, O. Shpyrko. “Novel comparison of microscopy and diffraction techniques on the structure of iron oxide nanoparticle monolayers transferred by Langmuir-Schaefer method.” *Rev. Sci. Instrum. 86*, 063704 (2015).

[52] S. Erokhina, V. Sorokin, V. Erokhin. “Polyaniline-based organic memristive device fabricated by layer-by-layer deposition technique.” *Electron. Mater. Lett. 11*, 801–805 (2015).

[53] A. G. Green, A. E. Woodhead. “Aniline-black and allied compounds. Part I.” *J. Chem. Soc. 97*, 2388–2403 (1910).

[54] A. G. Green, A. E. Woodhead. “Aniline-black and allied compounds. Part II.” *J. Chem. Soc. 101*, 1117–1123 (1912).

[55] E. T. Kang, K. G. Neoh, K. L. Tan. “Polyaniline: a polymer with many interesting intrinsic redox states.” *Prog. Polym. Sci 23*, 277–324 (1998).

[56] J. G. Masters, Y. Sun, A. G. Macdiarmid, A. J. Epstein. “Polyaniline: allowed oxidation states.” *Synth. Met. 41*, 715–718 (1991).

[57] J. G. Masters, J. M. Ginder, A. G. MacDiarmid, A. J. Epstein. “Thermochromism in the insulating forms of polyaniline: Role of ring-torsional conformation.” *J. Chem. Phys. 96*, 4768–4778 (1992).

[58] T. Fukuda, H. Takezoe, K. Ishikawa, A. Fukuda, H. S. Woo, S. K. Jeong, J. Oh, J. S. Suh. “IR and Raman studies in three polyanilines with different oxidation levels.” *Synth. Met. 69*, 175–176 (1995).

[59] L. Brožová, P. Holler, J. Kovářová, J. Stejskal, M. Trchová. “The stability of polyaniline in strongly alkaline or acidic aqueous media.” *Polym. Degrad. Stab. 93*, 592–600 (2008).

[60] G. E. Asturias, A. G. Macdiarmid, R. P. Mccall, A. J. Epstein. “The oxidation state of ‘emeraldine’ base.” *Synth. Met. 29*, E157–E162 (1989).

[61] K. Stejskal, R. G. Gilbert. “Polyaniline. preparation of a conducting polymer (IUPAC Technical Report).” *Pure Appl. Chem 74*, 857–867 (2002).

[62] F. Lux. “Properties of electronically conductive polyaniline: a comparison between well-known literature data and some recent experimental findings.” *Polymer (Guildf) 35*, 2915–2936 (1994).

[63] J. Stejskal, P. Kratochvil, A. D. Jenkins. “The formation of polyaniline and the nature of its structures.” *Polymer (Guildf) 37*, 367–369 (1996).

[64] J. W. Jeon, Y. Ma, J. F. Mike, L. Shao, P. B. Balbuena, J. L. Lutkenhaus. “Oxidatively stable polyaniline:polyacid electrodes for electrochemical energy storage.” *Phys. Chem. Chem. Phys. 15*, 9654–9662 (2013).

[65] G. D’Aprano, M. Leclerc, G. Zotti. “Stabilization and characterization of pernigraniline salt: the ‘acid-doped’ form of fully oxidized polyanilines.” *Macromol. 25*, 2145–2150 (1992).

[66] W. Lu, A. G. Fadeev, B. Qi, B. R. Mattes. “Fabricating conducting polymer electrochromic devices using ionic liquids.” *J. Electrochem. Soc. 151*, H33–H39 (2004).

[67] F. F. C. Bazito, L. T. Silveira, R. M. Torresi, S. I. Córdoba de Torresi. “On the stabilization of conducting pernigraniline salt by the synthesis and oxidation of polyaniline in hydrophobic ionic liquids.” *Phys. Chem. Chem. Phys. 10*, 1457–1462 (2008).

[68] A. Ray, A. F. Richter, A. G. Macdiarmid, A. J. Epstein. “Polyaniline: protonation/deprotonation of amine and imine sites.” *Synth. Met. 29*, E151–E156 (1989).

[69] E. T. Kang, K. G. Neoh, K. L. Tan, B. T. G. Tan. “Protonation of the amine nitrogens in emeraldine-evidence from X-ray photoelectron spectroscopy.” *Synth. Met. 46*, 227–233 (1992).

[70] P. Snauwaert, R. Lazzaroni, J. Riga, J. J. Verbist, D. Gonbeau. “A photoelectron spectroscopic study of the electrochemical processes in polyaniline.” *J. Chem. Phys. 92*, 2187–2193 (1990).

[71] K. G. Neoh, E. T. Kang, K. L. Tan. “Protonation of leucoemeraldine in the solid state and in solution.” *J. Polym. Sci. B Polym. Phys. 31*, 395–401 (1993).

[72] S. Stafström, J. L. Brédas, A. J. Epstein, H. S. Woo, D. B. Tanner, W. S. Huang, A. G. MacDiarmid. “Polaron lattice in highly conducting polyaniline: theoretical and optical studies.” *Phys. Rev. Lett. 59*, 1464–1467 (1987).

[73] A. J. Epstein, J. M. Ginder, F. Zuo, R. W. Bigelow, H.-S. Woo, D. B. Tanner, A. F. Richter, W.-S. Huang, A. G. Macdiarmid. “Insulator-to-metal transition in polyaniline.” *Synth. Met. 18*, 303–309 (1987).

[74] A. J. Epstein, J. M. Ginder, F. Zuo, H.-S. Woo, D. B. Tanner, A. F. Richter, M. Angelopoulos, W.-S. Huang, A. G. Macdiarmid. "Insulator-to-metal transition in polyaniline: effect of protonation in emeraldine." *Synth. Met. 21*, 63–70 (1987).

[75] S. Kumar Gupta, V. Luthra, R. Singh. "Electrical transport and EPR investigations: a comparative study for d.c. conduction mechanism in monovalent and multivalent ions doped polyaniline." *Bull. Mater. Sci 35*, 787–794 (2012).

[76] M. B. Inoue, K. W. Nebesny, Q. Fernandoa, M. Lnoueb. "X-Ray photoelectron spectroscopy of new soluble polyaniline perchlorates: evidence for the coexistence of polarons and bipolarons." *J. Mater. Chem. 1*, 213–216 (1991).

[77] T. Hagiwara, T. Demura, K. Iwata. "Synthesis and properties of electrically conducting polymers from aromatic amines." *Synth. Met. 18*, 317–322 (1987).

[78] E. T. Kang, K. G. Neoh, S. H. Khor, K. L. Tan, B. T. G. Tan. "Structural determination of polyaniline by X-Ray photoelectron spectroscopy." *J. Chem. Soc. Chem. Commun.* 695–697 (1989).

[79] K. L. Tan, B. T. G. Tan, E. T. Kang, K. G. Neoh. "X-ray photoelectron spectroscopy studies of the chemical structure of polyaniline." *Phys. Rev. B 39*, 8070–8073 (1989).

[80] J. Yue, A. J. Epstein. "Synthesis of Self-Doped Conducting Polyaniline." *J. Am. Chem. Soc. 112*, 2800–2801 (1990).

[81] A. G. MacDiarmid, J. C. Chiang, A. F. Richter, A. J. Epstein. "Polyaniline: a new concept in conducting polymers." *Synth. Met. 18*, 285–290 (1987).

[82] W. W. Focke. "Conduction mechanisms in polyaniline." (1987).

[83] W. W. Focke, G. E. Wnek, Y. Wei. "Influence of oxidation state, pH, and counterion on the conductivity of polyaniline." *J. Phys.Chem. 91*, 5813–5818 (1987).

[84] G. B. Appetecchi, F. Alessandrini, M. Carewska, T. Caruso, P. P. Prosini, S. Scaccia, S. Passerini. "Investigation on lithium-polymer electrolyte batteries." *J. Power Sources 97*, 790–794 (2001).

[85] Z. Xue, D. He, X. Xie. "Poly(ethylene oxide)-based electrolytes for lithium-ion batteries." *J. Mater. Chem. A 3*, 19218–19253 (2015).

[86] S. Zhao, Q. Wu, W. Ma, L. Yang. "Polyethylene oxide-based composites as solid-state polymer electrolytes for lithium metal batteries: a mini review." *Front. Chem. 8*, 640 (2020).

[87] T. Berzina, V. Erokhin, M. P. Fontana. "Spectroscopic investigation of an electrochemically controlled conducting polymer-solid electrolyte junction." *J. Appl. Phys. 101*, 024501 (2007).

[88] T. Berzina, S. Erokhina, P. Camorani, O. Konovalov, V. Erokhin, M. P. Fontana. "Electrochemical control of the conductivity in an organic memristor: A time-resolved X-ray fluorescence study of ionic drift as a function of the applied voltage." *ACS Appl. Mater. Interfaces 1*, 2115–2118 (2009).

[89] V. Erokhin, T. Berzina, A. Smerieri, P. Camorani, S. Erokhina, M. P. Fontana. "Bio-inspired adaptive networks based on organic memristors." *Nano Commun. Netw. 1*, 108–117 (2010).

[90] E. M. Geniès, M. Lapkowski, J. F. Penneau. "Cyclic voltammetry of polyaniline: interpretation of the middle peak." *J. Electroanal. Chem 249*, 97–107 (1988).

[91] E. M. Geniès, M. Lapkowski. "Spectroelectrochemical evidence for an intermediate in the electropolymerization of aniline." *J. Electroanal. Chem 236*, 189–197 (1987).

[92] S. Pruneanu, E. Veress, I. Marian, L. Oniciu. "Characterization of polyaniline by cyclic voltammetry and UV-Vis absorption spectroscopy." *J. Mater. Sci. 34*, 2733–2739 (1999).

[93] A. Smerieri, V. Erokhin, M. P. Fontana. "Origin of current oscillations in a polymeric electrochemically controlled element." *J. Appl. Phys. 103*, 094517 (2008).

[94] V. A. Demin, V. v. Erokhin, P. K. Kashkarov, M. v. Kovalchuk. "Electrochemical model of the polyaniline based organic memristive device." *J. Appl. Phys. 116*, 064507 (2014).

[95] N. S. Sariciftci, H. Kuzmany, H. Neugebauer, A. Neckel. "Structural and electronic transitions in polyaniline: A Fourier transform infrared spectroscopic study." *J. Chem. Phys. 92*, 4530–4539 (1990).

[96] S. I. Zheludeva, M. v. Kovalchuk, S. Lagomarsino, N. N. Novikova, I. N. Bashelkhanov, V. v. Erokhin, L. A. Feigin. "Observation of evanescent and standing X-ray waves in region of total external reflection from molecular Langmuir-Blodgett films." *JEPT Lett. 52*, 170–175 (1990).

[97] S. H. Jo, T. Chang, I. Ebong, B. B. Bhadviya, P. Mazumder, W. Lu. "Nanoscale memristor device as synapse in neuromorphic systems." *Nano Lett. 10*, 1297–1301 (2010).

[98] L. Deng, G. Li, N. Deng, D. Wang, Z. Zhang, W. He, H. Li, J. Pei, L. Shi. "Complex learning in bio-plausible memristive networks." *Sci. Rep. 5*, 1–10 (2015).

[99] Z. Wang *et al.* "Memristors with diffusive dynamics as synaptic emulators for neuromorphic computing." *Nat. Mater. 16*, 101–108 (2017).

[100] S. Battistoni, V. Erokhin, S. Iannotta. "Frequency driven organic memristive devices for neuromorphic short term and long term plasticity." *Org. Electron. 65*, 434–438 (2019).

[101] A. Smerieri, T. Berzina, V. Erokhin, M. P. Fontana. "Polymeric electrochemical element for adaptive networks: Pulse mode." *J. Appl. Phys. 104*, 1–7 (2008).

[102] E. Juzekaeva, A. Nasretdinov, S. Battistoni, T. Berzina, S. Iannotta, R. Khazipov, V. Erokhin, M. Mukhtarov. "Coupling cortical neurons through electronic memristive synapse." *Adv. Mater. Technol. 4*, 1800350 (2019).

[103] A. v. Emelyanov *et al.* "First steps towards the realization of a double layer perceptron based on organic memristive devices." *AIP Advances 6*, 111301 (2016).

[104] S. Battistoni, V. Erokhin, S. Iannotta. "Organic memristive devices for perceptron applications." *J. Phys. D Appl. Phys. 51*, 284002 (2018).

[105] V. Erokhin, T. Berzina, P. Camorani, A. Smerieri, D. Vavoulis, J. Feng, M. P. Fontana. "Material memristive device circuits with synaptic plasticity: learning and memory." *Bionanoscience 1*, 24–30 (2011).

[106] M. Ziegler, R. Soni, T. Patelczyk, M. Ignatov, T. Bartsch, P. Meuffels, H. Kohlstedt. "An electronic version of Pavlov's Dog." *Adv. Funct. Mater. 22*, 2744–2749 (2012).

[107] G. B. Ermentrout, R. F. Galán, N. N. Urban. "Reliability, synchrony and noise." *Trends Neurosci. 31*, 428–434 (2008).

[108] J. D. Hunter, J. G. Milton, P. J. Thomas, J. D. Cowan. "Resonance effect for neural spike time reliability." *J. Neurophysiol. 80*, 1427–1438 (1998).

[109] K. Gorshkov, T. Berzina. "On the hysteresis loop of organic memristive device." *BioNanoSci. 1*, 198–201 (2011).

[110] S. Battistoni, R. Sajapin, V. Erokhin, A. Verna, M. Cocuzza, S. L. Marasso, S. Iannotta. "Effects of noise sourcing on organic memristive devices." *Chaos, Solitons Fractals 141*, 110319 (2020).

[111] D. A. Bernards, G. G. Malliaras. "Steady-state and transient behavior of organic electrochemical transistors." *Adv. Funct. Mater. 17*, 3538–3544 (2007).

[112] X. Strakosas, M. Bongo, R. M. Owens. "The organic electrochemical transistor for biological applications." *J. Appl. Polym. Sci. 132*, 41735 (2015).

[113] J. Rivnay, S. Inal, A. Salleo, R. M. Owens, M. Berggren, G. G. Malliaras. "Organic electrochemical transistors." *Nat. Rev. Mater. 3*, 17086 (2018).

[114] A. Cifarelli, T. Berzina, A. Parisini, S. Iannotta. "Memristive response and electrochemical processes in polyaniline based organic devices." *Org. Electron. 83*, 105757 (2020).

[115] D. Orata, D. A. Buttry. "Determination of ion populations and solvent content as functions of redox state and pH in polyaniline." *J. Am. Chem. Soc. 109*, 3574–3581 (1987).

[116] N. Agmon. "The Grotthuss mechanism." *Chemical Physics Letters 244*, 456–462 (1995).

[117] E. Ventosa, W. Schuhmann. "Scanning electrochemical microscopy of Li-ion batteries." *Phys. Chem. Chem. Phys. 17*, 28441–28450 (2015).

[118] H. Ha, J. Payer. "The effect of silver chloride formation on the kinetics of silver dissolution in chloride solution." *Electrochim. Acta 56*, 2781–2791 (2011).

[119] V. I. Birss, C. K. Smith. "The anodic behavior the formation and reduction thin silver chloride films." *Electrochim. Acta 32*, 259–268 (1987).

[120] S. Jaya, T. P. Rao, G. P. Rao. "Mono- and multilayer formation studies of silver iodide on silver electrode from iodide-containing solutions." *J. Appl. Electrochem. 17*, 997–1001 (1987).

[121] B. M. Jović, V. D. Jović, D. M. Dražić. "Kinetics of chloride ion adsorption and the mechanism of AgCl layer formation on the (111), (100) and (110) faces of silver." *J. Electroanal. Chem 399*, 197–206 (1995).

[122] P. Bro, N. Marincic. "The high rate oxidation of silver electrodes in chloride solutions." *J. Electrochem. Soc. 116*, 1338 (1969).

[123] C. Cachet, I. Epelboin, M. Keddam, R. Wiart. "The Ag/Ag+ system: an impedance model for nucleation and growth." *J. Electroanal. Chem 100*, 745–757 (1979).

[124] S. B. Aziz, T. J. Woo, M. F. Z. Kadir, H. M. Ahmed. "A conceptual review on polymer electrolytes and ion transport models." *J. Sci. Adv. Mater. Dev. 3*, 1–17 (2018).

[125] R. Sajapin, T. Berzina, R. Burganova, S. Iannotta. "New insight in the operation mechanism of organic memristive devices: The role of PEO-based polyelectrolyte solute ions." *Org. Electron. 94*, 106173 (2021).

[126] R. Burganova, A. Parisini, S. Vantaggio, R. Sajapin, T. Berzina. "The role of the polyelectrolyte composition in kinetic behaviour of organic memristive device." *Microelectron. Eng. 239–240*, 111527 (2021).

[127] S. H. Lee, J. C. Rasaiah. "Molecular dynamics simulation of ion mobility. 2. Alkali metal and halide ions using the SPC/E model for water at 25 °C." *J. Phys. Chem. 100*, 1420–1425 (1996).

[128] R. E. A. Dillon, D. F. Shriver. "Ion transport in cryptand and crown ether lithium salt complexes." *Chem. Mater. 11*, 3296–3301 (1999).

[129] M. L. Kaplan, E. A. Rietman, R. J. Cava, L. K. Holt, E. A. Chandross. "Crown ether enhancement of ionic conductivity in a polymer-salt system." *Solid State Ion. 25*, 37–40 (1987).

[130] M. Jóźwiak, L. Madej. "Complex formation of crown ethers and cations in water-organic solvent mixtures: The thermodynamic functions of complex formation of benzo-15-crown-5 with Na+ in water + ethanol at 298.15 K." *J. Chem. Eng. Data 55*, 1965–1970 (2010).

[131] L. C. Manege, T. Takayanagi, M. Oshima, S. Motomizu. "Ion association reactions in aqueous solutions between non-UV-absorbing crown ether-alkali metal complexes with picrate ion by capillary zone electrophoresis." *Analyst 125*, 1928–1932 (2000).

[132] M. Rashid, A. A. Rahim, M. J. Noordin. "Electropolymerization of p-toluene sulfonic acid doped polyaniline on copper and its application as a corrosion inhibitor." *Anti-Corros. Method. Mater. 58*, 131–139 (2011).

[133] M. Babazadeh. "Aqueous dispersions of DBSA-doped polyaniline: one-pot preparation, characterization, and properties study." *J. Appl. Polym. Sci. 113*, 3980–3984 (2009).

[134] L. F. Nims. "The second dissociation constant of phosphoric acid from 20 to 50°." *J. Am. Chem. Soc. 55*, 1946–1951 (1933).

[135] P. H. Barry, J. W. Lynch. "Liquid junction potentials and small cell effects in patch-clamp analysis." *J. Membrane Biol. 121*, 101–117 (1991).

[136] U. W. Grummt, A. Pron, M. Zagorska, S. Lefrant. "Polyaniline based optical pH sensor." *Anal. Chim. Acta 357*, 253–259 (1997).

[137] G. R. Silva, E. Y. Matsubara, P. Corio, J. M. Rosolen, M. Mulato. “Carbon felt/carbon nanotubes/pani as pH sensor.” *Mater. Res. Soc. Symposium Proceedings 1018*, 174–179 (2007).

[138] Y. Li, Y. Mao, C. Xiao, X. Xu, X. Li. “Flexible pH sensor based on a conductive PANI membrane for pH monitoring.” *RSC Adv. 10*, 21–28 (2019).

[139] J. Bjerrum, L. G. Sillén, G. K. Schwarzenbach, C. Berecki-Biedermann. *Stability constants of metal-ion complexes, with solubility products of inorganic substances. 2 : Inorganic ligands*. (The Chemical Society, 1958).

[140] E. P. Serjeant, Boyd. Dempsey. *Ionisation constants of organic acids in aqueous solution*. (Pergamon Press, 1979).

[141] M. J. O’Neil. *The Merck index: an encyclopedia of chemicals, drugs, and biologicals*.

[142] T. Arakawa, S. N. Timasheff. “Mechanism of protein salting in and salting out by divalent cation salts: balance between hydration and salt binding.” *Biochemistry 23*, 5912–5923 (1984).

[143] R. K. Scopes. *Protein purification: principles and practice*. (Springer Science & Business Media, 1993).

[144] K. C. Duong-Ly, S. B. Gabelli. *Salting out of proteins using ammonium sulfate precipitation. Methods in Enzymology* vol. 541 (Elsevier Inc., 2014).

[145] K. I. M. D. Collins, M. W. Washabaugh. “The Hofmeister effect and the behaviour of water at interfaces.” *Q. Rev. Biophys. 4*, 323–422 (1985).

[146] M. C. Gurau, S. M. Lim, E. T. Castellana, F. Albertorio, S. Kataoka, P. S. Cremer. “On the mechanism of the Hofmeister effect.” *J. Am. Chem. Soc. 126*, 10522–10523 (2004).

[147] X. Chen, T. Yang, S. Kataoka, P. S. Cremer. “Specific ion effects on interfacial water structure near macromolecules.” *J. Am. Chem. Soc. 129*, 12272–12279 (2007).

[148] W. Kunz, J. Henle, B. W. Ninham. “About the science of the effect of salts: Franz Hofmeister’s historical papers.” *Curr. Opin. Colloid Interface Sci. 9*, 19–37 (2004).

[149] Y. Zhang, S. Furyk, D. E. Bergbreiter, P. S. Cremer. “Specific ion effects on the water solubility of macromolecules: PNIPAM and the Hofmeister series.” *J. Am. Chem. Soc. 127*, 14505–14510 (2005).

[150] Y. Zhang, P. S. Cremer. “Interactions between macromolecules and ions: the Hofmeister series.” *Curr. Opin. Chem. Biol. 10*, 658–663 (2006).

[151] S. Z. Moghaddam, E. Thormann. “The Hofmeister series: specific ion effects in aqueous polymer solutions.” *J. Colloid Interface Sci. 555*, 615–635 (2019).

[152] H. I. Okur, J. Hladílková, K. B. Rembert, Y. Cho, J. Heyda, J. Dzubiella, P. S. Cremer, P. Jungwirth. “Beyond the Hofmeister series: ion-specific effects on proteins and their biological functions.” *J. Phys. Chem. B 121*, 1997–2014 (2017).

[153] L. Zhao, K. Ma, Z. Yang. “Changes of water hydrogen bond network with different externalities.” *Int. J. Mol. Sci. 16*, 8454–8489 (2015).

[154] W. Kunz. “Specific ion effects in colloidal and biological systems.” *Curr. Opin. Colloid Interface Sci. 15*, 34–39 (2010).

[155] R. Sharma, P. Bahadur. “Effect of different additives on the cloud point of a polyethylene oxide-polypropylene oxide-polyethylene oxide block copolymer in aqueous solution.” *J. Surfactants Deterg. 5*, 263–268 (2002).

[156] T. Arakawa, S. N. Timasheff. “Preferential interactions of proteins with salts in concentrated solutions.” *Biochemistry 21*, 6545–6552 (1982).

[157] D. A. Lapkin, A. v. Emelyanov, V. A. Demin, V. v. Erokhin, L. A. Feigin, P. K. Kashkarov, M. v. Kovalchuk. “Polyaniline-based memristive microdevice with high switching rate and endurance.” *Appl. Phys. Lett. 112*, 043302 (2018).

[158] M. Kulkarni, S. K. Apte, S. D. Naik, J. D. Ambekar, B. B. Kale. “Ink-jet printed conducting polyaniline based flexible humidity sensor.” *Sensors and Actuators, B: Chemical 178*, 140–143 (2013).

[159] M. Kulkarni, A. K. Viswanath. “Sulphonic acids doped poly(N-ethyl aniline): A material for humidity sensing application.” *Polym. Eng. Sci. 47*, 1621–1629 (2007).

[160] K. Lee, S. Cho, H. P. Sung, A. J. Heeger, C. W. Lee, S. H. Lee. “Metallic transport in polyaniline.” *Nature 441*, 65–68 (2006).

[161] E. T. Kang, K. G. Neoh, K. L. Tan. “The protonation-deprotonation hysteresis in polyaniline.” *Polymer (Guildf) 37*, 925–929 (1996).

[162] S. di Tommaso, P. Rotureau, O. Crescenzi, C. Adamo. “Oxidation mechanism of diethyl ether: A complex process for a simple molecule.” *Phys. Chem. Chem. Phys. 13*, 14636–14645 (2011).

[163] W. G. Lloyd. “The low temperature autoxidation of diethylene glycol.” *J. Am. Chem. Soc. 78*, 72–75 (1956).

[164] F. E. Bailey, R. W. Callard. “Some properties of poly(ethylene oxide) in aqueous solution.” *J. Appl. Polym. Sci. 1*, 56–62 (1959).

[165] E. Itabashi. “Identification of electrooxidation products of thiocyanate in acidic solution by thin-layer spectroelectrochemistry.” *J. Electroonal. Chem., 177*, 311–315 (1984).

[166] F. Seel, E. Müller. “Zur Kenntnis des Rhodans und seiner Verbindungen.” *Chem. Ber. 88*, 1747–1755 (1955).

[167] H. Lecher, M. Wittwer, W. Speer. “Über die Amide der unterrhodanigen Säure.” *Ber. Dtsch. Chem. Ges. 56*, 1104–1112 (1923).

[168] G. Stedman, P. A. E. Whincup. “Oxidation of metal thiocyanates by nitric and nitrous acid. Part I. Products.” *J. Chem. Soc. A* 1145–1148 (1967).

[169] K. Xu. “Nonaqueous liquid electrolytes for lithium-based rechargeable batteries.” *Chem. Rev. 104*, 4303–4417 (2004).

[170] P. W. Atkins. *Physical Chemistry*. (W.H. Freeman & Co, 1997).

[171] P. Vanýsek. "Electrochemical series." in *Handbook of Chemistry and Physics* (ed. Haynes, W. M.) 5–80 (CRC Press, 2012).

[172] L. Pauling. "The sizes of ions and the structure of ionic crystals." *J. Am. Chem. Soc. 49*, 765–790 (1927).

[173] J. P. Guthrie. "Hydrolysis of esters of oxy acids: pKa values for strong acids; Brønsted relationship for attack of water at methyl; free energies of hydrolysis of esters of oxy acids; and a linear relationship between free energy of hydrolysis and pKa holding over a ran." *Can. J. Chem. 56*, 2342–2354 (1979).

[174] B. Brunetti, V. Piacente, P. Scardala. "Torsion vapor pressures and sublimation enthalpies of aluminum trifluoride and aluminum trichloride." *J. Chem. Eng. Data 54*, 940–944 (2009).

[175] B. Stöffler, G. Luft. "Oxidative degradation of p-toluenesulfonic acid." *Chemosphere 38*, 1035–1047 (1999).

[176] J. G. Hardy, L. M. Römer, T. R. Scheibel. "Polymeric materials based on silk proteins." *Polymer (Guildf) 49*, 4309–4327 (2008).

[177] C. Tanford, K. Kawahara, S. Lapanje. "Proteins in 6-M guanidine hydrochloride. Demonstration of random coil behavior." *J. Biol. Chem. 241*, 1921–1923 (1966).

[178] G. I. Makhatadze, P. L. Privalov. "Protein interactions with urea and guanidinium chloride. A calorimetric study." *J. Mol. Biol. 226*, 491–505 (1992).

[179] E. P. O'Brien, R. I. Dima, B. Brooks, D. Thirumalai. "Interactions between hydrophobic and ionic solutes in aqueous guanidinium chloride and urea solutions: Lessons for protein denaturation mechanism." *J. Am. Chem. Soc. 129*, 7346–7353 (2007).

[180] A. Albert, R. Goldacre, J. Phillips. "The strength of heterocyclic bases." *J. Chem. Soc. 455*, 2240–2249 (1948).

[181] S. Battistoni, A. Verna, S. L. Marasso, M. Cocuzza, V. Erokhin. "On the Interpretation of Hysteresis Loop for Electronic and Ionic Currents in Organic Memristive Devices." *Phys. Status Solidi A 217*, 4–7 (2020).

[182] R. S. Geeley, W. T. Smith, R. W. Stoughton, M. H. Lietzke. "Electromotive force studies in aqueous solutions at elevated temperatures. I. The standard potential of the silver-silver chloride electrode." *J. Phys. Chem. 64*, 652–657 (1960).

[183] S. Battistoni, A. Dimonte, V. Erokhin. "Spectrophotometric characterization of organic memristive devices." *Org. Electron. 38*, 79–83 (2016).

[184] R. Sajapin, R. Burganova, T. Berzina, S. Iannotta. "Observation and visualization of the Observation and visualization of the redox transient switching process of a PANI-based organic memristive device." *MEMRISYS 2019 Proceedings* (2019).

[185] M. Kalaji, L. Nyholm, L. M. Peter. "A microelectrode study of the influence of pH and solution composition on the electrochemical behaviour of polyaniline films." *J. Electroanal. Chem. 313*, 271–289 (1991).

[186] X. H. Xia, J. P. Tu, J. Zhang, X. L. Wang, W. K. Zhang, H. Huang. "A highly porous NiO/polyaniline composite film prepared by combining chemical bath deposition and electro-polymerization, and its electrochromic performance." *Nanotechnol. 19*, 465701 (2008).

[187] D. A. Lapkin, A. N. Korovin, S. N. Malakhov, A. v. Emelyanov, V. A. Demin, V. v. Erokhin. "Optical monitoring of the resistive states of a polyaniline-based memristive device." *Adv. Electron. Mater. 6*, 1–5 (2020).

[188] R. Cox, C. Guan, D. J. Hayes. "Microjet printing of micro-optical interconnects and sensors." *SPIE Proceedings 3952*, 400–407 (2000).

[189] S. Khan, L. Lorenzelli, R. S. Dahiya. "Technologies for printing sensors and electronics over large flexible substrates: A review." *IEEE Sens. J. 15*, 3164–3185 (2015).

[190] J. Alamán, R. Alicante, J. I. Peña, C. Sánchez-Somolinos. "Inkjet printing of functional materials for optical and photonic applications." *Materials 9*, 910 (2016).

[191] K. K. B. Hon, L. Li, I. M. Hutchings. "Direct writing technology-Advances and developments." *CIRP Ann. Manuf. Technol. 57*, 601–620 (2008).

[192] J. U. Park *et al.* "High-resolution electrohydrodynamic jet printing." *Nat. Mater. 6*, 782–789 (2007).

[193] G. H. McKinley, M. Renardy. "Wolfgang von Ohnesorge." *Physics of Fluids 23*, 127101 (2011).

[194] N. Reis, C. Ainsley, B. Derby. "Ink-jet delivery of particle suspensions by piezoelectric droplet ejectors." *J. Appl. Phys. 97*, 094903 (2005).

[195] D. Soltman, V. Subramanian. "Inkjet-printed line morphologies and temperature control of the coffee ring effect." *Langmuir 24*, 2224–2231 (2008).

[196] P. He, B. Derby. "Controlling coffee ring formation during drying of inkjet printed 2D inks." *Adv. Mater. Interfaces 4*, 1700944 (2017).

[197] T. Kajiya, W. Kobayashi, T. Okuzono, M. Doi. "Controlling the drying and film formation processes of polymer solution droplets with addition of small amount of surfactants." *J. Phys. Chem. B 113*, 15460–15466 (2009).

[198] L. Wang, J. Wang, Y. Huang, M. Liu, M. Kuang, Y. Li, L. Jiang, Y. Song. "Inkjet printed colloidal photonic crystal microdot with fast response induced by hydrophobic transition of poly(N-isopropyl acrylamide)." *J. Mater. Chem. 22*, 21405–21411 (2012).

[199] G. Hu *et al.* "A general ink formulation of 2D crystals for wafer-scale inkjet printing." *Sci. Adv. 6*, eaba5029 (2020).

[200] M. Majumder *et al.* "Overcoming the 'coffee-stain' effect by compositional marangoni-flow-assisted drop-drying." *J. Phys. Chem. B 116*, 6536–6542 (2012).

[201] B. J. Kang, C. K. Lee, J. H. Oh. "All-inkjet-printed electrical components and circuit fabrication on a plastic substrate." *Microelectron. Eng. 97*, 251–254 (2012).

[202] V. Gevaerts, A. Biezemans, H. Mannetje, J. Bosman, H. Linden. “Inkjet printing assisted monolithic interconnection of CIGS using shunt-free laser scribing.” *IEEE Photovoltaic Specialists Conference Proceedings* 1779–1781 (2020).

[203] M. Buffiere, K. Ali, E. Fares, A. Samara, A. R. Shetty, O. al Hassan, A. Belaidi. “Inkjet-printed compact TiO2 electron transport layer for perovskite solar cells.” *Energy Technol. 8*, 2000330 (2020).

[204] B. A. Kuzubasoglu, E. Sayar, S. K. Bahadir. “Inkjet-Printed CNT/PEDOT:PSS temperature sensor on a textile substrate for wearable intelligent systems.” *IEEE Sens. J. 21*, 13090–13097 (2021).

[205] X. Wu *et al.* “Large-area fabrication of high-performance flexible and wearable pressure sensors.” *Adv. Electron. Mater. 6*, 1901310 (2020).

[206] E. Bihar, S. Wustoni, A. M. Pappa, K. N. Salama, D. Baran, S. Inal. “A fully inkjet-printed disposable glucose sensor on paper.” *npj Flex. Electron. 2*, 1–8 (2018).

[207] M. Medina-Sánchez, C. Martínez-Domingo, E. Ramon, A. Merkoçi. “An inkjet-printed field-effect transistor for label-free biosensing.” *Adv. Funct. Mater. 24*, 6291–6302 (2014).

[208] Y. Li, N. Wang, A. Yang, H. Ling, F. Yan. “Biomimicking stretchable Organic Electrochemical Transistor.” *Adv. Electron. Mater. 5*, 1900566 (2019).

[209] E. Bilbao, S. Kapadia, V. Riechert, J. Amalvy, F. N. Molinari, M. M. Escobar, R. R. Baumann, L. N. Monsalve. “Functional aqueous-based polyaniline inkjet inks for fully printed high-performance pH-sensitive electrodes.” *Sens. Actuator B Chem. 346*, 130558 (2021).

[210] O. Ngamna, A. Morrin, A. J. Killard, S. E. Moulton, M. R. Smyth, G. G. Wallace. “Inkjet printable polyaniline nanoformulations.” *Langmuir 23*, 8569–8574 (2007).

[211] G. J. Marquez, M. J. Renn, W. D. Miller. “Aerosol-based direct-write of biological materials for biomedical applications.” *MRS Proceedings 698*, Q5.2.1-Q5.2.7 (2002).

[212] M. Smith, Y. S. Choi, C. Boughey, S. Kar-Narayan. “Controlling and assessing the quality of aerosol jet printed features for large area and flexible electronics.” *Flex. Print. Electron. 2*, 015004 (2017).

[213] J. Navratil, A. Hamacek, J. Reboun, R. Soukup. “Perspective methods of creating conductive paths by Aerosol Jet Printing technology.” *Int. Spring Semin. Electron. Technol. Proceedings* 36–39 (2015).

[214] N. J. Wilkinson, M. A. A. Smith, R. W. Kay, R. A. Harris. “A review of aerosol jet printing - a non-traditional hybrid process for micro-manufacturing.” *J. Adv. Manuf. Technol. 105*, 4599–4619 (2019).

[215] E. B. Secor. “Principles of Aerosol jet Printing.” *Flex. Print. Electron. 3*, 035002 (2018).

[216] C. Goth, S. Putzo, J. Franke. “Aerosol Jet Printing on rapid prototyping materials for fine pitch electronic applications.” *IEEE Electron. Comp. Technol. Conf. Proceedings* 1211–1216 (2011).

[217] G. Chen, Y. Gu, H. Tsang, D. R. Hines, S. Das. "The effect of droplet sizes on overspray in Aerosol-Jet Printing." *Adv. Eng. Mater. 20*, 1701084 (2018).

[218] A. Mahajan, C. D. Frisbie, L. F. Francis. "Optimization of aerosol jet printing for high-resolution, high-aspect ratio silver lines." *ACS Appl. Mater. Interfaces 5*, 4856–4864 (2013).

[219] J. A. Paulsen, M. Renn, K. Christenson, R. Plourde. "Printing conformal electronics on 3D structures with aerosol jet technology." *Future of Instrument. Int. Workshop Proceedings* 47–50 (2012).

[220] A. Mette, P. L. Richter, M. Hörteis, S. W. Glunz. "Metal aerosol jet printing for solar cell metallization." *Prog. Photovolt.: Res. Appl. 15*, 621–627 (2007).

[221] S. Padovani, S. Sinesi, S. Priante, M. Antonipieri, A. del Negro, V. Zoellmer, M. Maiwald, M. Hedges. "New method for head-up display realization by mean of chip on board and aerosol jet process." *ESTC 2010 Proceedings* 3–5 (2010).

[222] Z. Zhan, L. Yu, J. Wei, C. Zheng, D. Sun, L. Wang. "Application of aerosol jet technology in through-via interconnection for MEMS wafer-level packaging." *Microsyst. Technol. 21*, 451–455 (2015).

[223] A. A. Gupta, A. Bolduc, S. G. Cloutier, R. Izquierdo. "Aerosol jet printing for printed electronics rapid prototyping." *IEEE ISCAS Proceedings* 866–869 (2016).

[224] W. Xie, X. Zhang, C. Leighton, C. D. Frisbie. "2D Insulator–metal transition in aerosol-jet-printed electrolyte-gated indium oxide thin film transistors." *Adv. Electron. Mater. 3*, 1600369 (2017).

[225] F. Zare Bidoky, W. J. Hyun, D. Song, C. D. Frisbie. "Printed, 1 V electrolyte-gated transistors based on poly(3-hexylthiophene) operating at >10 kHz on plastic." *Appl. Phys. Lett. 113*, 053301 (2018).

[226] P. Yang, T. Zhai, B. Yu, G. Du, B. Mi, X. Zhao, W. Deng. "Toward all aerosol printing of high-efficiency organic solar cells using environmentally friendly solvents in ambient air." *Journal of Materials Chemistry A 9*, 17198–17210 (2021).

[227] R. Eckstein, T. Rödlmeier, T. Glaser, S. Valouch, R. Mauer, U. Lemmer, G. Hernandez-Sosa. "Aerosol-jet printed flexible organic photodiodes: semi-transparent, color neutral, and highly efficient." *Adv. Electron. Mater. 1*, 1500101 (2015).

[228] C. S. Jones, X. Lu, M. Renn, M. Stroder, W. S. Shih. "Aerosol-jet-printed, high-speed, flexible thin-film transistor made using single-walled carbon nanotube solution." *Microelectron. Eng. 87*, 434–437 (2010).

[229] R. Liu, F. Shen, H. Ding, J. Lin, W. Gu, Z. Cui, T. Zhang. "All-carbon-based field effect transistors fabricated by aerosol jet printing on flexible substrates." *J. Micromech Microeng. 23*, 065027 (2013).

[230] I. Grunwald, E. Groth, I. Wirth, J. Schumacher, M. Maiwald, V. Zoellmer, M. Busse. "Surface biofunctionalization and production of miniaturized sensor structures using aerosol printing technologies." *Biofabrication 2*, 014106 (2010).

[231] G. Tarabella, D. Vurro, S. Lai, P. D'Angelo, L. Ascari, S. Iannotta. "Aerosol jet printing of PEDOT:PSS for large area flexible electronics." *Flex. Print. Electron. 5*, 014005 (2020).

[232] J. Fan, A. A. Forero Pico, M. Gupta. "A functionalization study of aerosol jet printed organic electrochemical transistors (OECTs) for glucose detection." *Materials Advances 2*, 7445–7455 (2021).

[233] D. Majak, J. Fan, S. Kang, M. Gupta. "Delta-9-tetrahydrocannabinol (Δ9-THC) sensing using an aerosol jet printed organic electrochemical transistor (OECT)." *J. Mater. Chem. B 9*, 2107–2117 (2021).

[234] K. Parate *et al.* "Aerosol-jet-printed graphene immunosensor for label-free cytokine monitoring in serum." *ACS Appl. Mater. Interfaces 12*, 8592–8603 (2020).

[235] C. Fisher, B. J. Warmack, Y. Yu, L. N. Skolrood, K. Li, P. C. Joshi, T. Saito, T. Aytug. "All-aerosol-jet-printed highly sensitive and selective polyaniline-based ammonia sensors: a route toward low-cost, low-power gas detection." *J. Mater. Sci. 56*, 12596–12606 (2021).

[236] F. Ratuchne, M. Danczuck, E. G. de Castro. "Enhanced stability and conductivity of (polyaniline/chitosan) composites." *Orbital 10*, 239–246 (2018).

[237] A. Cifarelli, A. Parisini, T. Berzina, S. Iannotta. "Organic memristive element with chitosan as solid polyelectrolyte." *Microelectron. Eng. 193*, 65–70 (2018).

[238] A. Lesch, D. Momotenko, F. Cortés-Salazar, I. Wirth, U. M. Tefashe, F. Meiners, B. Vaske, H. H. Girault, G. Wittstock. "Fabrication of soft gold microelectrode arrays as probes for scanning electrochemical microscopy." *J. Electroanal. Chem 666*, 52–61 (2012).

[239] A. Cifarelli, T. Berzina, A. Parisini, V. Erokhin, S. Iannotta. "Polysaccarides-based gels and solid-state electronic devices with memresistive properties: Synergy between polyaniline electrochemistry and biology." *AIP Advances 6*, 111302 (2016).

[240] A. Cifarelli, A. Parisini, S. Iannotta, T. Berzina. "Organic memristive devices based on pectin as a solid polyelectrolyte." *Microelectron. Eng. 185–186*, 55–60 (2018).

[241] L. D. Koh *et al.* "Structures, mechanical properties and applications of silk fibroin materials." *Prog. Polym. Sci. 46*, 86–110 (2015).

[242] D. N. Rockwood, R. C. Preda, T. Yücel, X. Wang, M. L. Lovett, D. L. Kaplan. "Materials fabrication from Bombyx mori silk fibroin." *Nature Protoc. 6*, 1612–1631 (2011).

[243] D. H. Kim *et al.* "Dissolvable films of silk fibroin for ultrathin conformal bio-integrated electronics." *Nat. Materials 9*, 511–517 (2010).

[244] C. Vepari, D. L. Kaplan. "Silk as a biomaterial." *Prog. Polym. Sci. 32*, 991–1007 (2007).

[245] X. Wang, E. Wenk, A. Matsumoto, L. Meinel, C. Li, D. L. Kaplan. "Silk microspheres for encapsulation and controlled release." *J. Control. Release 117*, 360–370 (2007).

[246] M. A. Tomeh, R. Hadianamrei, X. Zhao. "Silk fibroin as a functional biomaterial for drug and gene delivery." *Pharmaceutics 11*, 494 (2019).

[247] H. J. Kim, H. S. Kim, A. Matsumoto, I. J. Chin, H. J. Jin, D. L. Kaplan. “Processing windows for forming silk fibroin biomaterials into a 3D porous matrix.” *Aust. J. Chem. 58*, 716–720 (2005).

[248] Y. Wang, H. J. Kim, G. Vunjak-Novakovic, D. L. Kaplan. “Stem cell-based tissue engineering with silk biomaterials.” *Biomaterials 27*, 6064–6082 (2006).

[249] U.-J. Kim, J. Park, C. Li, H.-J. Jin, R. Valluzzi, D. L. Kaplan. “Structure and properties of silk hydrogels.” *Biomacromol. 5*, 786–792 (2004).

[250] C. H. Wang, C. Y. Hsieh, J. C. Hwang. “Flexible organic thin-film transistors with silk fibroin as the gate dielectric.” *Adv. Mater. 23*, 1630–1634 (2011).

[251] Y. Xiao, K. Kalaitzidou, D. Yao, W. H. Yeo, T. A. L. Harris. “Challenges and advances in Aerosol Jet Printing of regenerated silk fibroin solutions.” *Adv. Mater. interfaces 7*, 1902005 (2020).

[252] J. W. Seo, H. Kim, K. H. Kim, S. Q. Choi, H. J. Lee. “Calcium-modified silk as a biocompatible and strong adhesive for epidermal electronics.” *Adv. Funct. Mater. 28*, 1800802 (2018).